Alma Mater Studiorum – Università di Bologna

DOTTORATO DI RICERCA IN

Ingegneria Civile, Chimica, Ambientale e dei materiali

Ciclo XXXI

Settore Concorsuale: 08/B1 – GEOTECNICA

Settore Scientifico Disciplinare: ICAR/07 – GEOTECNICA

Dynamic analyses of geotechnical problems using advanced constitutive formulations: soil parameter calibration and numerical implementation

Presentata da: Arianna Poli - 0000771886

Coordinatore Dottorato

Prof. Luca Vittuari

Supervisore

Prof.ssa Laura Tonni

Co-supervisore

Prof. Guido Gottardi

Esame finale anno 2019

Abstract

The doctoral research has focused on an accurate study of granular soil behaviour in static and seismic conditions, with special reference to seismic-induced phenomena such as liquefaction and lateral spreading whose evidences have been observed during the 2012 Emilia earthquake. The basic aim of the study has been to develop an innovative numerical tool for reproducing the mechanical response of silty-sand soils under different loading and drainage conditions adopting an advanced constitutive model, which could be calibrated from tests that are routinely performed in geotechnical laboratory. Thus, an experimental testing programme, including triaxial tests, standard and K_0-cell oedometer tests, has been carried out on a number of sandy and silty samples extracted from the subsoil of Scortichino (Emilia-Romagna, Northern Italy), a village struck by the 2012 seismic sequence. Therefore, the experimental results have been interpreted taking a *Generalized Plasticity*-based model for sands as reference constitutive framework. In particular, starting from the existing formulation devised by Pastor et al. (1990) and later extended by Tonni et al. (2006) and Cola et al. (2008), a few modifications have been introduced to the original constitutive equations in order to improve the predictive capability. An in-depth calibration study has been performed and an effective procedure to obtain the model parameters has been defined. For this purpose, a *MATLAB* numerical routine has been developed. Finally, the constitutive equations have been implemented in a *2D FE* code (*GeHoMADRID*) and a detailed numerical model of the riverbank has been realized in order to perform advanced dynamic analyses and to study both the stress-strain behaviour and the seismic-induced effects within the investigated granular deposits during the 2012 Emilia earthquake.

Acknowledgments

At the end of this wonderful experience, I am extremely grateful for all the teachings and people I got to be in contact with and helped me out every single day: this aim would not have been possible without each lovely person that has crossed my path.

First, I would like to acknowledge my advisor Prof. Tonni for giving me the chance to undertake this experience as a PhD student. She has been a constant source of ideas and guidance in the development of this research.

I would like to express my sincere appreciation to Irene, who supported me during the beginning of this study, the laboratory technician Mario, for kindly helping me out throughout the experimental programme, and all my coworkers at the University of Bologna. The support of this study by the *CEDEX* is gratefully acknowledged. In particular, my most felt thanks is to my supervisor Pablo for any brilliant advices, both as a teacher and as a person. I wish to express my sincere gratitude for giving me the valuable opportunity to work with him.

A special thanks goes to my family for the time dedicated and for the sacrifices made for me in the daily life. I would like also to thank my wonderful friends for their encouragements and understanding during the realization of this thesis.

Last, but definitely not least, a very heartfelt thanks to Simone for his love, for taking care of me and for sharing each moment: you are the better half.

In conclusion, it has been a great experience and I would suggest everybody, if given the possibility, to live this adventure which enriched me so much: I learnt, I grew, and it most certainly defined who I am as a researcher and a person.

"*If a little dreaming is dangerous, the cure for it is not to dream less, but to dream more, to dream all the time.*" *(Marcel Proust)*

Table of contents

List of figures

List of tables

List of symbols and acronyms

$A = NaAlSi_3O_8$: Albite

A_c: current cross-sectional sample area (m^2, cm^2, mm^2)

A_{co}: constant cross-sectional sample area (m^2, cm^2, mm^2)

$A_d, d_0, D_0, k_d, k_H, M_f, M_f^*, m_d,\ n^*, n_f, R_d, \alpha_f, \beta_s, \beta_{g0}, \beta_H, \ddot{\gamma}, \ddot{\mu}$: model parameters

A_i: partial derivatives of the stress invariants

$ASTM$: American Society for Testing Materials

b: body force per unit mass vector (N/kg)

$B = SN$: matrix with the derivates of the shape functions N

B_s: Skempton parameter

BH: borehole

$C = CaCO_3$: Calcium Carbonate

C: compliance coefficient tensor, with superscript e for elastic; with subscript L for loading and U for unloading

C_c: compressibility matrix

C_i: components of the loading vector

CH: inorganic fat clay with high plasticity

CO_2: Carbon dioxide

$CPTU$: Cone Penetration Test

CS: $Critical\ State$

CSL: $Critical\ State$ Line

CSS: $Critical\ Steady\ State$

$CSS - n$: Cyclic Simple Shear test, with n for number of test

$Cu\ K\alpha$: $X-$ray diffraction pattern (copper)

d_f: gradient to yield surface

d_g: dilatancy

D_t: tangent elasto − plastic stiffness tensor, with superscript e for elastic; with subscript L for loading and U for unloading

D_t^e: tangent elastic stiffness tensor

D_{50}: diameter corresponding to 50 % of passing mass (mm)

$d\sigma$: total stress increment (Pa, kPa, MPa)

$d\sigma'$: effective stress increment (Pa, kPa, MPa)

$d\sigma^e$: elastic stress increment (Pa, kPa, MPa)

$d\sigma^p$: plastic stress increment (Pa, kPa, MPa)

dq: deviatoric increment (Pa, kPa, MPa)

DR: Relative Density (%)

$d\varepsilon$: strain increment, with subscript a for axial, r for radial, s for shear and v for volumetric; with superscript e for elastic and p for plastic

e: current void ratio

E: Young's modulus (Pa, kPa, MPa)

e_{crit}: void ratio at $Critical\ State$ condition

f: yield surface

F: force of the load cell (N, kN)

f^{ext}: vector of external forces

f^{int}: vector of internal forces

F^p: force vector in terms of pore pressure

F^u: force vector in terms of displacement

F_i: components of the plastic flow vector

F_p: applied vertical force (N, kN)

f_p: pore pressure load vector

f_s: lateral friction (Pa, kPa, MPa)

f_u: displacement load vector

$f(x), f(\eta), g(\eta), \beta_g$: function

$f'(x)$: derivative of the function $f(x)$

FC: Fine Content (%)

FE: Finite Element

g: plastic potential surface

G: residual force vector, with superscript p for pore pressure and u for displacement

$G_{max,N}$: maximum shear modulus at cycle N

G_n: vectorial equivalence at the boundary

G_s: specific gravity of soil grains

G_{sN}: secant shear modulus at cycle N

G_t: elastic shear stiffness modulus, with subscript ini for initial (Pa, kPa, MPa)

GNM: Generalized Newmark Method

Gp: Gauss point

GP: $Generalized\ Plasticity$

H: permeability matrix

H_f: "failure" component of H_L

H_{FC}: height of sample computed at the end of compression (cm, mm)

H_i: initial height (cm, mm)

$H_{L/U}$: plastic modulus under loading/unloading conditions (Pa, kPa, MPa)

h_n: height of specimen at the top of the current $l-$ th layer (cm, mm)

h_p: height of sample at the appearance of the shear plane (cm, mm)

H_s: component of H_L which accounts for the plastic stiffness degradation of soil

h_t: final height of specimen (cm, mm)

H_0: component of H_L which governs the isotropic compression of sands (Pa, kPa, MPa)

HDM: discrete memory factor

HR: Relative Humidity (%)

I: identity matrix

I_1: first invariant of the stress tensor

$ITACA$: Italian Accelerometric Archive

J: Jacobian matrix

J_2: second invariant of the deviatoric stress tensor

J_3: third invariant of the deviatoric stress tensor

k: permeability (m^3s/kg)

K: overall modulus computed on the NCL at the end of loading (Pa, kPa, MPa)

K_0: at rest coefficient of earth pressure

$K_0 - NCL$: $K_0 -$ Normal Compression Line

K_s: modulus of the grains (Pa, kPa, MPa)

K_t: tangent stiffness matrix

K_t^e: elastic volumetric stiffness modulus, with subscript ini for initial and ref for reference value (Pa, kPa, MPa)

K_{ts}: average bulk modulus of the soil skeleton (Pa, kPa, MPa)

K_w: bulk modulus of void fluid i.e. water (Pa, kPa, MPa)

K_π: bulk modulus of the phase π (Pa, kPa, MPa)

LL: Liquid Limit (%)

LP: loading path during the isotropic compression phase

LQ: liquefaction ratio

m: scale vector

M: mass matrix

M_g: slope of the $Critical\ State$ Line in the $q - p'$ plane

M_w: moment magnitude

MRN: Mirandola recording station

MT: moist tamping

n: normal at the boundary or normalized direction in the stress space

N: shape functions, with subscript p for pore pressure and u for displacement; with superscript e for element

N_c: number of test cycles

$n_g = \left(n_{g,v}, n_{g,s}\right)^T$: plastic flow direction vector, with subscript L for loading and U for unloading

n_j: j − th component of the normal n at the boundary

$n_l = (n_{l,v}, n_{l,s})^T$: loading direction vector

n_{li}: number of the current layer

n_p: porosity

n_t: total amounts of layers

NCL: Normal Compression Line

NR: Newton − Raphson

O: organic content (%)

OC: overconsolidated clay

OCR: overconsolidation ratio

$P = KMg_3(AlSi_3O_{10})(OH_2)$: Phlogopite

p': current mean effective stress (Pa, kPa, MPa)

p'_0: initial mean effective stress (Pa, kPa, MPa)

$\bar{p}$: pore pressure in vetorial notation

$\dot{p}$: velocity of the fluid flow with accent $\dot{\bar{p}}$ for the vectorial notation (m/s)

$\tilde{p}, \tilde{q}, \tilde{t}, \tilde{u}$: boundary conditions, with p for pressure of water, q for the normal outflow, t for traction and u for displacement

p_f: fluid component in the effective stress relationship (Pa, kPa, MPa)

p_g: air pressure (Pa, kPa, MPa)

p_w: pressure of water , with superscript e for element; with the accent $\bar{p}_w$ for the vectorial notation (Pa, kPa, MPa)

p_π: macroscopic pression of the phase π (Pa, kPa, MPa)

PGA: Peak Ground Acceleration (g)

PI: Plasticity Index (%)

PL: Plastic Limit (%)

PTP: Phase Transformation Point

q: deviatoric stress (Pa, kPa, MPa)

q_n: normal outflow

q_t: cone resistance (Pa, kPa, MPa)

$Q = SiO_2$: Quartz

Q: coupling matrix

Q^*: compressibility of water and grains (Pa^{-1}, kPa^{-1}, MPa^{-1})

QSS: $Quasi\ Steady\ State$

$Q4$: quadratic quadrilateral element

R_u: residual cyclic pore pressure

r: radius, with subscript c for current cross − sectional sample radius and FC at the end of compression (cm, mm)

R^2: coefficient of determination

RAN: Italian strong − motion network

S: strain matrix

S_g: degree of air saturation

S_w: degree of water saturation

$SandPZ$: Pastor et al. (1990) sand model

SBT: Soil behaviour type

$SDMT$: Seismic Dilatometer test

t: total traction

T: temperature (°)

t_i: time, with subscript f for failure, 100 for the end of consolidation (s, min)

tol: tollerance, followed by f for residual force and v for displacement and pore pressure

$TXCID$: Consolidated Drained Triaxial test

$TXCIU$: Consolidated Undrained Triaxial test

$T6$: quadratic triangular element

u: pore pressure (Pa, kPa, MPa)

$u = \left(u_{x,} u_y\right)^T$: displacement of the solid matrix , with superscript e for element; with the accent $\bar{u}$ for the vectorial notation (m, cm, mm)

U: coefficient of uniformity

u^*: normalized excess pore water pressure

$\dot{u}$: velocity, with the accent $\dot{\bar{u}}$ for the vectorial notation (m/s)

$\ddot{u}$: acceleration, with the accent $\ddot{\bar{u}}$ for the vectorial notation (N/kg)

U_n: under − compaction amounts calculated for the current li − th layer (%)

U_{ni}: under − compaction amounts chosen for the first layer (%)

U_{nt}: under − compaction amounts chosen for the final layer i.e. equal to zero (%)

UP: unloading path during the isotropic compression phase

$USCS$: Unified Soil Classification System

USS: $Ultimate\ \ Steady\ State$

v: current specific volume, with subscript f for final and 0 or ini for the initial condition

v_{crit} or v_c: specific volume at the $Critical\ State$

V_i: initial volume (mm^3)

v_{shear}: shear velocity (mm/s)

w: water content (%)

W_l: wet weight of soil for the l − th layer (N/m^3)

W_t: wet weight of soil (N/m^3)

x_i: i − th solution of a system of equations

XRD: X − ray diffractometer

α: slope of shear plane (rad)

α^*: constant parameter in the effective stress relationship

β_i: parameters of the truncated series expansion (i = 1,2,3)

γ: shear strain , with subscript c for cyclic, N for cycle N and tv for volumetric cyclic threshold (%)

γ_i: specific unit weight, with subscript d for dry, f for final, w for water and 0 for initial (N/m^3)

Γ_{CSL}: specific volume on the CSL at $p' = 1$kPa in the $v - p'$ plane

Γ_i: boundary, with subscript p for pressure of water, q for the normal outflow, t for traction and u for displacement

δ: partial derivate

δ^*: ratio at the appearance of the shearing plane

Δ: variation of measurement

ΔH: variation of the sample height (cm, mm)

Δu: pore pressure variation (Pa, kPa, MPa)

ΔV_{back}: variation of the back volume (cm^3, mm^3)

$\Delta\sigma_c$: cell pressure difference (Pa, kPa, MPa)

ε: strain, with subscript a for axial, f for failure, r for radial, s for shear and v for volumetric

ε_{err}: iterative error

ε_v^{π}: volumetric strain related to the pression p_{π} in the fluid phase

ζ: mobilized stress function, with subscript max for maximum

$\eta = \frac{q}{p'}$: stress ratio, with subscript p for peak and PTP for Phase Transformation Point

θ: diffraction angle (°) or stress invariant

$\hat{\theta}$: Lode angle (°)

ϑ: angle related to area correction due to shearing plane appearance (°)

κ_u: slope of the elastic unloading path in the $v - p'$ plane

λ: wavelength (Å, m)

λ_i: slope of CSL and NCL in the $v - p'$ plane with subscript NCL for the slope of NCL corresponding to a unloading – reloading cycle

ν: Poisson's ratio

ξ: accumulated deviatoric plastic strain

φ': angle of shearing resistance of the soil (°)

π: phase

ρ: density of the total composite (kg/m^3)

ρ_s: density of the solid particles (kg/m^3)

ρ_w: density of the water (kg/m^3)

σ: total stress tensor (Pa, kPa, MPa)

$\sigma' = \left(\sigma'_x, \sigma'_y, \sigma'_z, \tau'_{xy}\right)^T$: effective stress tensor with subscript a for axial, h for horizontal, r for radial, v for vertical and 0 for initial (Pa, kPa, MPa)

τ or τ_d: shear stress, with subscript c for cyclic (Pa, kPa, MPa) and N for cycle N

τ': normalized shear stress

$\psi = v - v_{crit}$: state parameter, with subscript ini for initial and PTP for Phase Transformation Point

Ω: domain

$\nabla = (\frac{\delta}{\delta x}, \frac{\delta}{\delta y})^T$: differential operator vector

$1D$: one dimensional

$2D$: two dimensional

1. Introduction

The proposed project aims at developing an analysis tool in order to study a number of liquefaction and lateral spreading phenomena occurred during the 2012 Emilia earthquake, using an advanced constitutive formulation: the *Generalized Plasticity* (*GP*) model originally designed by Pastor et al. (1990). In particular, the adopted constitutive formulation is a development of a *GP*-based model (Tonni et al., 2006; Cola et al., 2008) used to describe the stress-strain behaviour of loose and dense sands in drained and undrained conditions under static and cyclic loading, thus including soil liquefaction and cyclic mobility. The constitutive formulation combines the basic premises of *GP* theory with the *Critical State* framework and the state parameter concept, ψ (Been and Jefferies, 2000). In more detail, the research takes as reference a number of cases involving liquefaction and lateral spreading phenomena occurred in the provinces of Modena and Ferrara, partly of them recently analyzed using simplified methods (e.g. Vannucchi et al., 2012; Gottardi et al., 2014; Tonni et al., 2015a) and numerical approaches (Sinatra et al., 2015). This study is based on an existing database of geotechnical investigations, including both in-situ and laboratory tests, as well as on available soil samples recently taken from one of the sites struck by the seismic sequence. After a first interpretation of all the available experimental data, an additional testing programme has been performed in order to add further information on the mechanical response of soils. Particular attention is focused on sands, silty-sands and sandy-silts forming a riverbank and the relevant foundation subsoil, i.e. those sediments which experienced liquefaction and cyclic mobility phenomena during the 2012 Emilia earthquake. The experimental programme includes triaxial compression tests under drained (*TXCID*) and undrained (*TXCIU*) conditions, standard oedometer tests and K_0-oedometer tests (Dyvik et al., 1985), aimed at providing a better insight into static, cyclic and

dynamic characterization of soils. The abovementioned tests have been performed with the equipment currently in use at the geotechnical laboratory of Department of Civil, Chemical, Environmental and Materials Engineering (*DICAM*). Within the *GP*-constitutive framework, an in-depth calibration has been achieved to estimate the model parameters; for this aim, a numerical tool developed in a *MATLAB* code has allowed the comparison between experimental and predictive curves. A standard procedure to calibrate all the 12 independent model parameters has been proposed and the dependency on the state parameter (ψ) has permitted to define a single set of values over a wide range of confining pressures and densities. The *GP* equations have been implemented into a Finite Element numerical platform (*GeHoMADRID*), which allows coupled analyses in order to simulate the interaction between soil skeleton and pore pressure response in geotechnical problems. Advanced two-dimensional (*2D*) numerical analyses of the selected case-study have been performed: the accurate calibration in conjunction with the use of *GeHoMADRID*, developed by Prof. Manuel Pastor, Dr. Pablo Mira Mc Williams (PhD) and their coworkers at the Centro de Estudios y Experimentacion de Obras Publicas (*CEDEX*, Madrid, Spain), has allowed to reproduce the stress-strain behaviour of granular soils with good agreement between experimental and predictive data.

The outline of this study is exposed below in order to give a complete and coherent description on the research carried out. After the presentation of the significance of the topic and its potential outcomes in Chapter 1, Chapter 2 points out the background regarding advanced constitutive modelling to predict more accurately the stress-strain behaviour of soils under different loading conditions (i.e. seismic sequence). Chapter 3 deals with a theoretical framework of liquefaction with the aim to provide some insights to the characteristics of granular deposits prone to such phenomenon and to emphasize some of the key issues of current interest in the

subject area for exhaustive discussions in the following session (e.g. monotonic and cyclic responses). In Chapter 4, a specific case-study from the 2012 Emilia earthquake, concerning a riverbank severely damaged by the seismic sequence, is presented in detail, outlying the peculiarity of the seismic events. In particular, the earthquake sequence occurred in the Eastern part of the Po river valley brought human losses and significant damages to infrastructures and buildings in conjunction with evidences of extensive phenomena referable to cyclic mobility and liquefaction (e.g. sand boils, large surface cracks). Chapter 5 reviews the performed laboratory testing programme which consists of the geotechnical characterization of the soils tested, the description of the equipment and the interpretation of soil mechanical response. The *GP*-based constitutive model applied to predict the behaviour of both granular and cohesive soils is developed in Chapter 6, where the meaningful laws are also discussed somewhat in detail into the light of the recent innovations (e.g. stress-dilatancy and plastic modulus law). Chapter 7 reports the accurate calibration procedure of the constitutive parameters which permits to simulate isotropic triaxial drained/undrained tests. In particular, the plots of experimental and predictive response are shown to be consistent with a number of sandy/silty sandy samples extracted from the investigated area. Once verified that the model could be a useful tool at the macroscopic level, the formulation has been applied to realize a series of mesoscale analyses with respect to the whole riverbank. Thus, Chapters 8 summarizes the governing field equations used within the numerical code *GeHoMADRID*, paying particular attention to the algorithms adopted to solve the non-linear geotechnical problem. The *FE* modelling of the levee and the advanced analyses carried out are extensively depicted in Chapter 9, with emphasis on the numerical results. In the last chapter, conclusions are drawn and the future research is outlined with the hope to stimulate new developments

regarding this topic which has long been recognized as one of the most problematic and destructive features of sand behaviour.

2. State of art

Over the last 30 years, different constitutive laws have been proposed in geotechnical literature to describe soil behaviour. Indeed, the growing complexity of geotechnical problems to be solved has encouraged the development of advanced constitutive models, capable to simulate soil response in a large variety of loading conditions, taking the ever increasing quantity of reliable experimental data as a base.

It is worth observing that, in order to simulate soil behaviour under simple loading conditions, such as static, monotonic loading paths, standard elasto-plastic constitutive formulations generally turn out to be a rather satisfactory approach.

Figure 1 Liquefaction sand boils developed during the 2012 Emilia earthquake in the cemetery located in Sant'Agostino (Lo Presti et al., 2013).

Figure 2 Lateral spreading deformations along the river embankment of Scortichino (Lo Presti et al., 2013).

On the other hand, in seismic conditions, basic elasto-plastic constitutive formulations are not able to properly simulate the complex soil behaviour and the coupled response of soil skeleton and pore fluid, generally described by accumulation of plastic deformations and excess pore pressure development. As a result, typical seismic-induced phenomena in granular soils, such as liquefaction and cyclic mobility, cannot be appropriately analyzed. Indeed, it is well known that cyclic liquefaction implies the accumulation of pore pressures and the consequent tendency of effective stresses to decrease close to zero: it may occur in saturated loose deposits with contractive behaviour, causing some typical ground effects like sand boils (Figure 1) to tremendous instabilities known as flow failures. Cyclic mobility occurs in saturated dense sands with dilative behaviour and includes accumulation of permanent deformations: these deformations, termed lateral spreading (Figure 2), can occur on very gently sloping ground or on virtually flat ground adjacent to bodies of water and, when structures are present, can cause significant damages.

Due to the difficulties in the development, implementation and calibration of versatile and powerful constitutive formulations, geotechnical problems in seismic conditions are often solved using simplified approaches. These may include a large variety of analytical strategies: as an example, pseudo-static analyses assume very simple constitutive laws (tipically, rigid-plastic) and allow the assessment of global stability, whilst empirical methods (e.g. Youd et al., 2002; Kramer and Baska, 2007; Zhang et al., 2004), typically derived from back analyses of field case histories and based on simple constitutive laws, rely on the use of correlations to evaluate displacement entities taking in-situ testing as reference.

More sophisticated analyses, although still referred as “simplified dynamic analyses”, assume simplified constitutive law (e.g. visco-elastic models) and

generally provide predictions in terms of displacements: such approaches are generally adopted in numerical codes used for site response analyses.

Advanced dynamic analyses are assumed to provide a general description of a dynamic geotechnical problem, including prediction of effective stress amount, pore pressure distribution, strain assessment, permanent displacements and failure mechanisms. Such amount of information requires the use of an appropriate constitutive model implemented into a numerical code which allows coupled analyses to simulate the interaction between soil skeleton and pore pressure responses.

In this context, different and sophisticated research contributions may be found in geotechnical literature (e.g. Pastor et al., 1990; Park and Desai, 2000; Elgamal et al., 2003; Yang et al., 2003; Wu and Bauer, 1993; Kolymbas and Herle, 2005; Muir Wood, 1991, Mroz et al., 1978).

Among them, it is worth mentioning the versatile and innovative approach proposed by Pastor et al. (1990) and the one more recently formulation developed by Elgamal et al. (2003): both have been implemented into *FE* numerical platforms and can be used for solving general boundary value problems in seismic conditions. The first *GP* model has been developed by Pastor and Zienkiewicz in 1986, later dealt in Pastor et al. (1990), extending a bounding surface model (Zienkiewicz et al., 1985; Pastor et al., 1985). From this starting point, several recent improvements have been proposed in literature (Tonni et al., 2006; Cola and Tonni, 2007; Cola et al., 2008). According to *GP* premises, in Pastor et al. (1990), plastic deformations in soils occur at any stress level, irrespective of the stress increment direction, i.e. both in loading and unloading conditions. Besides, irreversible deformations are introduced without specifying any yield or plastic potential surfaces: indeed, the

gradients to these surfaces are explicitly defined instead of the functions themselves. The keystones of a *GP* model are the tangent elastic stiffness tensor (D_t^e), the loading direction (n_l), the plastic flow direction ($n_{gL/U}$) and the plastic moduli (H_L and H_U) under loading and unloading conditions.

The main advantage of the Pastor et al. (1990) sand model relies in its simplicity, versatility as well as in the ability to reproduce with good accuracy the stress-strain behaviour of dense and loose sands under both monotonic and cyclic loading conditions. As a result, it is able to simulate cyclic mobility and liquefaction and can therefore be successfully applied in seismic analysis of geotechnical problems.

The other constitutive approach is based on an elasto-plastic formulation with kinematic hardening and multiple yield surfaces: it is the Elgamal et al. (2003) model, suitable to describe liquefaction and cyclic mobility in sands. Multi-surface kinematic plasticity is an effective strategy in order to model soil hysteretic response. In this formulation, special attention is given to the deviatoric-volumetric strain coupling strength at large cyclic shear strain excursions (i.e. cyclic mobility). The yield surface is defined by the Lade and Duncan (1975) function. A number of similar surfaces, having a common apex, form the hardening zone. Each surface is associated with a constant plastic modulus. The outmost surface is designated as the failure surface. As usually postulated (Prevost, 1985), the low-strain (elastic) moduli and plastic yield surface moduli increase in proportion to the square root of effective confinement. In this model, the phenomenological interaction between shear and volume change (contraction or dilation) is typically handled by developing an appropriate flow rule, which significantly changes the characteristics of model response, in order to reproduce the salient cyclic mobility mechanisms and exercise more direct control over shear strain accumulation.

So far a substantial lack of research studies on advanced analyses of liquefaction and lateral spreading phenomena occurred during the May 2012 earthquake has been found, hence the application of the family of *GP* model turns out to be a promising and challenging contribution in order to gain a better insight into soil deformations and geotechnical failures induced by the seismic sequence.

3. Liquefaction phenomena

This chapter presents a review of the liquefaction features within a *Critical State* framework through the description of the clean sand behaviour under monotonic and cyclic loading and the introduction of an adequate background typically adopted to characterize the investigated soil response i.e. the state parameter (ψ). In more detail, the term *Critical State* (*CS*) defines the soil condition where large plastic deformations indefinitely occur with no changes in stress behaviour. Reached the *CS*, the rate of volumetric variation under drained conditions or the rate of pore pressure generation in undrained ones drops close to zero. Liquefaction is a phenomenon in which a soil turns out to be unstable and suddenly loses its strength, behaving as a liquid until a new stability condition. The large amounts of historical cases of failure as a consequence of this phenomenon emphasise the importance to increase the knowledge of this process that involves soils which are saturated, cohesionless, graded from clean sands to non-plastic silts, in a loose state with tendency to contractive response, in conditions that do not permit drainage even if just temporarily. Thus, a brief discussion on sand-silt mixture with non-plastic fines has been illustrated. Although the first studies of liquefaction have focused on clean sands, it is well known the occurrence of such phenomenon on mixture deposit (Boulanger et al., 1998; Bray et al., 2004). In particular, it has been understood that the presence of fine-grained percentage influences the resistance to liquefaction of the sand matrix (Carrera et al., 2011). On the contrary, the *CS* for sands does not depend on sample preparation technique (Ishihara, 1993; Zlatovic and Ishihara, 1997; Murthy et al., 2007), initial condition (Ishihara, 1993; Coop and Lee, 1993), stress history (Kato et al., 2001), shearing rate and path (Been et al., 1991) and drainage settings (Verdugo and Ishihara, 1996; Riemer and Seed, 1997).

3.1. Liquefaction within a *Critical State* framework

The phenomenon of liquefaction is widely described in the pioneering work by Kramer (1996), in which it is explained: "*The term liquefaction describes a number of different, though related phenomena in which the stiffness and the strength of the soil are reduced by earthquake shaking or other sudden loading*". The terminology, originally coined by Mogami and Kubo (1953), has historically been employed in conjunction with a variety of events that includes soil deformations caused by monotonic, transient or repeated disturbance of saturated cohesionless soils under undrained conditions (Kramer, 1996), since the duration of the cyclic shear stress application is shorter than the time required for drainage of water. Due to the occurrence of such mechanism, the pore water pressure increases and, when it becomes equal to the initial effective stress, soil particles of the granular material start to float in the fluid since no effective stress is acting on the sand matrix (Figure 3(b)); then, if drainage is permitted, the excess of pore water pressure dissipates expelling water towards the surface of the ground and the soil sedimentation takes place within layer (Figure 3(c)).

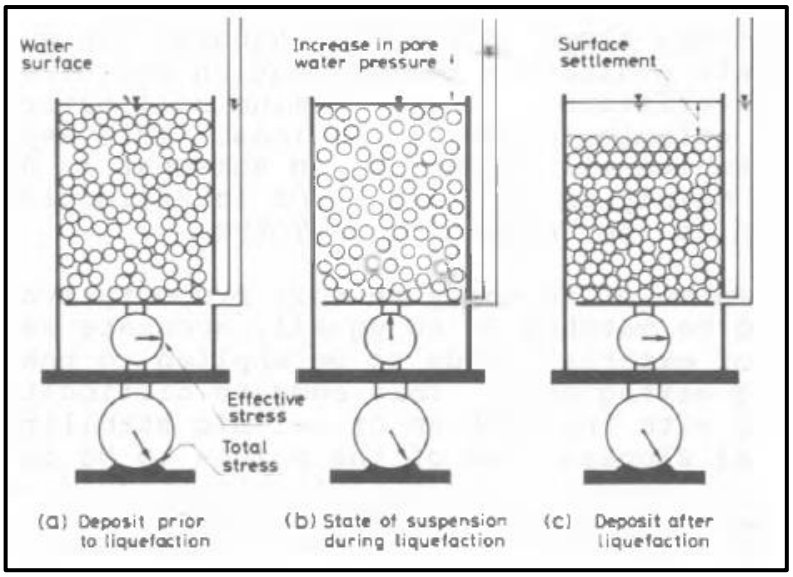

Figure 3 Transfer of state of deposition via liquefaction (Ishihara, 1985).

As well as Marcuson (1978) defined the liquefaction as the transformation of a granular soils from a solid to a liquefied state due to increased pore water and reduced effective pressure. The soils most susceptible of liquefaction are recent fills and Holocene deposits of alluvial, fluvial, marine, deltaic and wind-blown sediments that include cohesionless soils such as sands and very low plasticity silts. The compositional (e.g. grain size distribution, shape of granular soils) and state criteria (e.g. relative density, confining pressure) are significant for a complete understanding of the phenomenon (Kramer, 1996). In particular, well-graded soils are typically less susceptible to liquefaction than poorly graded ones since the reduced tendency for volumetric deformation of a well-graded deposit, due to the filling of voids with smaller particles (i.e. silts) within the solid structure, decreases the amount of excess pore pressure that can build up under undrained conditions. As widely studied by Altuhafi et al. (2013), particle morphology influences sand mechanical reponse; thus, liquefaction susceptibility depends also on the shape of the matrix grains i.e. soil deposits with rounded particles, such as depositional and fluvial areas, result more prone to liquefaction compared to soils with angular ones, which show higher friction characteristics. Liquefaction and related evidences have been responsible for tremendous amounts of damages in historical earthquakes around the world. Niigata earthquake in 1964 is one of the most meaningful cases that puts attention to this topic and, over the last years, many authors have given their contribution to analyze this phenomenon (e.g. Castro, 1969; Bardet, 2003; Yoshimine et al., 2006; Idriss and Boulanger, 2008) and in general the response of granular materials (e.g. McDowell, 2002; McDowell and Hau, 2004; Vincens et al., 2010; Sands et al., 2011). The shear-strain response of granular soils under monotonic or cyclic loading depends on several factors such as relative density (*DR*), confining effective pressure, fabric state, stress history and process of

deposition. It is well documented that liquefaction is not only a consequence of earthquakes. The Stava tailings dams, indeed, are examples of structures that were subject to static liquefaction in 1985 causing extensive destruction, as investigated in Carrera et al. (2011). Static liquefaction occurs in loose deposits subjected to monotonic shear stress under undrained conditions: during the loading stages, indeed, the pore pressure rises until soils liquefy. Monotonic undrained shear tests have been adopted by Yoshimine and Ishihara (1998) for the evaluation of the shear responses of sands. In a saturated soil element, the *Steady State* is a condition of deformation without increments of effective stress, flow of pore water and volume change. In a dense/medium dense sample, the shearing resistance under large strains is termed *Ultimate Steady State* (*USS*) of deformation. A dense soil reaches the *USS* developing a dilative behaviour (Figure 4(A)). In Figure 4 (B) and (C), intermediate specimens show a *Phase Transformation Point* (*PTP*), where the sand response changes from contractive to dilative. When the sand is relatively looser (Figure 4(C)), the *PTP* corresponds to a state of minimum of the mean effective stress, termed *Quasi Steady State* (*QSS*) of deformation (Alarcon-Guzman et al., 1988). Loose sands achieve the *Critical Steady State* (*CSS*) with a strain-softening response (Figure 4(D)): the deviator stress (q) after reaching an initial peak, reduces with shearing up to such minimum value. When the *SS* strength is zero, Lade and Yamamuro (1997) referred to "*complete liquefaction*". The deviatoric stress-strain and effective stress behaviour of a sandy soil under undrained shearing conditions can be also identified as flow (Figure 4(D)), non-flow (Figure 4(A)) and limited-flow (Figure 4(B)-(C)). As regards flow behaviour, Casagrande (1936) performed drained, strain-controlled triaxial tests on initially loose and initially dense specimens of sand at the same effective confining pressure.

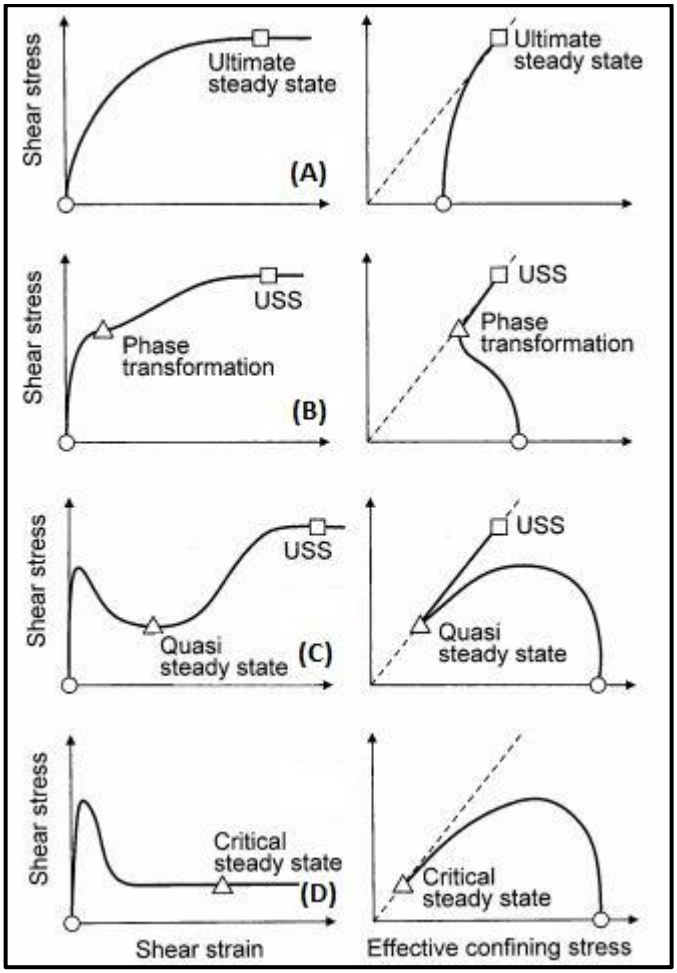

Figure 4 Undrained shear responses of granular soils (Yoshimine and Ishihara, 1998).

During the shearing phase, loose sands exhibit a contractive behaviour, decreasing the specific volumes; whereas, dense samples first slightly contract and later show a dilative response, increasing the specific volume (Figure 5).

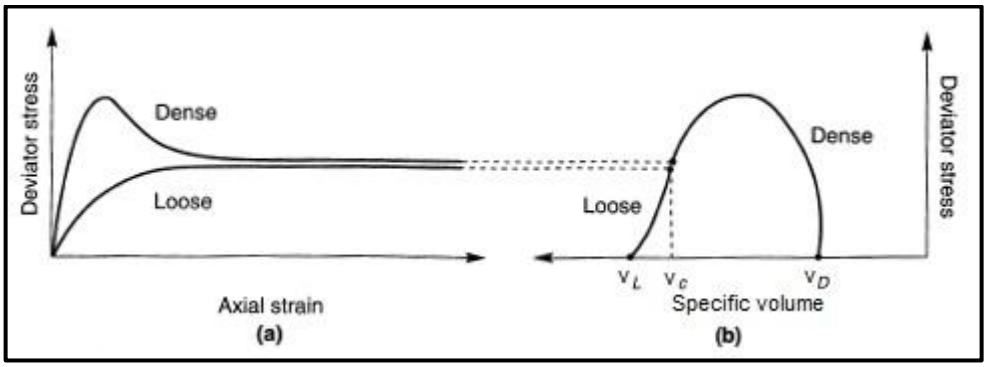

Figure 5 (a) Stress-strain and (b) stress-specific volume curves for loose and dense sands at the same confining effective pressure under drained conditions (Kramer, 1996).

At large deformations, both the specimens reach the same specific volume, termed *critical specific volume* (v_C or v_{CSL}), and mobilize an equivalent shearing resistance. It is important noting that sand fabric (i.e. the orientation of particle contact planes) evolves during shear occurrence and such reorientation ceases only at *Critical State* (Oda et al., 1985).

Under undrained cyclic loads, i.e. an earthquake, the grain matrix initially tends to contract and the consequential rearrangement of particles transfers normal stresses to the pore water. If the stress path reaches the *PTP*, the soil can dilate: thus, the stiffness increases until stress reversal occurs. If the induced shear strain exceeds the volumetric threshold, the plastic volumetric contraction, indeed, is counterbalanced by an elastic rebound of the skeleton under a reduced effective stress: the soil particles slide and rotate in order to increase the dilation phenomenon. When the stress path reverses, the soil fabric may arrange causing a contraction. As a result, the pore pressure rate increases again and, after a sufficient number of cycles, the soil stiffness and resistance drop to a very low value. The large fluctuations in stiffness and effective stress distribution cause the so-called "*banana-shaped*" stress-strain loops. The responses under cyclic conditions depend on confining pressure and density of the granular deposit. In particular, cyclic liquefaction develops in saturated loose sands with contractive behaviour. The accumulation of pore pressures and the consequent tendency of effective stresses to drop may produce instability conditions (e.g. flow failures or lost of bearing capacity) if the strength at the *CSS* is lower than the value needed for equilibrium (driving stress); if no shear stresses are needed at equilibrium, the dissipation of excess pore pressure causes some typical ground effects such as sand boils and volcanos (Figure 6).

Figure 6 Ejection of sand from water wells during the 2012 Emilia earthquake in San Carlo (Lo Presti et al., 2013).

Cyclic mobility occurs in saturated dense deposits with dilative behaviour. The buildup of permanent deformations, known as lateral spreading (Figure 7), causes significant damages also on very gently sloping ground or on virtually flat ground adjacent to bodies of water.

Figure 7 Lateral spreading evidences developed during the 2012 Emilia earthquake in S.Carlo (Lo Presti et al., 2013).

Undrained cyclic loading tests (e.g. cyclic simple shear tests, cyclic triaxial tests) can be performed to simulate the stress-strain behaviour of saturated soils during earthquake shaking and can be used to reproduce cyclic mobility and cyclic liquefaction in sands.

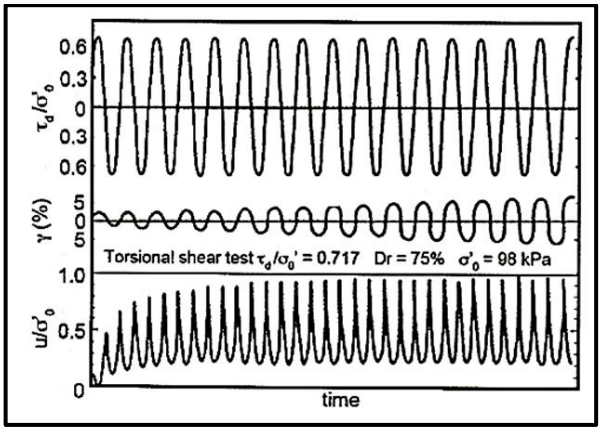

Figure 8 Results of torsional shear test on dense sand with DR = 75% (Ishihara, 1985).

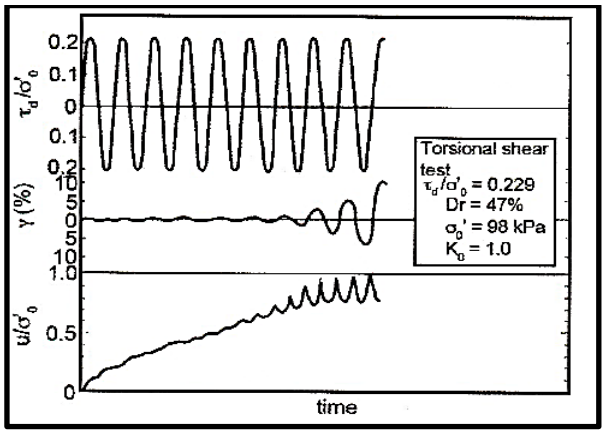

Figure 9 Results of torsional shear test on loose sand with DR = 47% (Ishihara, 1985).

As an example, Figure 8 shows typical results from a torsional shear test on a dense sand sample, which reaches cyclic mobility failure conditions. In Figure 9, cyclic liquefaction occurs in a loose specimen.

The non-linear cyclic response of soils can also employ the concept of the initial and degraded backbone curves in conjunction with the Masing criteria (Masing, 1926), originally devised for brass and then applied to liquefiable sands (e.g. Pyke and Beikae, 1993; Matasović and Vucetic, 1993; Pyke and Beikae, 1993) and to clays under triaxial (Idriss et al., 1978) and simple shear conditions (e.g. Idriss et al., 1980; Vucetic, 1990; Matasović and Vucetic, 1995; Lanzo et al., 1997). In greater detail, Vucetic (1994) shows as such shear modulus degradation and permanent pore water pressure development typically appear when the cyclic shear strain amplitude

exceeds a certain threshold value which alters irreversibly the microstructure and properties of soils. A representative soil element subjected to cyclic shear stresses (τ) and related shear strains (γ_c) which exceed a certain strain threshold (namely large strain level) results in a typical state of stresses depicted in Figure 10.

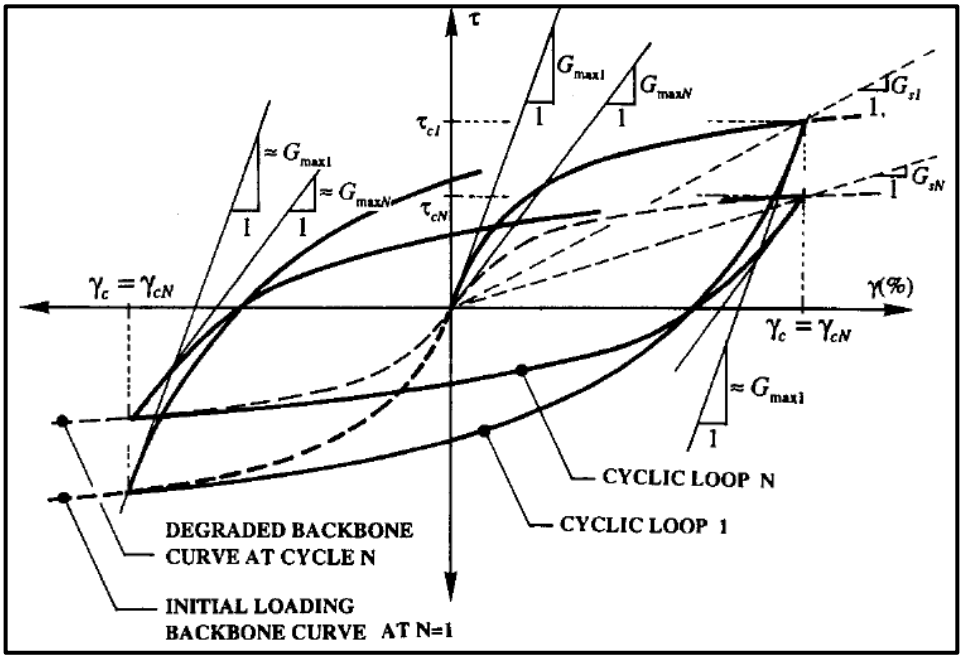

Figure 10 Schematic illustration of stress-strain behaviour during a cyclic strain-controlled simple shear test (Vucetic, 1994).

Figure 11 shows the results of cyclic degradation test on of saturated sands under undrained shear conditions. At large strain level, the pore-water pressure increase (Figure 11(c)) causing the drop of effective stresses, shear strength and moduli. Such process may trigger a full liquefaction and presents a reduction in normalized shear stress τ' (Figure 11(b)-(d)) and an increase in shear strain (Figure 11(a)-(d)) of the succeeding cyclic stress-strain loops in relation to that of the initial one. The positive part of the initial curve coincides with the initial monotonic stress-strain path, whereas its negative side is an extension into the negative region.

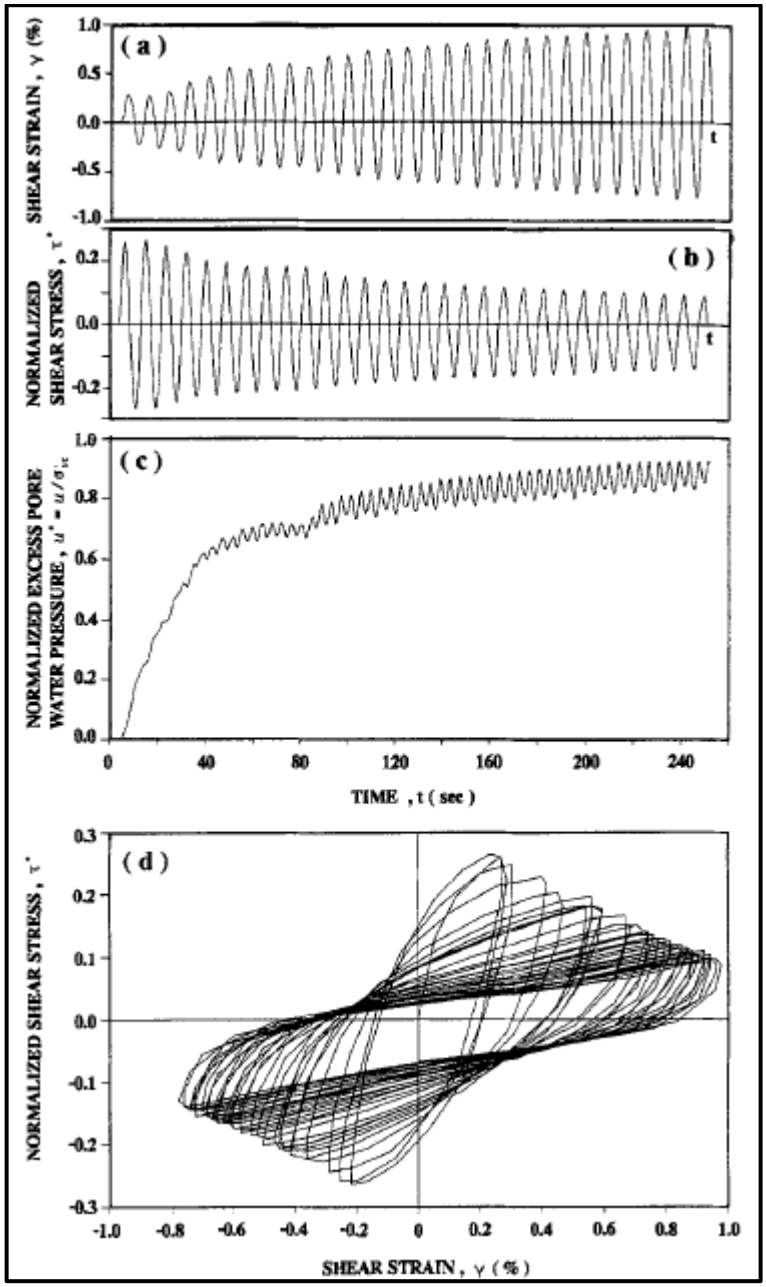

Figure 11 Results of a representative cyclic test on Santa Monica Beach Sand (Matasović and Vucetic, 1993).

Papadimitriou et al. (2001) presented a yield/bounding surface *Critical State* constitutive model in order to obtain accurate predictive results for the cyclic response of sands under both small and large strain levels, irrespective of initial density and stress level, taking as reference the work proposed by Manzari and Dafalias (1997). In fact, if the state of soil is described in terms of specific volume and effective confining pressure, the *Critical State Line* (*CSL*) could be used to mark the boundary between contractive and dilative states (Figure 12). It is well known

that *Critical State* soil mechanics is an effective stress framework specifying mechanical soil behaviour. In particular, the term "*Critical State*" (*CS*) refers to a condition in which soils and other granular materials come into if continuously sheared until a frictional fluid phase. At the onset of the *CS*, shear distortions develop with no any further changes in volume or stress.

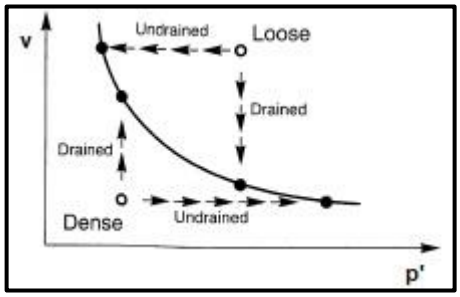

Figure 12 Behaviour of initially loose and dense specimens under drained/undrained monotonic loading (Kramer, 1996).

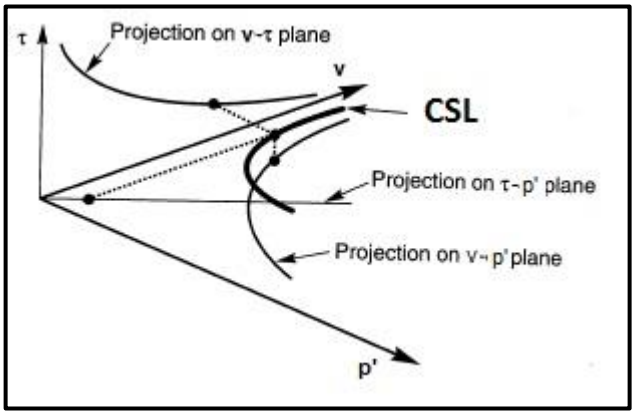

Figure 13 Three-dimensional CSL plot (Kramer, 1996).

Thus, the *CSL* is the locus that presents all the possible combinations of specific volume and confining stress at *CS*, depicted in Figure 13. The abovementioned *CSS* refers to the *Critical State* condition with the additional requirement of steady rate of deformation. The *Steady State* is assumed as equivalent to *Critical State* as discussed in detail in Bobei et al. (2009): thus, *CSL* and *Steady State Line* (*SSL*) are used interchangeably. In addition, the *CSL* may represent the boundary between states in which a particular soil is or is not susceptible to liquefaction. Saturated soils with initial specific volume high enough to plot above the line are

considered susceptible to liquefaction and soil with initial states plotting below are assumed non-susceptible. It is well-known that the volumetric and stress-strain behaviour of granular soils depends both on density and confining pressure level. As seen above, dilative response and strain softening are observed in dense granular soils, whereas contractive response and strain hardening in loose sands under drained shearing conditions. Besides, for a given specific volume value, granular soils may develop strong dilative response at low stress levels and fully contractive behaviour at high stress levels. In general, soil resistance increases at high values of *DR* and confining pressure since a dilatant volume-change tendency occurs (Yamamuro and Covert, 2001). A combination of confining pressure and density is needed to evaluate the soil response in granular deposit. The use of a unified parameter, such as the state parameter (ψ), which considers this double dependency, may be an appropriate approach (Tonni et al., 2006). The state parameter is a suitable property index which defines the relative position on the plane void ratio-effective mean pressure of the current state and the projection of the *CSL*. The introduction of such element to interpret the response of granular soils in a unified framework can be traced back to the works by many researchers such as Roscoe and Poorooshasb (1963), Seed and Lee (1967), Uriel (1975), Been and Jefferies (1985), Pastor (1991), Ishihara (1993), Jefferies (1993), Manzari and Dafalias (1997), Gajo and Wood (1999), Li et al. (1999), Zhang et al. (2001), Wang et al. (2002), Qadimi (2005), Ling and Yang (2006), Tonni et al. (2006), Qadimi and Coop (2007), Manzanal et al. (2011a; 2011b), Weng and Ling (2013), Qadimi and Mohammadi (2014) and Mohammadi and Qadimi (2015). The state parameter is assumed as proposed by Been and Jeffries (2000) in the equation (1):

$$\psi = e - e_{CSL} \qquad (1)$$

assuming that the *CSL* might be approximated by a straight line in the e-log(p') plane. In particular, in this study, ψ is defined in terms of specific volume $(= 1 + e)$ instead of void ratio, as shown in the equation (2):

$$\psi = v - v_{CSL} \qquad (2)$$

The soil states located below the *CSL*, which are defined like "dense", present $\psi < 0$, while those over it, which are defined like "loose", display $\psi > 0$ (Figure 14).

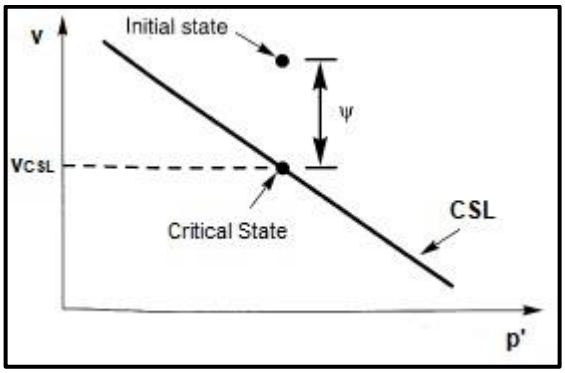

Figure 14 State parameter concept (Kramer, 1996).

Thus, the incorporation of the state parameter in the constitutive equations permits to describe the soil response under different confining pressures, ranging from low pressures (20 kPa) to high ones (800 kPa), and densities by adopting a single set of constitutive parameters in the calibration procedure, such as developed in the next chapters.

3.2. Influence of non-plastic fine-grained soils on liquefaction

As already described, liquefaction is a state of soil suspension resulting from release of contacts between particles of the solid matrix. If the soil contains some amounts of fines, cohesion or adhesion appears between the soil structure, making difficult to separate the particle. As a consequence, a smaller susceptibility to liquefaction is pointed out. Nonetheless, Ishihara (1993) illustrated as this propensity depends on the nature of the fines contained in the mixture (e.g. fines fraction composed by

minerals with a dry surface texture free from adhesion). To have a more accurate frame of reference, Yamamuro and Covert (2001) have postulated that most manifestations of seismic-induced liquefaction phenomena have actually triggered in silty sands. Such soils, indeed, are susceptible to softening and strength reduction due to earthquake occurrence as much as relatively clean sands (Boulanger et al., 1998; Bray et al., 2004). Wood et al. (2008) has suggested that the effects of fabric are mostly marked in mixtures of sands and silts i.e. the soil responses are related to the different type of contact between the particles and the different proportions of coarse/fine-grained soils. Natural sand deposits are characterized by non-identical quantity of fine content (*FC*) percentage; thus, this aspect influences the type of stress-strain behaviour. The plasticity of the fines in a sand matrix can also affect the soil responses under seismic conditions (Ishihara, 1993) i.e. typically, high values of plasticity act to increase the liquefaction resistance. Different authors (e.g. Ishihara and Koseki, 1989; Yamamuro and Lade, 1998; Cubrinovski and Ishihara, 2000; Seed et al., 2003; Boulanger and Idriss, 2004, 2006; Chang and Hong, 2008; Cubrinovski and Rees, 2011) studied the effects of the abovementioned factors on liquefaction susceptibility. In particular, Seed et al. (2003) proposed a recent guideline, shown in Figure 15 , where three zones on the *Atterberg Limits Chart* can be identified: Zone A includes soils that are "*potentially susceptible to classic cyclically induced liquefaction*"; within Zone B, soils may be liquefiable; the remaining area of the chart is not generally "*susceptible to classic cyclic liquefaction*", but the potential sensitivity, i.e. loss of strength with remoulding or monotonic accumulation of shear deformation, has to be evaluated. Boulanger and Idriss (2004, 2006) defined two different classes of the fine-grained soils under monotonic and cyclic undrained shear loading according to their plasticity: "*sand-like behaviour*" and "*clay-like behaviour*" i.e. fine-grained soils

whose response reproduces, most likely, the stress-strain behaviour of sands (liquefaction) and clays (cyclic softening), respectively. Such difference is related to the *Casagrande Plasticity Chart* (Figure 16).

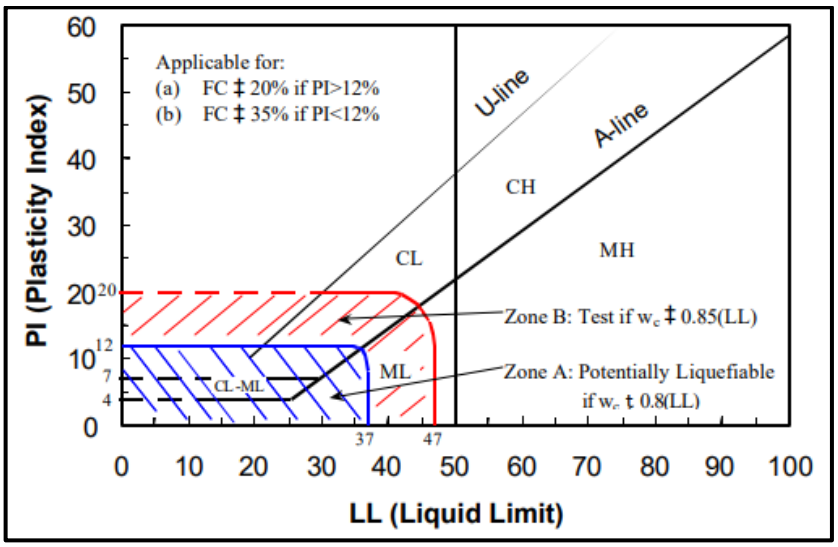

Figure 15 Recommendations regarding assessment of "liquefiable" soil types (Seed et al., 2003).

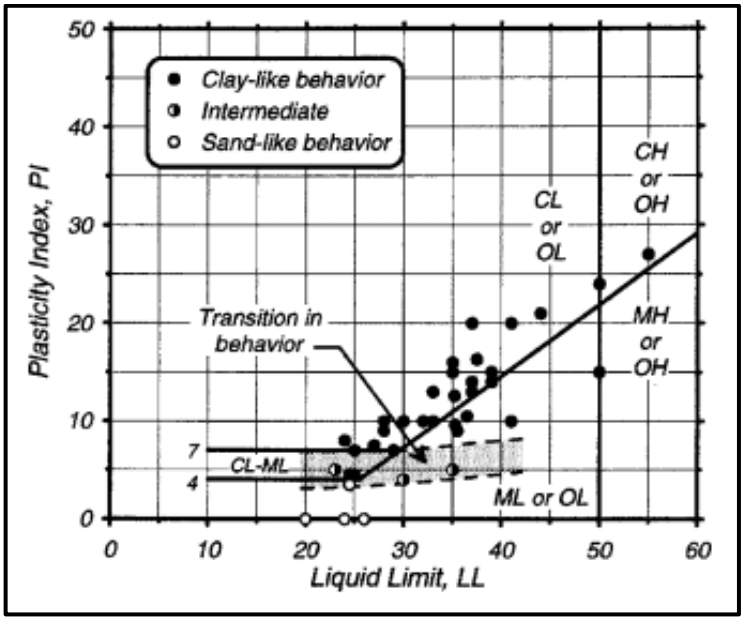

Figure 16 Atterberg Limits Chart in conjunction with some representative values for each soil that exhibit clay-like, sand-like, or intermediate behaviour (Boulanger and Idriss, 2006).

Cubrinovski and Rees (2011) suggested that, at a given specific volume, loose samples with high fines content exhibit more contractive response and greater potential for strain softening than clean sands; furthermore, the liquefaction

resistance of loose specimens is marginally influenced by the plasticity of fines (Park and Kim, 2013).

Some case histories have outcome that liquefaction in sand-silt deposit is a tangible reality and not purely related to laboratory tests. In his study on Fukui, Mino-Owar and Tohankai earthquakes, Kishida (1969) confirmed the occurrence of the phenomenon within sandy strata containing up to 70% fines; Tohno and Yasuda (1981) showed evidences in subsoils with fines up to 90% during the 1978 Miyagiken-Oki earthquake. The role of non-plastic fines on liquefaction resistance of soil sediments and the relative assessment of their liquefaction susceptibility through routinely used *CPTU*-based methods are widely discussed (e.g. Kokusho et al., 2012; Boulanger et al., 2016), due to a series of factors pertaining to the practice of the cone penetrometer, such potential partial drainage effects (Tonni and Gottardi, 2010; García Martínez et al., 2016).

Seed et al. (1985) has postulated that for sands with less than 5% fines, the influence of fines may be neglected, whereas with more than 5% fines, the liquefaction resistance increases. Yamamuro and Lade (1998) noted that sandy-silty soil becomes more liquefiable when undrained shearing begins at lower effective pressures respect to that at higher values. Such response is opposite to the commonly tendency of clean sand. Thus, the term "*reverse behaviour*" was coined to define such trend, caused by the increase of compressibility and creation of a meta-stable soil fabric where the fine-grained particles are located between the sand matrix. Such latter finding was confirmed by Amini and Qi (2000) who carried out cyclic triaxial tests on Ottawa Sand with *FC* ranged from 10% to 50% and demonstrated as the liquefaction susceptibility of silty sands typically decreases with increasing silt content and decreasing confining pressure.

An increase in the *CS* ratio (*q/p'*) with increasing non-plastic silt fraction could be explained by recognizing that the angularity of fines-grained particles furnishes a positive contribution to the soil shear strength. In fact, Carraro et al. (2007) suggests that the more angular the silt particles are and the more rounded the sand particles are, the higher the influence of the silt to the *CS* condition will be (Carraro et al., 2007).

On the basis of the several proposed studies, the influence of fine content (*FC*) and plasticity on sandy soil behaviour has been investigated extensively but it is undeniable a significant controversy related to the currently available approaches to describe the earthquake response of fine-grained soils (Seed et al., 2001; Youd et al., 2001). All such considerations have to be taken into account within the interpretation of the susceptibility to liquefaction of the deposits composed by sandy-silty soils.

4. An Italian case-study: Scortichino

Over the last years, the seismic-induced phenomena such as liquefaction and lateral spreading have been extensively studied since their occurrences have caused tremendous amounts of damage in historical events around the world. The 2012 Emilia earthquake is an example of moderate seismic sequence yielding extensive liquefaction in a range of 21.50 km radius from the epicentres located in the Eastern part of the Po River Plain. In fact, two main events have taken place: the first with magnitude 5.9 occurred near Finale Emilia on May 20th at a depth of 6.30 km, whereas the second with magnitude 5.8 occurred near Cavezzo on May 29th at a depth of 10.20 km (Lo Presti et al., 2013). In the succeeding weeks, a series of aftershocks were recorded with magnitude higher than 5.0 and the epicentre locations moving westwards. The sequence produced human losses, significant damages to buildings and infrastructures, and soil manifestations (i.e. large grounds cracks like lateral spreading displacements, copious ejections of sand and water from surface fractures and wells, and sand boils). In particular, some 700 liquefaction cases were recorded (Crespellani et al., 2012) in the investigated zone: most likely, the phenomena developed over an area (1200 km^2 of extension) which essentially corresponds to the Reno river paleochannel and the surrounding lowlands (Alessio et al., 2013; Lai et al., 2015; Facciorusso et al., 2016). It is important to highlight that, within the Italian seismic history, recent manifestations of soil liquefaction are limited (Galli, 2000), thus the case-study results to be very interesting. In particular, a number of surface deformations and longitudinally-oriented ground fractures were also observed in a series of riverbanks. One of the worst hit sites is located in Scortichino, municipality of Bondeno, province of Ferrara, where a 3-km stretch of the river embankment, known as *Canale Diversivo di Burana*, has been characterized by several seismic-induced manifestations at

ground level (Gottardi et al., 2014). Liquefaction effects such as sand eruptions have been mainly individuated pretty far from this mixed-use channel with both drain and irrigation function. Nevertheless, according to Kramer et al. (2015) study regarding the process of liquefaction and the effects that identified its occurrence (i.e. hydraulic conditions), the presence of the artificial river embankment may clarify why such phenomenon developed within the shallow granular stratum without any evidence of sand boil at ground level (Chiaradonna et al., 2018). On the other hand, along the levee crown, the longitudinal pattern of cracks seems to be compatible with a lateral spreading mechanism. The majority of such fissures, which typically run according to the same alignments, are characterized by 1-5 m length and 2-3 cm horizontal wide on the average (Chiaradonna et al., 2018). A number of geotechnical and geophysical investigations have been carried out by a consistent group of experts and researchers composed by the academic framework (e.g. University of Bologna, University of Florence, University of Naples "Federico II", University of Ferrara, University of Rome "La Sapienza", University of Aquila, University of Reggio Calabria "Mediterranea", University of Naples "Parthenope") and some institutions (e.g. Istituto Nazionale di Geofisica e Vulganologia – *INGV*, Servizio Geologico, Sismico e dei Suoli of Emilia-Romagna Regional Government). Thus, this research study is based on an existing database of geotechnical investigations, including both in-situ and laboratory tests (Tonni et al., 2015a), as well as on available soil samples recently taken from different sites struck by the seismic sequence. In particular, a number of interpretation procedures for the assessment of soil liquefaction susceptibility, based on either piezocone (*CPTU*) measurements (Idriss and Boulanger, 2008; Andrus and Stokoe, 2000) and seismic dilatometer (*SDMT*) profiles (e.g. Robertson, 2012), have pointed out that, most likely, cyclic liquefaction phenomena have been triggered in the heterogeneous layer of sands, silty sands

and sandy silts, forming the shallow strata of the deposit (Tonni et al., 2015c; Monaco et al., 2016). This result has been validated by independent numerical studies based on *1D* dynamic effective stress analyses developed by Tonni et al. (2015b) and by Chiaradonna et al. (2018). After the interpretation of all the available experimental data, an additional testing programme has been realized in order to add further information on the mechanical response of soils. Particular attention has been focused on sands, silty-sands and sandy-silts, involved in liquefaction and cyclic mobility phenomena during the 2012 seismic sequence, recently analysed by the Geotechnical Group of *DICAM*. Nowadays, a variety of geotechnical approaches are available to study actual soil behaviour and seismic-induced evidences, ranging from simple empirical equations to complex numerical analyses based on non-linear constitutive models. So far, the application of advanced constitutive models to describe liquefaction and lateral spreading phenomena occurred during the Emilia earthquake appears a significant contribution in order to improve the knowledge into geotechnical problems induced by the seismic sequence.

4.1. Geological and geomorphological setting of the investigated area

The epicentral area of the 2012 seismic sequence lies within the center of Padana Plain, between the provinces of Modena and Ferrara, where a complex tectonic system is located at the base of a thick sedimentary fill (Fioravante et al., 2013; Maesano et al., 2015; Minarelli et al., 2016). The seismicity of the site is mainly related to a structure of buried compressive faults, termed "*Ferrara folds*". The subsoil is characterized by silty-sands, sandy-silts and clays in the upper layers and medium-coarse sands in the lower ones, described more in detail later. Two different cycles of sedimentation are identified: the oldest one, termed "*Sistema Alluvionale Emiliano-Romagnolo Inferiore*" and developed between 650.000 to 450.000 years

ago, and the newest, known as "*Sintema Alluvionale Emiliano-Romagnolo Superiore*", settled during the last 450.000 years. The ground level varies between 25-30 m a.s.l. in the West side near Novi di Modena to 10-15 m a.s.l in the East side near Vigarano Mainarda. In the locality of Scortichino, the abovementioned levee, result of the depositional activity of the Panaro river, is oriented from East to West: the bank crown decreases from West to East (from 9-10 m near the urbanized area up to 8-9 m near Malcantone and Guattarella). It reaches 16-17 m and 15-16 m in proximity of the infrastructures called "*Ponte di Scortichino*" and "*Ponte della Guattarella*", respectively. A picture of the investigated area is shown in Figure 17. It is worth noting that some critical areas (one kilometer far away) have been examined during the experimental programme (i.e. cross-sections A, B, C, D in Figure 17), since the strain phenomena due to the 2012 earthquake did not affect the entire riverbank.

Figure 17 Area of investigation (Gottardi et al., 2014).

The in-situ campaign (i.e. coring with sampling, *CPTU* and *SDMT*) allows to classify in detail the soil profile under both a static and dynamic point of view. A series of boreholes has been realized reaching a depth of 20 m (e.g. *S2, S4, S5*), 30 m (*S1*) and 50 m (*S3*) from the ground surface, respectively (Figure 18).

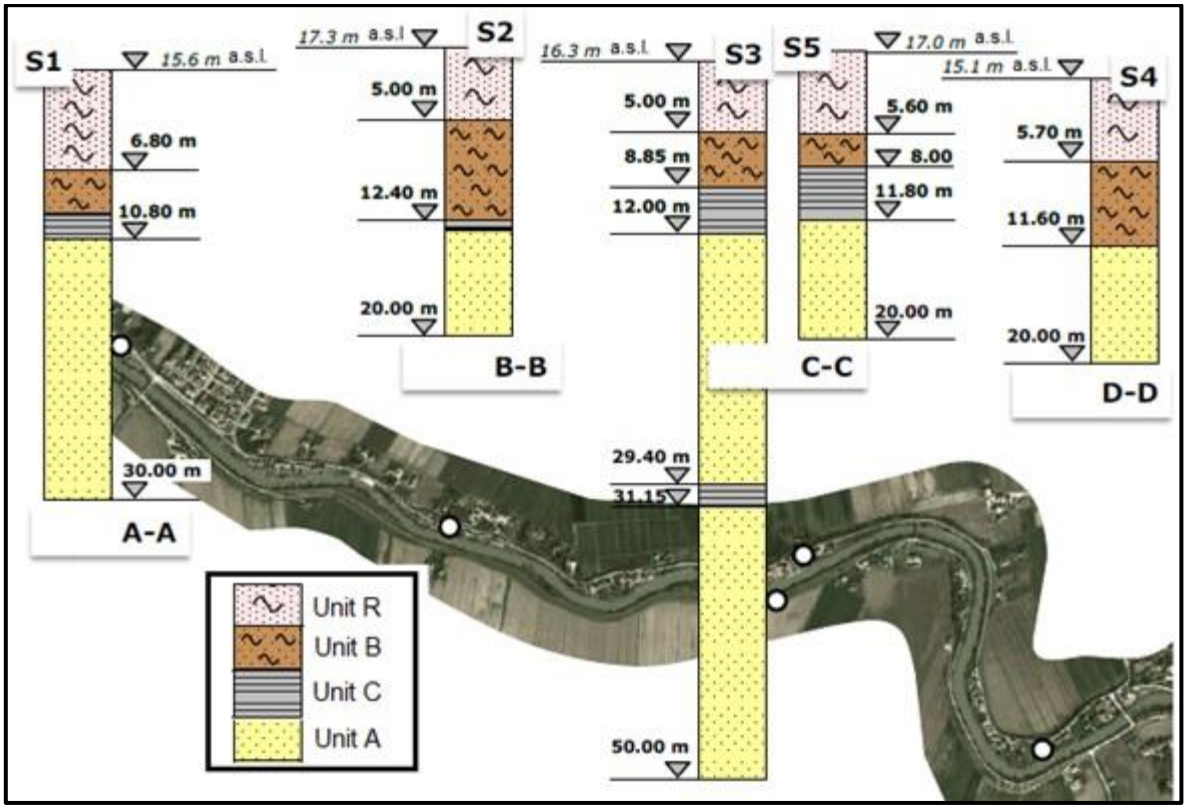

Figure 18 In-situ drilling campaign along the Canale Diversivo di Burana (Gottardi et al., 2014).

The interpretation of the database has revealed that the shallow deposit (9-10 m) is composed by silty-sands and sandy-silts: the upper layer (6-8 m), called *Unit R*, identifies the artificial river embankment; the lower one, termed *Unit B*, represents the natural one. A thin layer of about 2 m (Unit C) is formed by clays/silty-clays whose thickness is not uniform along the examined area. At greater depths, the medium-coarse sands of *Padano Aquifer* belong to the Unit A. Some clayey rods lie between 30-34 m from the crown. The deepest stratum (Unit A) is fairly homogeneous in the whole investigated area; whereas Unit R and Unit B consist of by intrinsic heterogeneous granular soils. This research project focus on sections A and C which fall in two of the most damaged segments of the levee. In Figure 19, the stratigraphic model of section C is depicted as obtained from the interpretation of borehole logs (*BH*), piezocone (*CPTU*) and seismic dilatometer (*SDMT*) tests carried out along cross-sectional alignments. The soil profile and the water table

location are representative of the whole studied bank stretch, with a certain longitudinal spatial variability in terms of both thickness and fine content (*FC*) as shown in Tonni et al. (2015a).

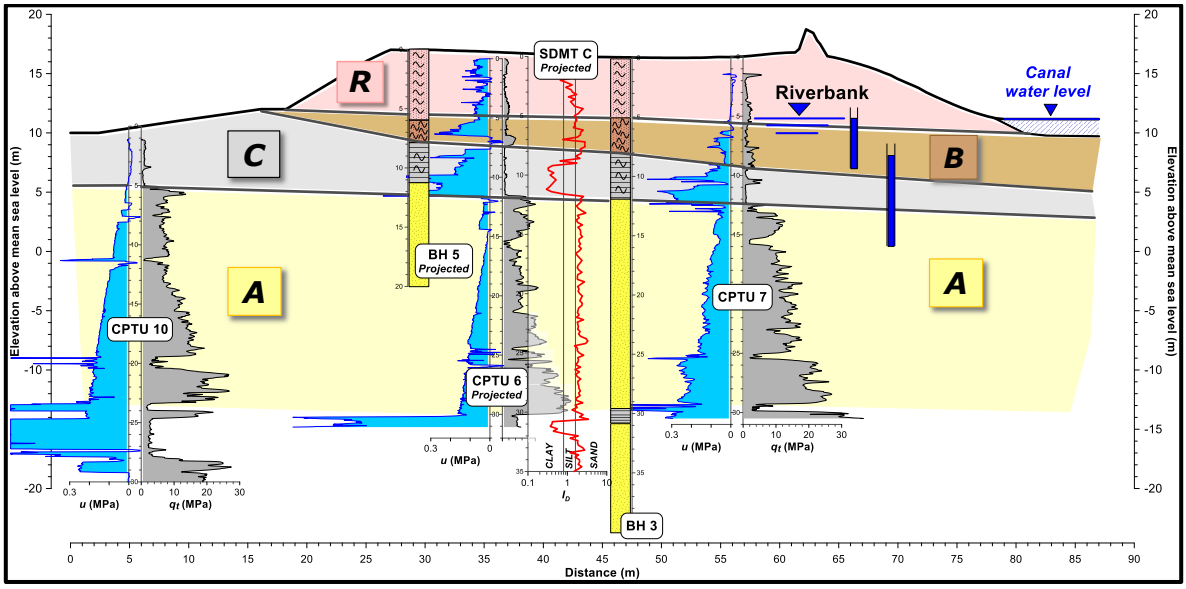

Figure 19 Canale Diversivo di Burana - Section C

Since the piezocone is a suitable and of common use tool for evaluating stratigraphy and liquefaction susceptibility, a series of *CPTU* has been considered for the examined sections. In fact, the experimental results of *CPTU3* (section A) and *CPTU6* (section C) will be interpreted during calibration procedure of the constitutive model parameters (e.g. M_f); on the other hand, the *CPTU7* (section C) will be used to realize an adequate *2D FE* geotechnical model of the investigated levee on the cross-section C. Thus, the cone resistance (q_t), the pore pressure (u), the lateral friction (f_s) and the *SBT* profiles of this last test are plotted in Figure 20.

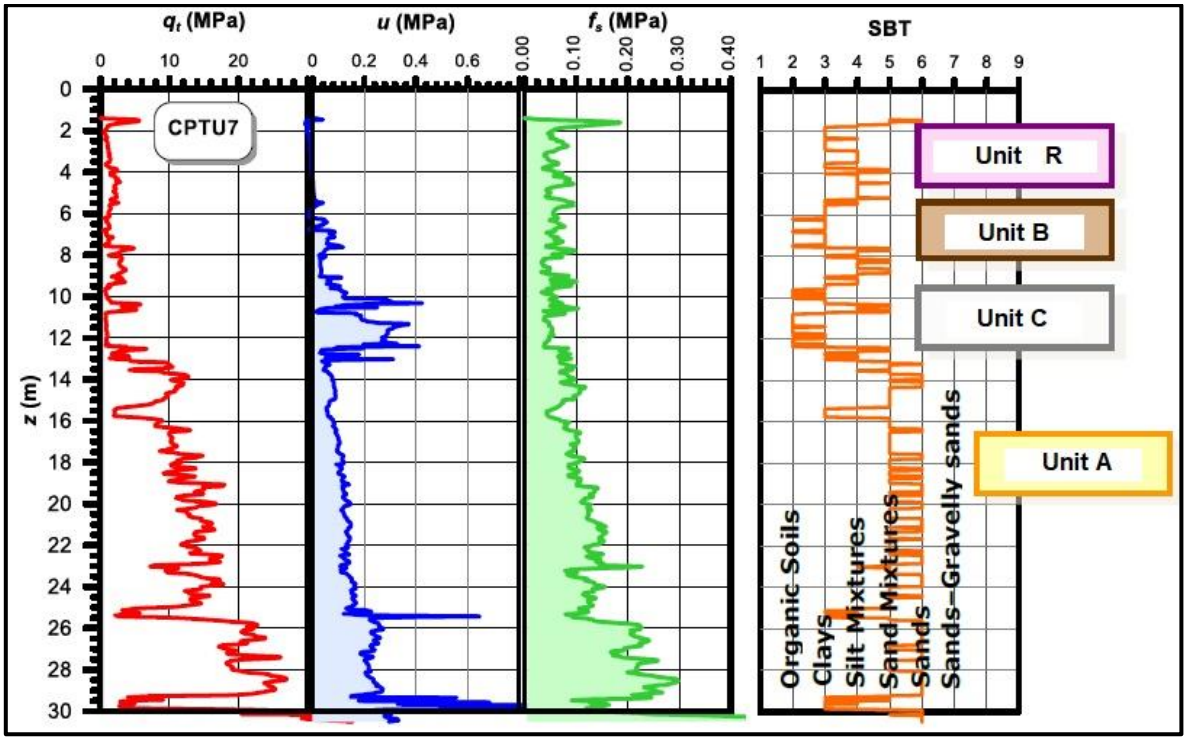

Figure 20 CPTU7 interpretation by Gottardi et al. (2014).

5. Laboratory testing programme

The detailed testing programme has mainly focused on experimental activities in order to obtain an exhaustive geotechnical characterization of granular samples extracted from the subsoil of Scortichino embankment. Previous applications of a variety of site investigation-based methods for the assessment of soil liquefaction susceptibility (e.g. Tonni et al., 2015a) have shown that liquefaction phenomena affected a number of granular subsoil layers, for an earthquake moment-magnitude equal to the May 2012 main events. The granular samples analyzed are particularly worthy to investigate because they were collected from some boreholes located in the most damaged sections of the riverbank (section A and C). Hence, a more detailed geotechnical characterization, together with an appropriate mathematical modelling of the experimental observed soil behavior, may help in understanding the mechanisms which caused the large, longitudinally-oriented ground cracks and the severe structural damages. According to this goal, after a basic characterization of physical properties of the tested materials, the laboratory tests carried out have mainly dealt with the characterization of the available soil samples under static load, including standard triaxial tests (No.13), in both drained and undrained conditions, and standard floating-ring cell and K_0-cell oedometer tests (No.9). Since the previous triaxial programme solely focuses on undrained triaxial tests, the preference has been given to tests in drained conditions in order to achieve an exhaustive set of triaxial data. These tests have been performed with the equipment currently in use at the Geotechnical Laboratory of the University of Bologna (*DICAM*). Most of the specimen tested have been reconstituted using the moist tamping technique with under-compaction (Ladd, 1978) in order to ensure the uniformity of the soil sample and avoid potential particle segregation; whereas the undisturbed samples have been generally recovered from Unit B. Higher values of

p'₀ have been adopted in order to better identify the *Critical State Line* (Klotz and Coop, 2002; Luzzani and Coop, 2002) and to validate the adopted constitutive law in isotropic compression: a number of unloading-reloading cycles have been performed during the consolidation stages. In collaboration with the laboratory *LASTM* of *DICAM*, the mineralogical analysis has been carried out using a computer-controlled *X-ray* diffractometer, *XRD* (*Philips PW1840 generator,* operating at 40 kV/20 mA; *Cu Kα* radiation with λ = 1.54184 Å = $1.54184 \cdot 10^{-10}$ m, scan range $2\theta = 5 \div 80°$, step size $2\theta = 0.020°$, scan speed 2θ/s = 0.020, overall scan time 63 min).

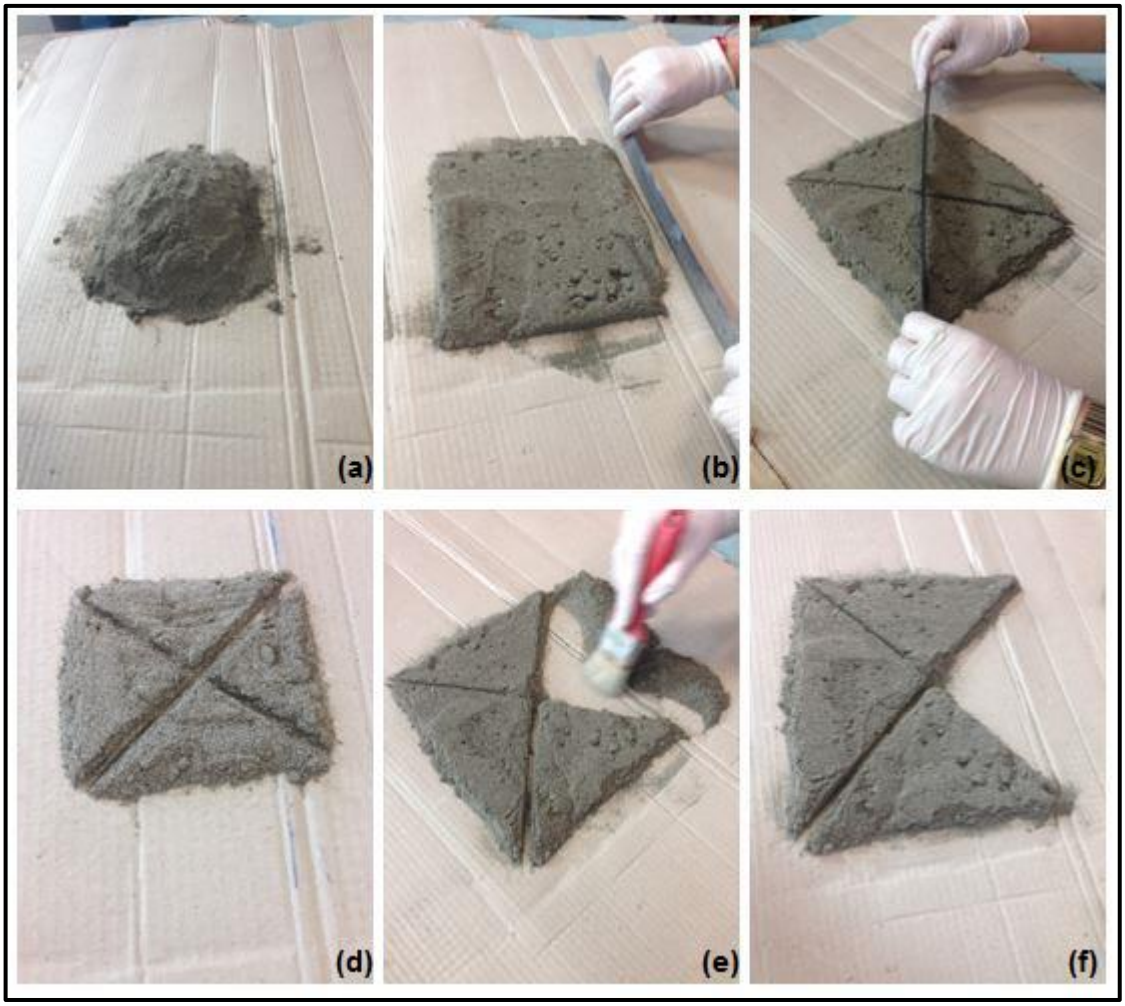

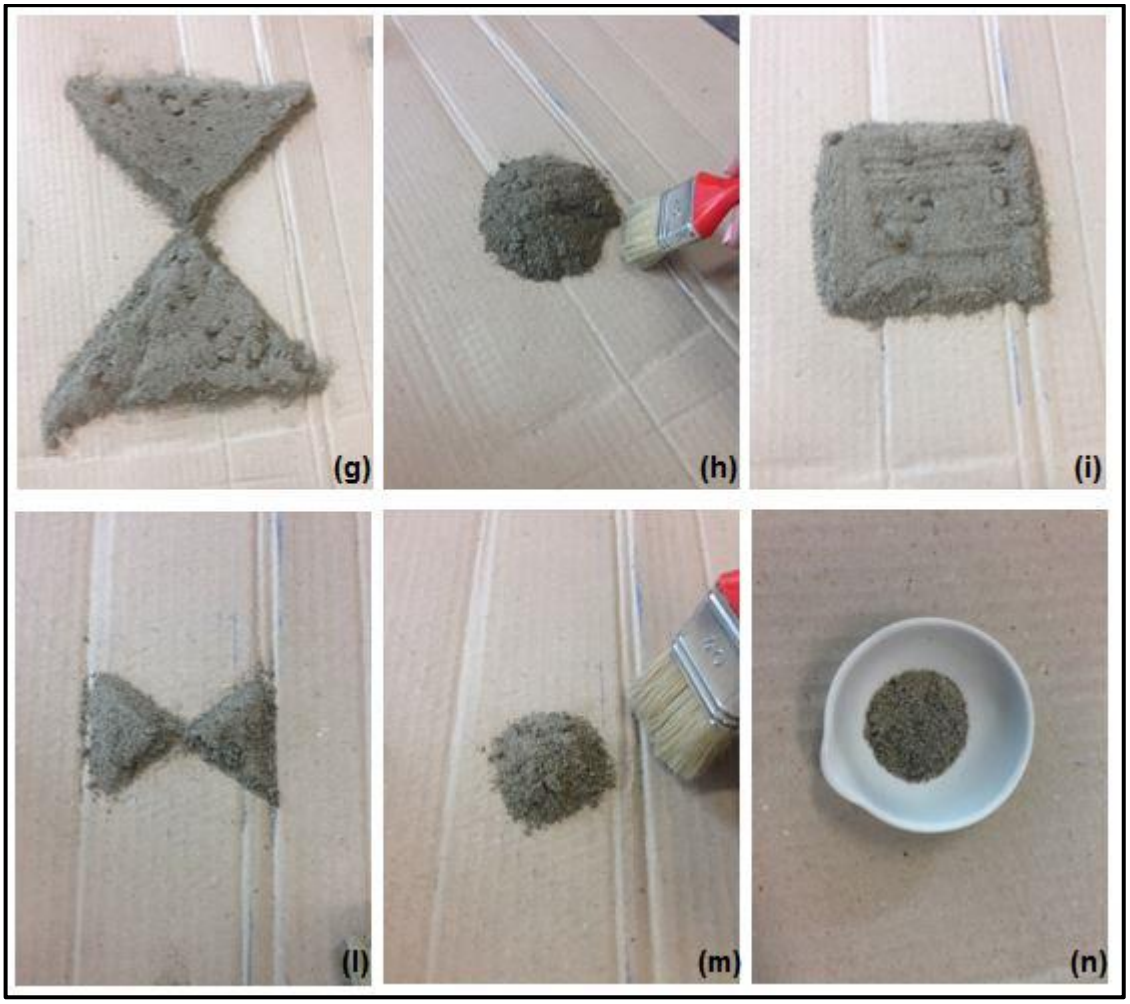

Figure 21 Quartering procedure.

A preliminary quartering has been performed in order to minimize variations in the aggregate characteristics between the small amount of soil tested and the representative samples of each unit, according to the procedure depicted in Figure 21(a)-(n). Then, the soil has been carefully located into a slide (Figure 22(a)-(c)) and in the *XRD apparatus*.

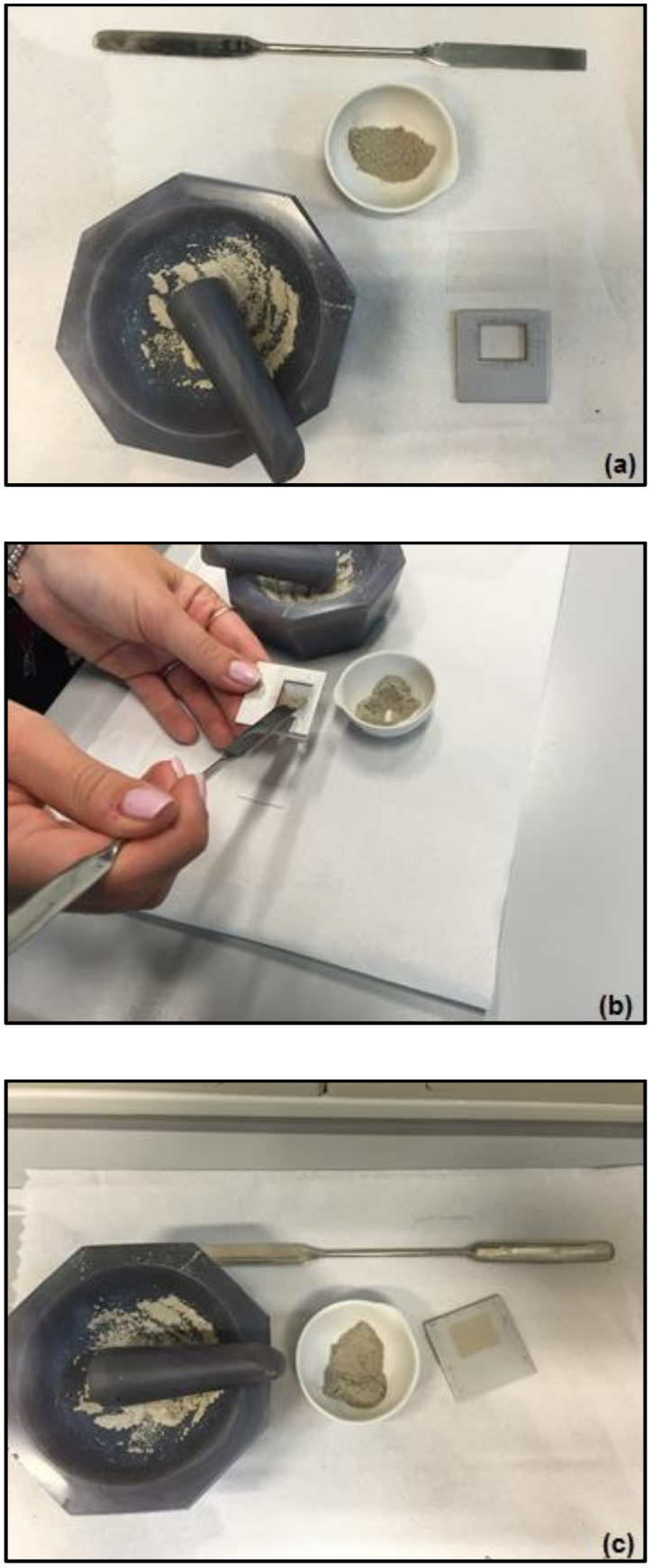

Figure 22 Preparation of the soil sample analyzed in the X-ray diffractometer.

Figure 23 X-ray *diffractometer (LASTM, DICAM).*

The experimental results of the analyses have been interpreted according to the diffractogram processing procedure presented in Sandrolini and Franzoni (2010). For granular soils, the combination of such experimental data and the existing database from the previous testing programme has allowed to achieve an in-depth calibration of the model parameters required by *GP* formulation. The method is validated by comparing the experimental results obtained from drained and undrained triaxial compression tests on natural and reconstituted samples with model predictions.

5.1. Basic features of granular soils

The investigated granular soils are respectively a fine sand forming the upper part of a sandy layer attributable to a fluvial channel depositional environment, typically referred to as *Padano Aquifer* (Unit A), and a number of silty sands and sandy silts which constitutes the artificial (Unit R) and natural riverbank (Unit B). The *Padano Aquifer* deposit, generally composed of medium-coarse sands grading upwards into fine sands, is almost continuously detected between 10 m and 50 m in depth from

the bank crest under a thin silty-clayey soil unit. The uppermost layers of silty sands-sandy silts develop from the top of river embankment up to 8-10 m.

A mineralogical analysis, carried out using a computer-controlled *X-ray* diffractometer (*PW 1830 generator, Philips*), has revealed that grains of *Padano Aquifer* sand of Section C are mainly composed of quartz and albite, with traces of calcium carbonate, $CaCO_3$, and phlogopite. This latter is a mica mineral, also known as magnesium mica. The results of the mineralogical characterization are provided in Figure 24 in terms of a series of reflections with different intensities as function of the diffraction angle (θ).

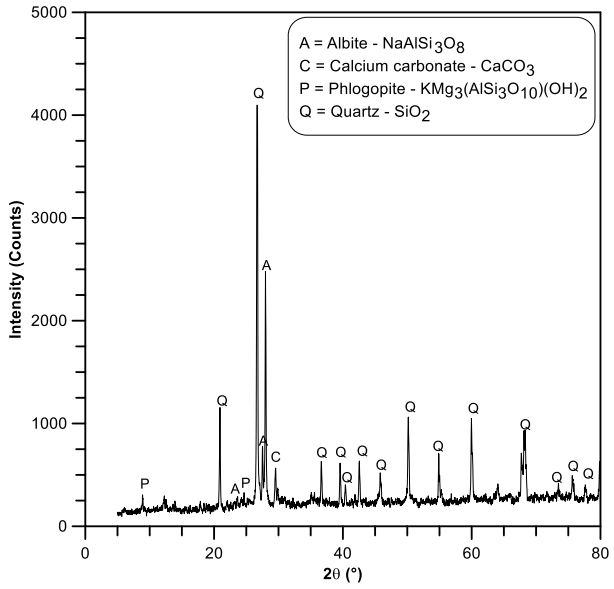

Figure 24 Chemical components of Padano Aquifer sand particles from X-ray diffractometer analysis.

Figure 25 shows the representative grain size distribution curve of the *Padano Aquifer* sand (G_s = 2.643), obtained from sieve analysis and sedimentation. The coarse fraction corresponds to a poorly-graded medium-fine sand, whereas the fine content (i.e. the material passing the No. 200 *U.S.* standard sieve, diameter = 0.075mm) is approximately 6.16%. The coefficient of uniformity (U) is approximately equal to 2.70, with grain diameter at 50% passing (D_{50}) estimated at 0.31 mm. Furthermore, the determination of the Atterberg limits on the fraction passing the

75-μm sieve revealed that fines are basically non-plastic, thus most likely corresponding to silts. At the same time, the organic content (*O*) of the samples was found to be low, generally 5.73%. The abovementioned results are in substantial good agreement with the analyses reported in Tonni et al. (2015a) for sediments of the *Padano Aquifer* deposit.

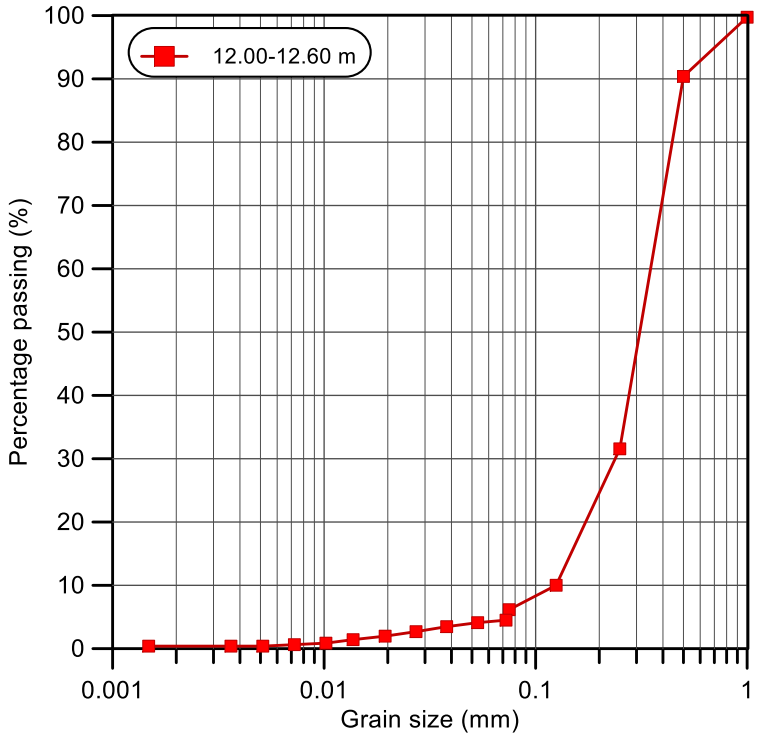

Figure 25 Particle size distribution of a representative sample for Padano Aquifer sand.

The riverbank, partly arises from a floodplain environment of deposition, is characterized by heterogeneous granular soils, in particular, by sandy silts in the upper part and silty sands in the lower unit. The particles size distribution curves of the tested samples are represented in Figure 26, while some physical properties on the grading characteristics are summarized in Table 1, i.e. grain diameter at 50% passing D_{50}, coefficient of uniformity *U*, and fine content *FC*, together with the values of the specific gravity G_s (*ASTM D854* - Standard Test Methods for Specific Gravity of Soil Solids by Water Pycnometer; *ASTM D2216* - Standard Test Method for Laboratory Determination of Water Moisture Content of Soil and Rock by Mass) and

the organic content *O* (*ASTM D2974* - Standard Test Methods for Moisture, Ash, and Organic Matter of Peat and Other Organic Soils).

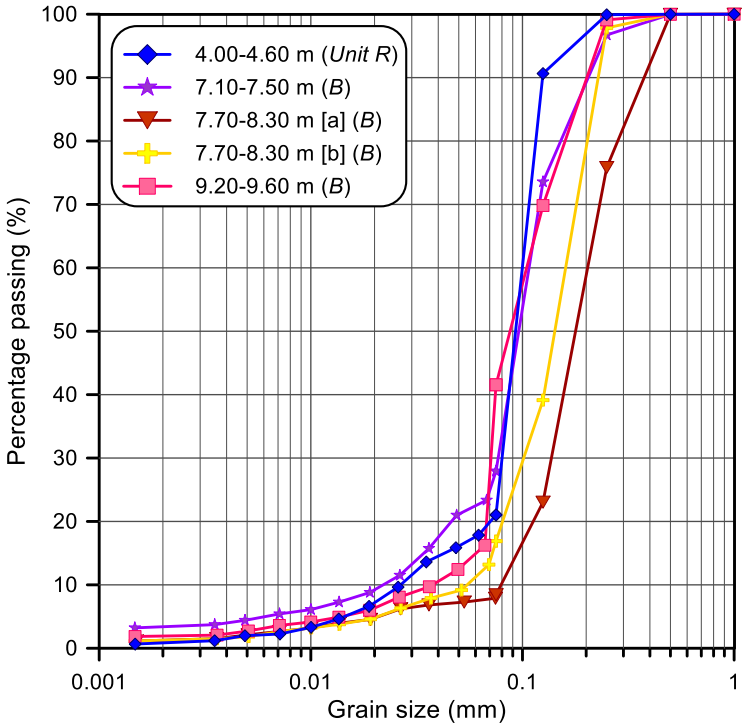

Figure 26 Particle size distribution of a representative sample for river embankment granular soils.

It is important to highlight that the sample extracted from 9.00-9.60 m consists of two different material types (Figure 27): between 9.00-9.20 m the soil has the peculiarities of *Padano Aquifer* sand, as shown in Figure 28; whereas, from 9.20-9.60 m the soil is a silty-sand mixture, which can be associated to the levee deposit. Thus, from an experimental point of view, the behaviour of the abovementioned sandy sample will be analyzed within the framework of Unit A.

Figure 27 Soil coring extracted from 9.00-9.60 m.

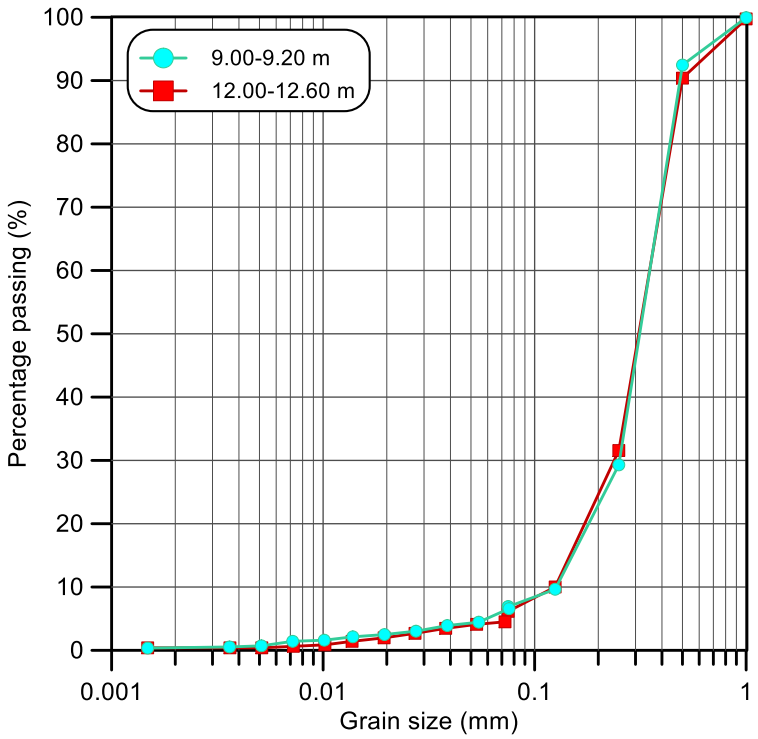

Figure 28 Particle size distribution of the sandy sample extracted between 9.00-9.20 m compared to the curve of Padano Aquifer unit.

It is relevant to note that the granular soils of Unit R and Unit B are characterized by a fine content in a range from 8% up to 42% with low plasticity silts: thus, this cohesionless strata are exposed to the liquefaction susceptibility. It is important to highlight that Units R and B may be regarded as a unique macro-unit with intrinsic heterogeneity because of the very similar grading characteristics, except for the abovementioned sandy sample at 9.00-9.20 m. Therefore, in this work, the term used to refer to such macro-unit is "*granular soil of river embankment*" or "*Macro-unit R & B*".

Depth (m)	*Section - Soil unit*	*G_s (-)*	*O (%)*	*U (-)*	*D_{50} (mm)*	*FC (%)*
4.00-4.60	C - R	2.644	2.44	3.8	0.09	21.03
7.10-7.50	C - B	2.610	1.74	5.2	0.10	27.93
7.70-8.30 [a]	A - B	2.652	1.64	2.5	0.18	8.43
7.70-8.30 [b]	A - B	2.648	1.44	3.6	0.15	16.90
9.00-9.20	A - B	2.668	1.07	2.7	0.31	6.89
9.20-9.60	A - B	2.618	1.37	3.0	0.09	41.56

Table 1 Basic soil characteristics of granular soils of Units R and B.

The mineralogical characterization of a representative soil sample of Unit B, as achieved from the *X-ray* diffractometer, is similar to the composition of Unit A in different proportions. In fact, a limited amount of feldspars (albite) appears within sediments of Unit B and phlogopite is absent, as shown in Figure 29.

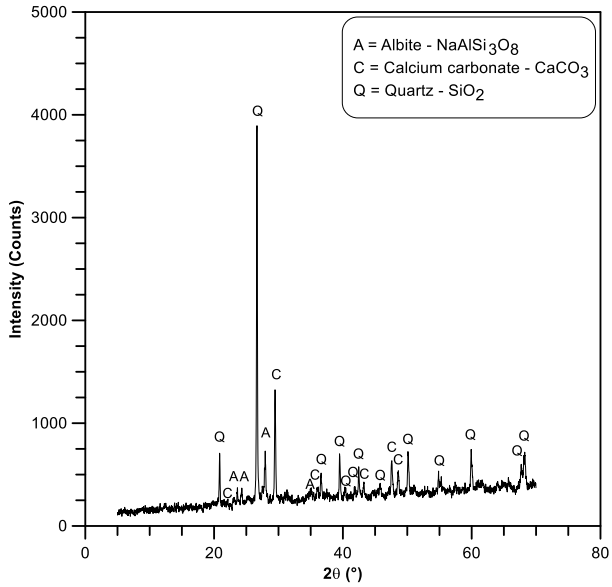

Figure 29 Chemical components of Unit B particles from X-ray diffractometer analysis.

5.2. Basic features of cohesive deposit

A basic characterization of the physical properties of the fine-grained material which belongs to Unit C has been carried out. The cohesive layer, generally composed of clays and silty-clays, has a thickness ranging from 2 m up to 5 m. In Figure 30 the representative grain size distribution curve is depicted (G_s = 2.650), through sieve analysis and sedimentation.

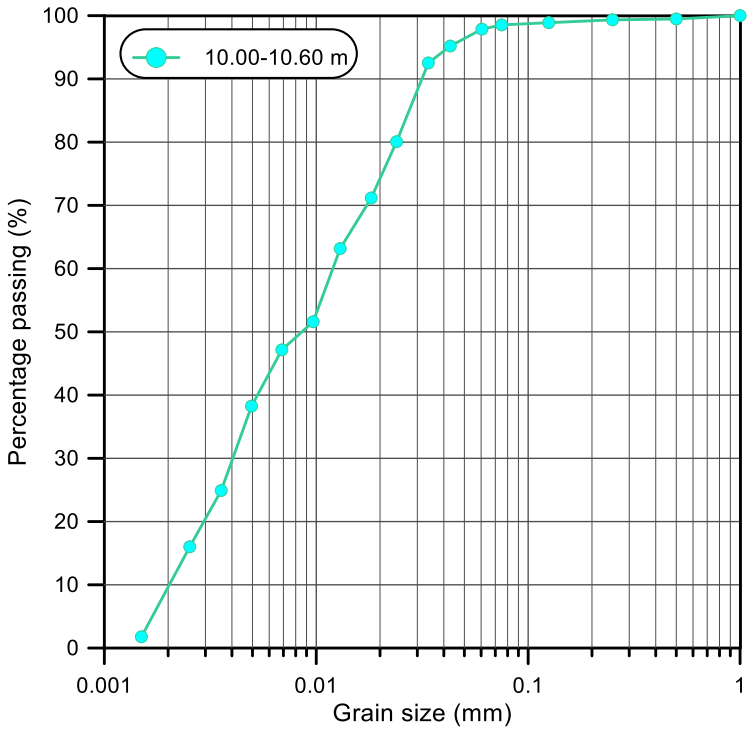

Figure 30 Particle size distribution of a representative sample for clayey deposit.

The coarse fraction (particles which do not pass the 75-μm sieve) is less than 2%, whereas the fine content is approximately 98%. The coefficient of uniformity (*U*) is approximately equal to 6.50, with D_{50} = 0.0085 mm. For classification purposes, the Atterberg limits have been carried out on the fine fraction (*ASTM D4318* - Standard Test Methods for Liquid Limit, Plastic Limit, and Plasticity Index of Soils). In particular, the Liquid Limit (*LL*), which is the water content in percent of a cohesive material at the arbitrarily defined boundary between the semi-liquid and plastic states, is equal to 62.36%. It has been determined through the fall cone method, i.e. a simple testing procedure in which a cone is penetrated into a cohesive soil specimen by its self-weight and the penetration depth is measured. The layout of the equipment located at the Geotechnical Laboratory of *DICAM* is depicted in (Figure 31).

Figure 31 Fall cone setup.

The Plastic Limit (*PL*), i.e. the water content in percent of a soil at the boundary between the plastic and semi-solid states, has been found by rolling a small soil sample into thin threads, i.e. 3 mm in diameter, until it crumbles (Figure 32). The obtained value is 29.54%.

Figure 32 Plastic Limit determination: clayey threads.

Vucetic and Dobry (1991) postulated that, for cohesive soils, the cyclic shear response depends strongly on the Plasticity Index (*PI*). Thus, such soil parameter is considered one of the most meaningful index properties for engineering practice (e.g. site-response evaluations, seismic microzonation). In particular, Lambe and Whitman (1969) suggested that the Atterberg limits are among the simplest and most inexpensive geotechnical tests to determine it. Thus, the Plasticity Index (*PI*)

of the investigated cohesive material is estimated equal to 32.82%. According to the *Casagrande Plasticity Chart*, the tested sample from Unit C is mainly composed by inorganic fat clays with high plasticity (*CH*), as shown in Figure 33 (USCS: ASTM D2487 and ASTM D2488). As seen in the previous sections, Seed et al. (2003) guideline evidences that, based on this result, the investigated deposit (Unit C) can be considered as not generally "*susceptible to classic cyclic liquefaction*". The organic content of the sample was defined to be low, in the range 3-4%.

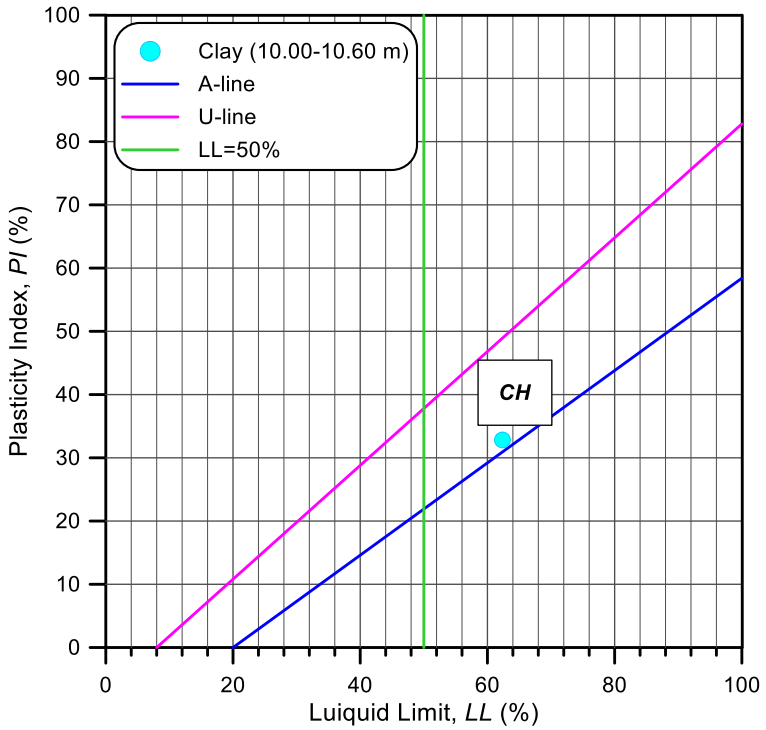

Figure 33 Casagrande Plasticity Chart (USCS – Fine-grained soils).

The basic soil properties of the cohesive layer determined by the laboratory testing programme reflect the results presented in Tonni et al. (2015a); thus, the interpretation of the mechanical response is based on this experimental database.

5.3. Triaxial test device

The triaxial tests have been carried out in a computer-controlled hydraulic triaxial apparatus (*Wille Geotechnik*), which layout is represented in Figure 34.

Figure 34 Triaxial apparatus setup (Wille Geotechnik).

This device is based on a load frame testing system, which is operated by *Wille GEOsys* software, with a capability of about 97 mm in displacement and 100 kN in pressure, pledging a measurement accuracy equal to 1% of the final value. The *Wille Perspex* cell can withstand up to 1 MPa and is filled with de-aerated distilled water that falls due to gravity from a container coupled with a tube to the basement of the apparatus. The cell pressure and the back-pressure are controlled by *Wille DV20 Pressure Generating* and *Volume Measuring* devices which consist of pressure cylinder and control system. An internal pressure transducer measures and controls the pressure according to the specified set value. In particular, for a measuring range of 1 MPa the values from 0-1 MPa are displayed with a resolution of 1 kPa and an absolute accuracy of about 2% of the full range output. The volume is estimated within the pressure cylinder (volumetric capacity of 1 l): the distance travelled by the working piston is measured and converted into a volume change with a resolution of 0.1 cm^3. The back pressure is gauged from the bottom of the specimen through an external pressure transducer with a capability of 1 MPa and a resolution of 1 kPa. An internal submersible load cell of 5 kN, adopted to evaluated the deviatoric force applied, is linked to the end part of the load ram. The system "load ram-press crossbar" acts as a constraint while the basement of cell goes up,

generating the axial loading. The displacement is measured by means of a *Mitutoyo* digital gauge with a 50 mm range and a resolution of 0.001 mm, clamped to the load ram in order to calculate the axial deformation. A series of screws are needed in order to clamp the upper part of the cell to the base plate, making the assembly and disassemble of the apparatus a fast and simple operation. The acquisition software *GEOsys* collects the digital readings taken from the data acquisition unit in a "*.dat*" file, which allows the interpretation of the experimental results.

5.4. Specimen preparation

Since the difficulty to obtain high quality undisturbed samples of granular soils (e.g. tube sampling, ground freezing), the tests have been carried out on both reconstituted and undisturbed cylindrical specimens over a wide range of initial densities and confining pressures. In particular, each sample has been approximately characterized by a diameter of 50 mm and a height of 100 mm, with the exception of *TXCID1A* on *Padano Aquifer* sand which has been built with a diameter of 38 mm and a height of 76 mm since preliminary the triaxial apparatus was assembled through a smaller pedestal. The depositional method for specimen preparation has effects on the undrained behaviour of sands and silty sands (Vaid et. al. 1999; Høeg et al. 2000; Yamamuro and Wood, 2004). In literature, a lot of different techniques have been presented to prepare remolded samples, such as dry or wet pluviation, slurry deposition, vibration and moist tamping (*MT*). This latter method shows significant advantages (Ladd, 1978; Frost and Park, 2003): it allows to create specimens with consistent specific volume in a wide density range; it eliminates segregation problems related to the pluviation; it permits to create loose specimens, which are desirable in liquefaction testing. In the light of the above considerations, the moist tamping procedure has been chosen for this research

work. In particular, the tested sandy specimens of *Padano Aquifer* have been all reconstituted because the granular soil has been picked into enclosed bags from the struck site. As regards the reconstituted sandy/silty specimens of Macro-unit R & B, the undercompaction steps as recommended by Ladd (1978) have been adopted; whereas, a driven mould has been used as corer for creating undisturbed samples.

5.5. Undercompaction procedure

It is well known that some elements affect the soil characterization i.e. the quality of undisturbed coring and the specimen reconstituition technique which play a key role in defining the stress-strain behaviour. In the light of the above evaluations and based on the reconnaissance experiences performed in literature (Chan, 1985; Yang et al., 2006; Lo et al., 2010; Benahmed et al., 2015; Karim and Alam, 2016), the moist tamping procedure has been identified as the method of sample preparation. In particular, a number of specimens have been achieved by applying the technique of undercompaction. This practice assures the creation of a sample which is characterized by relatively uniform unit weight, although it is well known the impossibility to eliminate completely the non-uniform phenomena within the granular material (Gilbert and Marcuson, 1988). Indeed, during the compaction of a sand/silty sand in layers, the realization of each overlying stratum can further densify the previous one, bringing the bottom region of the specimen to result denser (Mulilis et al., 1977). To avoid this undesirable inconvenient, within the under-compaction framework, each layer is generally compacted to a lower density respect to the final target through the percentage of under-compaction (U_n) i.e. the relation (3) illustrated by Ladd (1978).

$$U_n = U_{ni} - (\frac{(U_{ni} - U_{nt})}{n_t - 1}(n_{li} - 1)) \qquad (3)$$

With:

U_n: under-compaction amounts calculated for the current l-th layer (%)

U_{ni}: under-compaction amounts chosen for the first layer (%)

U_{nt}: under-compaction amounts chosen for the final layer i.e. equal to zero (%)

n_{li}: number of the current layer

n_t: total amounts of layers (in this study 8)

Such percentage changes linearly from the bottom to the top of the height of the sample, as depicted in Figure 35.

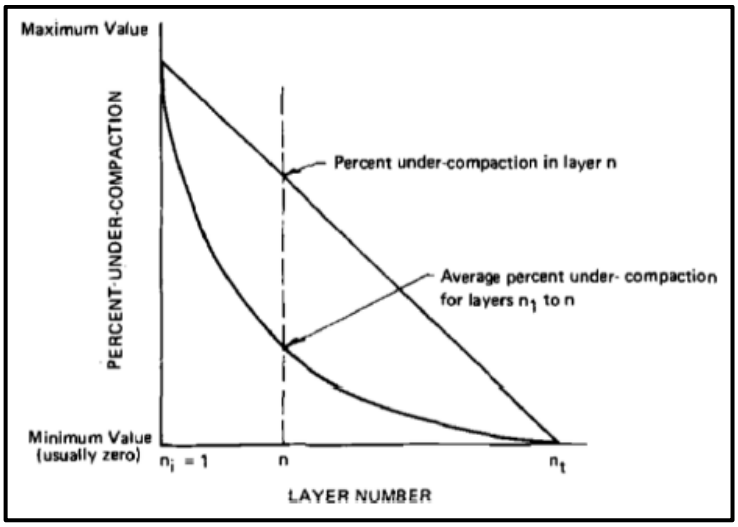

Figure 35 Undercompaction technique (Ladd, 1978).

By analyzing in more detail the procedure, the adopted technique consists of placing a small amount of soil in a container with some distilled water, such that particles cannot segregate, and mixing until to create a homogeneous slurry with an initial water content (*w*) equal to 10% for each stratum. A number of eight layers have been selected to create the specimen within a split mould where a rubber membrane has been located earlier. Ladd (1978) recommend that the maximum thickness of

each layer should not exceed 25 mm for diameters less than 102 mm: thus, 12-mm strata have been realized. The total wet weight of soil (W_t) required for the preparation of sample is calculated as

$$W_t = \gamma_d (1 + w) \qquad (4)$$

Dividing W_t by the total number of layers, the weight needed for each layer (W_l) has been estimated. Such amounts of material have been put inside a number of sealed containers and added gradually. The height of the specimen at the top of the current *l-th* layer is equal to:

$$h_n = \frac{h_t}{n_t}((n_{li} - 1) + \left(1 + \frac{U_n}{100}\right)) \qquad (5)$$

With:

h_t: final height of the specimen

A saturated ceramic porous stone and a dampened filter paper are placed on the pedestal to facilitate draining during test, without including air boils, and then a slit mould and a latex membrane are arranged. The membrane is stretched using a vacuum pump. The material for the first layer is placed by a spoon and then compacted with a manual tamper following a circular pattern starting from the edges and arriving to the center up to achieve the correct height, h_n. This is measured by means of a digital gauge. The moist soil is weighed on a scale before and after the creation of each stratum in order to estimate the residual amount that may be stuck to the surfaces of the tools used. The same procedure has been repeated for each stratum: overlapping thin layers of soil are set, paying attention to avoid any losses of grains. To guarantee an overall homogeneous sample is essential to study the stress-strain behaviour of tested soils, therefore, to avoid discontinuities, it is

suitable to scarify the previous layer surface before placing a new stratum of material. Reached the set height, a dampened filter paper and an additional saturated ceramic porous stone are located. The water sealing is assured by placing a layer of silicon grease on the pedestal and two *O*-rings at the top and bottom. If dense specimens are realized compacting the soil with the pivot, looser samples are generated by creating a soft and open structure, eliminating vacuum. The drainage line at the bottom of the specimen is opened to a small suction so that the effective stress permits the specimen to stand. In particular, the suction is applied using a container with distilled water placed below the level of the triaxial sample. The drainage line is closed before to collect the dimensions of the specimen in order to avoid changes in volume.

5.6. Undisturbed granular samples

For the undisturbed samples, the core (i.e. 100 mm of diameter and 600 mm of length) is divided into homogenous sub-samples. Particular care is dedicated to this phase since the disturbance is crucial in determining a successful analysis of the response of intact soils. Since the sampling process should preserve the in-situ properties, each sub-sample is coated with plastic wrap and stored into the temperature and humidity-controlled room (HR = 87% and T = 19.2°) in order to avoid any changes in moisture content. The undisturbed specimens are obtained using a hand-operated soil lathe and trimming vertically the sub-samples by means of a 50-mm diameter mould paying attention to remove carefully the surplus material (Figure 36(a) and (b)), as suggested by Head (1986).

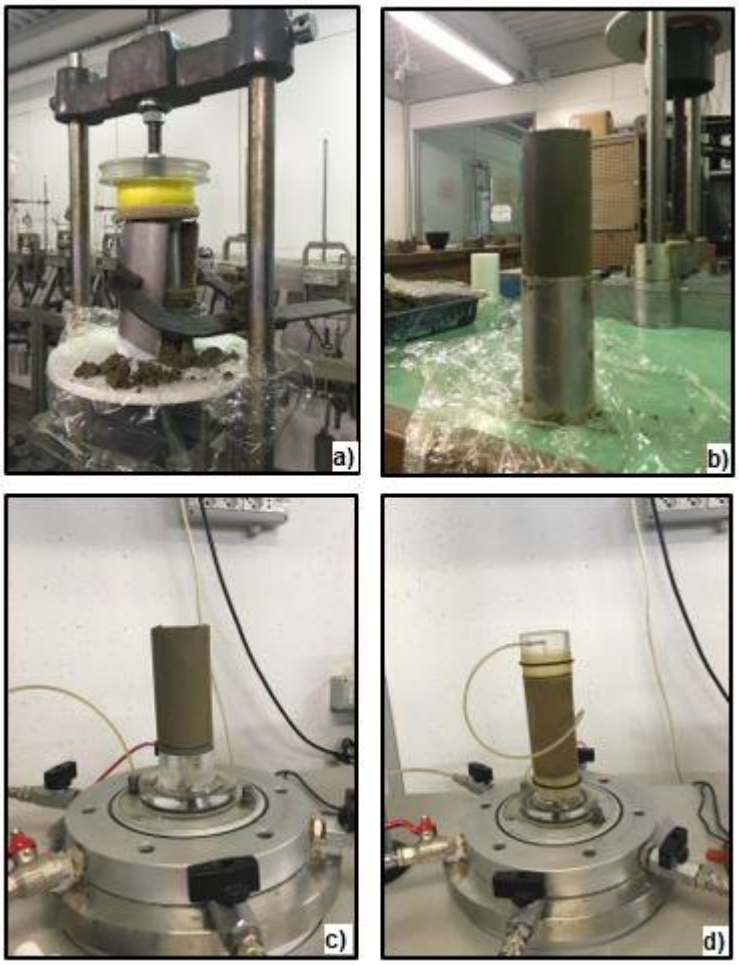

Figure 36 Procedure to create undisturbed triaxial samples: a) hand-operated soil lathe; b) extrusion; c) placement on the pedestal; d) final configuration.

Each portion is cut longer than the required test height in order to make the faces flat and parallel each other. The sample is mounted on the pedestal, laying a saturated porous stone and a dampened filter paper which are placed at the bottom and at the top of the specimen (Figure 36(c)). A latex membrane is fitted to the sample through a membrane stretcher. A layer of silicon grease and two *O*-rings are placed at the top and bottom (Figure 36(d)).

5.7. Triaxial test procedure

Measurements of dimensions and weight of both reconstituted and undisturbed specimens are recorded. The initial height is evaluated as the mean value calculated from readings taken at different sides of the sample. The initial diameter is measured

in different positions and heights using a caliber and applying the correction term due to membrane thickness (i.e. 0.15-0.30 mm). A checking procedure on triaxial apparatus before use is necessary with the aim of eliminating all traces of air and water leaks. In order to reach a higher degree of saturation, a carbon dioxide (CO_2) cycle is performed for about two hours (0.5 bar). Indeed, the soil voids are filled earlier by CO_2, which is more soluble in water than air, and then a cycle of de-aerated water is made through the specimen from the bottom to the top. The saturation phase under a low effective stress is performed by a linear increase of the cell and the back-pressure for several days. The cell pressure and back-pressure, in fact, are increased step by step keeping the difference in a range of 15-50 kPa. To check the degree of saturation is sufficiently suitable before starting consolidation phase, *B*-check test is performed determining the *Skempton's* B_s-value as (eq.(6)):

$$B_s = \frac{\Delta u}{\Delta \sigma_c} \qquad (6)$$

Where Δu defines the change in pore pressure and $\Delta \sigma_c$ cell pressure increment. An appropriate *B*-value for granular soils equal to 0.97 has been reached. Each sample is subjected to an isotropic consolidation phase adopting a stress control approach, which is carried out by increasing the cell pressure till the effective stress state required for shearing. A constant rate of 10 kPa/h is assumed for the loading stages, and 20 kPa/h for the unloading paths in order to assure the overall drainage. Samples are isotropically consolidated at different confining pressures: from 100 to 800 kPa for *Padano Aquifer* sandy soils and from 80-200 kPa for river embankment. The lower values of effective stress are justified by the lower depths; while the higher values are useful to better identify the *Critical State Line* (Klotz and Coop, 2002; Luzzani and Coop, 2002) and to validate the constitutive law in isotropic

compression. For this reason, a number of unloading-reloading cycles have been carried out during consolidation in *TXCID4A* and *TXCID5* tests on samples from *Padano Aquifer* and in all the tests on the river embankment samples. Instead, *TXCID1A*, *TXCID2A* and *TXCID3A* on samples from *Padano Aquifer* have been performed by increasing the cell pressure monotonically whilst maintaining a constant back pressure.

When the isotropic consolidation is accomplished, a drained/undrained shearing stage can begin. The contact between the top of the sample and the load cell is established after the isotropic consolidation, lowering slowly the submersible load cell without increasing the effective stress. The shear phase is performed in strain rate control by applying an axial strain at a constant velocity through upward movement of the basement of the triaxial cell. The suitable rate is estimated according to the test type (drained/undrained) and the height of sample at the end of the isotropic consolidation stage.

In particular, a rate of strain equal to 0.1% per hour is assumed to perform drained triaxial tests. Since the axial compression of the sample related to a strain of 0.1% is $(\frac{0.1\%}{100}) \cdot H_{FC}$, where H_{FC} is the height of sample computed at the end of consolidation in mm, the maximum rate of axial displacement is calculated as (eq.(7)):

$$v_{shear} = \frac{0.001 * H_{FC}}{3600} \ (\frac{mm}{s}) \qquad (7)$$

The standard value assumed for the tested granular soils is 0.0001 mm/s, checking that no overpressure is generated through the external pore pressure transducer.

As suggested by Head (1986), for undrained triaxial tests, the maximum rate of axial strain to be imposed is equal to $\frac{\varepsilon_f}{t_f}$ % per minute. Overcoming this threshold produces the development of inhomogeneous overpressures which brings to overestimate the peak value. Thus, the maximum rate of axial displacement is estimated for each test as (eq.(8)):

$$v_{shear} = \frac{\varepsilon_f * H_{FC}}{100 t_f} \left(\frac{mm}{min}\right) \quad (8)$$

Where t_f is the time of failure in minutes, without side drains, estimated as (eq.(9)):

$$t_f = 0.51 t_{100} \quad (9)$$

Consistent with t_{100} evaluated by K_0-oedometrer tests on samples of river embankment and in order to have a suitable amount of information to describe the modulus reduction curve, the standard range assumed is 0.0100-0.0189 mm/min according to the fine granular soil percentage.

Each test is continued until a specific value of axial strain (ε_a) is reached, verifying the development of the plateau which highlights no further changes in volume or stress. The proposed ranges of strains at failure in triaxial tests are shown in Table 2, summarized below (Head, 1986):

	Typical ranges of strain at failure ε_f (%) (maximum deviator stress)	
Soil type	*TXCIU test*	*TXCID test*
Compacted sandy silts	8-15	10-15
Saturated sand:		
Dense	25+	5-7
Loose	12-18	15-20

Table 2 Suggested failure strains in triaxial tests (Head, 1986).

The drained triaxial tests carried out on *Padano Aquifer* samples are stopped when it is reached an axial strain equal to 25-40%. Regarding the river embankment specimens, the selected range is 10-20% and 15-25% for drained/undrained triaxial tests, respectively.

At the end of the shearing stage, the cell pressure is reduced up to the atmosphere pressure (101 kPa), closing the drainages to avoid further volume changes of the sample. The triaxial apparatus is emptied and carefully dismantled. The final dimensions of the sample are measured using a caliper, before to place the sample into a container and to weigh it. The residual material on filter papers and membrane is gathered using a squeeze bottle with distilled water. The moist specimen and the material collected are put into the oven at 105°C. The dry weight is used to determine the final water content.

5.8. Interpretation of triaxial test results

At the end of each test, an accurate data processing has been accomplished. The axial, ε_a, and volumetric strains, ε_v, are calculated as (eqs.(10)-(11)):

$$\varepsilon_a = \frac{(\Delta H)}{H_i} \qquad (10)$$

$$\varepsilon_v = \frac{(\Delta V_{back})}{V_i} \qquad (11)$$

Where ΔH or ΔV_{back} is the difference between the height or volume of sample corresponding to the current reading of axial displacement and the value, H_i or V_i, at the beginning of the test for the isotropic compression and at the end of consolidation for the shearing, respectively.

The specific volume, *v*, is determined as (eq.(12)):

$$v = v_0(1 - \varepsilon_v) \quad (12)$$

The initial specific volume, v_0, is determined as an average value (Rocchi and Coop, 2014) adopting two relationships based on independent measurements (eqs.(13)-(14)):

$$v_0 = \frac{G_s \cdot \gamma_w}{\gamma_{d,0}} \quad (13)$$

$$v_0 = \frac{G_s \cdot \gamma_w}{\gamma_{d,f}} \frac{1}{(1 - \varepsilon_v)} \quad (14)$$

Where γ_w is the unit weight of water; $\gamma_{d,0}$ and $\gamma_{d,f}$ are the dry unit weight of the soil before and at the end of the test, respectively; ε_v is the cumulated volumetric strains.

The mean effective stress, p', is calculated as (eq.(15)):

$$p' = \frac{(2\sigma'_r + \sigma'_a)}{3} \quad (15)$$

Where σ'_r and σ'_a are the radial and axial effective stress, respectively.

The deviatoric stress, q, cannot be measured directly, but as derived quantity from the force, F, using the internal submersible load cell (eq.(16)).

$$q = \frac{F}{A_c} \quad (16)$$

The current cross-section area (A_c) of the specimen (eq.(17)) is evaluated assuming a right-cylindrical deformation of the sample during shear (Bishop and Henkel, 1957) and is estimated by the volumetric strain (eqs.(18)-(19)):

$$A_c = (\pi r_c^2) \quad (17)$$

$$r_c = r_{FC}(1 - \varepsilon_r) \quad (18)$$

$$\varepsilon_r = -\frac{\varepsilon_a}{2}(1 - \varepsilon_v) \quad (19)$$

Where r_c is the current radius of the specimen and r_{FC} is the radius at the end of the consolidation phase.

Typically, the tested specimen show a “barrel” deformation or a failure mechanism which concerns the sliding of rigid blocks along the shear plane due to the localization of strains that is a severe problem at lower stress levels when trying to identify *Critical State* position (Lopez-Querol and Coop, 2012). In this case, the current area was corrected by applying the formulation proposed by La Rochelle et al. (1988), as depicted in Figure 37 according to the equations (20) - (22).

$$\delta^* = \frac{-\Delta(h_p)}{h_p} \tag{20}$$

h_p: height of sample at the appearance of the shear plane

$\Delta(h_p)$: decrease of height after the appearance of the shear plane

$$\vartheta = 2\arccos\left[\frac{2\delta^*}{tan(\alpha)}\right] \tag{21}$$

α: slope of shear plane (rad), measured through a goniometer

$$A_c = r_c^2(\vartheta - \sin\vartheta) \tag{22}$$

From the experimental point of view, the stress-strain curve drops slowly due to the progressive reduction of area.

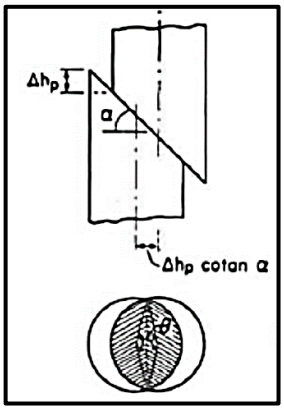

Figure 37 Area correction due to shearing plane appearance (La Rochelle et al., 1988).

5.9. K_0-oedometer and standard oedometer test device

The oedometer compression test consists of applying a sequence of vertical loads to a laterally confined specimen, ensuring one-dimensional consolidation. The loading frame involves a metal structure, which allows the application of the loads to the soil specimen. A saturated porous stone and a dampened filter paper are placed at the bottom and at the top of the specimen to allow the vertical water flow and to prevent the migration of soil grains. The floating-ring cell provides for the ring is supported on lower porous disc having a diameter large as that of the specimen. An outer casing with distilled water prevents drying of sample and saturated porous discs during the test. A dial gauge allows to evaluate the setting due to the application of the loads, with a resolution of 0.01 mm and a maximum displacement measurable of 100 mm. Two types of oedometer systems, known as *Belladonna* and *Bishop* apparatus, have been used to perform the tests at the Geotechnical Laboratory of the University of Bologna. The setups are depicted in Figure 39, respectively.

Figure 38 Belladonna equipment for standard oedometer tests.

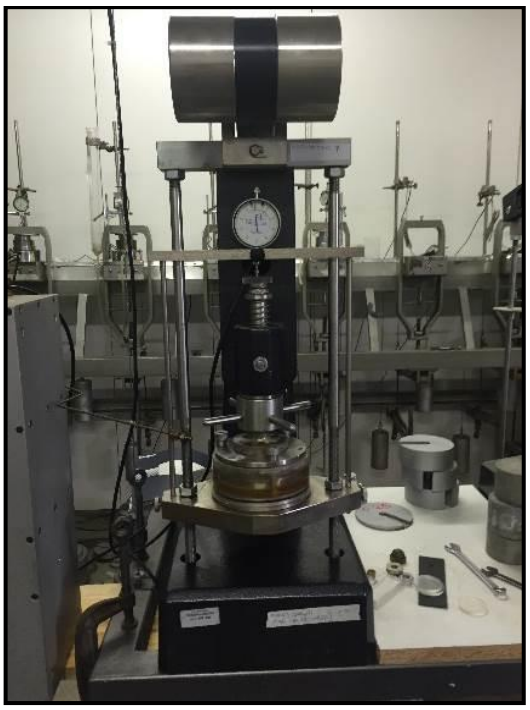

Figure 39 Bishop K_0-oedometer apparatus.

The standard tests have been carried out using *Belladonna* equipment. The sample is placed in a stiff metal ring, which avoids lateral deformations and allows only the vertical drainage. The frame bears a maximum weigh of about 24 MPa. Weights are suspended from a hanger, connected to a lever arm system, with a scale factor of 19.6, which multiplies the applied weigh to determine the correlated loads (*F*). In Belladonna oedometer, the load is applied on the upper face of the sample through a top platen. The K_0-oedometer tests have been performed in a *Bishop* apparatus. The frame bears a maximum weigh of about 25 MPa. The ratio between the longer and the shorter arm determines a scale factor of 10. In the *Bishop* device the load is applied through the cell base, which is thrust upward by the loads by means of the lever system. The sample is placed in a metal ring with an oil-filled chamber, which avoids lateral deformations and allows to determine the horizontal effective stresses. The chamber completely surrounds the perimeter of the specimen with a 0.3 mm internal foil and is equipped with four strain gauges. The inside diameter of the ring is equal to 69.85 mm and the height is 30 mm. The system consists of three

controllers: the K_0-strain unit to amplify the strain gauge signal; the motor-pump unit, which moves the piston to pressurize the oil in the chamber (the maximum value is 40 bar); the K_0-motor driver, which feeds the motor-pump unit with a negative (loading stages) or positive (unloading stages) stress proportional to the ring deformation. A correction factor of 0.92 has to be applied to the readings of the horizontal effective stress due to the calibration curve of the ring.

5.10. Specimen preparation and oedometer test procedure

Reconstituted and undisturbed specimens with different initial specific volume have been tested. The diameter of each sample corresponds to the cell diameter with initial height in the region of 20 mm. The ratio between the diameter and the height of sample is greater than two in order to decrease the effect of lateral friction (Bishop and Henkel, 1957). Before to begin the test, a preliminary reading is carried out. In fact, the initial height of the sample is determined taking the measurement from the displacement transducer immediately after the placement of the top platen and subtracting from it the reading on a dummy sample. This device is a stiff metal disk with known height (21.03 mm), which settlement permits to evaluate accurately the original dimensions of the sample. The stress and strain conditions are assumed to be axis-symmetric. The reconstituted samples have been prepared through the moist tamping procedure for both *Padano Aquifer* and river embankment granular soils. The undisturbed specimen of riverbank has been produced using the cutting ring on the extruded core, removing the excess of soil, as suggested by Head (1986). The specimen surfaces are trimmed flat and parallel in order to reduce errors due to the imperfect alignment. The initial water content has been evaluated putting it in the oven at 105°C a little amount of soil.

Each load step is maintained over a period of time of 24 hours. Unloading-reloading stages are performed. In the loading stages, weights are progressively doubled, whereas in the unloading phases weights are reduced four times every step.

At the end of the last unloading stage, the water bath is emptied before unloading totally and removing the specimen. Gradually the oedometer cell is dismantled. The final dimensions are recorded using a caliper and the readings are taken at different points across the diameter. The specimen and the collected residual material are weighed and placed into an oven at 105°C for 24 hours to estimate the final water content.

5.11. Interpretation of oedometer test results

Since the lateral restraint of the soil sample given by the oedometer cell, the axial and volumetric strains coincide and are estimate as:

$$\varepsilon_a = \frac{(\Delta H)}{H_i} \qquad (23)$$

Where ΔH is the difference between the height of the sample corresponding to the incremental loading step and the initial value (H_i). The current specific volume (v), i.e. the specific volume at the end of the one-dimensional consolidation process related to the sequence of vertical loads, is calculated using the equation (12). As shown for the triaxial test procedure, the initial specific volume has been estimated through independent measurements (Rocchi and Coop, 2014) i.e. the average value between the equation (13) and the equation (24):

$$v_0 = \frac{G_s \cdot \gamma_w}{\gamma_{d,f}} \frac{1}{(1-\varepsilon_a)} \qquad (24)$$

It is advisable that the saturation degree might be maintained in a range of 90-100% for each sample in order to assure that all the pores are saturated: according to this

aim, therefore, the specimens have been reconstituted with high water content. The vertical effective stress is assessed through the equation (29):

$$\sigma'_v = \frac{F_p}{A_{co}} \qquad (25)$$

where F_p corresponds to the applied total load, taking into account the relative levers for each apparatus, and A_{co} is the constant cross section of the laterally confined specimen. The experimental results of the oedometer tests are shown by plotting the mean effective pressure (p') against the current specific volume (v).

$$p' = \frac{(2\sigma'_h + \sigma'_v)}{3} \qquad (26)$$

Where the horizontal effective stress (σ'_h) is obtained using both the K_0-oedometer cell data and the laws proposed by some authors in literature, such described in detail in the next section.

5.12. Coefficient of pressure at rest (K_0)

The K_0-cell allows to evaluate the coefficient of pressure at rest, defined as the ratio between horizontal, σ'_h, and vertical effective stress, σ'_v, which are measured by means of the dial gauge and the motor-pump, respectively (eq.(27)).

$$K_0 = \frac{\sigma'_h}{\sigma'_v} \qquad (27)$$

The validation of the actual value of K_0 is performed using the experimental results of the triaxial tests. Since at the *Critical State* the slope of the envelope (M_g) is equal to the ratio q/p', the angle φ' is estimated by inverting the equation (28):

$$M_g = \frac{6\sin(\varphi')}{3 - \sin(\varphi')} \qquad (28)$$

By means of the Jaky's law, the K_0 coefficient is calculated (eq.(29)) as:

$$K_0 = 1 - \sin(\varphi') \quad (29)$$

Evaluating the mean value of K_0 between triaxial and K_0-oedometer tests, the assumed coefficients of pressure at rest are 0.40 (φ' = 37°) for *Padano Aquifer* sands; 0.45 (φ' = 33°) and 0.41 (φ' = 36.5°) for river embankment layers, which show two different envelopes due to soil heterogeneity. The mean coefficient of pressure at rest for the overconsolidated cohesive soil is 0.50 (φ' = 24°) according to Tonni et al. (2015a).

6. Constitutive model

A brief overview of the *GP* framework is presented in this session and the constitutive equations for both the granular and the clay materials are discussed in detail. This non-classical elasto-plastic model has been developed, most likely, in order to describe both the static and the cyclic behaviour of granular soils, thus covering liquefaction and cyclic mobility. Furthermore, the *GP* formulation is an advanced constitutive approach characterized by a small number of soil parameters i.e. 12, which can be calibrated using experimental tests regularly carried out in a geotechnical laboratory. Since the most significant *GP*-based studies in literature focus on a well-known experimental database (e.g. *Toyoura* sand by Verdugo and Ishihara, 1996; *Banding* sand by Castro, 1969; *Kurnell* sand by Russell and Khalili, 2004), the purpose of this study research is to apply the model to natural granular specimens which reproduce in-situ conditions in terms of fabric and grading. As regards the terminology, stress and strain distribution is considered positive in tension and negative in compression. All the normal stresses are effective, thus drained and undrained conditions may be analysed adopting the same framework.

6.1. *Generalized Plasticity* framework

The Generalized Plasticity is a well-established non-linear constitutive framework (Mroz and Zienkiewicz, 1984; Zienkiewicz and Mroz, 1984) that allows for plastic deformations at any stress level, both in loading (*L*) and in unloading (*U*) conditions.

As illustrated by Taiebat and Dafalias (2010), the crucial difference between sands and clays from the perspective of plastic constitutive modeling is the loading direction which is normal to the yield surface. Regarding the first ones, because of their granular nature, the main mechanism of plastic deformation is related to a

change in stress ratio (*q/p'*); the purely elastic region bounded through the yield surface tends to be much smaller than that for cohesive materials, even though in general a pure elastic field for soils is almost non-existing; in the triaxial space, the yield surface must be characterized by a shape that develops along a constant stress ratio line and closed at higher pressure levels where the crushing of the grains can generate plastic deformation. As regards the clays, loading under constant stress ratio creates large plastic deformation (e.g. under K_0 condition); thus, a yield surface must be a closed surface bringing plastic strain early in loading stages with a constant stress ratio. Within the *GP* framework, irreversible plastic deformations are introduced without specifying any yield or plastic potential surfaces: instead, the normal to these surfaces are explicitly defined.

The elasto-plastic behaviour of the material is described by the general incremental relationship (eq.(30)):

$$d\sigma = D_t : d\varepsilon = (C_t)^{-1} : d\varepsilon \tag{30}$$

The current stress state, the direction of the stress increment and a number of internal variables determine the tangent elasto-plastic stiffness tensor (D_t) of order four. The dependence of D_t on the direction of $d\sigma$ has been expressed by simply distinguishing between two different loading classes, namely *loading* (*L*) and *unloading* (*U*). For each stress condition, a normalized direction (*n*) is determined in the stress space. Loading/unloading states are defined by considering the sign of the dot product below (eqs.(31)-(33)):

$$n : d\sigma^e > 0 \; Loading \; condition \tag{31}$$

$$n : d\sigma^e = 0 \; Neutral \; loading \; condition \tag{32}$$

$$n : d\sigma^e < 0 \; Unloading \; condition \tag{33}$$

The limit neutral case corresponds to stress increments for which the material behaviour is elastic and reversible: no plastic deformations occurs.

The strain increment ($d\varepsilon$) can be decomposed into an elastic component and a plastic component (eq.(34)):

$$d\varepsilon = d\varepsilon^e + d\varepsilon^p \tag{34}$$

To ensure continuity between loading and unloading, the tangent elasto-plastic stiffness $D_{t,L/U}$ is defined as a function of directions of unit norm ($n_{g,L/U}$), two scalar functions (H_L and H_U) and the tangent elastic stiffness tensor ($D^e{}_{t,L/U}$).

$$D_{t,L/U}^{-1} = C_{t,L/U} = (D_{t,L/U}^e)^{-1} + \frac{1}{H_{L/U}}(n_{g,L/U} \otimes n_l) \tag{35}$$

$$(D_{t,L/U}^e)^{-1} = C_{t,L/U}^e = \begin{bmatrix} K_t^e & 0 \\ 0 & 3G_t \end{bmatrix} \tag{36}$$

And inserting the equation (35) in the equation (34):

$$d\varepsilon^e = (D_{t,L/U}^e)^{-1} : d\sigma \tag{37}$$

$$d\varepsilon^p = \frac{1}{H_{L/U}}(n_{g,L/U} \otimes n_l) : d\sigma \tag{38}$$

A *Generalized Plasticity* model is therefore fully determined by specifying the tangent elastic stiffness tensor (D_t^e), the loading direction (n_l), the plastic flow direction ($n_{gL/U}$) and the plastic moduli, H_L and H_U (Tonni et al., 2005). Besides, consistency conditions do not have to be fulfilled and a convenient expression for the plastic moduli can be defined on the basis of the experimental evidence. The undefined plastic potential and yield surfaces can be established a posteriori, by integrating directions $n_{gL/U}$ and n_l (Pastor et al., 1990).

6.2. Constitutive model of sand behaviour

Pastor et al. (1990) sand model (i.e. *SandPZ* in literature) simulates with good accuracy the stress-strain behaviour of dense and loose sands under both monotonic and cyclic loading conditions. The original version requires the definition of a series of material parameters, which can be calibrated from tests that are usually performed in a laboratory campaign, such as drained and undrained monotonic triaxial tests or undrained cyclic triaxial tests (Zienkiewicz et al., 1999). Different research contributions (e.g. Pastor et al., 1990; Fernández Merodo et al., 2004; Mira et al., 2009) dealt with an accurate description of the earliest constitutive formulation, along with the several numerical procedures developed for their integration and implementation into a *FE* platform. The original equations of *SandPZ* did not explicitly take into account the dependence of soil response on the internal state, such as a number of constitutive models dating back to '80s and '90s (e.g. Nova and Wood, 1979; Lade and Kim, 1988). Thus, it was a common practice using multiple sets of parameters for the same material under different initial conditions in terms of densities and confining pressures. The constitutive approach adopted in this study is a particular type of *Generalized Plasticity* model, obtained by modifying the model for sands originally developed by Pastor et al. (1990). In particular, the formulation used to simulate the experimental results encompasses the modifications discussed in Tonni et al. (2006), Cola and Tonni (2007) and Cola et al. (2008). The constitutive parameters of the model are 12 and, as a major innovation, the revised constitutive equations include a dependence on a state parameter ψ (Jefferies and Been, 2000) referred to as *Critical State*, with the aim of capturing the combined effect of stress and density on granular soil behaviour. The *Critical State Line* (*CSL*) in the *v*- log *p'* plane is described by the following equation (39):

$$v = \Gamma_{CSL} - \lambda \log(p') \quad (39)$$

The above law postulates a straight line in the *v*-log*p'* plane which is parallel to the so-called *Normal Consolidation Line* (*NCL*), where all the possible states found that a soil should reach when it is subjected to an increasing isotropic compression. It is worth mentioning here that a crucial feature of the constitutive formulation is the expression of dilatancy d_g, given by Li and Dafalias (2000) and adjustments to the plastic modulus expression are introduced by this parameter.

Since the model material response is isotropic in both the elastic and plastic components, the constitutive equations are function of the three invariants of the effective stress tensor (*p*, *q*, *θ*) and the work-conjugate strain invariants ($d\varepsilon_v$, $d\varepsilon_s$). Furthermore, it is advisable that the model is presented in the *q*-*p'* formulation, since the validation of the constitutive equations (eqs.(40)-(47)) is restricted to the performed triaxial tests.

$$p' = -I_1 \quad (40)$$

$$q = \sqrt{3J_2} \quad (41)$$

$$d\varepsilon_v = tr(d\varepsilon) \quad (42)$$

$$d\varepsilon_s = \sqrt{\frac{2}{3}}(dev(d\varepsilon)) \quad (43)$$

Where:

$$I_1 = \frac{1}{3} tr(\sigma') \quad (44)$$

$$J_2 = \frac{1}{2} dev(\sigma') : dev(\sigma') \quad (45)$$

$$J_3 = \frac{1}{3} dev(\sigma') : dev(\sigma') \quad (46)$$

$$-\frac{\pi}{6} < \theta = \frac{1}{3} sen^{-1}\left(-\frac{3\sqrt{3}}{2}\frac{J_3}{(J_2)^{\frac{3}{2}}}\right) < \frac{\pi}{6} \quad (47)$$

The loading vector n_l is computed as (eq.(48)):

$$n_l = \frac{\delta f}{\delta \sigma'} = \frac{\delta f}{\delta p'}\frac{\delta p'}{\delta \sigma'} + \frac{\delta f}{\delta q}\frac{\delta q}{\delta \sigma'} + \frac{\delta f}{\delta \theta}\frac{\delta \theta}{\delta \sigma'} = C_1 A_1 + C_2 A_2 + C_3 A_3 \quad (48)$$

Where the base vectors A_i are the partial derivatives of the stress invariants p, q, θ with respect to the effective stress σ'.

The components of the loading vector C_i are defined below (eqs.(49)-(51)):

$$C_1 = n_{l,v,L} = \frac{d_f}{\sqrt{(1 + (d_f)^2)}} \quad (49)$$

$$C_2 = n_{l,s,L} = \frac{1}{\sqrt{(1 + (d_f)^2)}} \quad (50)$$

$$C_3 = n_{l,\theta,L} = -\frac{q M_f \cos(3\theta)}{2\sqrt{(1 + (d_f)^2)}} \quad (51)$$

In the absence of meaningful experimental data carrying out specific insights into the yield locus and thus its gradient, the Pastor et al. (1990) relation (eq.(52)) has been used:

$$d_f = (1 + \alpha_f)(M_f - \eta) \quad (52)$$

Where d_f is a function of the stress ratio $\eta = q/p'$ and the material parameters α_f and M_f. The component M_f is evaluated as a function of the slope of *CSL* (M_g) and the state parameter ($\psi_{ini} = \frac{v_{ini}}{v_{CSL}}$) at the beginning of the isotropic compression/shearing phase (eq.(53)).

$$M_f = M_g \exp(-R_d \frac{v_{ini}}{v_{CSL}}) \quad (53)$$

Where R_d is a material parameter.

The model adopts a non-associated flow rule; therefore, the flow direction n_g is different from the loading path, n_l, and cam be expressed as (eq.(54)):

$$n_g = \frac{\delta g}{\delta \sigma'} = \frac{\delta g}{\delta p'}\frac{\delta p'}{\delta \sigma'} + \frac{\delta g}{\delta q}\frac{\delta q}{\delta \sigma'} + \frac{\delta g}{\delta \theta}\frac{\delta \theta}{\delta \sigma'} = F_1 A_1 + F_2 A_2 + F_3 A_3 \quad (54)$$

The components of the plastic flow vector F_i are calculated as (eqs.(55)-(57)):

$$F_1 = n_{g,v,L} = \frac{d_g}{\sqrt{(1 + (d_g)^2)}} \quad (55)$$

$$F_2 = n_{g,s,L} = \frac{1}{\sqrt{(1 + (d_g)^2)}} \quad (56)$$

$$F_3 = n_{g,\theta,L} = -\frac{qM_g \cos(3\theta)}{2\sqrt{(1 + (d_g)^2)}} \quad (57)$$

Where d_g is the expression of dilatancy, given by Li and Dafalias (2000) law (eq.(58)):

$$d_g = \frac{d\varepsilon_v^p}{d\varepsilon_s^p} = D_0(M_g \exp(m_d \psi) - \frac{q}{p'}) \quad (58)$$

D_0 and m_d are material parameters. This state-dependent dilatancy law permits to model appropriately the behaviour of granular soils covering a wide range of pressures and densities, satisfying basic premises of *Critical State* soil mechanics. The effectiveness of the formulation (58) has been studied with respect to several classes of granular soils, such as clean sands (Li and Dafalias, 2000; Manzanal et al., 2011a, 2011b), fine silty sands/sandy silts of the Venetian lagoon subsoil (Tonni et al., 2006; Cola et al., 2008), air-fall volcanic (pyroclastic) soil (Cuomo et al., 2015) and blended waste materials from coal mining (Chiaro et al., 2015).

Since irreversible contractive strains developed in unloading paths, the volumetric component of plastic flow vector is assumed equal to (eq.(59)) during unloading in shear paths:

$$n_{g,U} = -\left|(n_{g,v,L})\right| \tag{59}$$

The failure envelope at *Critical State* in the *q* - *p'* effective stress plane is given by the classical formulation written in the equation (60):

$$q = M_g \cdot p' \tag{60}$$

Where the slope M_g is a function of the Lode angle ($\hat{\theta}$) according to a smoothed version of Mohr's criterion (eq.(61)).

$$M_g = \frac{6\sin(\varphi')}{3 - \sin(\varphi')\sin(3\hat{\theta})} \tag{61}$$

The plastic modulus components proposed in this study account for the stiffness decrease as the shear plastic deformation increases. A further key ingredient of the model is the plastic modulus in loading, H_L, expressed as (eqs.(62)-(66)):

$$H_L = H_0 \cdot H_f \cdot H_s \tag{62}$$

Together with

$$H_0 = \kappa_H \exp(-\beta_H \psi) K_t^e \tag{63}$$

$$H_s = \frac{1}{(1 + \xi^{\beta_s})} \tag{64}$$

$$H_f = (1 - \frac{\frac{q}{p'}}{M_g \exp(-n_f \psi)}) \tag{65}$$

Where H_0 is the plastic modulus governing isotropic compression of sands, as proposed by Jefferies and Been (2000), κ_H and β_H are material parameters, and K^t_e is the tangent elastic bulk modulus. It is worth noting that such equation (63) is a simplified formulation of that proposed by Tonni et al. (2006) and Cola et al. (2008), which was in turn originally defined by Jefferies and Been (2000) from the interpretation of a database of isotropic compression tests on *Erksak sand* (Been et al., 1991). The component H_0 is related to K^e_t through the sole state parameter (ψ),

without the influence of a stress factor which accounts for the current stress level effect and the grain crushing pressure in shear such as in Jefferies and Been (2000). Indeed, the pressure values included in the pressure range associated to the performed laboratory tests are far from the condition at which grain crushing becomes prevalent and therefore, in this study, the latter phenomenon has little small impact on H_0. High pressure tests could be useful to investigate the possible destructuration of the soils, but, in this study, considering a number of representative grading distributions post-triaxial and post-oedometer tests, it is clear how the grain crushing of the particles is not a relevant fraction.

The component H_s accounts for the plastic stiffness degradation of soils as a function of the accumulated deviatoric plastic strain, ξ, which simulates the effect of fabric evolution during shearing; n_f and β_s (often = 1) are model parameters.

The "failure" component H_f includes the idea that during the distorsional process the sand is striving to attain the current peak stress ratio.

$$\eta_p = M_g \exp(-n_f \psi) \tag{66}$$

According to eq.(66), η_p changes with ψ in a way that results in $\eta_p > M_g$ for dense states and $\eta_p < M_g$ for loose states. The concept of a virtual failure stress ratio depending on the material internal state was dealt by different authors (Muir Wood et al., 1994; Manzari and Dafalias, 1997; Wang et al., 2002). In this study the mobilized peak stress ratio was related to the state parameter (ψ) through an exponential function (Li and Dafalias, 2000). Moreover, during the unloading stages, the simplified assumption of a constant plastic modulus (H_U) has been hypothesized; whereas, in reloading paths, the discrete memory factor (HDM) of the plastic modulus (Pastor et al., 1990) has been neglected.

Finally, the constitutive approach assumes a simple non-linear hypoelastic formulation to define the reversible component of the stress-strain response of

sands, with the tangent bulk (K^e_t) and shear (G_t) moduli given by the laws (eqs.(67)-(68)):

$$K_t^e = K_{t,ini}^e \left(\frac{p'}{p'_0}\right)^{n^*} \quad (67)$$

$$G_t = G_{t,ini} \left(\frac{p'}{p'_0}\right)^{n^*} \quad (68)$$

$K^e_{t,ini}$ and $G_{t,ini}$ being the tangent bulk and shear moduli at the initial mean pressure p'_0, respectively, and n^* is a material parameter. Both the components are dependent only on the hydrostatic part of the stress tensor. According to the hypoelastic formulation, the behaviour in the elastic domain is non-conservative. The Young's modulus (E) is defined by (eq.(69)):

$$E = 3K_t^e(1 - 2\nu) \quad (69)$$

The model is calibrated using the performed triaxial compression tests for a wide range of confining pressures and densities for granular soils. The material has a non-linear elastic response, according to the following relationships (eqs.(70)-(71)):

$$dp' = K_t^e d\varepsilon_v^e \quad (70)$$

$$dq = 3G_t d\varepsilon_s^e \quad (71)$$

6.3. Constitutive model of clay behaviour

Within the *Critical State* framework, a *GP*-based model has been proposed by Pastor et al. (1990), obtaining a satisfactory approximation to deformation behaviour and failure conditions under monotonic loading guaranteeing uniqueness of solution. The material parameters can be obtained from tests that are usually performed in geotechnical laboratory, such as drained and undrained monotonic triaxial tests or standard isotropic compression tests. As already explained, the *CSL* is the locus where all residual states for a given clay should lie, regardless of the stress path (Pastor et al. 1990). The *CSL* is described in *q* - *p'* effective stress plane

by the relationship below (eq.(72)):

$$q = M_g \cdot p' \tag{72}$$

The slope M_g is a function of the Lode angle ($\hat{\theta}$) according to a smoothed version of Mohr's criterion (eq.(73)); thus

$$M_g = \frac{6\sin(\varphi')}{3 - \sin(\varphi')\sin(3\hat{\theta})} \tag{73}$$

Plastic flow is assumed to be associated that is the "*normality rule*". It means that the yield envelope matches the plastic potential i.e. the plastic increment strain vector n_g is in the direction of the outward normal to the yield surface (n_l). The assumption of normality is incorporated in several predictive formulations for saturated clays (e.g. Roscoe and Burland, 1968; Dafalias, 1986; Wheeler et al., 2003; Baudet and Stallebras, 2004; Romero and Jommi, 2008).

Taking as reference the constant *q/p'* tests performed by Balasubramanian and Chaudhry (1978), the cohesive soil dilatancy is a linear function of η (eq.(74)).

$$d_g = \frac{d\varepsilon_v^p}{d\varepsilon_s^p} = (1 + \alpha_f)(M_g - \eta) \tag{74}$$

The direction of the loading vector and of the flow vector are defined below:

$$n_{l,v,L} = n_{g,v,L} = \frac{d_g}{\sqrt{(1 + (d_g)^2)}} \tag{75}$$

$$n_{l,s,L} = n_{g,s,L} = \frac{1}{\sqrt{(1 + (d_g)^2)}} \tag{76}$$

The plastic modulus is given by the equation (77):

$$H_L = H_0 p'(f(\eta) + g(\eta))\left(\frac{\zeta_{MAX}}{\zeta}\right)^{\ddot{\Upsilon}} \tag{77}$$

Where

$$H_0 = \frac{v_0}{\lambda_{NCL} - \kappa_U} \tag{78}$$

λ_{NCL} and κ_U are the slopes of *NCL* and of the elastic unloading path, respectively, for a loading-unloading-reloading cycle in the *v*-log*p'* plane.

$$f(\eta) = (1 - \frac{\eta}{M_g})^{\ddot{\mu}} \frac{(1 + {d_0}^2)}{(1 + {d_g}^2)} \left| sign(1 - \frac{\eta}{M_g}) \right| \tag{79}$$

The function *f(η)* is such that

$$f(\eta) = 1 \quad \eta = 0 \tag{80}$$

$$f(\eta) = 0 \quad \eta = M_g \tag{81}$$

And the constant parameter d_0 is defined as:

$$d_0 = (1 + \alpha_f) M_g \tag{82}$$

The exponent $\ddot{\mu}$ is assumed equal to 2 (Pastor et al., 1990). The deviator strain hardening function *g(η)* is expressed as

$$g(\eta) = \beta_g \exp(-\beta_g \xi) \tag{83}$$

$$\beta_g = \beta_{g0} (1 - \frac{\zeta}{\zeta_{max}}) \tag{84}$$

$\beta_{g0}, \ddot{\Upsilon}$ are constant material parameters. The mobilized stress function, which takes into account the stress history of the cohesive soil, is

$$\zeta = p' \left[1 - (\frac{\alpha_f}{1 + \alpha_f}) \frac{\eta}{M_g} \right]^{-\frac{1}{\alpha_f}} \tag{85}$$

ζ_{max} is its maximum value.

As regards overconsolidated clays, the constant β_g is 0 and consequently the function *g(η)* goes to 0. Thus, the plastic modulus presents a simplified law:

$$H_L = H_0 p' (f(\eta)) \tag{86}$$

A non-conservative energy model within the elastic domain is chosen: the

hypoelastic law is expressed by the following equations for the current volumetric stiffness modulus (eq.(87)) and the current shear stiffness modulus (eq.(88)), respectively:

$$K_t^e = K_{t,ini}^e \left(\frac{p'}{p'_0}\right) \quad (87)$$

$$G_t = G_{t,ini} \left(\frac{p'}{p'_0}\right) \quad (88)$$

It is widely recognized that the behaviour of cohesive soil in its intact and reconstituted state may differ meaningfully due to structure, which is identified as the combination of bonding and fabric (Leroueil and Vaughan, 1990; Cuccovillo and Coop, 1999; Cotecchia and Chandler, 2000; Rocchi, 2014). Thus, due to the lack of high quality undisturbed samples extracted from the cohesive layer at the studied site, the interpretation of the mechanical response is based on the experimental database proposed in Tonni et al. (2015a).

7. Calibration of the constitutive model parameters

A crucial issue in the use of constitutive formulations is represented by the calibration of model parameters. As regards the *GP* model, this process turns out to be a rather complex task. Thus, in this work a particular attention is focused on the determination of soil parameters, starting from the experimental database, performing an accurate soil parameter study. This implies a preliminary simple implementation of the adopted constitutive model for granular soils using a *MATLAB* code in conjunction with a single node integration for the simulation of the laboratory tests. The main aims are to define a standard calibration procedure of the *GP* model and to reproduce the soil response for a wide range of densities and confining pressures using a single set of constitutive parameters. The introduction of the state parameter (ψ) allows to realize this purpose. In addition, most of the model coefficients have been found adopting closed-form solutions and only a small amounts of them are achieved using a trial-and-error procedure. Isotropic compression and shearing phase have been computed separately in order to improve accuracy of results, using the same set of the constitutive parameters whenever that assumption appears internally consistent. As regards clayey deposit, model parameters (e.g. λ_{NCL} and κ_U) of Unit C have been defined in the next chapter using a reference calibration procedure. The accurate identification of the constitutive parameters of each soil unit is an essential starting point for the development of an adequate numerical model of the whole levee, defined within a constitutive framework suitable for seismic geotechnical problems. Sensitivity analyses of the original *GP*-model have been deeply debated in recent research contributions (e.g. Tonni, 2002).

7.1. Stress-Dilatancy law

One of the fundamental keystone in describing the stress-strain behaviour of the soil is to correctly define its dilatancy, which is the ratio of plastic volumetric strain increment to plastic deviatoric strain increment in the triaxial frame (Wood, 1990).

$$d_g = \frac{d\varepsilon_v^p}{d\varepsilon_s^p} \approx \frac{d\varepsilon_v}{d\varepsilon_s} \tag{89}$$

Wan and Guo (1998), Gajo and Muir Wood (1999) suggested to treat dilatancy as a state-dependent quantity, with the concept of *Critical State* as basis. The adopted stress-dilatancy law has been proposed by Li and Dafalias (2000).

$$d_g = D_0(M_g \exp(m_d\psi) - \frac{q}{p'}) \tag{90}$$

The material parameters, D_0 and m_d, are determined in order to find the best fit of the experimental curve through a trial and error procedure and minimizing the root mean square deviation, taking into account that at the phase transformation point (*PTP*), i.e. where the soil behaviour changes from contractive to dilatative, the dilatancy becomes equal to zero. As a result, m_d is given by:

$$m_d = \frac{1}{\psi_{PTP}} \ln\left[\frac{(\frac{q}{p'})_{PTP}}{M_g}\right] \tag{91}$$

being ψ_{PTP} and $(\frac{q}{p'})_{PTP}$ the value of ψ and *q/p'* at the phase transformation point, respectively. A number of tests which present a well-defined *PTP* have been chosen within the experimental database to preliminary define m_d and then D_0, i.e. *TXCID5A* for *Padano Aquifer* sand and *TXCID2*, *TXCID5* and *TXCID6* for Units R and B. In particular, in this latter series of triaxial tests, the calculated values of the two dilatancy parameters differ from each other a little because of a certain intrinsic heterogeneity of the artificial river embankment; nevertheless, a unique set of m_d (=

3.94) and D_0 (= 1.30) has been assumed and then applied to the other tests on silty sands.

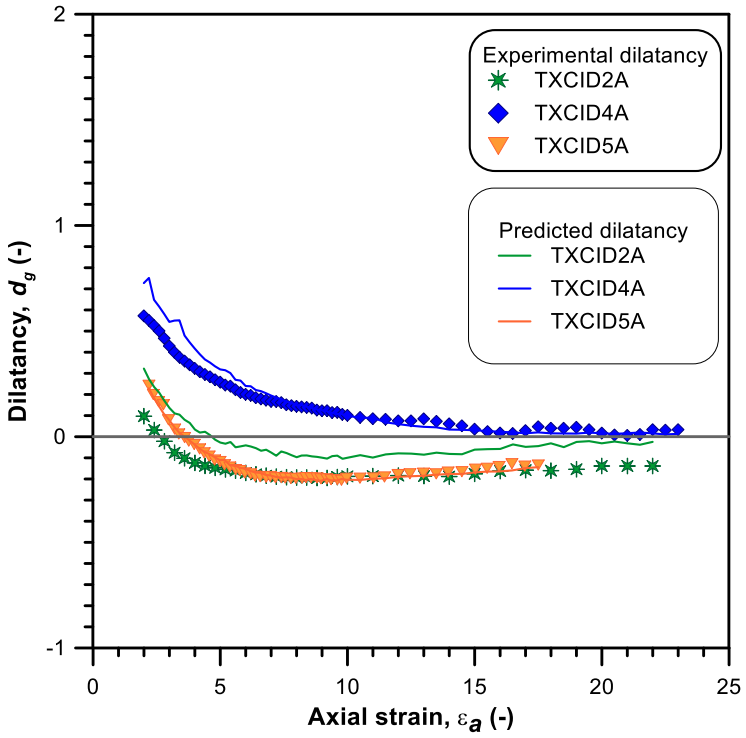

Figure 40 Stress-dilatancy law for Padano Aquifer sand.

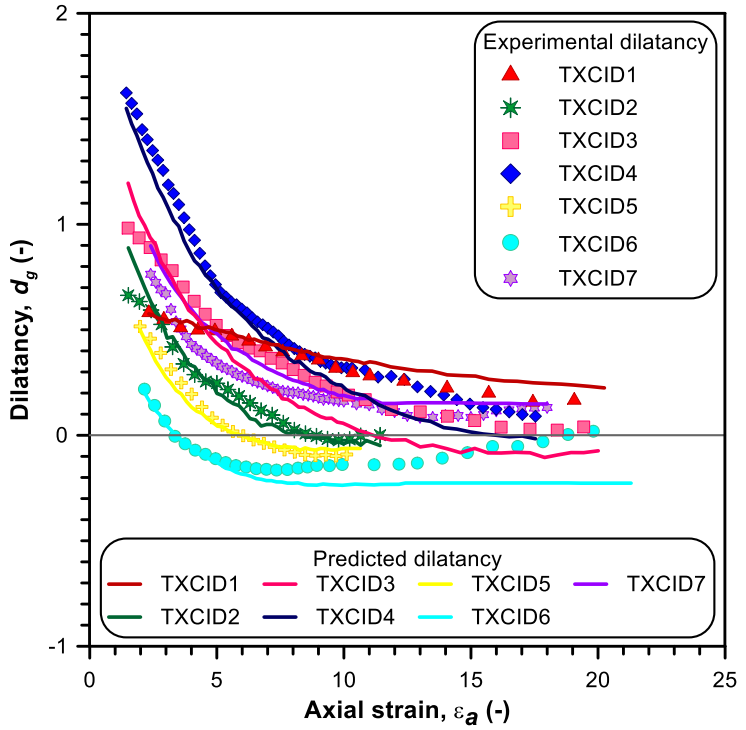

Figure 41 Stress-dilatancy law for river embankment samples.

As regards *TXCID1*, the best agreement of experimental results could be reached by adopting $m_d = 14$ and $D_0 = 0.20$. For the tested samples of the *Padano Aquifer* deposit, the dilatancy parameters have been identified equal to $m_d = 0.11$ and $D_0 = 1.30$, respectively. The prediction of the equation (90) is compared with experimental data in Figure 40 and Figure 41, confirming the reliability of such approach, apart from *TXCID2A* which seems not to obey the law.

In addition, as suggested in Cola and Tonni (2007), the study of stress-dilatancy law has been enriched by the introduction of the equation proposed by Gajo and Muir Wood (1999), where the dilatancy is still treated as a state-dependent quantity but using a linear relationship.

$$d_g = A_d(M_g(1 + k_d\psi) - \frac{q}{p'}) \qquad (92)$$

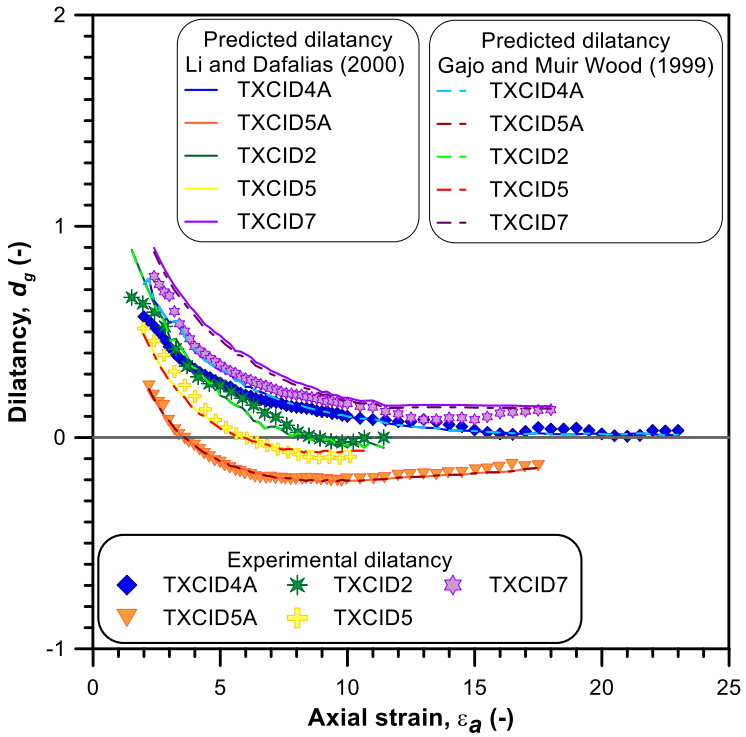

Figure 42 Stress-dilatancy law for some representative samples of Padano Aquifer sands and granular soils of Macro-unit R & B, using Li and Dafalias (2000) - continue line - and Gajo and Muir Wood (1999) - dash line - approach.

The formulation predicts in a very consistent manner the experimental response of the analysed soils and the computed curves match the results obtained from Li and

Dafalias (2000) version, without the need to make any adjustments to the material parameters, as shown in the plot for a number of representative tests. Hence, both the approaches may be used interchangeably, taking in consideration that a linear law alleviates the computational burden in numerical problems.

7.2. Plastic modulus

With particular reference to studies of Pestana and Whittle (1995), the relationship between elastic and plastic modulus are determined adopting the procedure proposed by Jefferies and Been (2000) and performing a deepen soil parameter calibration. The Jefferies-Been (2000) approach is considered because it relates the plastic modulus in isotropic compression (H_0) to the same state parameter (ψ) previously adopted in the dilatancy equation, thus allowing a unified modelling within the state parameter framework. The isotropic compression stages are performed using multiple unloading-reloading paths. Taking as starting point the general definition of stiffness (eq.(93)), each component of modulus is estimated using a linear central difference approximation over a small interval between adjacent readings, *j* and *j+1*, as show in the equation (94):

$$K = \frac{dp'}{d\varepsilon_v} = \frac{v\, dp'}{dv} \qquad (93)$$

$$K_{j+1/2} = \left|\frac{p'_{j+1} - p'_j}{v_j - v_{j+1}}\right| \left|\frac{v_j + v_{j+1}}{2}\right| \qquad (94)$$

The Figure 43 clarifies the adopted procedure. Elasticity properties are defined on the *Unloading-reloading Line*. In particular, K^e_t is the elastic modulus on the *Unloading-reloading Line* at the start of unloading; whereas, $K^e_{(j,j+1)}$ is the elastic modulus for each subsequent decrement of mean effective pressure ($\Delta p'$), assuming a range of 20-50 kPa. The overall modulus *K* is computed on the *Normal*

Compression Line at the end of loading, taking the same stress increment concerned for K^e_t. Plastic compliance is evaluated as the overall compliance (*1/K*) less the elastic compliance (K^e_t). The plastic modulus (H_0) has been determined as the inverse of the plastic compliance.

The dependency of the plastic modulus during isotropic compression on the specific volume and confining pressure is accounted for by the sole state parameter (ψ). With respect to Jefferies and Been (2000) approach, the influence of the stress factor, i.e. the current stress level normalized to the grain crushing pressure in shear, has not been taken into consideration. Indeed, this latter contribution seems to have a minor effect on the value assumed by H_0 in the rather limited range of pressures of the tests carried out which is below the threshold at which grain crushing becomes prevalent. Thus, the ratio between the plastic and elastic modulus has been plotted as a function of ψ: the trend line is described by an exponential law, depicted in Figure 44 and Figure 45 for *Padano Aquifer* sandy materials (eq.(95)) and for river embankment samples (eq.(96)), respectively.

$$H_0 = 0.14 \exp(-3.80\psi)\, K_t^e \qquad (95)$$

$$H_0 = 0.26 \exp(-3.44\psi)\, K_t^e \qquad (96)$$

with $k_H = 0.14$ and $\beta_H = 3.80$, with a coefficient of determination $R^2 = 0.62$ for Unit A; $k_H = 0.26$, $\beta_H = 3.44$ and $R^2 = 0.52$ for Macro-unit R & B.

It is worth noting that, in Jefferies and Been (2000), the abovementioned material parameters assume the values $k_H = 0.30$ and $\beta_H = 6.50$ for the clean, uniformly graded, medium-grained *Erksak* sand. The experimental results of several isotropic compression tests and the corresponding regression laws are shown Figure 44 and Figure 45.

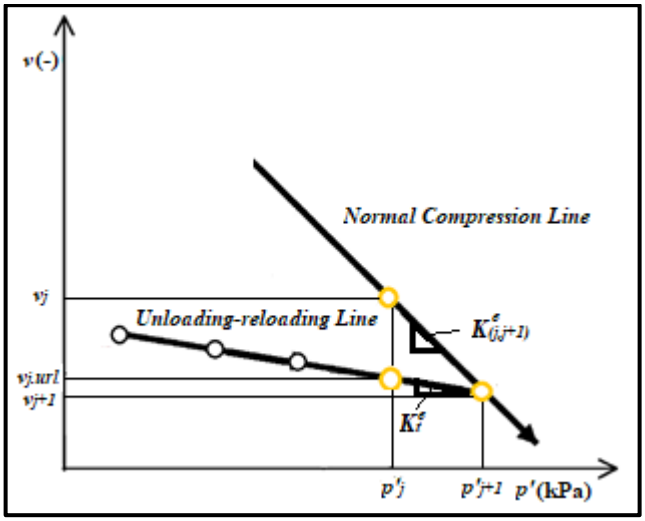

Figure 43 Conceptual model of an isotropic compression loading-unloading-reloading cycle.

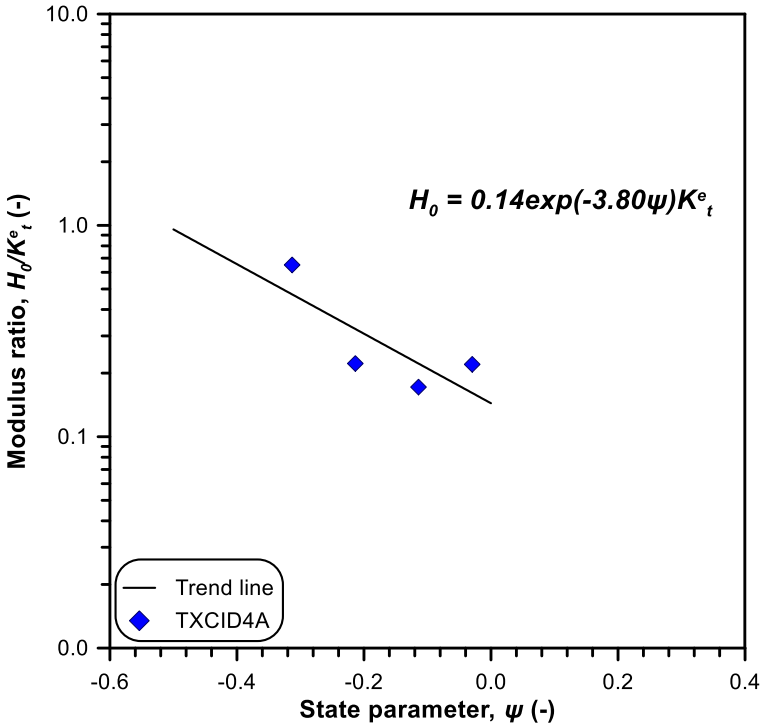

Figure 44 The trend line between state parameter and plastic modulus for Padano Aquifer isotropic compression test (TXCID4A).

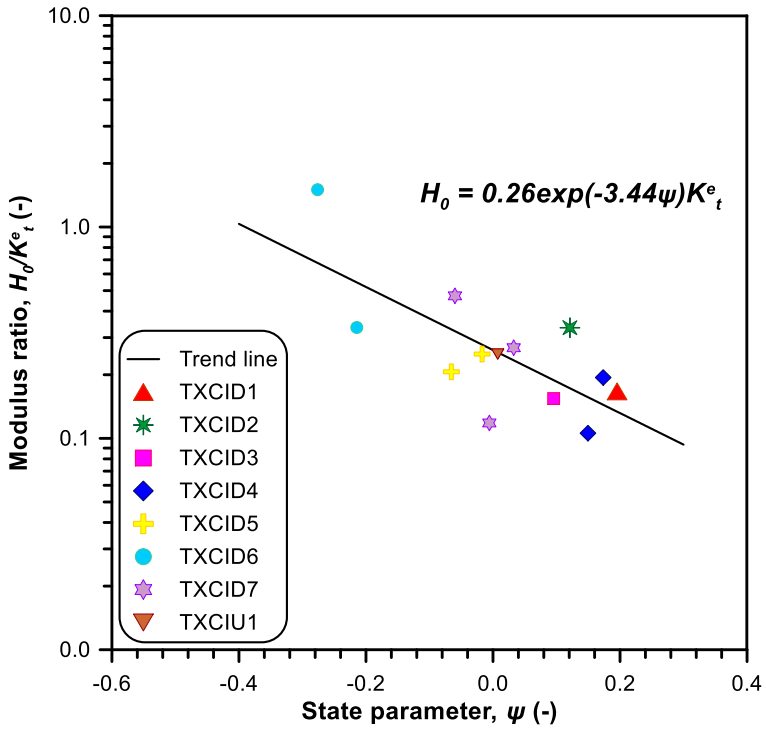

Figure 45 The trend line between state parameter and plastic modulus for river embankment isotropic compression tests.

7.3. Non-linear hypoelastic law

The initial volumetric stiffness ($K^e_{t,ini}$) is estimated using the slope of the unloading-reloading path during the isotropic compression cycles, following the equation (93). The initial shear stiffness ($G_{t,ini}$) has been found by matching the initial slope of the *q*-ε_a curve, also taking into account the well-known correlation to $K^e_{t,ini}$ via a constant coefficient of Poisson in a suitable range for granular soils (ν = 0.20-0.30).

$$G_{t,ini} = \frac{K^e_{t,ini}(3-6\nu)}{2(1+\nu)} \qquad (97)$$

Taking some reference tests, i.e. *TXCID4A* for the *Padano Aquifer* sands and *TXCID1* for the river embankment soils, the initial moduli of each sample have been opportunely calibrated according to the relative initial mean effective pressure through the equations (65) and (66). In details, Section 7.6 deals with the performed computations.

7.4. The *Critical State Line*

Experimental evidence suggests that a *Critical State* is achieved in both soil classes and the *CSL* is described by the following equations for *Padano Aquifer* sands (eq.(98)) and river embankment granular soils (eq.(99)), respectively:

$$v = 2.88 - 0.38\log(p') \quad (98)$$

$$v = 2.15 - 0.24\log(p') \quad (99)$$

These laws have been achieved by the linear regression of the whole experimental database at failure within *v*-log*p'*. Furthermore, the *K_0-Normal Compression Line* (*K_0-NCL*) has been identified from both *K_0*-cell and standard oedometer tests on granular samples, whose equations are, respectively, for Unit A and Macro-unit R & B:

$$v = 2.94 - 0.38\log(p') \quad (100)$$

$$v = 2.20 - 0.24\log(p') \quad (101)$$

The purpose is essentially to gain a better insight into the compression behaviour of soil units A, R and B and subsequently define potential differences in the response as a consequence of their grading characteristics.

As regards the abovementioned equations, it is worth noting that a linear approximation of the *CSL* on the *v*-log*p'* plane has been assumed as acceptable for the pressure level range carried out in this research (corresponding to those generally encountered in engineering practice). In fact, it is extensively documented that non-linearity of the *CSL* must be taken into account over stress intervals wide enough to present the onset of particle breakage (e.g. Been et al., 1991; Li and Wang, 1998; Coop et al., 2004; Altuhafi and Coop, 2011; Bandini and Coop, 2011; Ghafghazi et al., 2011; Yu, 2017).

7.5. Constant material parameters

Since a number of samples have shown the peak in stress-strain behavior curve, n_f (eqs. (65)-(66)) is assumed equal to 0.80 for the *Padano Aquifer* deposit and 4.20 for the granular soils of the Macro-unit R & B. The calibration of n_f can be easily performed at the drained peak stress state, at which the component of the plastic modulus H_f becomes equal to zero. The *TXCID2A* and *TXCID6* have been taken as reference tests in order to determine n_f within the corresponding soil units.

$$n_f = \frac{\ln\left(\frac{\eta_{peak}}{M_g}\right)}{\psi_{peak}} \qquad (102)$$

where η_{peak} and ψ_{peak} are the value of η and ψ at the peak stress state, measured from experimental data.

Through a linear regression of the experimental database, the slope of *CSL* (M_g) is determined, verifying that the value is consistent with the friction angle. The parameter M_f (eq. (53)) is calibrated by M_g and the state parameter at the beginning of shear phase (ψ_{ini}). Preliminarily, such approach needs in turn the determination of the contribution R_d. According to this goal, firstly, R_d has been defined with reference to a single triaxial test for each soil unit, i.e. *TXCID4A* and *TXCID6* for the *Padano Aquifer* sands and the Macro-unit R & B, respectively. As regards Unit A, the sample of the triaxial test *TXCID4A* has been reconstituted at a similar void ratio (v = 1.85) of an undisturbed sample which belongs to a previous laboratory programme (Tonni et al., 2015a) extracted at the same depth, and isotropically consolidated at p'= 400 kPa. The test *TXCID6* has been carried out on an undisturbed sample of Unit B isotropically consolidated at p'= 80 kPa. The relative density (*DR*), i.e. ≈ 50% for *TXCID4A* and ≈ 45% for *TXCID6*, respectively, has been achieved from the interpretation of a series of *CPTU* performed close to the boreholes (Tonni et al., 2015a). In this way, a first evaluation of M_f, termed M_f*, has

been obtained using the procedure proposed by Zienkiewicz et al. (1999) by the equations (103)-(104) for the two relevant soil deposits (Unit A and Macro-unit R & B, respectively):

$$M_f{}^* = DR \cdot M_g = 0.75 \qquad (103)$$

$$M_f{}^* = DR \cdot M_g = 0.67 \qquad (104)$$

Thus, the parameter R_d could be easily back-calculated, consistent with the expression below (eq.(105)):

$$R_d = -\frac{v_{CSL}}{v_{ini}} ln\left[\frac{M_f^*}{M_g}\right] \qquad (105)$$

being v_{ini} = 1.853 and M_g = 1.501 for the *TXCID4A*, v_{ini} = 1.606 and M_g= 1.484 for *TXCID6*. By following the abovementioned procedure, R_d is evaluated to be equal to 0.708 for the *Padano Aquifer* sands and 0.842 for the Macro-unit R & B. These values, which have been kept constant within the units analyzed, have been consequently substituted in equation (53) to obtain M_f related to each sample. The constant material parameters α_f, n^* and β_s (often equal to 1) have been assumed from literature (Tonni et al., 2006; Cola et al., 2008).

7.6. Basic soil characteristics and material parameters of granular samples

The basic soil features of *Padano Aquifer* sand and granular soils of river embankment are listed in the Table 3 - Table 4 and Table 5 - Table 6, respectively. Because of the dependency of the stress-strain behaviour of the granular soil from both the density and the confining pressure condition, the specific volume and the confining stress of each sample are specified. As seen in the previous section, the sandy sample extracted from 9.00-9.20 m has the same basic soil characteristics of

Unit A: thus, the experimental response (i.e. *TXCID5A*) is interpreted within such unit.

As regards the isotropic compression stages of *Padano Aquifer* sands:

Test	*Type of sample*	*Initial v* v_0 *(-)*	*Final v* v_f *(-)*	*Confining stress* p'_0 *(kPa)*	*Depth (m)*	*Section (-)*
TXCID1A	Reconst.	1.987	1.828	15	12.00-12.60	C
TXCID2A	Reconst.	1.929	1.913	15	12.00-12.60	C
TXCID3A	Reconst.	2.057	1.859	20	12.00-12.60	C
TXCID4A	Reconst.	1.934	1.853	20	12.00-12.60	C
TXCID5A	Reconst.	1.872	1.844	25	9.00-9.20	A

Table 3 Triaxial test database adopted for the Generalized Plasticity model calibration of Padano Aquifer sands (isotropic compression phase).

As regards the shearing phase of *Padano Aquifer* sands:

Test	*Type of sample*	*Initial v* $^{(*)}$ v_0 *(-)*	*Final v* v_f *(-)*	*Confining stress* p'_0 *(kPa)*	*Depth (m)*	*Section (-)*
TXCID1A	Reconst.	1.828	1.695	800	12.00-12.60	C
TXCID2A	Reconst.	1.913	1.992	100	12.00-12.60	C
TXCID3A	Reconst.	1.859	1.688	800	12.00-12.60	C
TXCID4A	Reconst.	1.853	1.790	400	12.00-12.60	C
TXCID5A	Reconst.	1.844	1.880	200	9.00-9.20	A
(*) Computed at the end of consolidation						

Table 4 Triaxial test database adopted for the Generalized Plasticity model calibration of Padano Aquifer sands (shearing phase).

As regards the isotropic compression stages of granular soils of river embankment:

Test	*Type of sample*	*Initial v* v_0 *(-)*	*Final v* v_f *(-)*	*Confining stress* p'_0 *(kPa)*	*Depth (m)*	*Section (-)*
TXCID1	Reconst.	1.732	1.718	50	4.00-4.60	C
TXCID2	Reconst.	1.653	1.647	50	4.00-4.60	C
TXCID3	Reconst.	1.767	1.647	50	4.00-4.60	C
TXCID4	Undist.	1.782	1.672	50	7.10-7.50	C
TXCID5	Undist.	1.593	1.551	25	7.70-8.30b	A
TXCID6	Undist.	1.623	1.606	20	7.70-8.30b	A
TXCID7	Undist.	1.697	1.622	25	9.20-9.60	A
TXCIU1	Reconst.	1.685	1.597	50	7.70-8.30a	A

Table 5 Triaxial test database adopted for the Generalized Plasticity model calibration of river embankment granular soils (isotropic compression phase).

As regards the shearing phase of granular soils of river embankment:

Test	*Type of sample*	*Initial v* $^{(*)}$ v_0 *(-)*	*Final v* v_f *(-)*	*Confining stress* p'_0 *(kPa)*	*Depth (m)*	*Section (-)*
TXCID1	Reconst.	1.718	1.609	100	4.00-4.60	C
TXCID2	Reconst.	1.647	1.607	100	4.00-4.60	C
TXCID3	Reconst.	1.647	1.570	150	4.00-4.60	C
TXCID4	Undist.	1.672	1.533	200	7.10-7.50	C
TXCID5	Undist.	1.551	1.529	200	7.70-8.30b	A
TXCID6	Undist.	1.606	1.619	80	7.70-8.30b	A
TXCID7	Undist.	1.622	1.543	200	9.20-9.60	A
TXCIU1	Reconst.	1.597	1.597	150	7.70-8.30a	A
(*) Computed at the end of consolidation						

Table 6 Triaxial test database adopted for the Generalized Plasticity model calibration of river embankment granular soils (shearing phase).

The model parameters of *Padano Aquifer* sands and granular soils of river embankment are shown in the Table 7 - Table 8 and Table 9 - Table 10, respectively. They were determined by considering the reference calibration procedure described in the previous sections. It is worth mentioning that some constitutive parameters have been kept constant within the same soil layer, whenever possible, according to the idea of unified modelling of granular soils based on *GP*. As a consequence of the initial conditions of the soil samples in terms of confining pressure, a different

set of the initial elastic moduli $K^e_{t,ini}$ and $G_{t,ini}$ have been assumed. Similarly, the parameter M_f changes for each performed test due to the initial relative density.

As regards the isotropic compression stages of *Padano Aquifer* sands:

	$K^e_{t,ini}$ (kPa)	$G_{t,ini}$ (kPa)	M_f (-)	D_0 (-)	m_d (-)
TXCID1A	8500	6400	0.71	1.30	0.11
TXCID2A	8500	6400	0.86	1.30	0.11
TXCID3A	10000	7500	0.82	1.30	0.11
TXCID4A	10000	7500	0.85	1.30	0.11
TXCID5A	13000	10000	0.86	1.30	0.11
Parameters common to all tests					
M_g: 1.506 (*)	n^*: 0.60	n_f: 0.80	k_H: 0.14	α_f: 0.45	β_H: 3.80
R_d: 0.708	β_s: 1				

(*) *A different failure envelope has been considered within the test TXCID1A i.e. Mg: 1.261*

Table 7 Model parameters from calibration of Padano Aquifer sands (isotropic compression phase).

All the performed tests follow a monotonic path during the isotropic compression stages, except for the *TXCID4A* and *TXCID5A*. Thus, the calibration of $K^e_{t,ini}$ for the monotonic curves has been carried out using the unloading-reloading cycle at low pressure of *TXCID4A* i.e. $K^e_{t,ini,ref}$ = 10000 kPa at $p'_{0,ref}$ = 20 kPa, determined by the experimental data according to the formulation (93). By inserting the reference values in the equation (106), which reproduces the equation (67), and the p'_{ini} of each test, the tangent bulk moduli of the Table 7 have been obtained.

$$K^e_{t,ini} = K^e_{t,ini,ref}\left(\frac{p'_{ini}}{p'_{0,ref}}\right)^{n^*} \qquad (106)$$

The initial elastic moduli of *TXCID5A* has been evaluated equal to 13000 kPa at $p'_{0,ref}$ = 25 kPa through the experimental unloading-reloading curve as shown in equation (93). The initial shear stiffness $G_{t,ini}$ has been found through the coefficient of Poisson in a suitable range, as described in the previous section.

As regards the shearing phase of *Padano Aquifer* sands:

	$K^e_{t,ini}$ (kPa)	$G_{t,ini}$ (kPa)	M_f (-)	D_0 (-)	m_d (-)
TXCID1A	220000	170000	0.61	1.30	0.11
TXCID2A	53000	40000	0.80	1.30	0.11
TXCID3A	185000	140000	0.72	1.30	0.11
TXCID4A	160000	120000	0.75	1.30	0.11
TXCID5A	120000	90000	0.79	1.30	0.11
Parameters common to all tests					
M_g: 1.506 (*)	n^*: 0.60	n_f : 0.80	k_H: 0.14	α_f: 0.45	β_H: 3.80
R_d: 0.708	β_s: 1				

(*) *A different failure envelope has been considered within the test TXCID1A i.e.* M_g: 1.261

Table 8 Model parameters from calibration of Padano Aquifer sands (shearing phase).

The elastic modulus $K^e_{t,ini,ref}$ = 99000 kPa at $p'_{0,ref}$ = 400 kPa, determined as proposed in eq. (93), has been used as target value during the calibration procedure of the stiffness characteristics listed in Table 8 for *TXCID1A*,*TXCID2*A and *TXCDID3A*. In particular, the process consists of opportunely inserting the reference rate in the equation (106) and making some improvements in order to match suitably the soil responses.

As regards the isotropic compression stages of granular soils of river embankment:

	$K^e_{t,ini}$ (kPa)	$G_{t,ini}$ (kPa)	M_f (-)	D_0 (-)	m_d (-)	M_g (-)
TXCID1	23000	17000	0.58	1.30	3.94	1.331
TXCID2	20000	15000	0.60	1.30	3.94	1.331
TXCID3	10000	7500	0.63	1.30	3.94	1.484
TXCID4	10000	7500	0.56	1.30	3.94	1.331
TXCID5	10000	7500	0.71	1.30	3.94	1.484
TXCID6	9000	7000	0.71	1.30	3.94	1.484
TXCID7	10000	7500	0.61	1.30	3.94	1.331
TXCIU1	15000	12000	0.66	1.30	3.94	1.484
Parameters common to all tests						
n^*: 0.60	n_f : 4.20	k_H: 0.26	α_f: 0.45	β_H: 3.44	R_d: 0.842	β_s: 1

Table 9 Model parameters from calibration of river embankment granular soils (isotropic compression phase).

All the tests listed in Table 9 have been performed through isotropic compression loading-unloading-reloading cycles which permits to calibrate opportunely the initial elastic moduli.

As regards the shearing phase of granular soils of river embankment:

	$K^e_{t,ini}$ (kPa)	$G_{t,ini}$ (kPa)	M_f (-)	D_0 (-)	m_d (-)	M_g (-)
TXCID1	35000	27000	0.56	1.30	3.94	1.331
TXCID2	30000	23000	0.58	1.30	3.94	1.331
TXCID3	51000	39000	0.63	1.30	3.94	1.484
TXCID4	60000	45000	0.55	1.30	3.94	1.331
TXCID5	60000	45000	0.66	1.30	3.94	1.484
TXCID6	26000	20000	0.67	1.30	3.94	1.484
TXCID7	80000	60000	0.57	1.30	3.94	1.331
TXCIU1	20000	15000	0.65	1.30	3.94	1.484
Parameters common to all tests						
n^*: 0.60	n_f : 4.20	k_H: 0.26	α_f: 0.45	β_H: 3.44	R_d: 0.842	β_s: 1

Table 10 Model parameters from calibration of river embankment granular soils (shearing phase).

The stiffness moduli listed in Table 10 have been obtained by the experimental curves at the end of the isotropic compression cycles. Nevertheless, since the heterogeneity of the soil of the Macro-unit R & B, a series of improved value has been adopted to reproduce correctly the experimental curves, taking into account both the confining pressure and the initial specific volume of each samples.

Granular soil specimens characterized by different densities have been tested using both the K_0-cell and the standard oedometer tests. The specific volumes at the beginning and at the end of the consolidation process on *Padano Aquifer* and river embankment materials are specified in Table 11 and Table 12, respectively.

Test	Initial v v_0 (-)	Final v v_f (-)	Maximum applied stress (kPa)	Type of sample
K_0-oedometer 1A (12.00-12.60 m; Sec.C)	1.483	1.454	1672	Reconst.
K_0-oedometer 2A (12.00-12.60 m; Sec.C)	1.511	1.473	1672	Reconst.
Oedometer 1A (12.00-12.60 m; Sec.C)	1.916	1.456	17323	Reconst.
Oedometer 2A (12.00-12.60 m; Sec.C)	1.812	1.435	17323	Reconst.
Oedometer 3A (12.00-12.60 m; Sec.C)	1.779	1.456	17323	Reconst.

Table 11 K_0-cell and standard oedometer test database adopted for the determination of the Normal Compression Line of Padano Aquifer sands.

Test	Initial v v_0 (-)	Final v v_f (-)	Maximum applied stress (kPa)	Type of sample
K_0-oedometer 1 (4-4.60 m; Sec.C)	1.746	1.510	1672	Reconst.
K_0-oedometer 2 (4-4.60 m; Sec.C)	1.664	1.486	1672	Reconst.
K_0-oedometer 3 (7.70-8.30 m [a]; Sec.A)	1.580	1.471	1672	Undist.
K_0-oedometer 4 (7.70-8.30 m [b]; Sec.A)	1.532	1.345	2090	Reconst.

Table 12 K_0-cell oedometer test database adopted for the determination of the Normal Compression Line of granular soils of river embankment.

7.7. Experimental and predictive curves – *Padano Aquifer* samples

The experimental data are plotted in terms of specific volume - vertical effective stress on a logarithmic scale for the standard and K_0-cell oedometer tests (Figure 46), specific volume - mean effective pressure on a logarithmic scale for the triaxial tests (Figure 47, Figure 48 and Figure 54), volumetric strain - axial strain (Figure 56), specific volume - axial strain (Figure 58), deviatoric stress - axial strain (Figure

60), stress ratio - axial strain (Figure 62) and deviatoric stress – mean effective pressure (Figure 64). In order to have an appropriate frame of reference, this study is not limited to the available laboratory data but includes an independent *TXCIU* testing programme on samples of the same soil unit (Tonni et al., 2015a).

The existence of a unique *NCL* within the *v-logσ'v* plane has been suggested by the convergent compression curves (Figure 46), whose slope increases at pressures slightly higher than 1 MPa. On the *NCL*, the steepening of the compression paths is related to the onset of substantial breakage effects (McDowell and Bolton, 1998), due to the strength of sole particles. Mesri and Vardhanabhuti (2009) illustrate that clean quartz sands achieve their *NCL* in the stress range 10-100 MPa, whereas Shipton and Coop (2012) show 1-3 MPa for the *Dogs Bay* carbonate sand, as detected for the *Padano Aquifer* sands.

The stress-strain curves highlight as the tests *TXCID1A* and *TXCID4A* are characterized by strain-hardening responses; whereas *TXCID2A* and *TXCID5A* present a moderate peak stress ratio. Regarding the influence of the mean effective stress on samples with similar initial state (e.g. *TXCID4A* and *TXCID5A*), the deviator stress increases with confining pressure and the response becomes more contractive. Within the volumetric framework, the *Padano Aquifer* sand exhibits typically a contractive response, except for the samples consolidated at the lowest confining pressure i.e. p'_0 = 100 kPa (*TXCID2A*) and 200 kPa (*TXCID5A*).

As regards the test *TXCID3A*, during the shearing stages, the load cell was not able to read the correct development of the deviatoric stress in time; thus, only the volumetric behaviour can be opportunely described. Nonetheless, the state at the end of the shear phase was manually recorded i.e. v = 1.688 at p' = 1535 kPa.

Considering the basic properties described in the previous sections (e.g. grain size distribution, *FC*), it is not surprising that the sandy sample of *TXCID5A* proves an experimental response in a good agreement with the other results.

The experimental curves *TXCID2A*, *TXCID4A* and *TXCID5A* exhibit an ultimate condition reached at large deformations, which is defined by a unique value of the stress ratio (i.e. q/p' = 1.506) irrespective of the relative density and confining pressure. This value, which detects the gradient M_g, presents a substantial agreement with results reported in Tonni et al. (2015a) for soils within the same unit. A similar consideration may be derived from the test *TXCID3A*, whose ultimate state tends to follow the *CSL* identified by a slightly slower M_g ($q/p' \approx 1.44$) in the effective stress plane. On contrary, the test *TXCID1A* seems to be inconsistent with the previous trend with an ultimate stress ratio q/p' = 1.261. Such discrepancy may be related to two different factors: the first is a sort of sample scale effect (Jefferies et al., 1990) since the specimen diameter in this case is equal to 38 mm instead of 50 mm; the second is the potential grain crushing caused by the high consolidation pressure (i.e. 800 kPa) which may affect the experimental response of the sand. Then, the results carried out suggest the use of different ultimate conditions to be introduced within the constitutive equations in order to improve its predictive capability and avoid that the data may get partly lost in the stress-strain plane. Thus, different failure envelopes have been implemented (Figure 64): in particular, a reference value M_g equal to 1.261 (φ' = 31.5°) has been taken for the test *TXCID1A* and equal to 1.506 (φ' = 37°) for the other tests. Symbols in grey, based on the results of a previous *TXCIU* testing programme (Tonni et al, 2015a) on samples of the same soil unit, result in a *CSL* slope M_g between 1.36 and 1.51.

Starting from a low initial isotropic stress state, drained compression/decompression stages have been simulated by applying to the sample increments/decrements of

confining pressures, maintaining the initial pore water pressure distribution; then, the shear phase has been reproduced in strain rate control. A number of unloading-reloading cycles have been carried out for the consolidation process in the tests *TXCID4A* and *TXCID5A*; whereas, the cell pressure is increased monotonically during the other simulations of the same soil unit. Isotropic unloading-reloading has been assumed elastic.

To assess the model predictive capability, experimental (lines characterized by symbols) and model prediction curves (solid lines) are compared for isotropic compression stages in Figure 49-Figure 53, and for shearing stages in Figure 55, Figure 57, Figure 59, Figure 61 and Figure 63. The isotropic compression phases in conjunction with the relative predictive curves are depicted singularly for each test in order to clarify the plots; instead, the responses during the shear stages are illustrated within global graphs to make comparisons.

The plots highlight as the application of the constitutive model to the analyses of *Padano Aquifer* soils resulted in rather acceptable predictions of the real behaviour. In particular, it is evident that the simulations derived from the application of an adequate set of parameters match well the stress-strain responses of the sandy samples; furthermore, good agreement between the experimental and predictive curves is found within the volumetric framework. As regards *TXCID3A*, the computed data reported in Figure 55 and Figure 63 cannot be compared with the experimental ones but for the ultimate state, which turns out to be successfully simulated.

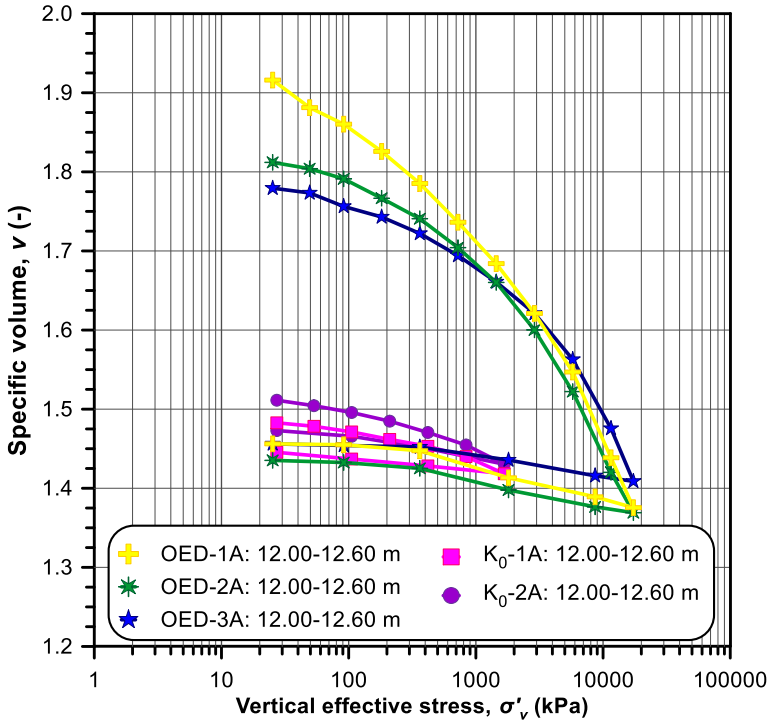

Figure 46 Standard and K_0-oedometer tests on Padano Aquifer sands.

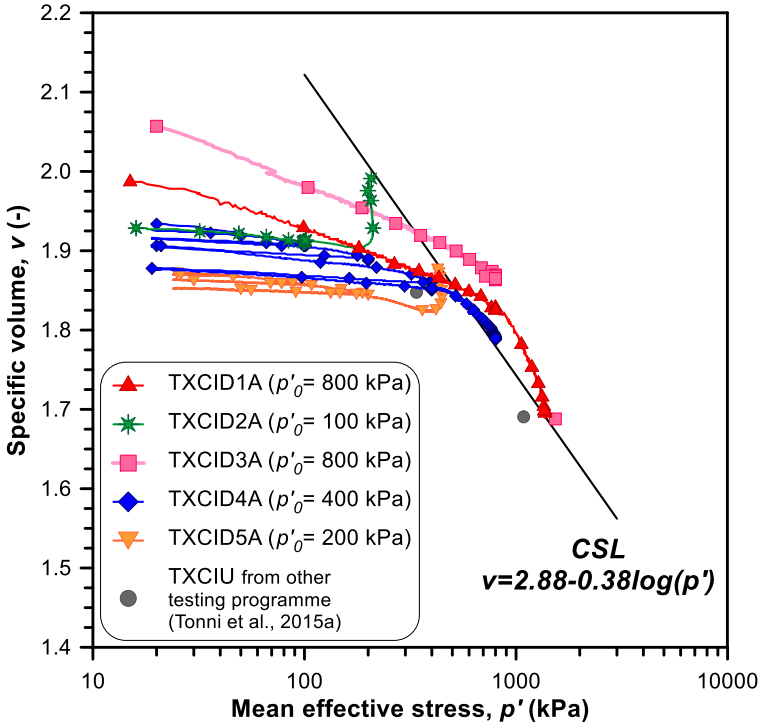

Figure 47 Experimental curves for Padano Aquifer samples in the v-logp' plane.

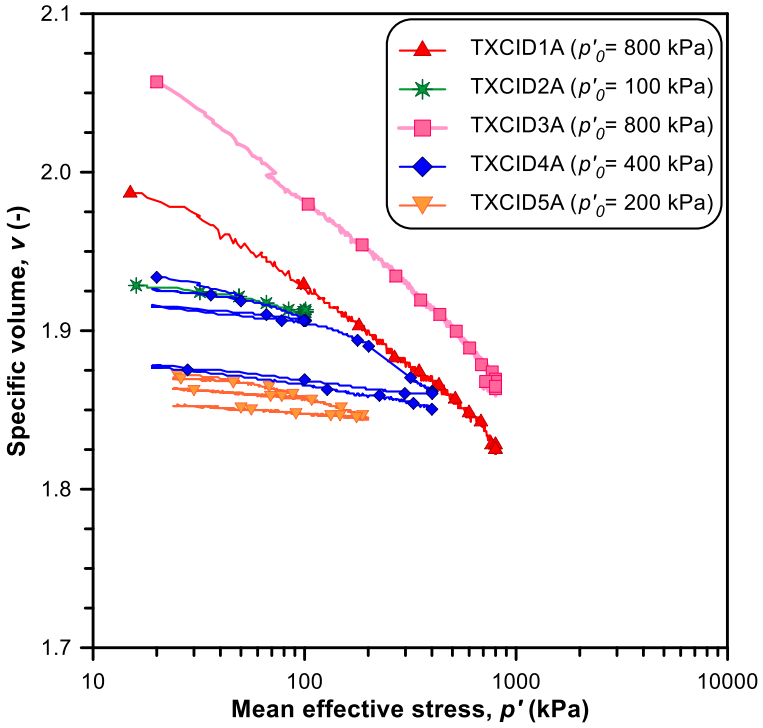

Figure 48 Experimental curves for Padano Aquifer samples in the v-logp' plane (isotropic compression stages).

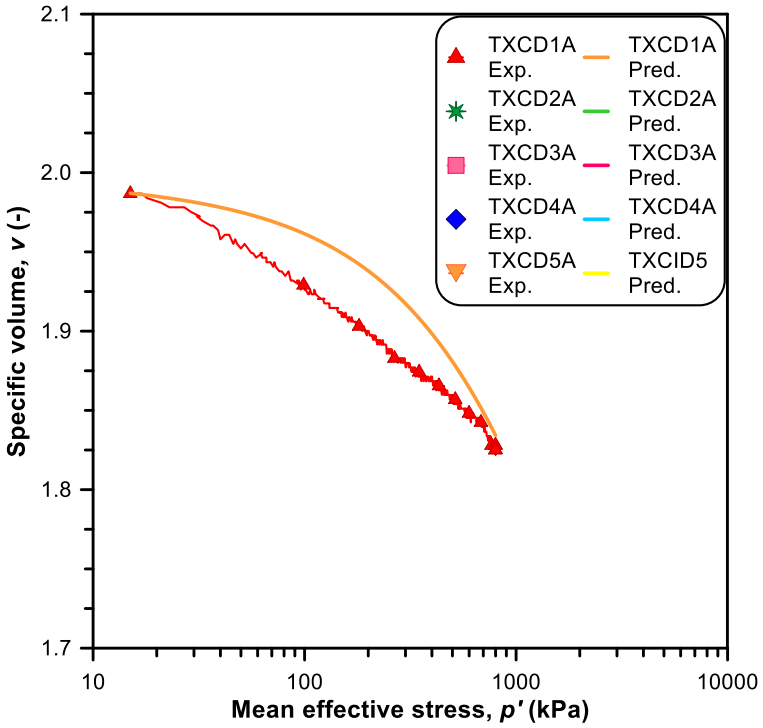

Figure 49 Experimental and predicted curves for triaxial drained tests TXCID1A in the v-logp' plane (isotropic compression stages).

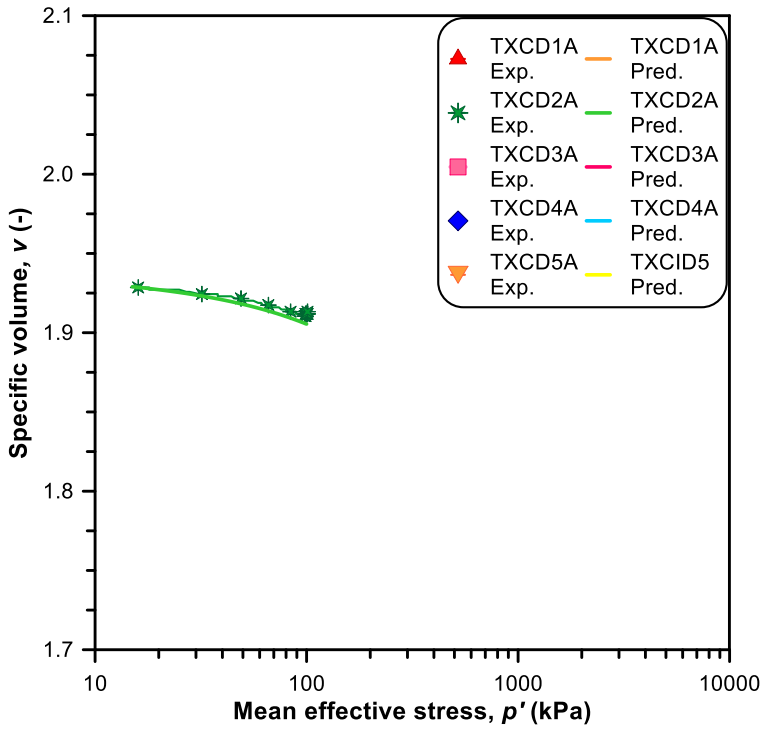

Figure 50 Experimental and predicted curves for triaxial drained tests TXCID2A in the v-logp' plane (isotropic compression stages).

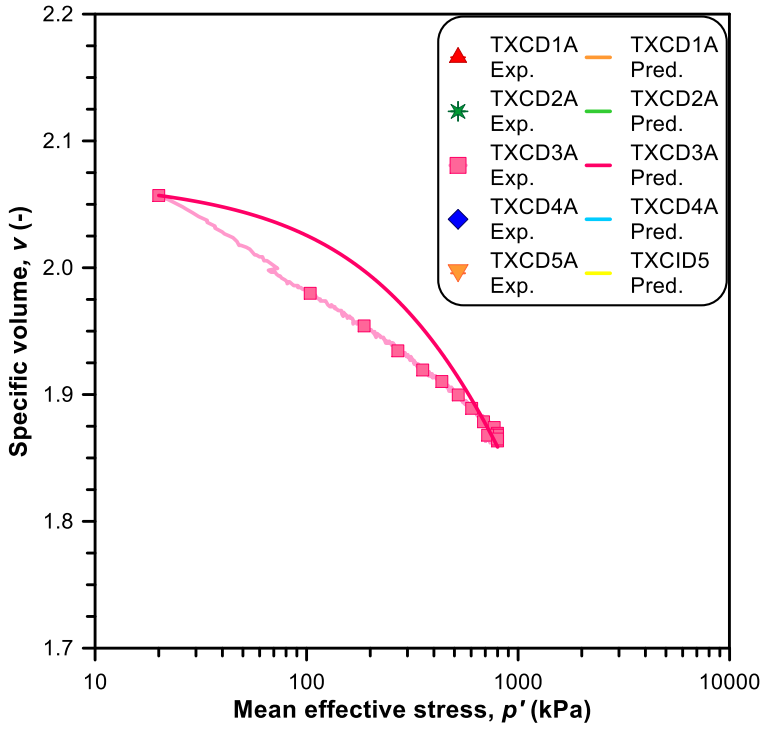

Figure 51 Experimental and predicted curves for triaxial drained tests TXCID3A in the v-logp' plane (isotropic compression stages).

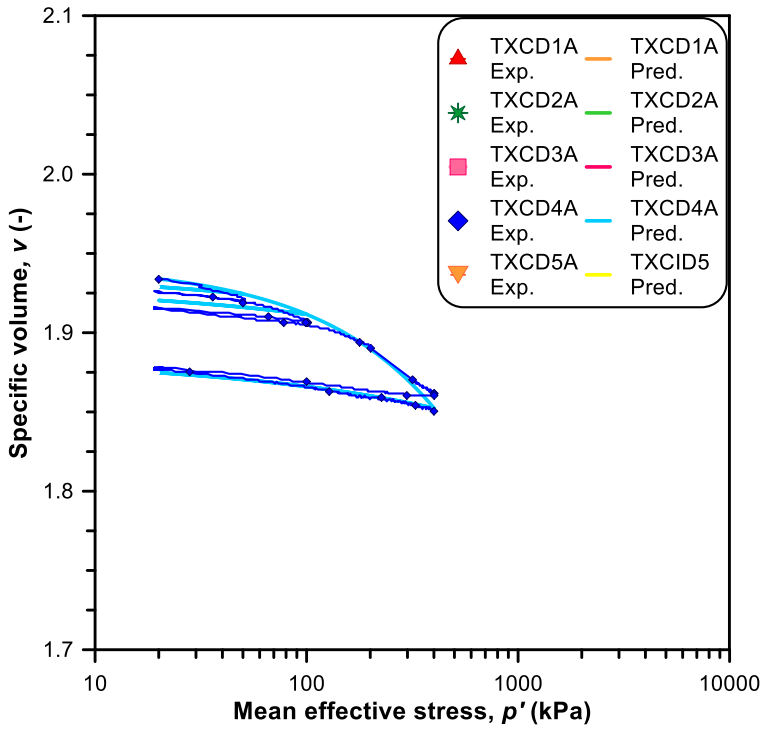

Figure 52 Experimental and predicted curves for triaxial drained tests TXCID4A in the v-logp' plane (isotropic compression stages).

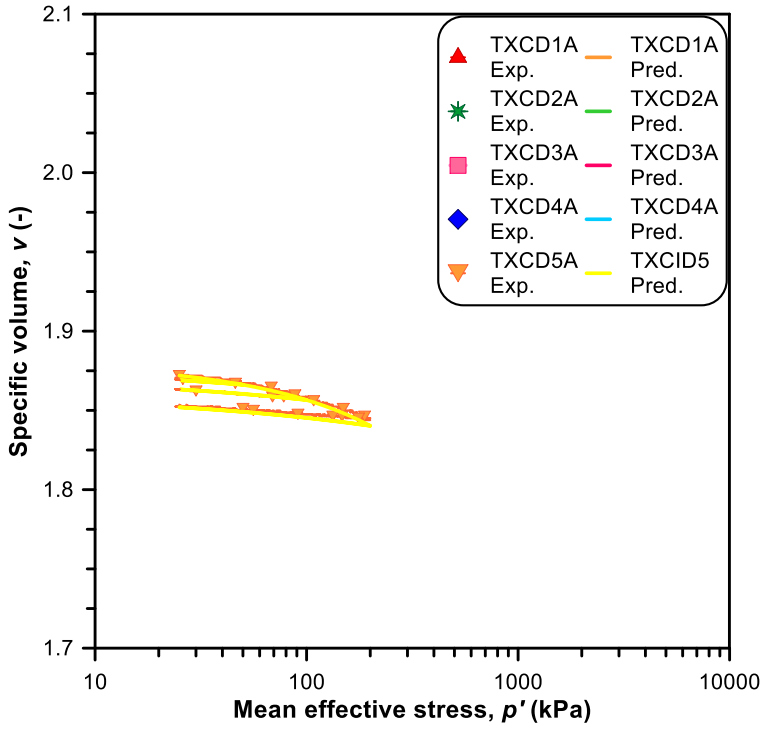

Figure 53 Experimental and predicted curves for triaxial drained tests TXCID5A in the v-logp' plane (isotropic compression stages).

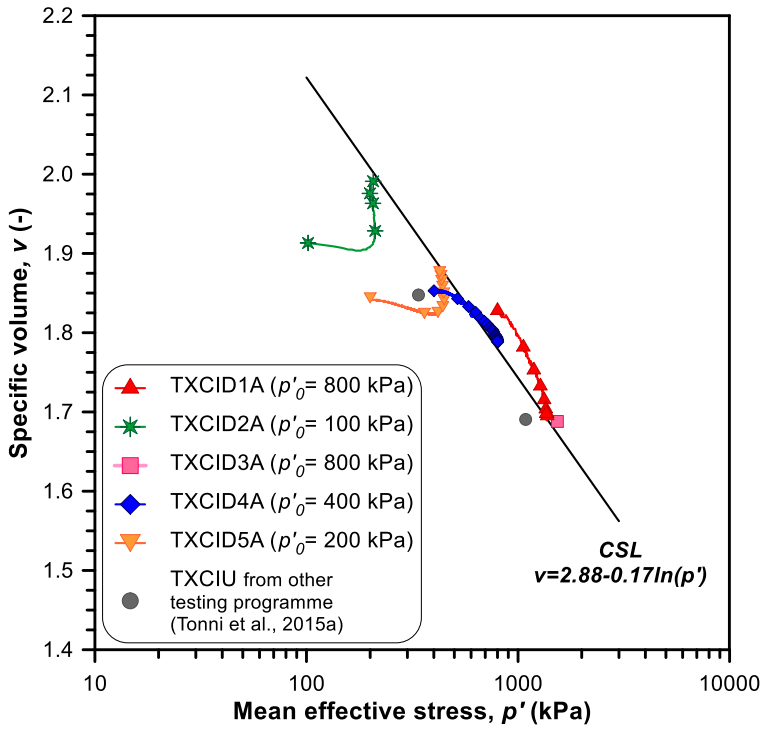

Figure 54 Experimental curves for Padano Aquifer samples in the v-logp' plane (shearing stages).

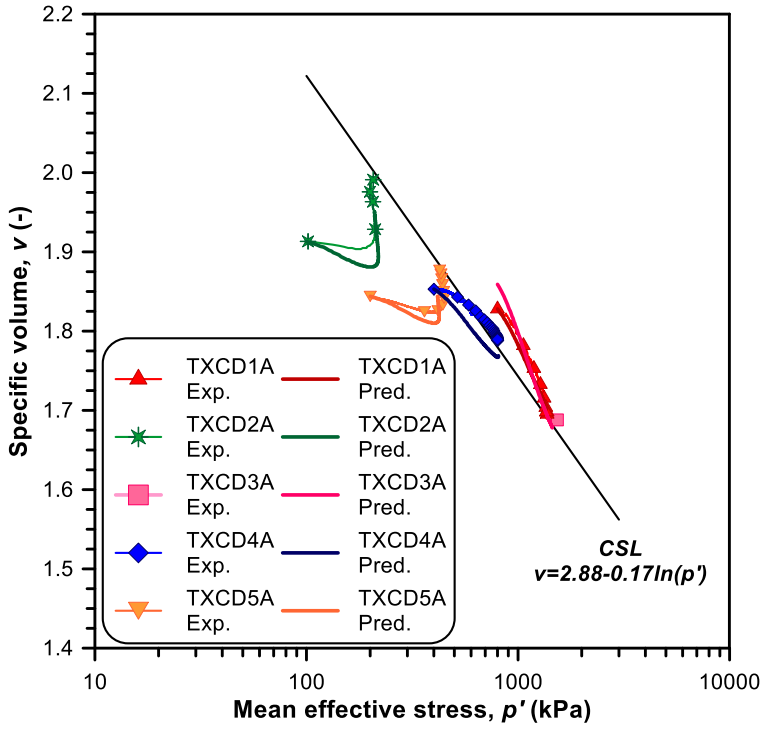

Figure 55 Experimental and predicted curves for triaxial drained tests in the v-logp' plane (shearing stages).

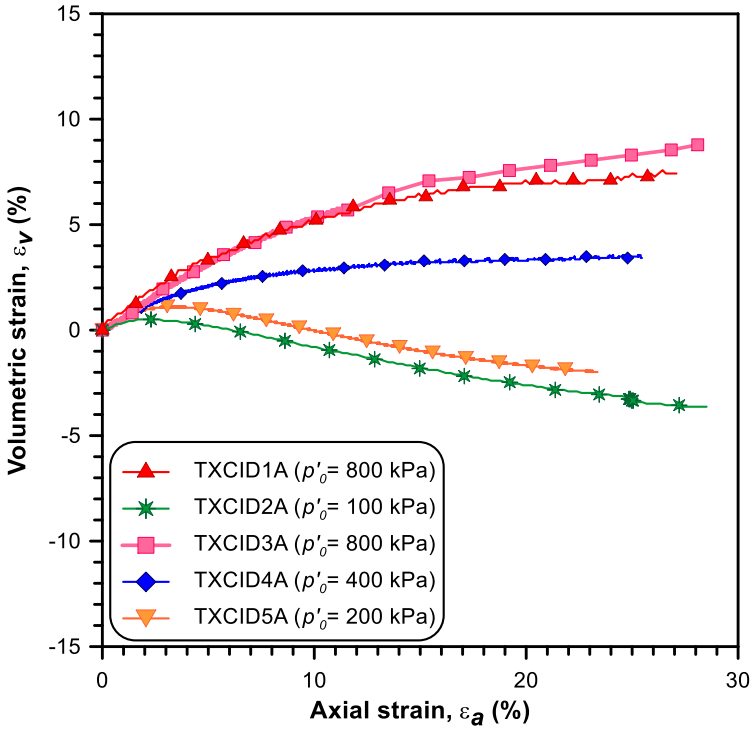

Figure 56 Experimental curves for Padano Aquifer samples in the strain plane.

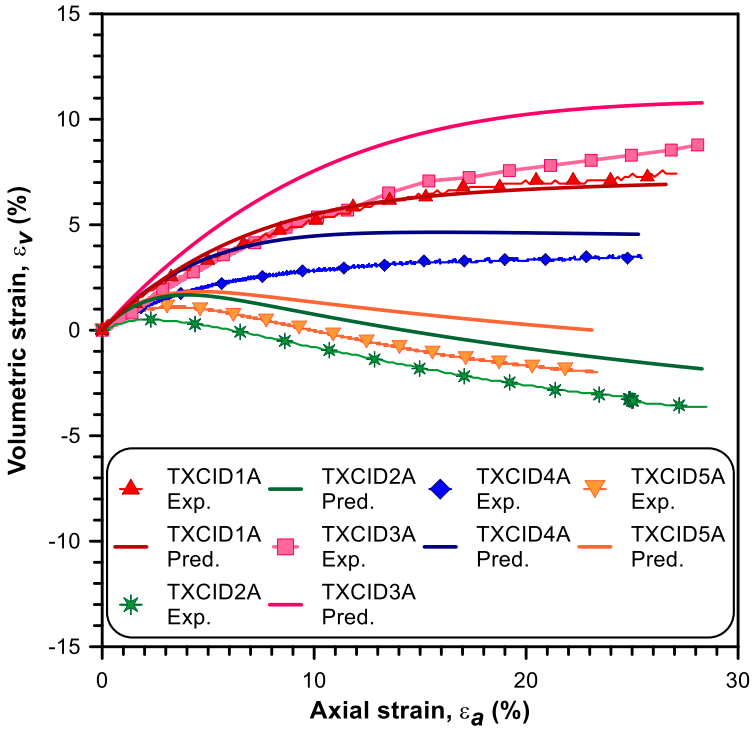

Figure 57 Experimental and predicted curves for triaxial drained tests in the strain plane.

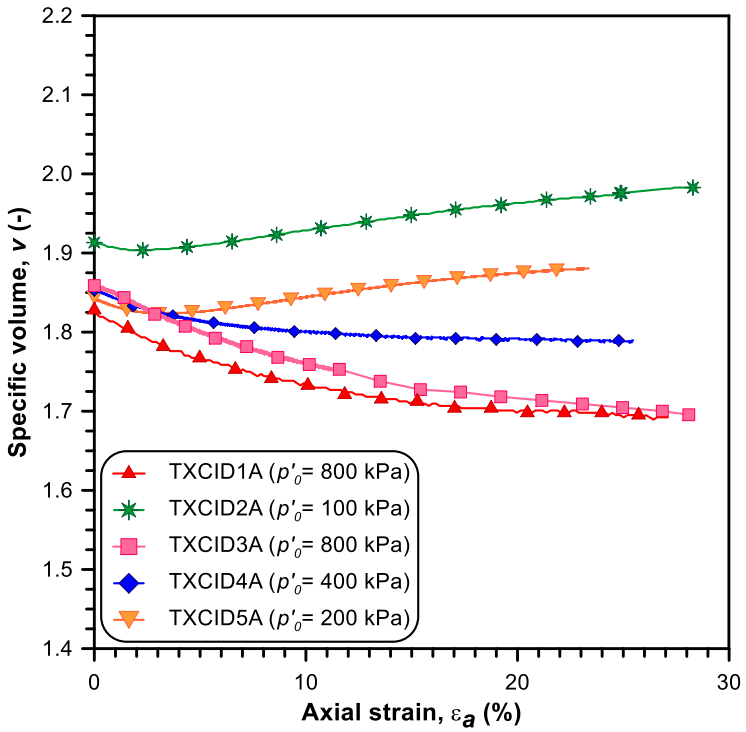

Figure 58 Experimental curves for Padano Aquifer samples in the v-εa plane.

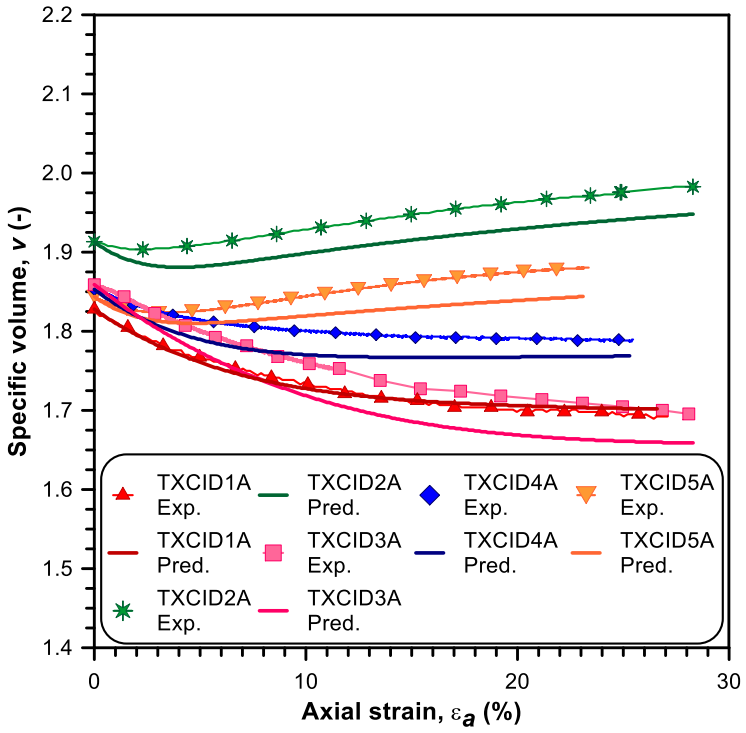

Figure 59 Experimental and predicted curves for triaxial drained tests in the v-εa plane.

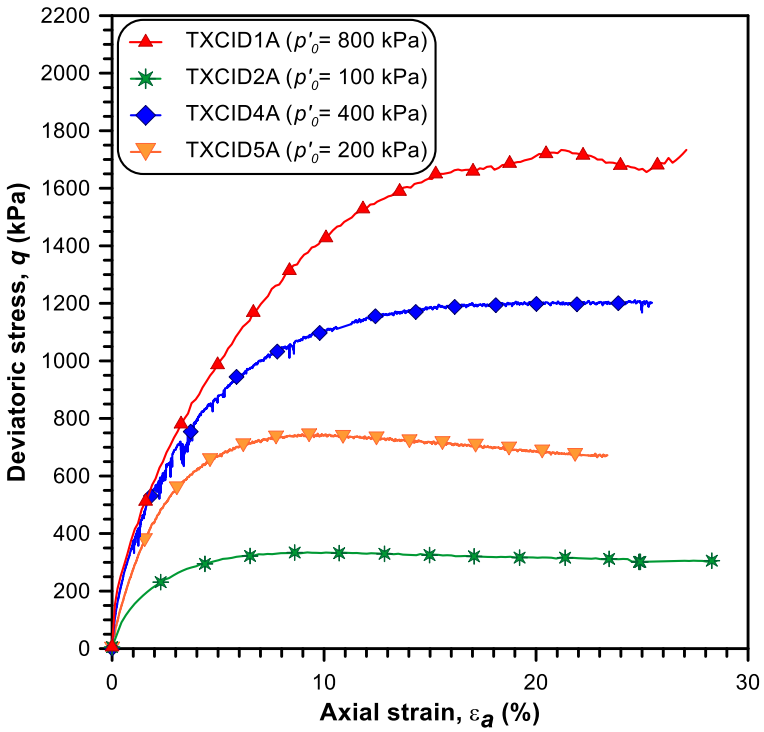

Figure 60 Experimental curves for Padano Aquifer samples in the stress-strain plane.

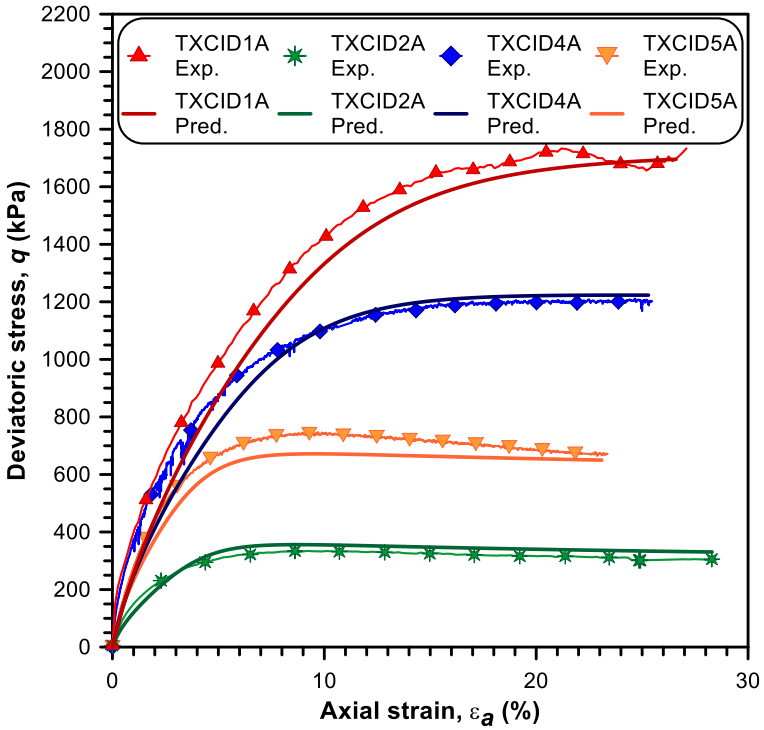

Figure 61 Experimental and predicted curves for triaxial drained tests in the stress-strain plane.

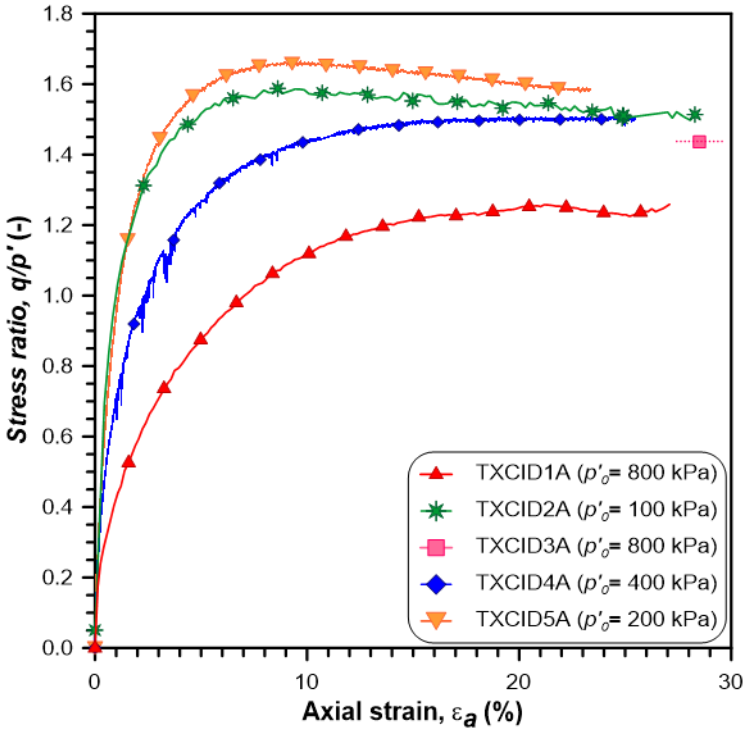

Figure 62 Experimental curves for Padano Aquifer samples in the stress ratio-ε_a plane.

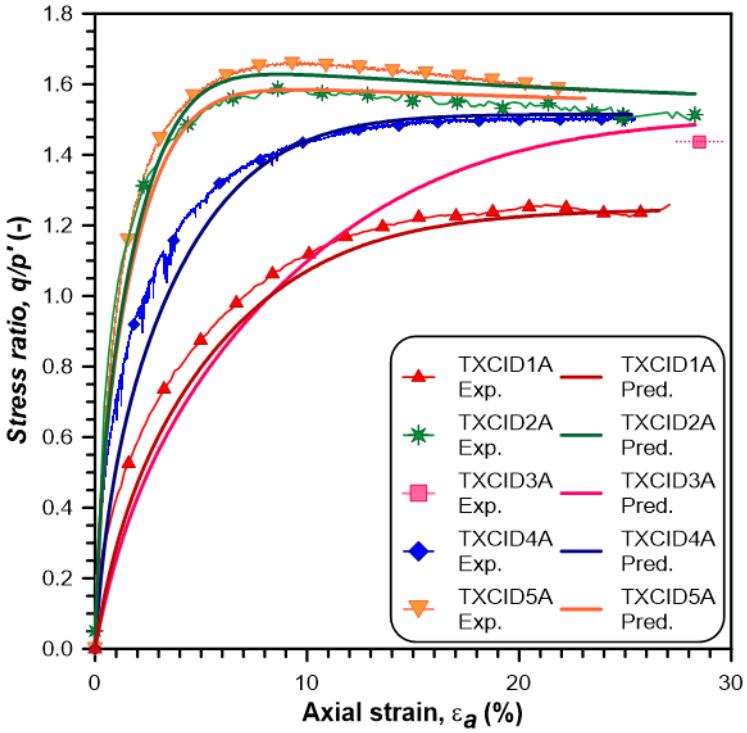

Figure 63 Experimental and predicted curves for triaxial drained tests in the stress ratio-ε_a plane.

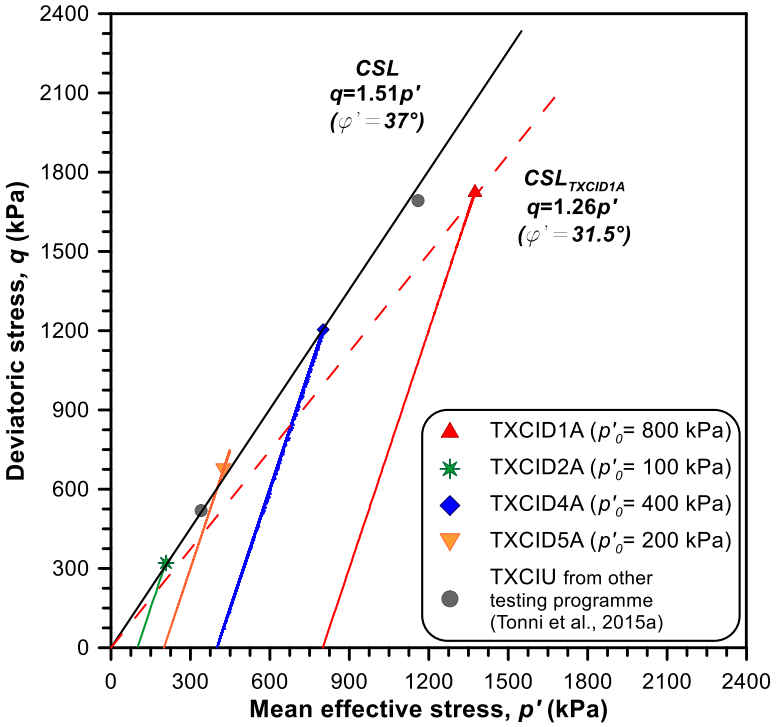

Figure 64 Failure envelopes for the Padano Aquifer sand in q-p' effective stress plane.

7.8. Experimental and predictive curves – Macro-unit R & B samples

As has been delineated previously, the artificial and natural river deposits are characterized by intrinsic heterogeneous soils, which present both a contractive and a dilative stress-strain response under shearing stages according to different state conditions (i.e. confining pressure, relative density) and properties (e.g. mineralogical composition, particle size distribution). Nonetheless, the experimental data show no appreciable differences between the samples extracted from Unit R and those of Unit B, as confirmation that such deposits may be treated as a unique soil macro-unit with respect to their mechanical behaviour. In detail, the results of the K_0-oedometer tests on the granular materials of the river embankment are plotted in Figure 66, where the compression curves are not parallel and converge at the pressure level of approximatively 1 MPa. Tests at higher stresses could be useful to unambiguously identify the uniqueness of the *NCL*. This behaviour reflects the compression response of carbonate sand-quartz silt mixtures reported in the

study of Shipton and Coop (2012), where convergent compression paths have been detected for different amounts of granular fractions. Nonetheless, the analyzed soil samples do not seem to be characterized by the "*transitional*" behaviour (e.g. Nocilla et al., 2006) generally shown by intermediate graded granular mixture, which would imply the non-uniqueness of *NCL* as well as *CSL*. In fact, Thevanayagam et al. (2002) observed an inversion of trend of the *CSL* when the *FC* was higher than 40% of the total weight. Furthermore, a well-graded material presents a lower compression index and less breakage in comparison to a poorly-graded one (Altuhafi and Coop, 2011), encountering a difficulty in defining the *NCL*. Nevertheless the absence of significant breakage, meaningful plastic volumetric compression can still develop in well-graded granular soils.

In detail, according to the stress-strain responses, most of the samples show a typical strain-hardening response and solely a few tests (i.e. *TXCID6* and *TXCID7*) exhibit a moderate peak stress ratio. Since the above mentioned intrinsic heterogeneity of the soil deposits, it is not possible to identify a unique value of the critical stress ratio M_g (Figure 87). Most of the samples reach the ultimate stress state at q/p' = 1.331, whereas a few other tests arrive up to a value of 1.484 (i.e. *TXCID3*, *TXCID5*, *TXCID6* and *TXCIU1*). The response of the sands/silty sands seem to be sensitive to small variations in terms of basic soil features, i.e. particle grading, in the p'-q effective stress plane, where the best fits between the experimental and the numerical data has been found by using different values of the gradient M_g; whereas, such sensitivity is not pronounced in the v-logp' plane, in which it is possible to identify a unique *CSL* for the investigated granular soils. The results (symbols in grey) of a number of tests carried out in a previous testing programme (Tonni et al., 2015a) plotted in the effective stress plane (Figure 87) confirm the presence of different failure envelopes. Furthermore, shear band

development and strain localization within dense samples at a medium stage of axial deformation (Figure 65) make it difficult to clearly define the *Critical State* conditions.

Figure 65 Shear band development within the sample at the end of the shearing phase of the test TXCID5.

As regards the volumetric behaviour, the experimental curves of silty sands generally present a contractive response, except for the undisturbed samples of *TXCID5* and *TXCID6*, both characterized by moderate dilation. Such predominantly contractive trend, resulting in positive excess pore pressures during undrained shearing condition, has been illustrated also in Tonni et al. (2015a) where silty sand samples, with an initial specific volume in the range 1.66-1.89 and confining pressures between 100 and 250 kPa, have been analyzed.

The experimental data (lines marked by symbols) and model prediction curves (solid lines) are compared in order to evaluate the model predictive capability on mixed soils (from Figure 69 up to Figure 86). Regarding the isotropic compression phase, a series of plots have been represented without the creep phenomenon (i.e. Figure 71, Figure 72 and Figure 76) because of the incapability of the adopted constitutive model to simulate it. The assumption of an elastic isotropic unloading-reloading has been used as for the *Padano Aquifer* sands.

The simulations of the undrained triaxial tests performed on both *Padano Aquifer* and Macro-unit R & B samples will be exposed in the next section.

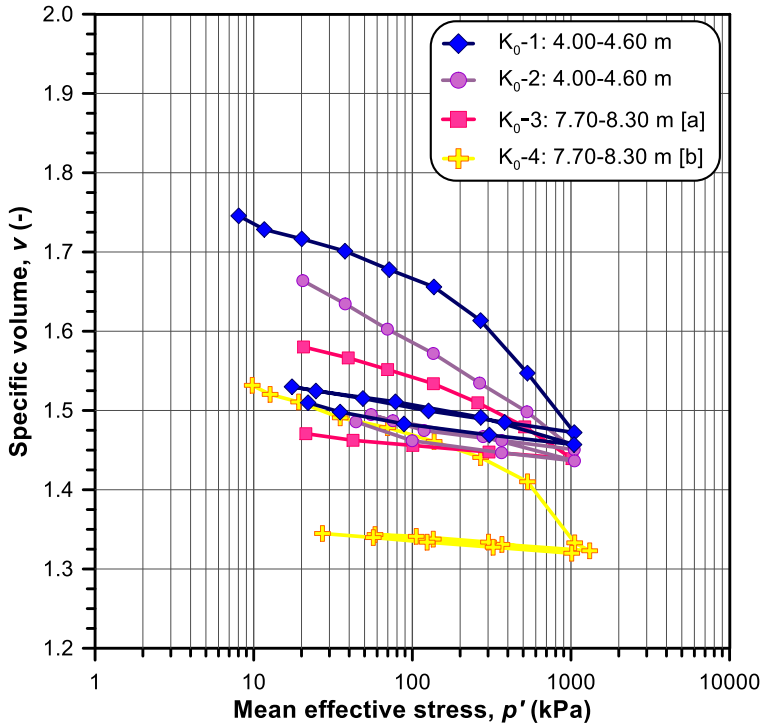

Figure 66 K_0-oedometer tests on river embankment granular soils.

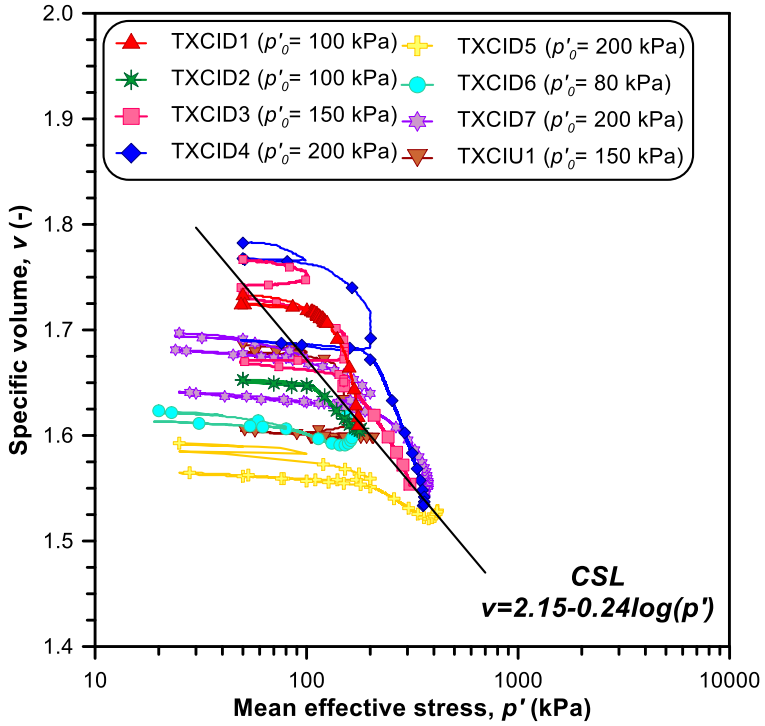

Figure 67 Experimental curves for river embankment samples in the v-logp' plane.

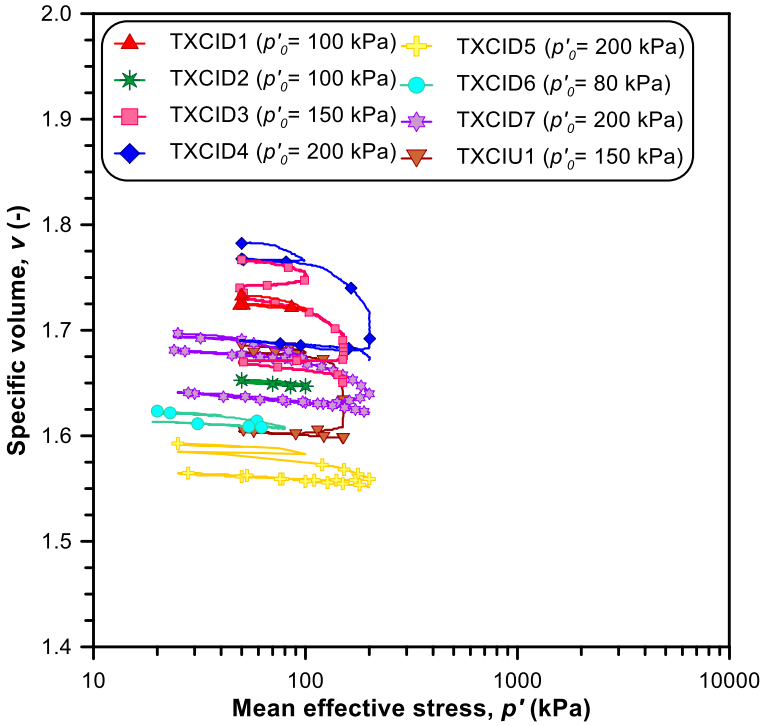

Figure 68 Experimental curves for river embankment samples in the v-logp' plane (isotropic compression stages).

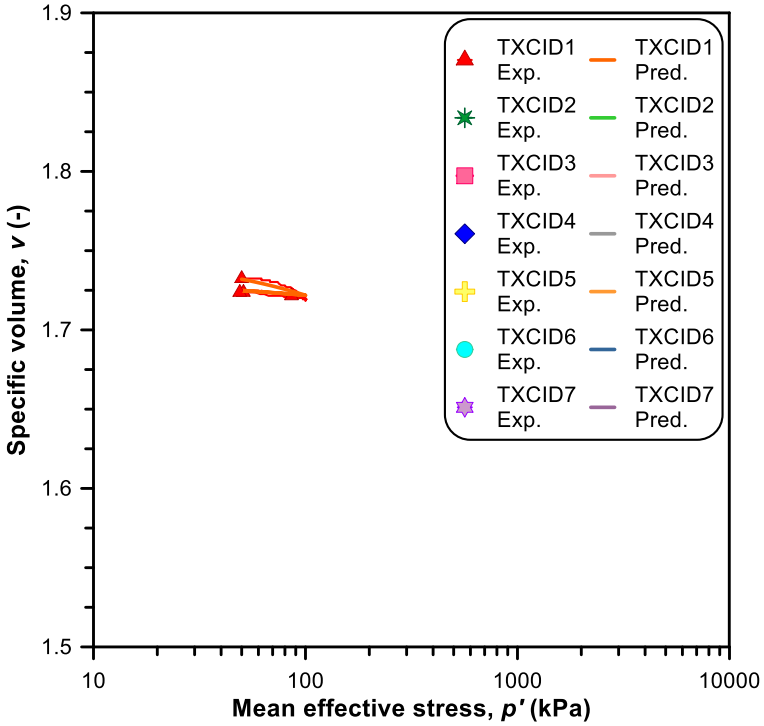

Figure 69 Experimental and predicted curves for the triaxial drained test TXCID1 in the v-logp' plane (isotropic compression stages).

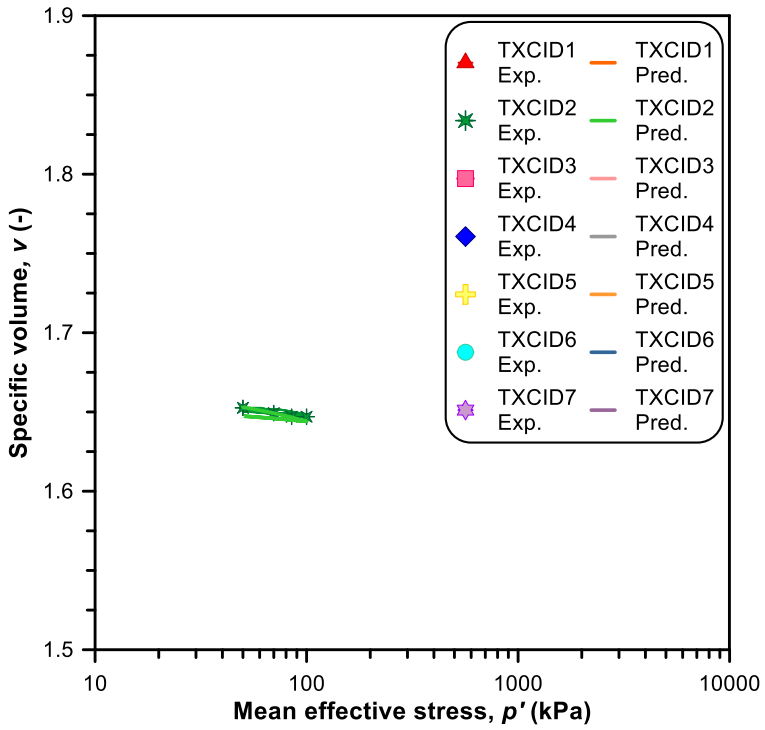

Figure 70 Experimental and predicted curves for the triaxial drained test TXCID2 in the v-logp' plane (isotropic compression stages).

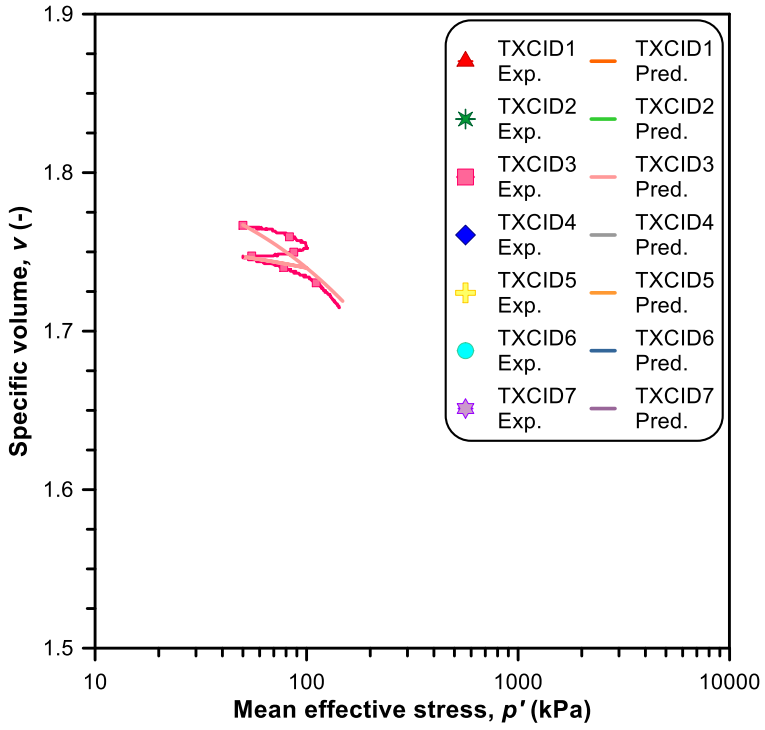

Figure 71 Experimental and predicted curves for the triaxial drained test TXCID3 in the v-logp' plane without the creep manifestation (isotropic compression stages).

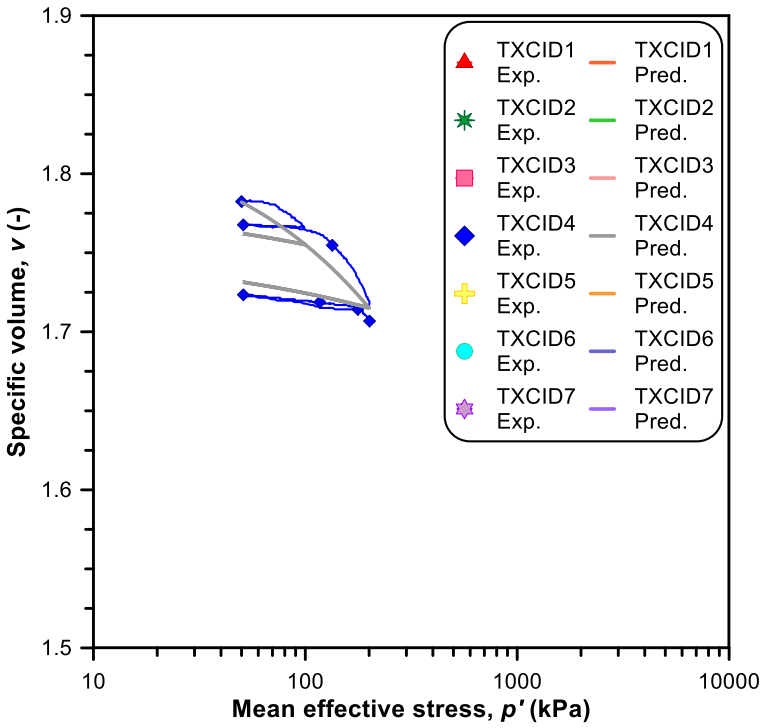

Figure 72 Experimental and predicted curves for the triaxial drained test TXCID4 in the v-logp' plane without the creep manifestation (isotropic compression stages).

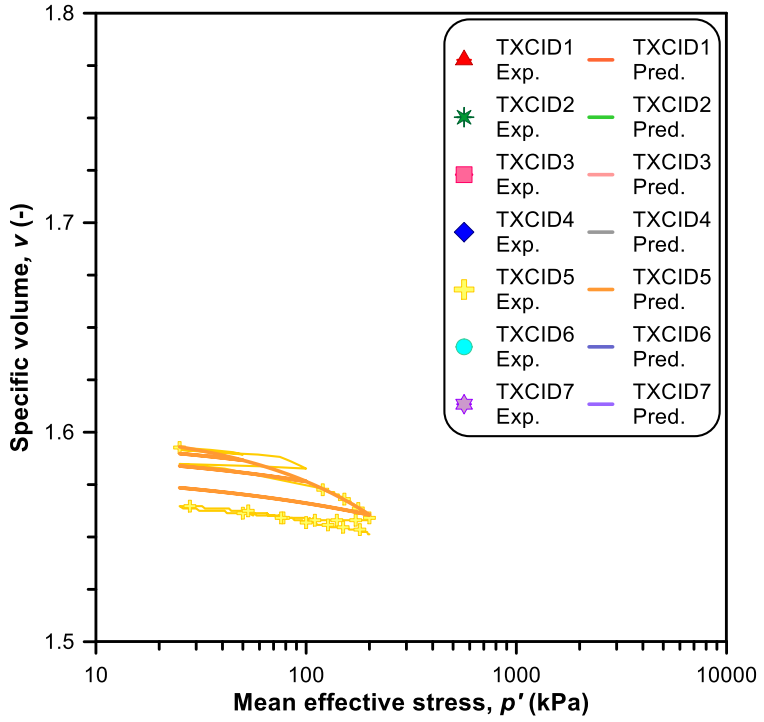

Figure 73 Experimental and predicted curves for the triaxial drained test TXCID5 in the v-logp' plane (isotropic compression stages).

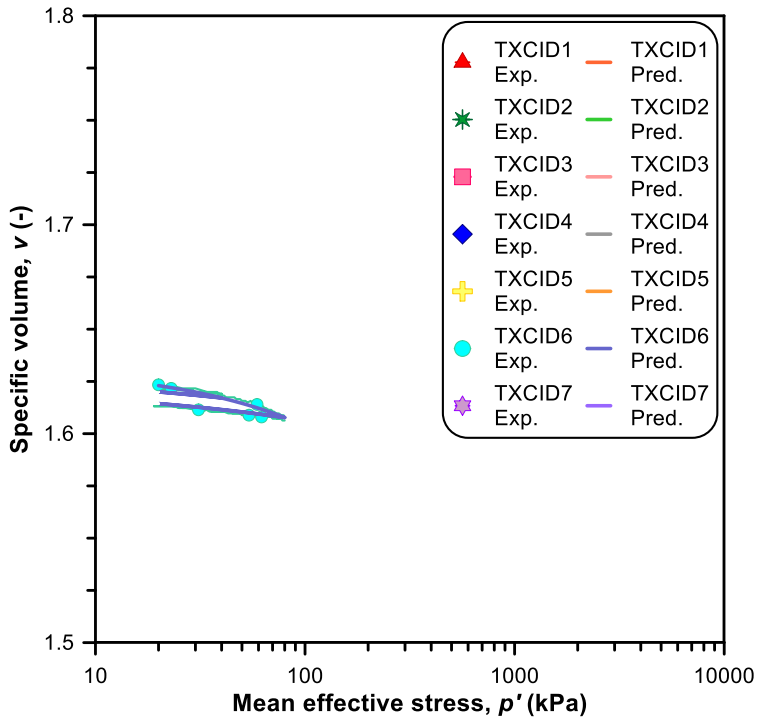

Figure 74 Experimental and predicted curves for the triaxial drained test TXCID6 in the v-logp' plane (isotropic compression stages).

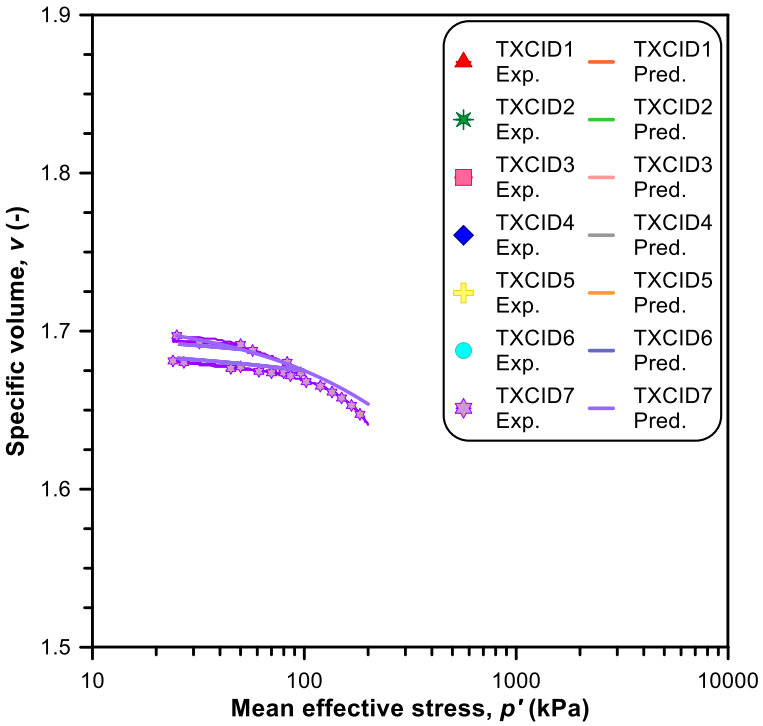

Figure 75 Experimental and predicted curves for the triaxial drained test TXCID7 in the v-logp' plane (isotropic compression stages).

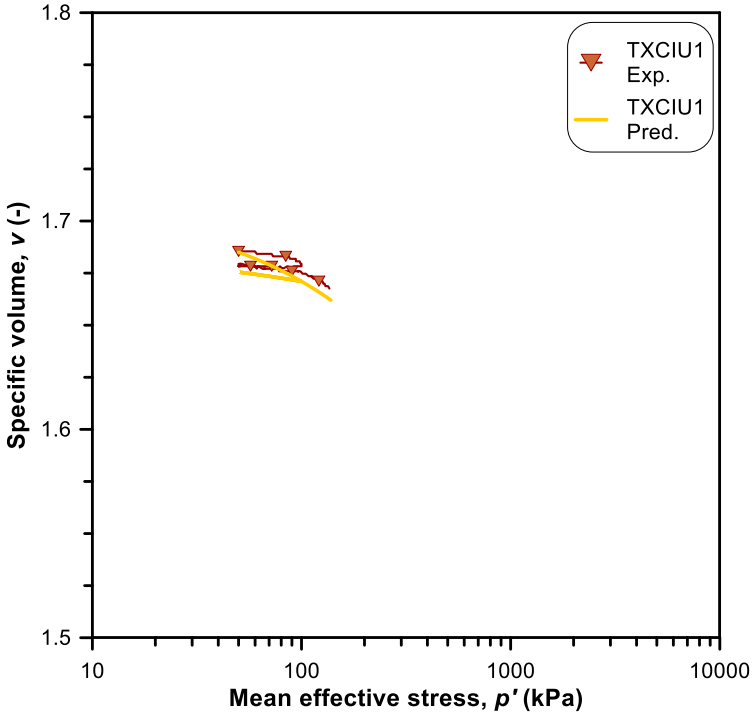

Figure 76 Experimental and predicted curves for the triaxial undrained test TXCIU1 in the v-logp' plane without the creep manifestation (isotropic compression stages).

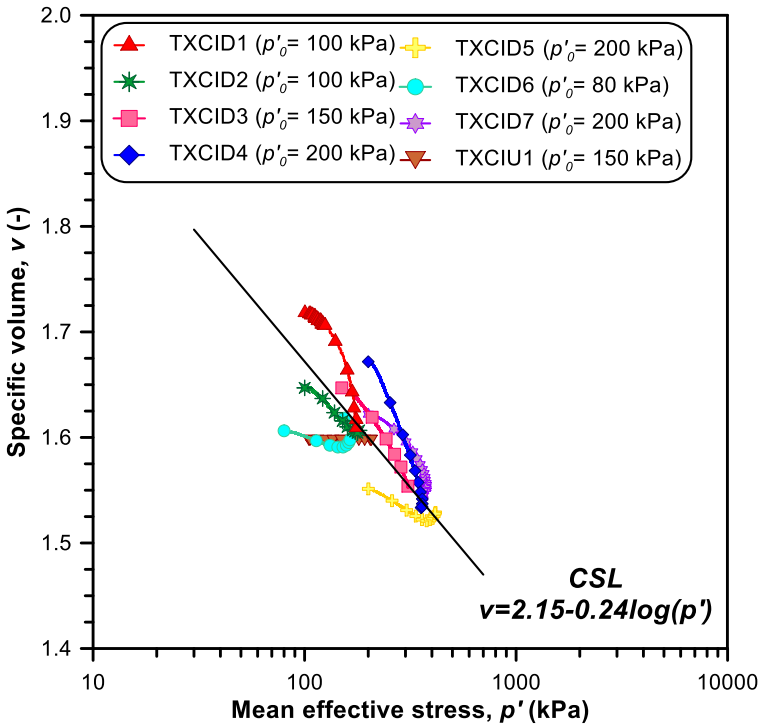

Figure 77 Experimental curves for river embankment samples in the v-logp' plane (shearing stages).

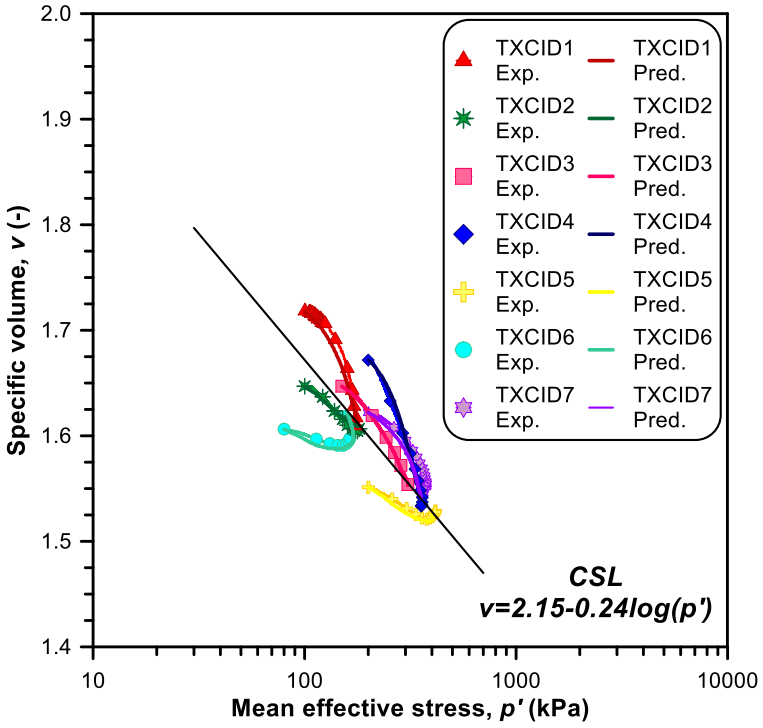

Figure 78 Experimental and predicted curves for triaxial drained tests in the v-logp' plane (shearing stages).

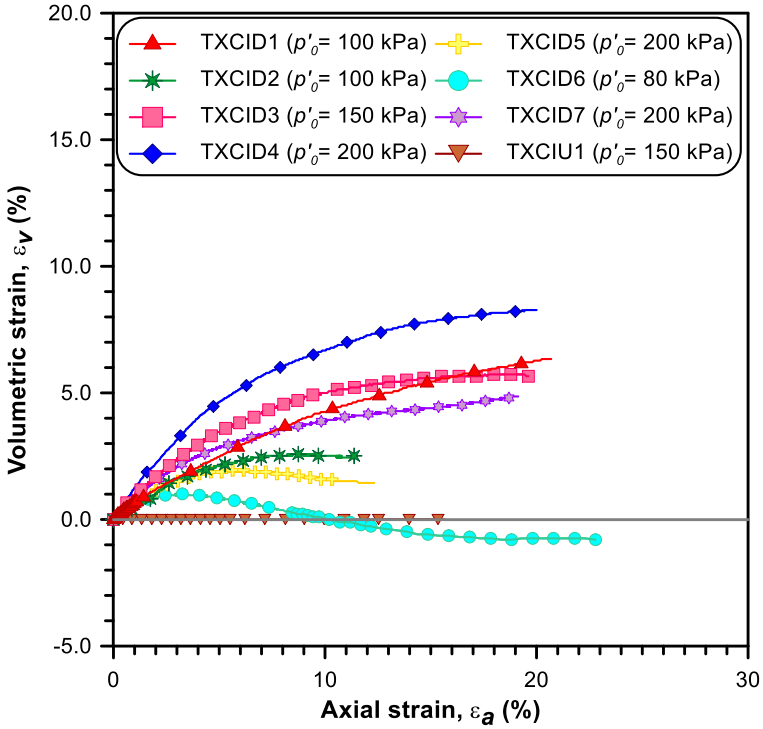

Figure 79 Experimental curves for river embankment samples in the strain plane.

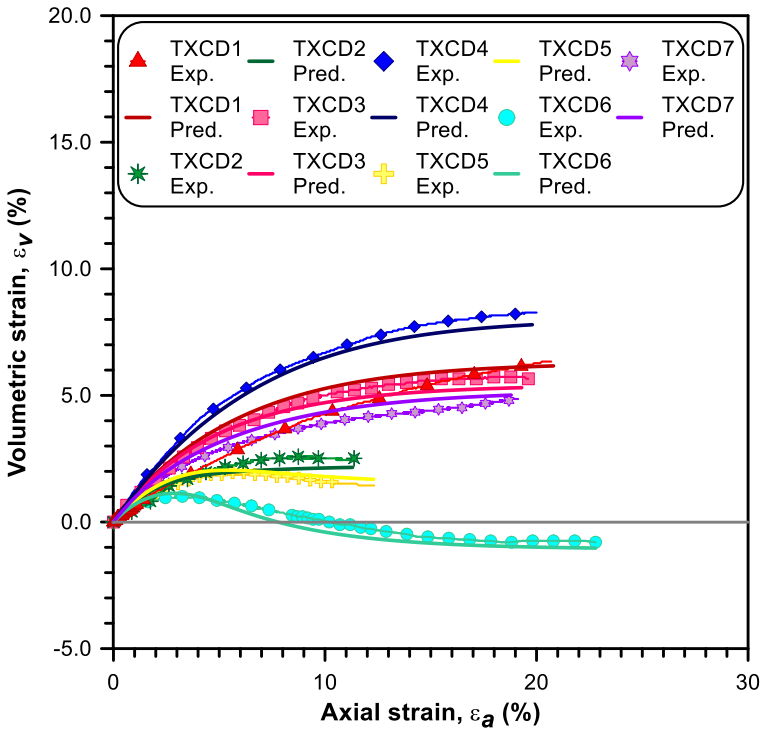

Figure 80 Experimental and predicted curves for triaxial drained/undrained tests in the strain plane.

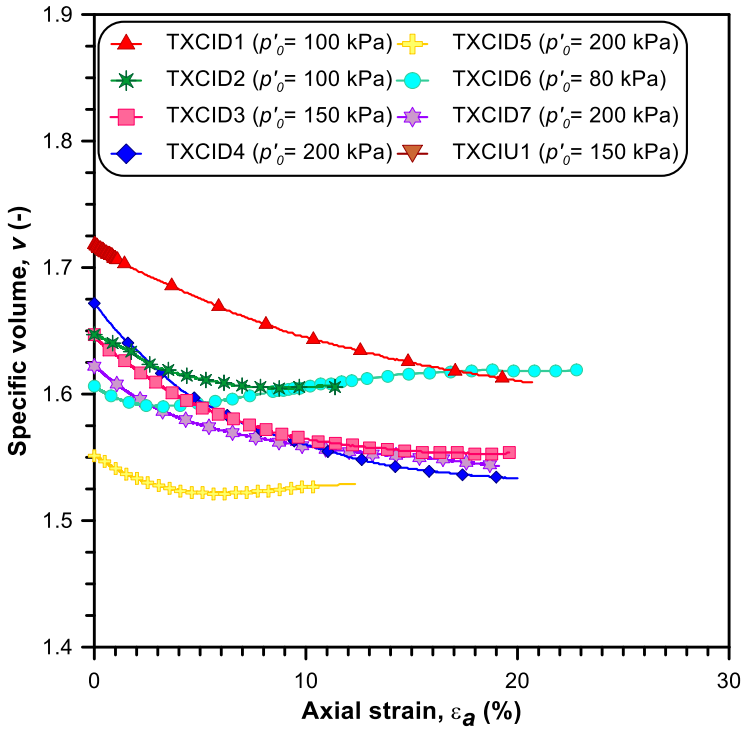

Figure 81 Experimental curves for river embankment samples in the v-ε_a plane.

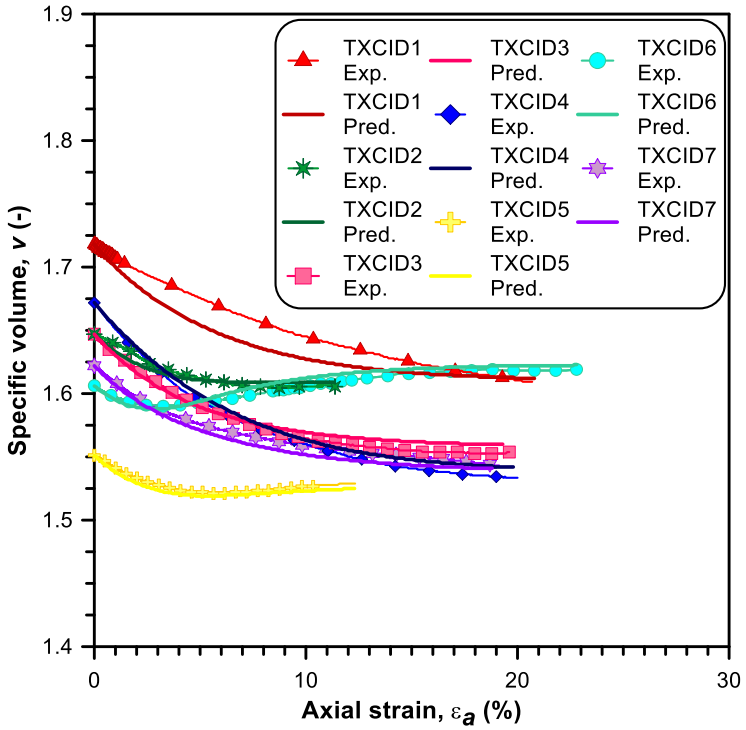

Figure 82 Experimental and predicted curves for triaxial drained/undrained tests in the v-ε_a plane.

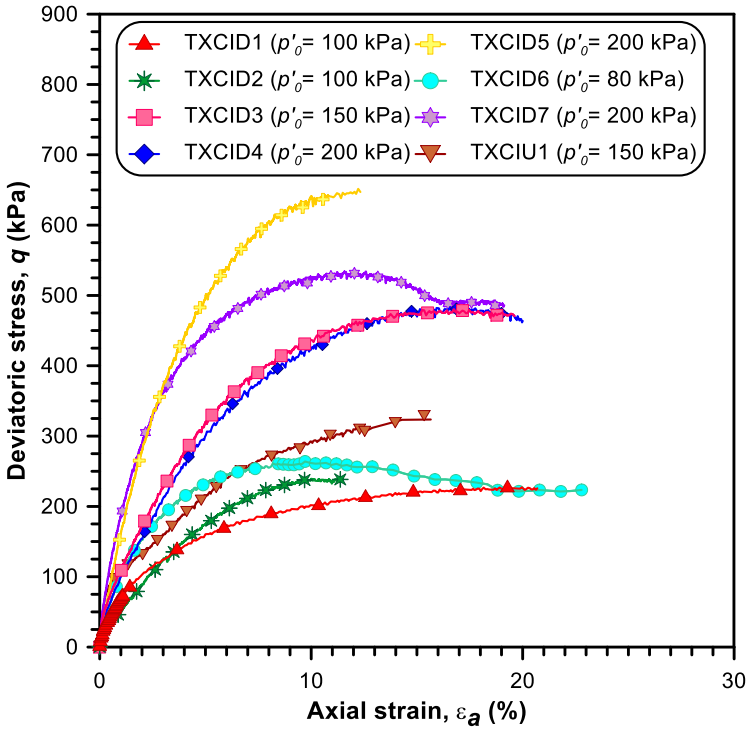

Figure 83 Experimental curves for river embankment samples in the stress-strain plane.

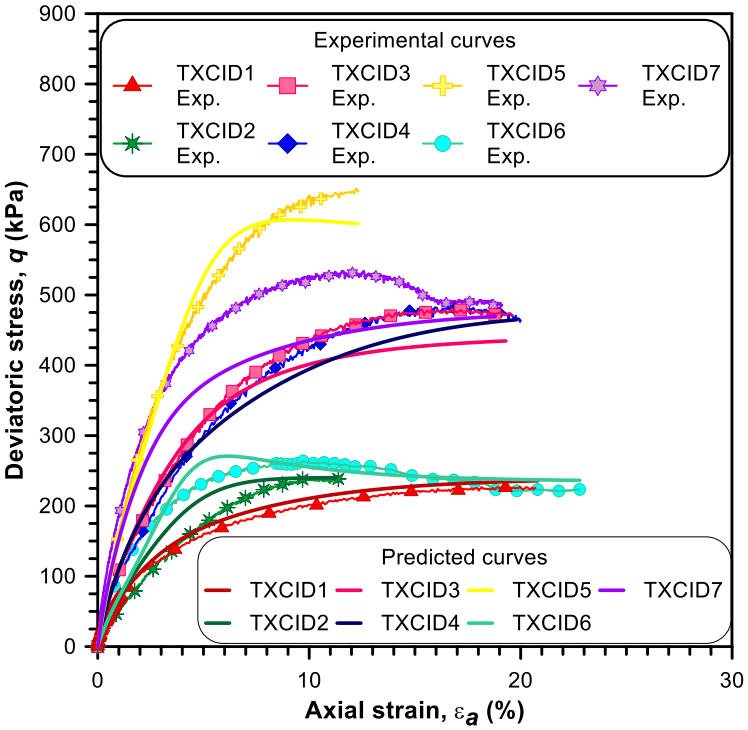

Figure 84 Experimental and predicted curves for triaxial drained tests in the stress-strain plane.

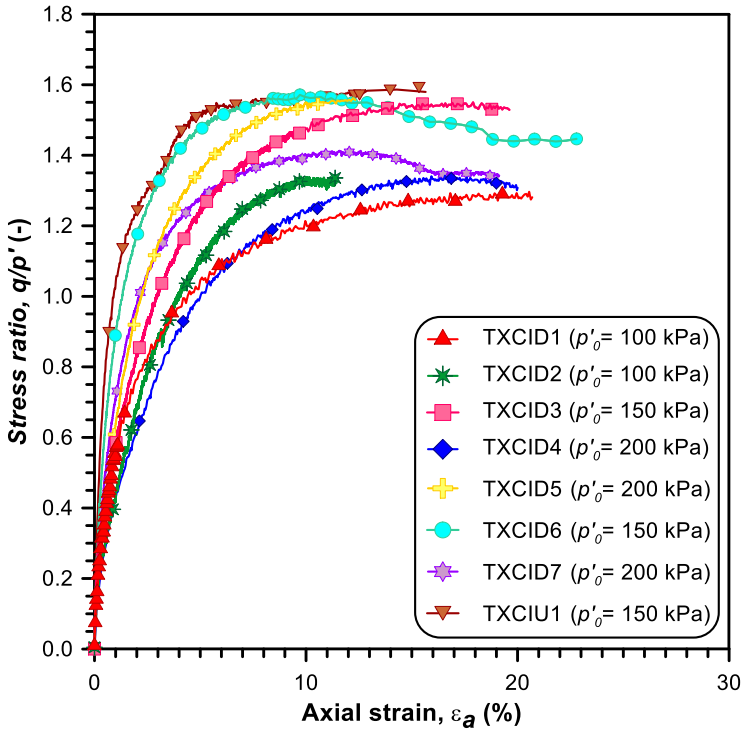

Figure 85 Experimental curves for river embankment samples in the stress ratio-ε_a plane.

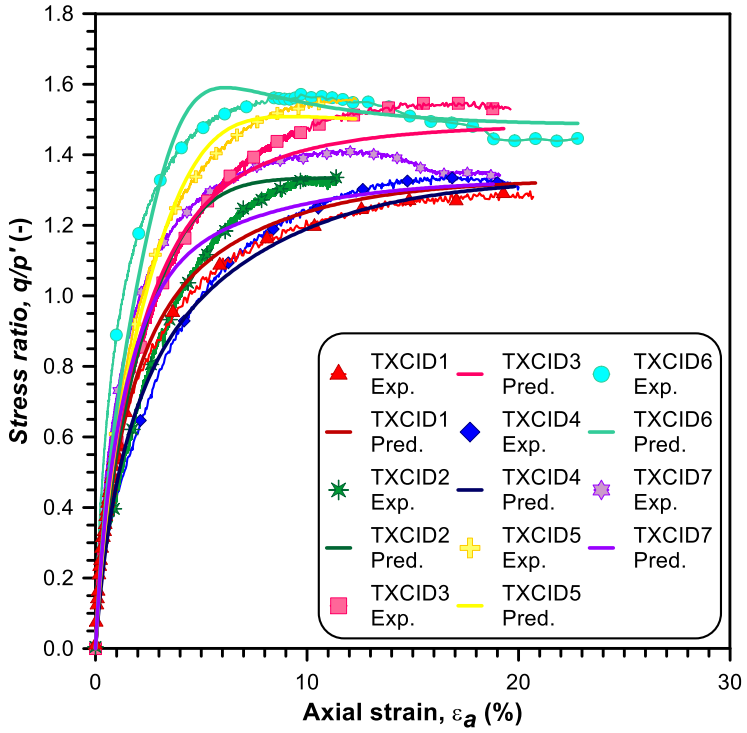

Figure 86 Experimental and predicted curves for triaxial drained tests in the stress ratio-ε_a plane.

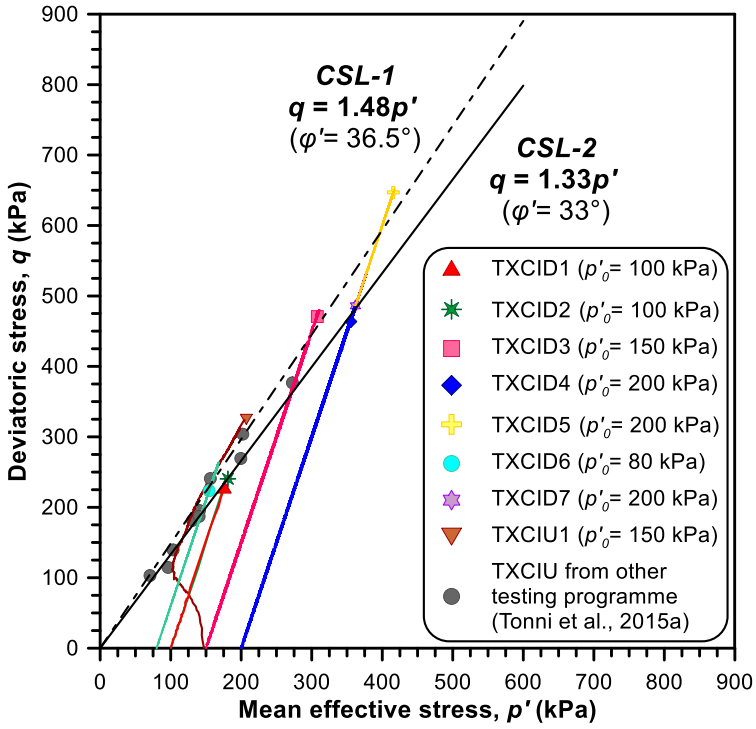

Figure 87 Failure data of the river embankment granular soils in the q-p' effective stress plane.

7.9. Experimental and predictive curves of triaxial undrained tests

In order to evaluate the predictive capability of the constitutive model and the effectiveness of the calibration procedure achieved by the drained triaxial test programme, the response of a number of undrained triaxial tests was simulated. In particular, the test *TXCIU1* was performed on an undisturbed sample of Unit B extracted at the depth of 7.70-8.30 m in correspondence of Section A; whilst, three additional undrained tests (*TXCIU1A*, *TXCIU2A* and *TXCIU3A*) on samples referable to the *Padano Aquifer* and *TXCIU2* on a riverbank specimen have been carried out in a previous testing programme (Tonni et al., 2015a). In particular, this latter undisturbed sample has been obtained from a 7.40-m coring with 13% fine fraction. The *Padano Aquifer* granular soils have been taken from two different boreholes, at rather different depths (11.20 m for tests *TXCIU1A* and *TXCIU3A*; 23.00 m for *TXCIU2A*), but with comparable fine content (*FC* ≈ 7-8%). The agreement between the predicted responses and the experimental data has been depicted in terms of deviatoric stress *q*-axial strain ε_a (Figure 89), effective stress path on the *q-p'* plane (Figure 90) and excess pore pressure ratio $\Delta u/p'_0$-ε_a (Figure 91). It is worth noting that the maximum pore water pressure (Δu_{max}) generated during the shearing phase is about 42 kPa for *TXCIU1A*, 174 kPa for *TXCIU2A*, 91 kPa for *TXCIU3A*, 90 kPa for *TXCIU1* and 101 kPa for *TXCIU2*, as shown in Figure 88. Such values characterize the point where there is a change from an increase to decrease in terms of Δu: after the peak, there is a gradual drop until specimen deforms at the end of the triaxial test without essentially variation of the pore water pressure.

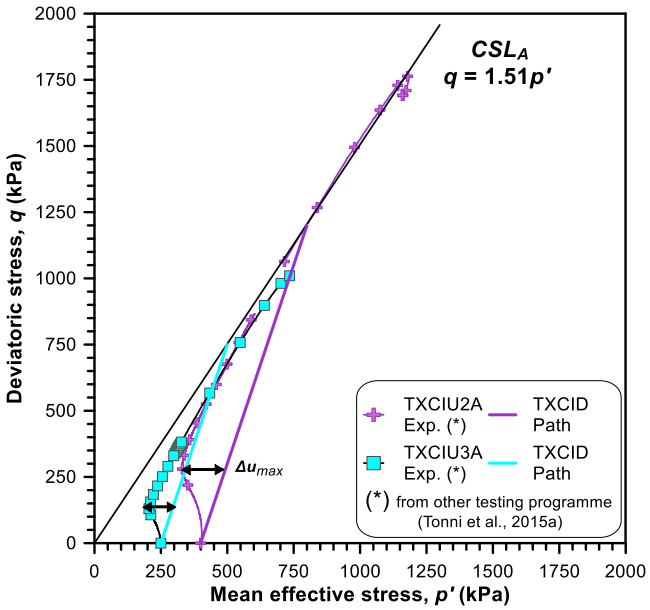

Figure 88 Conceptual model of the maximum pore water pressure (Δu_{max}) for some representative triaxial undrained tests in the q-p' effective stress plane.

According to Table 10, the simulation of test *TXCIU1* as well as *TXCIU2* has been performed adopting the same constitutive parameters (i.e. *Critical State* conditions, stress-dilatancy and plastic modulus law) calibrated on drained tests described in the previous section. M_f and initial elastic moduli ($K^e_{t,ini}$ and $G_{t,ini}$) have been calculated consistently with the equations (53),(67),(68). As regards the *Padano Aquifer* sands, a few, generally minor improvements have been carried out into the set of model parameters in order to simulate the undrained experimental data obtained from *TXCIU1A* (p'_0 = 100 kPa, v_0 = 1.860), *TXCIU2A* (p'_0 = 400 kPa, v_0 = 1.690) and *TXCIU3A* (p'_0 = 250 kPa, v_0 = 1.840), as reported in Table 13.

Test	$K^e_{t,ini}$ *(kPa)*	$G_{t,ini}$ *(kPa)*	M_f *(-)*	D_0 *(-)*	m_d *(-)*	n_f *(-)*
*TXCIU1A**	40000	30000	0.81	0.10	1.26	0.50
*TXCIU2A**	92000	69000	0.80	0.20	1.73	0.50
*TXCIU3A**	70000	55000	0.78	0.50	4.56	0.50
*TXCIU2***	24000	18000	0.66	1.30	3.94	4.20
**Parameters common to all tests on Padano Aquifer sand*						
M_g: 1.506	k_H: 0.14	β_H: 3.80	β_s: 1	n: 0.60	α_f: 0.45	
***Parameters common to all tests on Macro-unit R & B*						
M_g: 1.484	k_H: 0.26	β_H: 3.44	β_s: 1	n: 0.60	α_f: 0.45	

Table 13 Model parameters from calibration of Padano Aquifer sand and Macro-unit R & B granular soils (undrained shearing phase).

The undrained experimental behaviour seems to be rather well represented by the predicted curves with particular reference to the effective stress response.

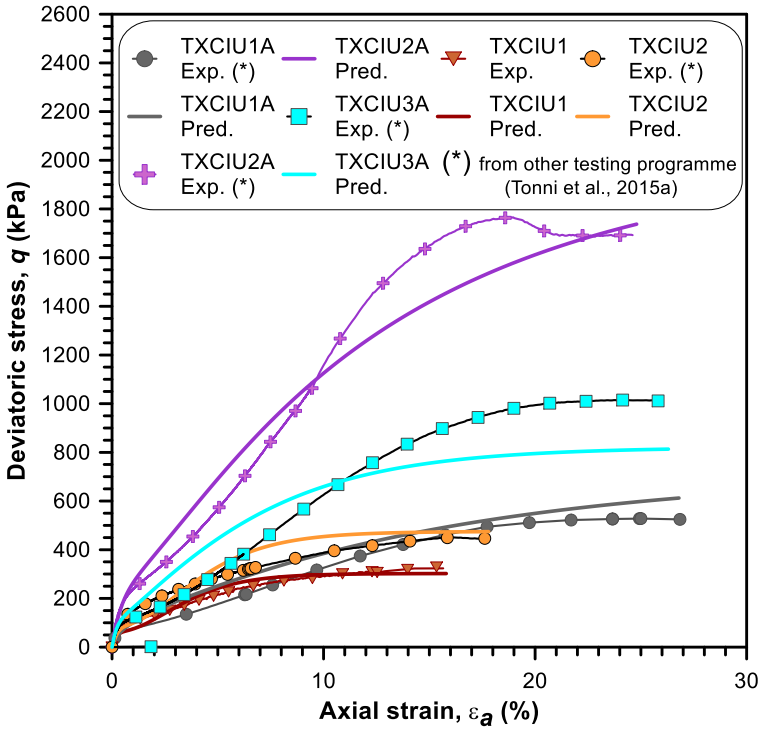

Figure 89 Experimental and predicted curves for triaxial undrained tests in the stress-strain plane.

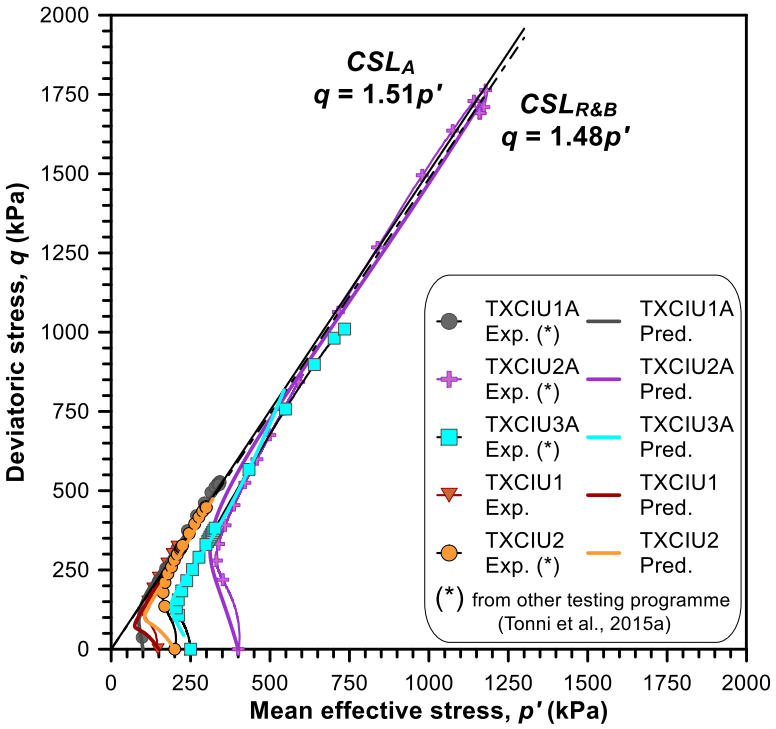

Figure 90 Experimental and predicted curves for triaxial undrained tests in the q-p' effective stress plane.

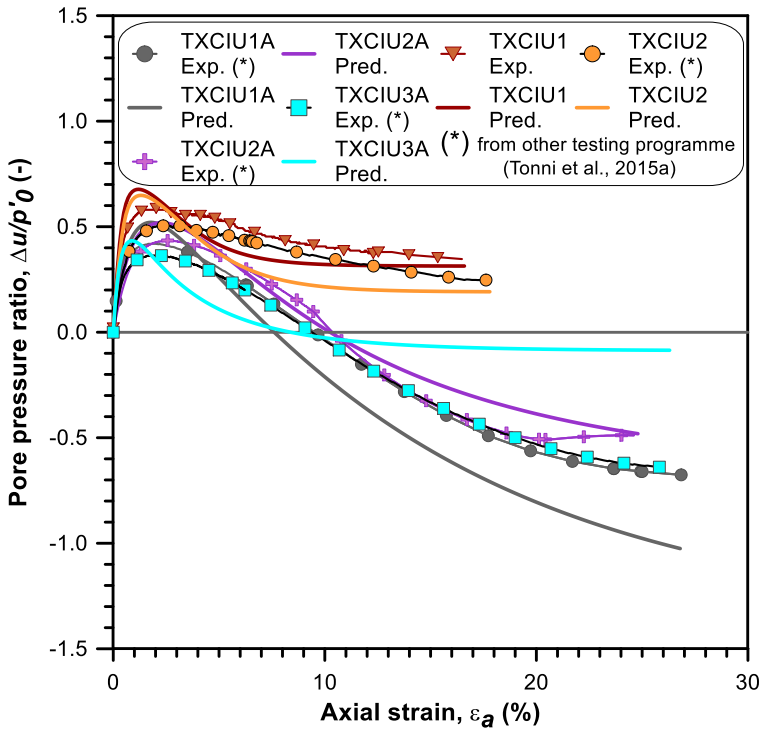

Figure 91 Experimental and predicted curves for triaxial undrained tests in the pore pressure ratio-ε_a plane.

7.10. Final evaluation of comparison experimental and computed soil response

The detailed parameter calibration procedure, based on drained triaxial tests, show a satisfactory applicability of the model for predicting the behaviour of almost clean as well as fine sands with a remarkable silt content under both drained and undrained conditions, within a unified framework. In fact, it is worth noting that the simulations allow capturing both the contractive and dilative curves of the granular soils in relation to the different initial conditions in terms of specific volume and confining stress. In particular, the computed curves match fairly well the experimental results for pre-peak deformations, whereas, sometimes, in the post-peak stages a lower rate of softening appears in the predicted trend: in fact, the steepness of the post-peak load-displacement data can be meaningfully overestimated in laboratory tests because of localization phenomena (i.e. shear

bands) frequently observed in very dense sandy samples which involve am inhomogeneous distribution of the stresses and strains in the specimens. Thus, both the laboratory tests and correspondening numerical analyses are in general pushed up to an axial strain of about 15-35% and the calibration is performed so as to achieve the best fit of test data before reaching the post-peak regime. It is clear that, at larger strain, the comparison is no longer meaningful, as correctly observed in Tonni et al. (2006).

Finally, it is worth noting that the *GP*-based constitutive model has been able to accurately predict the experimental responses of granular samples, considering that the approach in use cannot describe some phenomena, i.e. creep manifestation and localization of the shear bands, and that a unique set of constitutive parameters over a wide range of pressures and densities has been used. Bearing in mind the above outcomes, the study of undrained cyclic response as well as of the seismic behaviour of the whole levee could be opportunely undertaken.

8. Discretization of the field equations using a *FE* approach

This chapter deals with the standard discretization of the field equations. After the introduction of these equations including a series of differential laws i.e. effective stress, momentum balance and mass balance, the discretization in space, performed using the Finite Element method termed *Galerkin Residual Method*, and in time, based on a generalization of *Newmark* or Finite Difference approach know as *Generalized Newmark Method (GNM)* by Katona and Zienkiewicz (1985), have been explained. The resulting non-linear system of equations is solved using the *Newton-Raphson* iterative procedure. The general dynamic non-linear hydromechanics framework is developed to reproduce geotechnical problems under seismic conditions. Assuming a number of simplifications, this general framework can be transformed into a series of simplified formulations. If inertial effects are neglected the consolidation or quasi-static formulation is obtained. Additionally, if velocity terms (pore pressure and displacement derivatives in time) are deserted, the saturated static stationary formulation is found. In particular, the first is described because it has been applied to validate the *MATLAB* code predictions; the stationary case resolution has been adopted to perform the preliminary static analyses on the modelled river embankment. The meaningful reference literature consists of the contributions of Mira (2001) and Zienkiewicz et al. (1999).

8.1. Field equations

Despite the growing complexity of the investigated problems, the governing equations presented in this section, in conjunction with appropriately defined constitutive laws, are adequate for the study of many geomechanical applications. The basic relationships are reported using a matrix form which is convenient for the

finite element discretization. The effective stress formulation, the stress-strain response, the equilibrium and the mass balance equations have been presented in the following sections. This study is based on the assumption that the fluid acceleration relative to the soil skeleton is negligible.

8.1.1. Effective stress

As it is well known, the soil is composed by a solid skeleton and an interstitial space where fluids of different natures are located (i.e. water and air). The stress-strain response of the whole soil element depends on the interaction between the solid matrix and the interstitial fluids. One of the most important aspects of the present framework is the concept of effective stress: the soil is assumed to be a deformable triphasic system (eq.(107)).

$$\boldsymbol{\sigma}' = \boldsymbol{\sigma} + \alpha^* p_f \boldsymbol{I} \tag{107}$$

Where the variable related to the fluid part p_f is given by:

$$p_f = S_w p_w + S_g p_g \tag{108}$$

S_w, S_g are the saturation degrees for water and air, respectively; whereas p_w, p_g refer to water and air pressure.

The variable α^* is a function of bulk modulus of the grains (K_s) and of the average bulk modulus of the soil skeleton (K_{ts}), which takes in account the volumetric deformation of the grains due to the interstitial pressure.

$$\alpha^* = 1 - \frac{K_{ts}}{K_s} \tag{109}$$

In particular, α^* is a constant usually taken for the soils equal to 1. The sum of the saturation degrees of water (S_w) and air (S_g) is 1.

$$S_w + S_g = 1 \qquad (110)$$

For this study, the hypothesis of perfect saturated soil is assumed ($S_w = 1$) within the computational domain.

8.1.2. Stress-strain behaviour

As regards the solid skeleton, the stress-strain behaviour can be defined adopting a tensorial notation: the constitutive law generally is written as increments by the equation (111).

$$d\boldsymbol{\sigma}' = \boldsymbol{D}_t d\boldsymbol{\varepsilon} \qquad (111)$$

Whereas the fluid phase relationship is expressed as:

$$\varepsilon_v^{\pi} = -\frac{p_{\pi}}{3K_{\pi}} \qquad (112)$$

With K_{π} compressibility modulus for the phase π.

8.1.3. Equilibrium and mass balance relationships

The equations to describe the dynamic non-linear hydromechanical behaviour of a deformable triphasic system (i.e. solid, liquid and air) are identified in the equilibrium and mass balance relationships.

The equation of equilibrium or the momentum balance can be written as

$$\boldsymbol{S}^T\boldsymbol{\sigma} + \rho\boldsymbol{b} - \rho\ddot{\boldsymbol{u}} = 0 \qquad (113)$$

The relation between total and effective stress is described by

$$\boldsymbol{\sigma} = \boldsymbol{\sigma}' - \boldsymbol{m}S_w p_w \qquad (114)$$

Where $\boldsymbol{m}$ is the scale vector.

$$\boldsymbol{m} = (1\ 1\ 1\ 0)^T \tag{115}$$

In the context of the *2D FE* computation, the use of a vectoral notation for stresses, reducing the independent components to four rather than six.

$$\boldsymbol{\sigma'} \equiv (\sigma'_x, \sigma'_y, \sigma'_z, \tau'_{xy})^T \tag{116}$$

In equation (117), the vector of displacement is defined in a plane strain framework.

$$\boldsymbol{u} \equiv (u_x, u_y)^T \tag{117}$$

The displacement and the deformation are related through the strain differential operator (***S***) by the equation (118).

$$d\boldsymbol{\varepsilon} = \boldsymbol{S} d\boldsymbol{u} \tag{118}$$

For *2D* analyses, the strain differential operator is:

$$\boldsymbol{S} \equiv \begin{bmatrix} \frac{\delta}{\delta x} & 0 \\ 0 & \frac{\delta}{\delta y} \\ 0 & 0 \\ \frac{\delta}{\delta y} & \frac{\delta}{\delta x} \end{bmatrix} \tag{119}$$

The overall equilibrium equation becomes

$$\boldsymbol{S}^T(\boldsymbol{\sigma'} - \boldsymbol{m}p_w) + \rho\boldsymbol{b} - \rho\ddot{\boldsymbol{u}} = 0 \tag{120}$$

With ***b*** body force per unit mass and ρ density of the total composite, which is made explicit by the equation (121).

$$\rho = n_p\rho_w + (1 - n_p)\rho_s \tag{121}$$

ρ_w is the density of the water, ρ_s is density of the solid particles and n_p corresponds to the porosity.

The mass balance or flow conservation equation is defined as

$$\boldsymbol{m}^T \boldsymbol{S}\dot{\boldsymbol{u}} - \boldsymbol{\nabla}^T \boldsymbol{k}\boldsymbol{\nabla} p_w + \frac{\dot{p}_w}{Q^*} + \boldsymbol{\nabla}^T \boldsymbol{k}\rho_w \boldsymbol{b} = 0 \qquad (122)$$

Where $\boldsymbol{\nabla}$ is the differential operator.

$$\boldsymbol{\nabla} = \begin{bmatrix} \frac{\delta}{\delta x} \\ \frac{\delta}{\delta y} \end{bmatrix} \qquad (123)$$

Within the mass balance equation (122), the first term allows for the volume change velocity due to soil skeleton deformation. The second and fourth terms account for fluid flow into the representative unit volume according to *Darcy* law. The third term considers volumetric deformation velocity related to soil grain and fluid compressibility i.e. $1/K_s$ and $1/K_w$, respectively (eq.(124)).

$$\frac{1}{Q^*} = \frac{n_p}{K_w} \frac{(1 - n_p)}{K_s} \qquad (124)$$

K_w is the bulk modulus of fluid.

The aforementioned equations together with an appropriate constitutive formulation (i.e. eqs.(111)-(112)) define the geo-mechanical behaviour of the soil in dynamic conditions. The unknown variables in the system are:

- The pressure of water (p_w)
- The displacement of the solid matrix (***u***)

The boundary conditions, imposed on these variables, have to be fixed in order to complete the problem. In particular:

- For the equilibrium equation, on the part of boundary Γ_t, the total traction ***t*** is specified (as an alternative in terms of total stress $\sigma_{ij} n_j$ ***(σ·G$_n$)*** where n_j is the *j-th* component of the normal at the boundary and ***G$_n$*** is the appropriate vectoral equivalence); whereas, on the part of boundary Γ_u, the displacement ***u*** is given.

- For the fluid phase, the boundary is divided into two parts: Γ_p, where the value of p_w is specified, and Γ_q, where the normal outflow (q_n) is prescribed. The normal outward velocity (q_n) is set to zero on an impermeable boundary.

$$\begin{aligned} \boldsymbol{t} &= \tilde{\boldsymbol{t}} \; on \; \Gamma = \Gamma_t \\ \boldsymbol{u} &= \tilde{\boldsymbol{u}} \; on \; \Gamma = \Gamma_u \\ p_w &= \tilde{p} \; on \; \Gamma = \Gamma_p \\ q_n &= \tilde{q} \; on \; \Gamma = \Gamma_q \end{aligned} \qquad (125)$$

Where

$$\begin{aligned} \tilde{\boldsymbol{t}} &= \boldsymbol{\sigma} \boldsymbol{G}_{\boldsymbol{n}} = \boldsymbol{\sigma}' \boldsymbol{n} - \boldsymbol{n} p_w \\ \tilde{q} &= (-\boldsymbol{k} \boldsymbol{\nabla} p_w + \boldsymbol{k} \rho_w \boldsymbol{b}) \boldsymbol{n} \end{aligned} \qquad (126)$$

8.2. Discretization of the problem in space

The spatial discretization of the problem is accomplished through the introduction of suitable shape functions for variables $\boldsymbol{u}$ and p_w and the application of the *Galerkin Residual Method*. Generally, the interpolation degree of the displacement field (i.e. quadratic order) is required to be higher than the corresponding one within the pressure field (i.e. bilinear order) according to *Zienkiewicz-Taylor* approach. Mathematically, such assumption permits avoiding spurious oscillations and instabilities in the modelling. It is worth mentioning that it is possible to overcome the interpolation degree requirement through the so-called stabilization techniques such as the approach based on the *Simo-Rifai* enhanced strain element proposed by Mira et al. (2003).

Applying the *Galerkin Residual Method* on the equations (120) and (122)

$$\int \delta \boldsymbol{u}^T \rho \ddot{\boldsymbol{u}} d\Omega + \int \delta \varepsilon^T \boldsymbol{\sigma}' d\Omega - \int \delta \varepsilon^T S_w \boldsymbol{m} p_w d\Omega = \int \delta \boldsymbol{u}^T \rho \boldsymbol{b} d\Omega + \int \delta \boldsymbol{u}^T \boldsymbol{t} d\Gamma_t \quad (127)$$

$$\int \delta p S_w \boldsymbol{m}^T \boldsymbol{S} \dot{\boldsymbol{u}} d\Omega - \int \nabla \delta p_w \boldsymbol{k} \nabla p_w d\Omega + \int \delta p \frac{\dot{p_w}}{Q^*} d\Omega = \int \nabla \delta p_w \boldsymbol{k} \rho_w \mathbf{b} d\Omega - \int \delta p_w q_n d\Gamma_q \quad (128)$$

The domain Ω is divided into elements: the field of displacement ($\boldsymbol{u}$) and pore pressure (p_w) are represented by the shape functions (N).

$$u^e = \sum_{i=1,m} N_{ui}^e u_i^e = N_u^e \bar{u}^e$$
$$p_w^e = \sum_{j=1,n} N_{pj}^e p_{wj}^e = N_p^e \bar{p}_w^e \quad (129)$$

Where u_i^e and p_{wj}^e are the nodal values of displacement and pore pressure for each element, respectively.

In the vectoral notation, the previous relationships (129)) are written as

$$u = N_u \bar{u}$$
$$p_w = N_p \bar{p} \quad (130)$$

Substituting such approximations (eqs.(130)) in the equations (127) and (128) and after subsequent mathematical operations

$$\int N_u^T \rho N_u \ddot{\bar{u}} d\Omega + \int B^T \sigma' d\Omega - \int B^T S_w m N_p \bar{p} d\Omega = \int N_u^T \rho b d\Omega + \int N_u^T t d\Gamma_t \quad (131)$$

$$\int N_p^T S_w m^T S N_u \dot{\bar{u}} d\Omega - \int (\nabla N_p)^T k \nabla N_p \bar{p} d\Omega + \int N_p^T \frac{\dot{p}_w}{Q^*} N_p \dot{\bar{p}} d\Omega = \int (\nabla N_p)^T k \rho_w \mathrm{b} d\Omega - \int N_p^T q_n d\Gamma_q \quad (132)$$

Where B is the matrix of the spatial derivatives of the displacement shape functions.

$$B \equiv S N_u \quad (133)$$

Since the hypothesis of the small-strain behaviour of soils is assumed, B is constant.

By putting together the terms of equations (131) and (132), the following concise form is obtained:

$$M\ddot{u} + \int B^T \sigma' d\Omega - Q\bar{p} = f_u \qquad (134)$$

$$Q^T \dot{u} + H\bar{p} + C_c \dot{\bar{p}} = f_p \qquad (135)$$

Where

$$M = \int N_u^T \rho N_u d\Omega \ \ Mass\ matrix \qquad (136)$$

$$Q = \int B^T S_w m N_p d\Omega \ \ Coupling\ matrix \qquad (137)$$

$$f_u = \int N_u^T \rho b d\Omega + \int N_u^T t d\Gamma_t \ \ Displacement\ load\ vector \qquad (138)$$

$$H = \int \left(\nabla N_p\right)^T k \nabla N_p d\Omega \ \ Permeability\ matrix \qquad (139)$$

$$C_c = \int N_p^T \frac{\dot{p}_w}{Q^*} N_p d\Omega \ \ Compressibility\ matrix \qquad (140)$$

$$f_p = \int \left(\nabla N_p\right)^T k \rho_w \mathrm{b} d\Omega - \int N_p^T q_n d\Gamma_q \ Pressure\ load\ vector \qquad (141)$$

8.3. Discretization of the problem in time

To achieve the numerical solution, it is necessary to integrate the differential equations (134) and (135) in time. The single-step methods handle each step separately and may incorporate restart facilities with no particular changes in the algorithm. The adopted scheme is based on a generalization of *Newmark* or F*inite Difference approach*, renamed the *Generalized Newmark method (GNM)* by Katona and Zienkiewicz (1985). The governing equations have to be satisfied at each discrete time "*n*"

$$M\ddot{u}_n + \int B^T \sigma'_n d\Omega - Q\bar{p}_n = f_{u_n} \qquad (142)$$

$$Q^T \ddot{u}_n + H\bar{p}_n + C_c\dot{\bar{p}}_n = f_{p_n} \tag{143}$$

and "*n+1*"

$$M\ddot{u}_{n+1} + \int B^T \sigma'_{n+1} d\Omega - Q\bar{p}_{n+1} = f^u_{n+1} \tag{144}$$

$$Q^T \ddot{u}_{n+1} + H\bar{p}_{n+1} + C_c\dot{\bar{p}}_{n+1} = f^p_{n+1} \tag{145}$$

A second-order expansion for the displacement field is adopted.

$$\begin{aligned} \ddot{u}_{n+1} &= \ddot{u}_n + \Delta\ddot{u}_n \\ \dot{u}_{n+1} &= \dot{u}_n + \Delta t\ddot{u}_n + \beta_1 \Delta t \Delta\ddot{u}_n \\ \bar{u}_{n+1} &= \bar{u}_n + \Delta t\dot{u}_n + \frac{1}{2}\Delta t_n^2 \ddot{u}_n + \frac{1}{2}\beta_2 \Delta t^2 \Delta\ddot{u}_n \end{aligned} \tag{146}$$

A first-order expansion for the pore pressure displacement field is assumed.

$$\begin{aligned} \dot{\bar{p}}_{n+1} &= \dot{\bar{p}}_n + \Delta\dot{\bar{p}}_n \\ \bar{p}_{n+1} &= \bar{p}_n + \Delta t\dot{\bar{p}}_n + \beta_3 \Delta t \Delta\dot{\bar{p}}_n \end{aligned} \tag{147}$$

Inserting the relationships (146) and (147) into equations (142) - (145), a non-linear equation system is obtained:

$$G^u_{n+1} = M\Delta\ddot{u}_n + \int B^T \sigma'_{n+1} d\Omega - Q\beta_3 \Delta t \Delta\dot{\bar{p}}_n - F^u_{n+1} = 0 \tag{148}$$

$$G^p_{n+1} = Q^T \beta_1 \Delta t \Delta\ddot{u}_n + H\beta_3 \Delta t \Delta\dot{\bar{p}}_n + C_c \Delta\dot{\bar{p}}_n - F^p_{n+1} = 0 \tag{149}$$

Where

$$F^u_{n+1} = f^u_{n+1} - M\ddot{u}_n + Q(\bar{p}_n + \Delta t\dot{\bar{p}}_n) \tag{150}$$

$$F^p_{n+1} = f^p_{n+1} - Q^T(\dot{u}_n + \Delta t\ddot{u}_n) - H(\bar{p}_n + \Delta t\dot{\bar{p}}_n) - C_c\dot{\bar{p}}_n \tag{151}$$

In order to achieve the unconditional stability of the algorithm, the parameters β_1, β_2 and β_3 required:

$$\beta_2 \geq \beta_1 \geq \frac{1}{2} \; and \; \beta_3 \geq \frac{1}{2} \tag{152}$$

In the aforementioned equations, the unknow variables are the incremental values of the highest time derivatives: $\Delta\ddot{\vec{u}}$ and $\Delta\dot{\vec{p}}$.

8.4. The algorithm to solve the non-linear system: *Newton-Raphson method*

The *Newton-Raphson method* (*NR*) is a traditional one-dimensional root-finding algorithm (Press et al., 1992), where the variables *x* have to be estimated according to equation (153):

$$f(x) = 0 \tag{153}$$

determining the function *f(x)* and its derivate *f'(x)* in each iteration. In particular:

- In linear cases (i.e. elastic soil models), a single iteration solves the problem exactly.

- In non-linear cases (i.e *GP*-based soil models), a series of iterations are performed. Known the solution x_i of the *i-th* iteration, it is necessary to determine a value $x_{i+1} = x_i + dx_i$ which satisfies $f(x) = 0$.

The *NR* scheme is derived from the Taylor series expansion in the neighbourhood of a point:

$$x_{i+1} = x_i - \frac{f(x_i)}{f'(x_i)} \tag{154}$$

The method converges quadratically: the iterative error of the step $\varepsilon_{err,i+1}$ is proportional to the square of the previous one $\varepsilon_{err,i}$ and an acceptable evaluation of *f'(x)* should be reached to preserve the convergence.

$$\varepsilon_{err,i+1} \approx \frac{1}{2}\varepsilon_{err,i}^2 \frac{f''(x)}{f'(x)} \tag{155}$$

When integrating *GP* equations within *FE* models it is necessary to use consistent tangents to obtain the second-order accuracy.

In a *FE* context and a coupled static problem, the main goal is to determine a displacement and a pore pressure vector that permits to have a residual force vector $G(u,p_w)$, which is the difference between the external and the internal forces, close to zero. It means that the external forces are in equilibrium with the internal ones.

$$G(u,p_w) = \begin{Bmatrix} G_u\ (u,p_w) \\ G_p\ (u,p_w) \end{Bmatrix} = 0 \qquad (156)$$

The classical *NR* system of equations is given by

$$G_n = G_0 + J\delta x = 0 \qquad (157)$$

Where the Jacobian matrix *J* is

$$J = \begin{bmatrix} \dfrac{\delta G^u}{\delta u} & \dfrac{\delta G^u}{\delta p_w} \\ \dfrac{\delta G^p}{\delta u} & \dfrac{\delta G^p}{\delta p_w} \end{bmatrix} \qquad (158)$$

And the unknown variables

$$\delta x = \begin{Bmatrix} \delta u \\ \delta p_w \end{Bmatrix} \qquad (159)$$

In a coupled dynamic time-dependent problem, the procedure is summarized as below

$$G_{n+1}\left(u_{n+1}, \dot{u}_{n+1}, p_{n+1}, \dot{p}_{n+1}\ \right) = \begin{Bmatrix} G_u\ \left(u_{n+1}, \dot{u}_{n+1}, p_{n+1}, \dot{p}_{n+1}\ \right) \\ G_p\ \left(u_{n+1}, \dot{u}_{n+1}, p_{n+1}, \dot{p}_{n+1}\ \right) \end{Bmatrix} = 0 \qquad (160)$$

The classical *NR* system of equations is written as

$$G_{n+1,n} = G_{n+1,0} + J\delta x = 0 \qquad (161)$$

Where the Jacobian matrix *J* is

$$J = \begin{bmatrix} \frac{\delta G^u}{\delta \Delta \dot{u}_n} & \frac{\delta G^u}{\delta \Delta \dot{p}_n} \\ \frac{\delta G^p}{\delta \Delta \dot{u}_n} & \frac{\delta G^p}{\delta \Delta \dot{p}_n} \end{bmatrix} \quad (162)$$

And the unknown variables

$$\delta x = \begin{Bmatrix} \delta(\Delta \dot{u}_n) \\ \delta(\Delta \dot{p}_n) \end{Bmatrix} \quad (163)$$

The same technique with the second order derivates can be developed. In order to understand the procedure, a single field static problem is presented step by step, using a displacement control analysis (Mira and Pastor, 2002). The aim of the process is to find a displacement vector such as

$$G(u) = 0 \quad (164)$$

The problem is divided into a first step, which counts active degrees of freedom (superscript 1), and a second part corresponding to restricted ones (superscript 2).

1) It is necessary to assume a displacement state u_A such that

$$G(u_A) = f_A^{ext} - f_A^{int} = 0 \quad (165)$$

This process converges after several iterations according to the fixed tolerance.

$$\frac{\|G(u_A)\|}{\|f_A^{ext}\|} =< tol \quad (166)$$

2) The second step involves the determination of an unknown displacement vector $u_B^1 = u_A^1 + \Delta u^1$ associated to a given displacement array $u_B^2 = u_A^2 + \Delta u^2$. The increment Δu^1 is unknow whereas the term Δu^2 is given. The relationship (167) has to be verified:

$$G(u_B^1, u_B^2) = 0 \quad (167)$$

The solution of the system $G^{\underline{1}}(u_B^1, u_B^2) = 0$ permits to find Δu^1. The external force $f^{ext,2}$ is obtained by substituting Δu^1 and Δu^2 into $G^{\underline{2}}(u_B^1, u_B^2) = 0$. The first predictor of Δu^1, named Δu_1^1, is estimated solving the following equation system:

$$G_1^{\underline{1}} = G_A^{\underline{1}} + [K^{11} \quad K^{12}] \begin{Bmatrix} \Delta u_1^1 \\ \Delta u_1^2 \end{Bmatrix} = 0 \qquad (168)$$

3) Once Δu_1^1 is determined and the displacement vector is updated through $u_1^1 = u_A^1 + \Delta u_1^1$, the integration of the stresses at each Gauss point (*Gp*) allows to find the internal force vectors $f_1^{int,1}$ and $f_1^{int,2}$. The reactions f_1^{ext} are updated from the internal ones.
4) The convergence is verified by

$$\frac{\|G_1\|}{\|f_1^{ext}\|} =< tol \qquad (169)$$

The iterative procedure ends when the convergence is reached; otherwise a new stiffness matrix K_2, based on the new displacement state u^1, is calculated. The iterative procedure continues until at the *i-th* iteration the convergence condition is satisfied.

8.5. Saturated dynamic problem

The seismic coupled analyses, in terms of displacement and pore pressure, have been performed solving the system of the governing equations within dynamic case, after the imposition of the initial stationary conditions. By writing the equations (148) and (149) as the relationship (157), the problem is represented by the formulation (170)

$$G(x) = 0 \qquad (170)$$

Where

$$x = \begin{Bmatrix} \Delta\ddot{u} \\ \Delta\dot{p} \end{Bmatrix} \; and \; G = \begin{Bmatrix} G^u \\ G^p \end{Bmatrix} \tag{171}$$

The system (170) is solved by the abovementioned *NR* algorithm for each time step according to an established tolerance. Using the series expansion of Taylor and avoiding the second order term, the equation (170) is written as

$$G(x_i) + \frac{\delta G}{\delta x_{x=x_i}} dx_i = 0 \tag{172}$$

And the explaining the Jacobian matrix (*J*)

$$\frac{\delta G}{\delta x_{x=x_i}} dx_i = J dx_i = -\, G(x_i) \tag{173}$$

Where

$$J = \begin{bmatrix} \dfrac{\delta G^u}{\delta \Delta\ddot{u}} & \dfrac{\delta G^u}{\delta \Delta\dot{p}} \\ \dfrac{\delta G^p}{\delta \Delta\ddot{u}} & \dfrac{\delta G^p}{\delta \Delta\dot{p}} \end{bmatrix} = \begin{bmatrix} M + K_t \dfrac{1}{2} \beta_2 \Delta t^2 & -Q\beta_3 \Delta t \\ Q^T \beta_1 \Delta t & H\beta_3 \Delta t + C_c \end{bmatrix} \tag{174}$$

And K_t is the tangent stiffness matrix.

$$K_t = \int B^T D_t B d\Omega \tag{175}$$

By inserting the approximation (174) into (173), the non-symmetric system is

$$\begin{bmatrix} M + K_t \dfrac{1}{2} \beta_2 \Delta t^2 & -Q\beta_3 \Delta t \\ Q^T \beta_1 \Delta t & H\beta_3 \Delta t + C_c \end{bmatrix} \begin{Bmatrix} d(\Delta\ddot{u}_n) \\ d(\Delta\dot{p}_n) \end{Bmatrix} = -\begin{Bmatrix} G^u \\ G^p \end{Bmatrix} \tag{176}$$

If the tangent stiffnes matrix (K_t) is symmetric, the matrix in (176) can be made symmetric by a simple scalar multiplication of the second row.

$$\begin{bmatrix} M + K_t \dfrac{1}{2} \beta_2 \Delta t^2 & -Q\beta_3 \Delta t \\ -Q^T \beta_3 \Delta t & -\dfrac{\beta_3}{\beta_1}(H\beta_3 \Delta t + C_c) \end{bmatrix} \begin{Bmatrix} d(\Delta\ddot{u}_n) \\ d(\Delta\dot{p}_n) \end{Bmatrix} = -\begin{Bmatrix} G^u \\ -\dfrac{\beta_3}{\beta_1} G^p \end{Bmatrix} \tag{177}$$

The Jacobian matrix is updated at each iteration to solve the complete system of equations. Each iteration is composed by a factorization (i.e. reduction or decomposition) and a back substitution, using the *Gauss* algorithm (i.e. the sparse *Gauss LU* decomposition).

8.6. Saturated consolidation problem (quasi-static problem)

To validate the constitutive model implemented within *MATLAB* framework, a series of coupled analyses are performed using the *FE* code, considering a single element of soil. The triaxial drained/undrained tests are reproduced taking as reference the quasi-static problem, where the inertial effects are neglected, as represented by the following equations. This implies $\ddot{u} = 0$ in the equation (120).

- The equation of equilibrium

$$S^T(\sigma' - mp_w) + \rho b = 0 \qquad (178)$$

- The mass balance

$$m^T S\dot{u} - \nabla^T k \nabla p_w + \frac{\dot{p}_w}{Q^*} + \nabla^T k \rho_w b = 0 \qquad (179)$$

- The boundary conditions

$$\begin{aligned} t &= \tilde{t}\ on\ \Gamma = \Gamma_t \\ u &= \tilde{u}\ on\ \Gamma = \Gamma_u \\ p &= \tilde{p}\ on\ \Gamma = \Gamma_p \\ q_n &= \tilde{q}\ on\ \Gamma = \Gamma_q \end{aligned} \qquad (180)$$

Enforcing the *Galerkin Residual Method*, the equations (178) and (179) become:

$$\int \delta\varepsilon^T \sigma' d\Omega - \int \delta\varepsilon^T S_w m p_w d\Omega = \int \delta u^T \rho b d\Omega + \int \delta u^T t d\Gamma_t \qquad (181)$$

$$\int \delta p_w S_w m^T S\dot{u} d\Omega - \int \nabla \delta p_w k \nabla p d\Omega + \int \delta p_w \frac{\dot{p}_w}{Q^*} d\Omega = \int \nabla \delta p_w k \rho_w \mathrm{b} d\Omega - \int \delta p_w q_n d\Gamma_q \quad (182)$$

The domain Ω is divided into elements and the field of variables is represented by the shape functions (N), discretizing in space and time.

$$\int B^T \sigma'_{n+1} d\Omega - Q\bar{p}_{n+1} = f^u_{n+1} \quad (183)$$

$$Q^T \dot{\bar{u}}_{n+1} + H\bar{p}_{n+1} + C_c \dot{\bar{p}}_{n+1} = f^p_{n+1} \quad (184)$$

By using the *GNM*, the corresponding displacement, pore pressure and velocity expansions are shown below:

$$\dot{\bar{u}}_{n+1} = \dot{\bar{u}}_n + \Delta\dot{\bar{u}}_n$$
$$\bar{u}_{n+1} = \bar{u}_n + \Delta t\dot{\bar{u}}_n + \beta\Delta t\Delta\dot{\bar{u}}_n \quad (185)$$

$$\dot{\bar{p}}_{n+1} = \dot{\bar{p}}_n + \Delta\dot{\bar{p}}_n$$
$$\bar{p}_{n+1} = \bar{p}_n + \Delta t\dot{\bar{p}}_n + \beta_3\Delta t\Delta\dot{\bar{p}}_n \quad (186)$$

After a series of substitutions, the non-linear system of the governing equations is obtained:

$$G^u_{n+1} = \int B^T \sigma'_{n+1} d\Omega - Q\beta_3\Delta t\Delta\dot{\bar{p}}_n - F^u_{n+1} = 0 \quad (187)$$

$$G^p_{n+1} = Q^T \Delta\dot{\bar{u}}_n + H\beta_3\Delta t\Delta\dot{\bar{p}}_n + C_c\Delta\dot{\bar{p}}_n - F^p_{n+1} = 0 \quad (188)$$

Where

$$F^u_{n+1} = f^u_{n+1} + Q(\bar{p}_n + \Delta t\dot{\bar{p}}_n) \quad (189)$$

$$F^p_{n+1} = f^p_{n+1} - Q^T(\dot{\bar{u}}_n) - H(\bar{p}_n + \Delta t\dot{\bar{p}}_n) - C_c\dot{\bar{p}}_n \quad (190)$$

By writing the equations (189) and (190) as the relationship (149), the problem is represented by the formulation (160), where

$$x = \begin{Bmatrix} \Delta\dot{\bar{u}} \\ \Delta\dot{\bar{p}} \end{Bmatrix} \; and \; G = \begin{Bmatrix} G^u \\ G^p \end{Bmatrix} \tag{191}$$

Through the *NR* procedure

$$G(x_i) + \frac{\delta G}{\delta x}_{x=x_i} dx_i = G(x_i) + J dx_i = 0 \tag{192}$$

Where the Jacobian matrix (*J*) is

$$J = \begin{bmatrix} \frac{\delta G^u}{\delta \Delta\dot{\bar{u}}} & \frac{\delta G^u}{\delta \Delta\dot{\bar{p}}} \\ \frac{\delta G^p}{\delta \Delta\dot{\bar{u}}} & \frac{\delta G^p}{\delta \Delta\dot{\bar{p}}} \end{bmatrix} = \begin{bmatrix} K_t\beta_2\Delta t & -Q\beta_3\Delta t \\ Q^T & H\beta_3\Delta t + C_c \end{bmatrix} \tag{193}$$

By assuming the hypothesis that the tangent stiffnes matrix (K_t) is symmetric, the complete system is described by (194).

$$\begin{bmatrix} K_t\beta_2\Delta t & -Q\beta_3\Delta t \\ -Q^T\beta_3\Delta t & -\frac{\beta_3}{\beta_1}(H\beta_3\Delta t + C_c) \end{bmatrix} \begin{Bmatrix} d(\Delta\dot{\bar{u}}_n) \\ d(\Delta\dot{\bar{p}}_n) \end{Bmatrix} = - \begin{Bmatrix} G^u \\ -\frac{\beta_3}{\beta_1} G^p \end{Bmatrix} \tag{194}$$

8.7. Saturated static stationary problem

Quasi-static problems reach a stationary state at the end of the consolidation process. In a stationary problem respect to the previous section, the pore pressure and displacement velocities are additionally neglected ($\dot{p}_w$=0 and $\dot{u}$=0 in eq.(122)). The governing equations are simplified as below:

- The equation of equilibrium

$$S^T(\sigma' - mp_w) + \rho b = 0 \tag{195}$$

- The mass balance

$$-\nabla^t k \nabla p_w + \nabla^T k \rho_w b = 0 \tag{196}$$

The domain Ω is divided into elements and the field of variables is represented by the shape functions (*N*), discretizing in space and time.

$$\int B^T \sigma'_{n+1} d\Omega - Q\bar{p}_{n+1} = f^u_{n+1} \quad (197)$$

$$H\bar{p}_{n+1} = f^p_{n+1} \quad (198)$$

Following the same procedure of the previous section, the Jacobian matrix (*J*) is

$$J = \begin{bmatrix} K_t & -Q \\ 0 & H \end{bmatrix} \quad (199)$$

This coupled *u*-p_w approach has been used in the next chapters to get the preliminary static distribution of the stress and pore pressure due to gravity. The initial conditions embody the input for the consequent dynamic analyses.

8.8. Saturated static total stress problem

This approach is adopted to model dry soil deposit. In fact, in this static framework, the total stresses match the effective stresses (i.e. $\sigma = \sigma'$) because of the zero value of the pore pressure term (p_w). The system of governing laws becomes:

- The equation of equilibrium

$$S^T(\sigma) + \rho b = 0 \quad (200)$$

- The mass balance

$$-\nabla^t k \nabla p_w + \nabla^T k \rho_w b = 0 \quad (201)$$

9. Finite Element Model

The Finite Element (*FE*) method is a powerful tool to predict the failure mechanism and the limit load in geomechanical problems. Nevertheless, the use of this method shows several complications related to computational algorithms, element types and mesh, which lead to unreliable results (Mira and Pastor, 2002). At the *Centro de Estudios y Experimentación de Obras Públicas De Madrid* (*CEDEX*), working with Dr. Pablo Mira Mc Williams (PhD) and Prof. Manuel Pastor, the main goal has been to develop a numerical model of liquefaction phenomena using the *GP* theory and the program *GeHoMADRID* in order to simulate the observed damages in 2012 Emilia earthquake. *GeHoMADRID* is a Finite Element code for the coupled behaviour of saturated and unsaturated soils which permits to study the stress-strain response under different loading conditions. It has been jointly developed between the *Universidad Politécnica de Madrid*, *Centro de Estudios y Experimentación de Obras Públicas De Madrid* and *Hohai University*, hence its name. This *FE* code is implemented in an object-oriented language such as *FORTRAN90*, which allows to include advanced constitutive formulations such as *GP*-based model in a modular and very flexible manner. In this section, the implementation of the *GP* model into *GeHoMADRID*, using an explicit integration scheme for sands, is discussed and *2D* analyses of the case study have been performed. In fact, a substantial lack of advanced analyses of the seismic-induced phenomena occurred in Emilia led to create a reliable geotechnical model of the investigated area within a numerical framework. As regards the clayey deposit, an implicit integration of the *GP* constitutive equations in the stress framework has been adopted for the cohesive soils of Unit C (Tonni et al, 2003). After a brief discussion of the non-linear geotechnical problems, the structure of *GeHoMADRID* is presented. Then, the performance of the proposed numerical model has been verified by a validation

procedure, which compares *MATLAB* and *FE* results, in both static and dynamic conditions. In a preliminary phase, a *1D* coupled seismic analysis in effective stress has been carried out on a representative soil column in order to compute a first study of the dynamic response of the potentially liquefiable layers of the site. Finally, the whole riverbank model has been developed. In more detail, a series of static analyses, where the gravity force is applied, has allowed to define the initial distribution of stresses and pore pressures; then, the seismic input application has permitted to study the dynamic response of the soil deposit. Therefore, the geotechnical model has been developed to investigate qualitatively the response of the Scortichino river embankment at small displacement level and the potentiality of the *GP*-based constitutive model in a boundary value problem. The numerical results have been compared to seismic evidences observed in the area struck by the 2012 earthquake. Indeed, the reliability of geotechnical analyses has been evaluated taking as reference the data coming from some reports in terms of displacements (Chiaradonna et al., 2018). It is worth mentioning that the seismic sequence, which included evident liquefaction effects (e.g. surface crack pattern, sand boils) in the struck area, did not produce a dramatic collapse of the levee. Furthermore, the run length of the numerical simulations, from the mesoscale analyses up to the whole riverbank, is short due to the rapid increment of the excess pore pressures; therefore, a series of future improvements will be needed in order to achieve an adequate, stable numerical computation.

9.1. Non-linear framework

Soil mechanics problems are very clearly non-linear. Although the solutions based on linear models may be adopted as simplified approximations to geotechnical cases, the non-linearities are very often too significant to be neglected and special

non-linear strategies are required. Since the different natures of non-linearities, the model has to incorporate several types of algorithms in order to include the most typical non-linear conditions. In particular, *GeHoMADRID* allows to deal with constitutive non-linearities (e.g. non-linear elastic or elastoplastic material behaviour), in the framework of small displacements. Numerical techniques are required to obtain a satisfactory solution. The *Newton-Raphson* (*NR*) method, described in detail in the previous chapter, is an advisable tool to solve classical non-linear *FE* models: indeed, this scheme is appropriate for multidimensional geotechnical problems in the multifield and time dependent framework (Mira and Pastor, 2002).

9.2. Finite Element approach: the code structure

The proposed *GP*-based formulation has been implemented in *FORTRAN90*, which is an object-oriented platform. Within the code, the use of an adequate constitutive model and a precise, stable, robust integration algorithm of the governing equations is needed to obtain accurate numerical results in geotechnical problems. Indeed, since constitutive models for geomaterials are commonly expressed in an incremental form, the integration of such equation system along a given loading path cannot be performed analytically (Tonni et al., 2005). In particular, an explicit integration of the *GP* constitutive equations has been adopted for the granular soils; whereas an implicit scheme in the stress field has been chosen for the clayey layer (Tonni et al., 2003). A double loop is carried out within the program structure: the iterative procedure (i.e. *NR* method) is nested inside an incremental scheme, which shows the loading increments in which the total external load is divided. In detail, the iterative loop includes:

- The computation of the global stiffness matrix, which consists of the computation of tangent stiffness at each Gauss point (*Gp*), the integration of the stiffness matrix for each element and the subsequent assemblage into global stiffness matrix.
- The solution of the linear equation system through a direct algorithm known as the sparse *Gauss LU decomposition* which involves a matrix factorization (i.e. decomposition) and back substitution.
- The computation of the internal force vector, through the integration at each Gauss point (*Gp*), the integration of internal force vector for each element and the resulting assemblage into internal force vector.
- The assessment of the convergence.

The convergence test is evaluated using several norm operators:

- The square root of the sum of the squares of the components.
- The maximum of the absolute values of the components.

In the frame of a coupled approach (*u-pw*), the convergence criterion is based on:

1) The norm of the vector of the residual forces (*G*)

$$\frac{\|G\|}{\|f^{ext}\|} = \frac{\left\|f^{ext} - f^{int}\right\|}{\|f^{ext}\|} < tol\_f \qquad (202)$$

Where *G* is assumed equal to

$$\|G\| = \sqrt{\sum G_i^2} \qquad (203)$$

And

$$\|G\| = \max(abs(G_i)) \qquad (204)$$

2) The iterative displacement correction (*δu*)

$$\frac{\|\delta u\|}{\|\Delta u\|} =< tol\_v \quad (205)$$

Where

$$\|\delta u\| = \sqrt{\sum \delta u_i^2} \quad (206)$$

And

$$\|\delta u\| = \max(abs(\delta u_i)) \quad (207)$$

Δu is the incremental value of displacement.

3) The iterative pore pressure correction (*δp*)

$$\frac{\|\delta p\|}{\|\Delta p\|} =< tol\_v \quad (208)$$

Where

$$\|\delta p\| = \sqrt{\sum \delta p_i^2} \quad (209)$$

And

$$\|\delta p\| = \max(abs(\delta p_i)) \quad (210)$$

The abovementioned conditions (eqs.(202)-(210)) have to be satisfied to reach the convergence. The default value of *tol_f* is 10^{-5} whereas *tol_v* is assumed equal to 10^{-4} within non-linear analyses.

The analyses have been run in *FORTRAN90*, whereas an interactive graphical user interface allows both the definition and the visualization of the numerical simulations: *GiD* system, developed by the *International Center for Numerical Methods in Engineering (CIMNE)*. It has been adopted for the pre-processing (e.g. introduction of geometry and mesh, assignment of material types, groups and boundary conditions) and post-processing (i.e. representation of outputs of the performed analyses) phases.

9.3. Validation of the *GP* constitutive equations

The performance of the implemented constitutive model within the *FE* framework has been evaluated through the comparison of a series of numerical simulations achieved by both *MATLAB* and *GeHoMADRID* code. Hence, the starting point is testing the solution strategy at a single-element level in order to compare the stress-strain behaviour of *GeHoMADRID* results with the predictive curves obtained asdescribed in the previous chapters. In particular, the numerical simulations of the laboratory tests have been carried out using single quadrilateral eight-noded elements, with four integration points, in asymmetry. The stress and strain conditions are assumed uniform throughout and the constitutive soil parameters are equal to the values set in Table 8 and Table 10. For this purpose, a quasi-static analysis has been performed. A series of triaxial tests under different conditions in terms of densities, confining pressures, material and test types has been reproduced in order to compare a wide range of settings i.e. *TXCID4A* (v = 1.853, p'_0 = 400 kPa) for the *Padano Aquifer* sands, *TXCID1* (v = 1.718, p'_0 = 100 kPa) and *TXCIU1* (v = 1.597, p'_0 = 150 kPa) for granular soils of the river embankment.

On the basis of the numerical results obtained from the implementation of the same set of constitutive equations within the two codes, it is possible to postulate that the simulations achieved by *GeHoMADRID* are convergent and practically identical to the curves from *MATLAB* processing. In particular, Figure 92 and Figure 96 show the volumetric response and the stress-strain behaviour of the representative tests. As regards the undrained triaxial test *TXCIU1*, also the *q-p'* effective stress path (Figure 97) and the pore pressure ratio time history (Figure 98) have been plotted. In the figures, *MATLAB* simulations are depicted using a continuous line, whereas the *FE* ones through a dashed line.

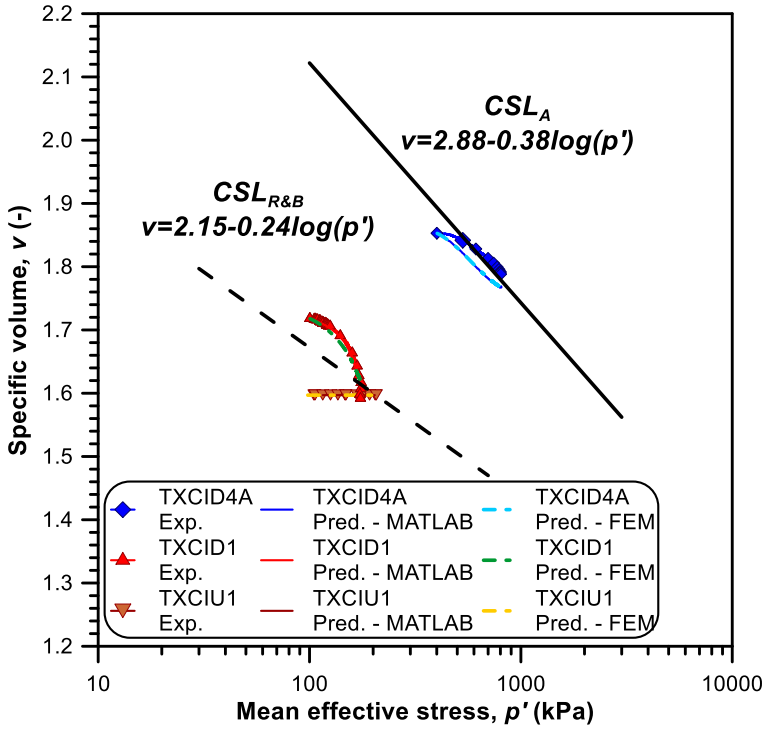

Figure 92 Experimental and predictive curves for Padano Aquifer sands (e.g. TXCID4A) and Macro-unit R & B (e.g. TXCID1 and TXCIU1) in the v-logp' plane.

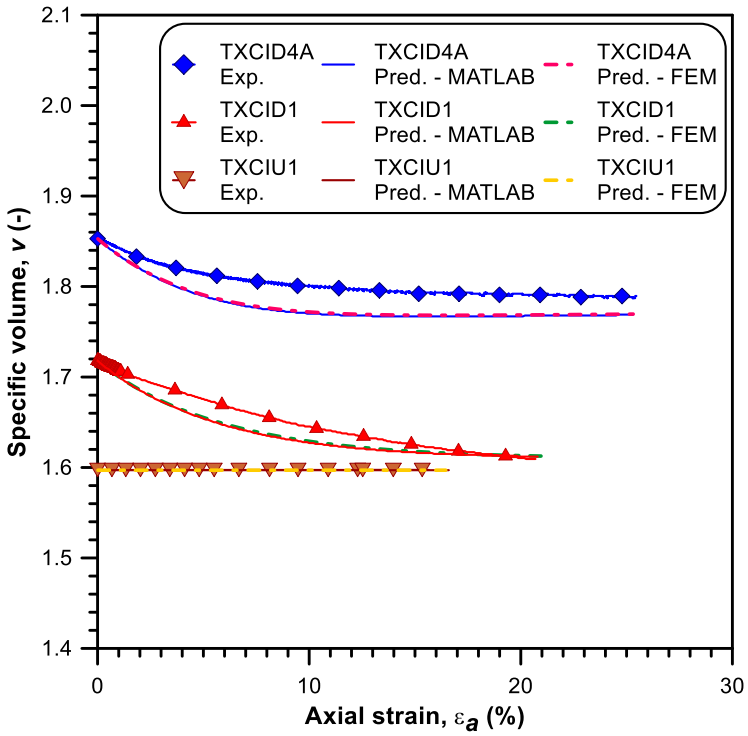

Figure 93 Experimental and predictive volumetric response for Padano Aquifer sands (TXCID4A) and Macro-unit R & B (e.g. TXCID1 and TXCIU1) in the v-ε_a plane.

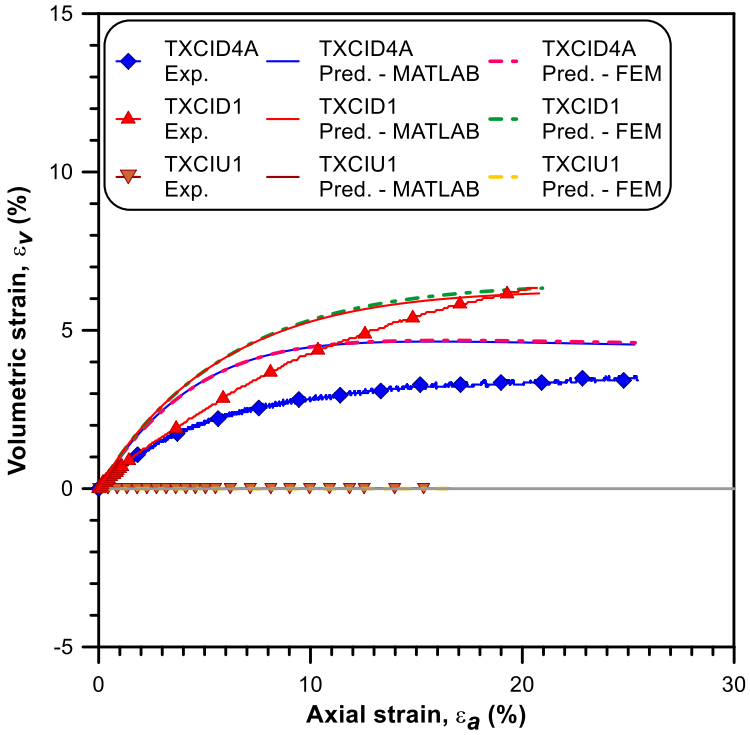

Figure 94 Experimental and predictive curves for Padano Aquifer sands (e.g. TXCID4A) and Macro-unit R & B (e.g. TXCID1 and TXCIU1) in the strain plane.

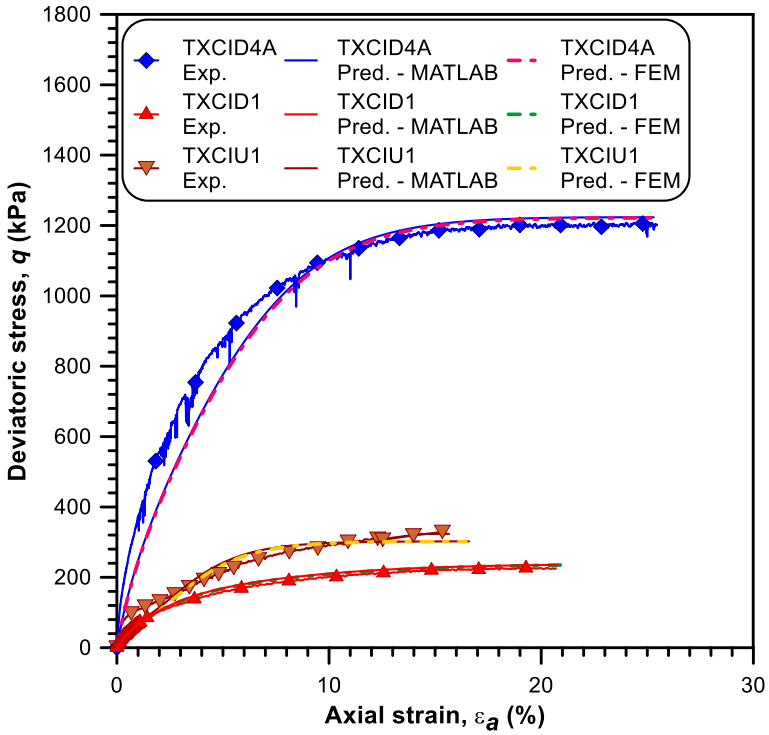

Figure 95 Experimental and predictive curves for Padano Aquifer sands (e.g. TXCID4A) and Macro-unit R & B (e.g. TXCID1 and TXCIU1) in the stress-strain plane.

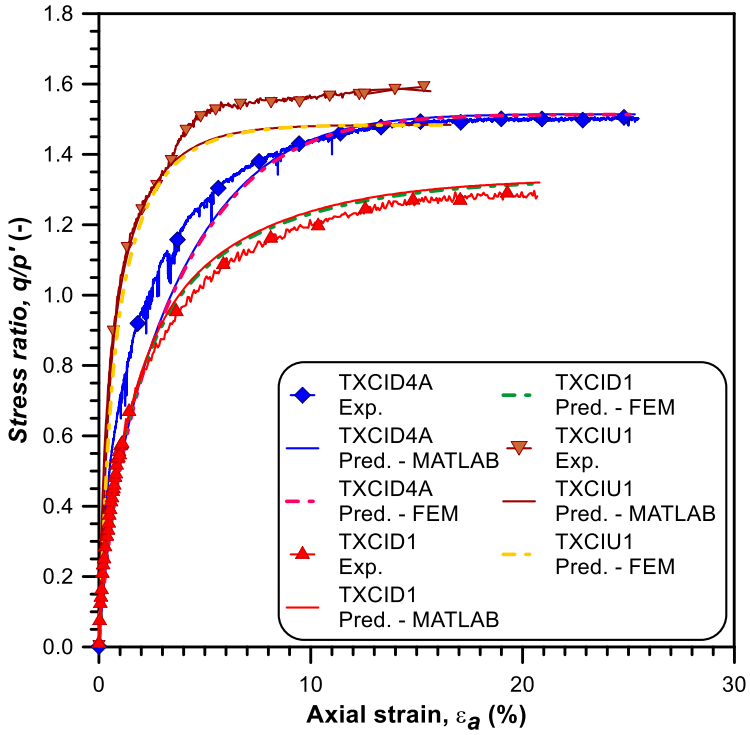

Figure 96 Experimental and predictive curves for Padano Aquifer sands (e.g. TXCID4A) and Macro-unit R & B (e.g. TXCID1 and TXCIU1) in the stress ratio-ε_a plane.

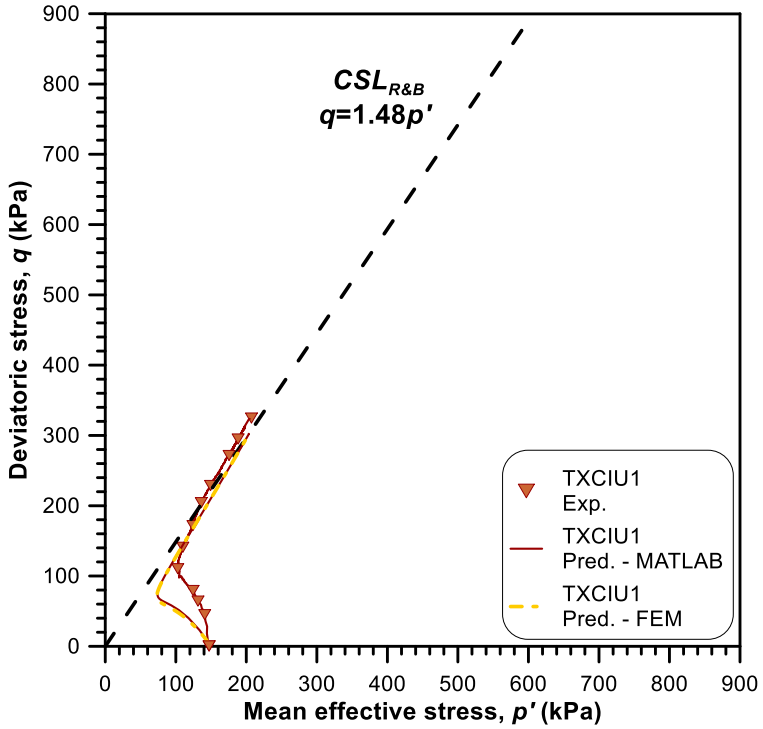

Figure 97 Experimental and predicted curves for the triaxial undrained test (TXCIU1) for river embankment granular soils in the q-p' effective stress plane.

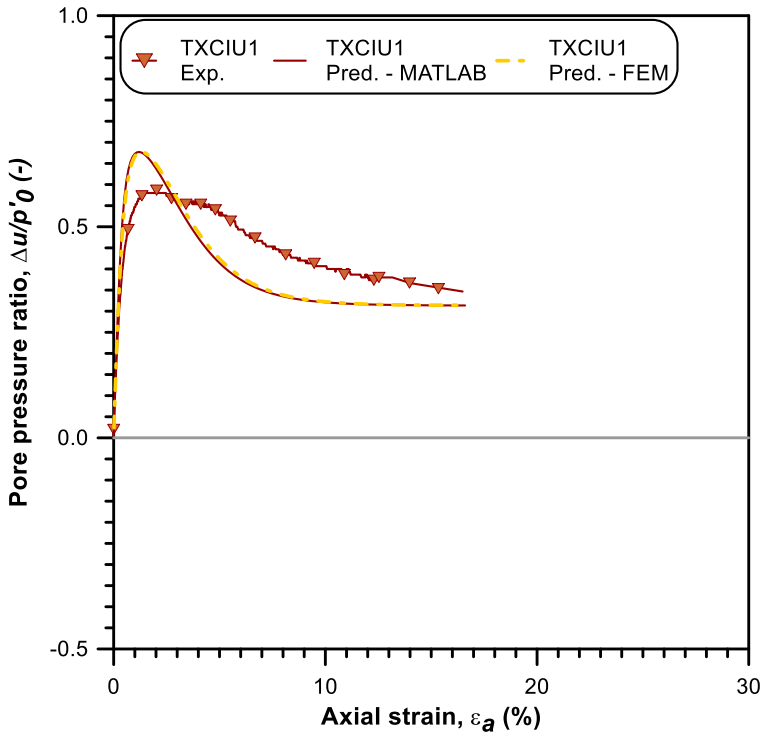

Figure 98 Experimental and predicted curves for the triaxial undrained test (TXCIU1) for river embankment granular soils in the pore pressure ratio-ε_a plane.

Therefore, the results show that the constitutive formulation in conjunction with the numerical approaches is able to properly simulate the soil behaviour and the coupled response of soil skeleton and pore fluid, typically defined by excess pore pressure development, in triaxial conditions.

9.4. Numerical simulations of undrained cyclic direct simple shear tests

Cyclic simple shear conditions represent a close simulation of the stresses induced under field conditions (Peacock and Seed, 1968). It is well known that, during the cyclic shearing of fully saturated sands in undrained conditions, the pore pressures build-up with the number of cycles (N_c) bringing the reduction of effective stresses and subsequently the shear strength and moduli. Hence, the associated backbone curves undergone a cyclic degradation. As already stated at the beginning of this research project, the soil microstructure is irreversibly altered by repetitive loading, which typically shows a relatively rapid variation of pore pressure, volume and soil

stiffness, if the cyclic shear strain amplitude exceeds a certain threshold (Vucetic, 1994). In particular, above the strain boundary (γ_{tv}), soil becomes increasingly nonlinear and inelastic, and the microstructural changes are evident in residual cyclic pore pressures in fully saturated soils and permanent volume variation in dry or partially saturated soils. On the contrary, under such value, which mainly depends on material type, the microstructure and physical properties essentially do not change. In this context, recent research contributions (e.g. di Lernia et al., 2014; Amorosi et al., 2018) aimed at simulating the undrained cyclic response of non-cohesive soils in conjunction with advanced constitutive models, accounting for the development of deformation and the accumulation of excess pore pressure. With the purpose of verifying the predictive capability of the *GP* model in the cyclic framework, a number of tests have been considered employing an undrained cyclic direct simple shear test device (*h-12 Norwegian Geotechnical Institute apparatus*). In particular, the experimental investigation is based on the previous database (Tonni et al., 2015a) developed on undisturbed silty sand samples extracted from 6.20 to 6.80 m. The tests are stress-controlled with an approximately sinusoidal shape of shear stress. The frequency, equal to 0.1 Hz, is lower than that typically a seismic sequence develops, but Hyodo et al. (1998) demonstrated that the liquefaction of granular soils is not frequency-dependent over the considered experimental range. Basic soil properties are listed in Table 14 along with the experimental test features. In particular, range of the specific volumes is between 1.55-1.60 and *FC* is found to be low, generally around 8%. Each sample was consolidated at 130 kPa, then undrained cyclic shearing was conducted with a different amplitude of the stress.

Test	*CSS-1*	*CSS-2*
Depth (m)	6.20-6.80	6.20-6.80
Section, Soil unit	A, Macro-unit R & B	A, Macro-unit R & B
Mean effective consolidation stress (kPa)	130	130
Cyclic shear stress amplitude (kPa)	26	32.50
Diameter (mm)	79	79
Height (mm)	21.78	21.98
Specific volume	1.55	1.60
Cyclic stress ratio	0.20	0.25

Table 14 Summary of cyclic shear testing programme.

The undrained behaviour of granular soils is typically described by means of the analysis of pore pressure time history (e.g. Erten and Maher, 1995; Hazirbaba and Rathje, 2009; Mohammadi and Qadimi, 2015). In particular, a shared definition of the point at which liquefaction happens is the number of cycles (N_c) associated to a value of the ratio of excess pore pressure to the mean effective consolidation stress (R_u) approximatively equal to 1. Based on a synthesis of available laboratory data, the experimental response has been examined in terms of shear stress (τ), shear strain (γ) and excess pore pressure evolution (Δu), as sketched in Figure 99, Figure 100 and Figure 101. The failure state has been reached at the 12th and 5th cycle for test *CSS-1* and *CSS-2*, respectively.

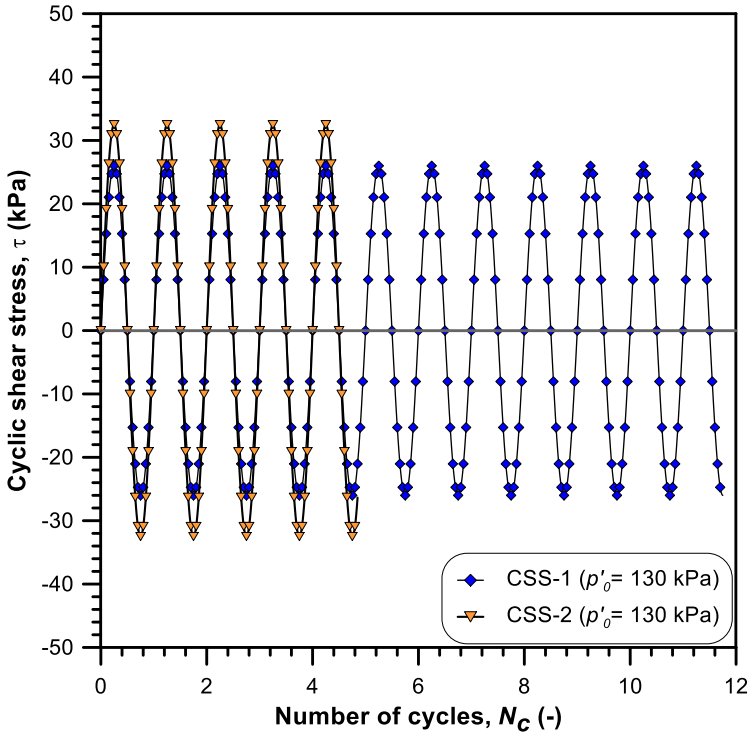

Figure 99 Variation of shear stress (τ) with number of cycles (Nc) in undrained cyclic direct simple shear tests.

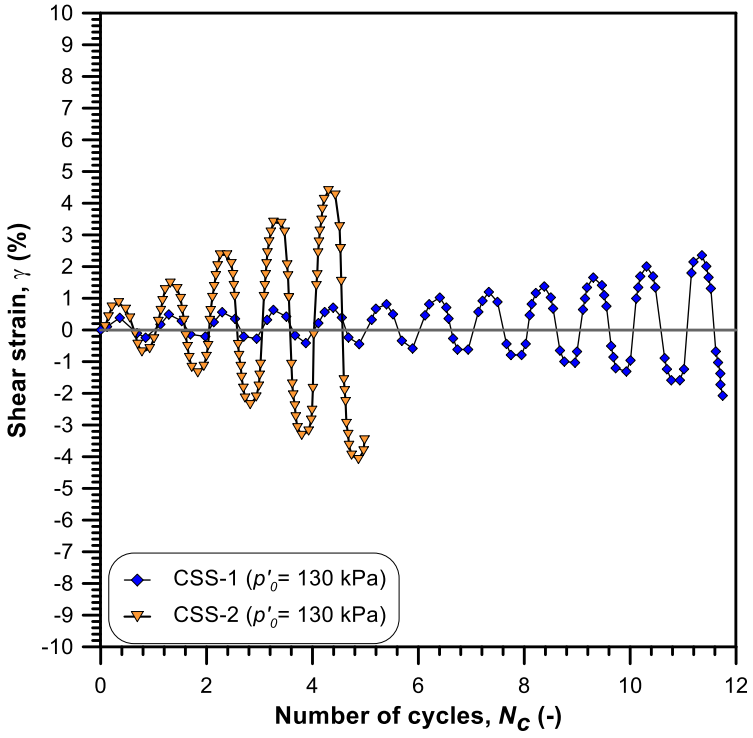

Figure 100 Variation of shear strain (γ) with number of cycles (Nc) in undrained cyclic direct simple shear tests.

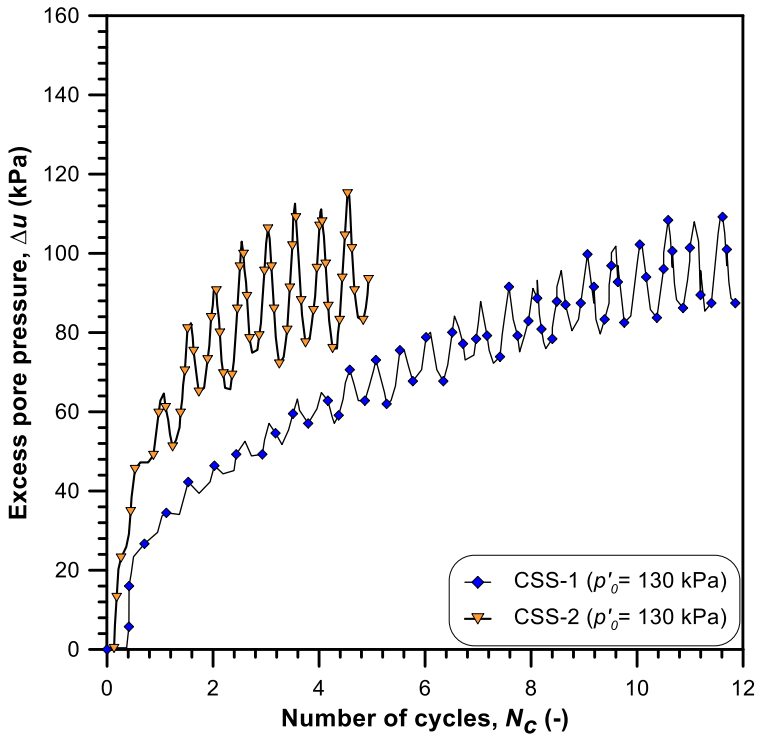

Figure 101 Variation of excess pore pressure (Δu) with number of cycles (Nc) in undrained cyclic direct simple shear tests.

In the light of the experimental response, the excess pore pressure (Δu) grows continuously during cycling, due to the tendency of the soil to contract under loading–unloading cycles. Both the samples reach a value of R_u corresponding to 0.95, but the densest specimen, which is subjected to a lower cyclic shear stress amplitude, shows higher resistance.

A series of *FE* analysis was carried out on single quadrilateral eight-noded elements in plain strain conditions in order to reproduce the cyclic response for a given number of cycles, as shown in Figure 102. Since basic physical characteristics reflect these of Macro-unit R & B samples, the set of constitutive parameters of *TXCIU1* may be applied to the cyclic simulations with a few, generally minor improvements into the set of model parameters ($K^e_{t,ini}$ = 20000 kPa and $G_{t,ini}$= 15000 kPa for *CSS-1*; $K^e_{t,ini}$ = 10000 kPa and $G_{t,ini}$= 8000 kPa for *CSS-2*).

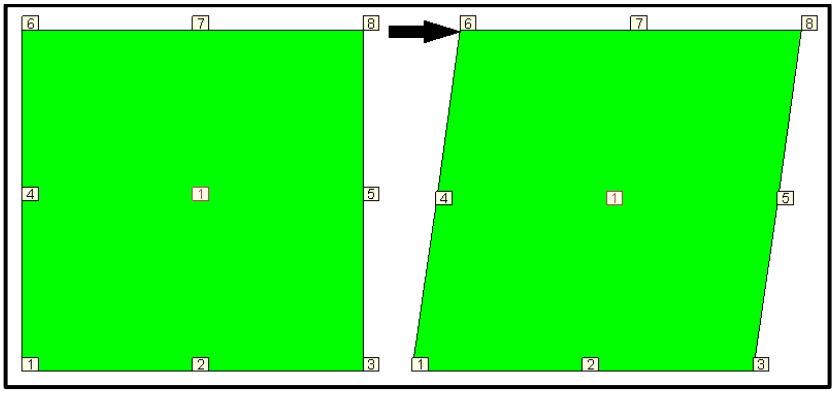

Figure 102 Numerical model for undrained cyclic simple shear test.

In Figure 103 - Figure 105, a fairly well agreement between the measured and calculated curves is obtained, although the results get worse during the increment of cycles. Hence, the adopted model is capable of describing the stress-strain loops, even in cases when soil degrades and liquefies in just a few cycles. The preceding conclusions verify that the concepts of *GP* approach in conjunction with the *FE* code may be used to study realistic stress paths experienced by the soil in cyclic conditions.

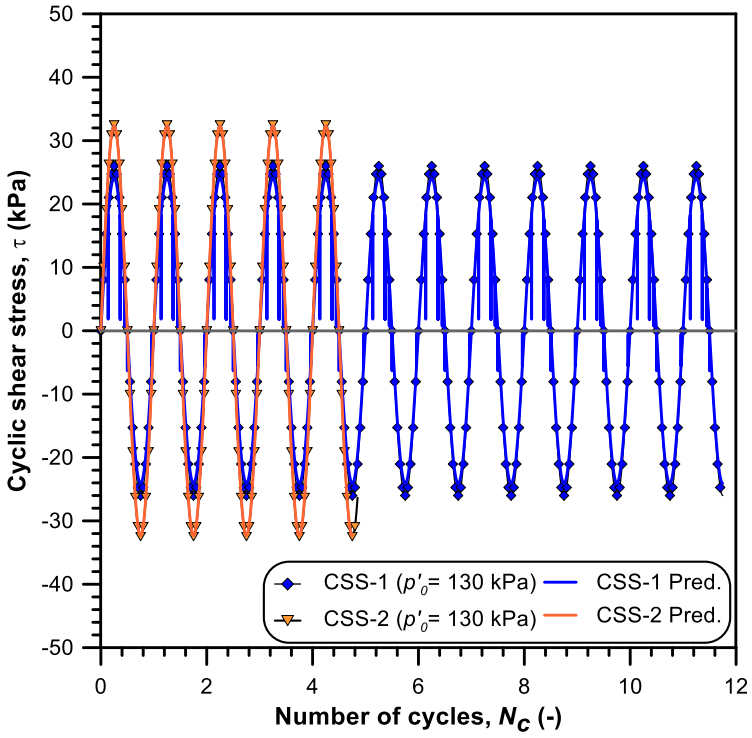

Figure 103 Experimental and predictive curves in the shear stress (τ) vs number of cycles (Nc) in undrained cyclic direct simple shear tests.

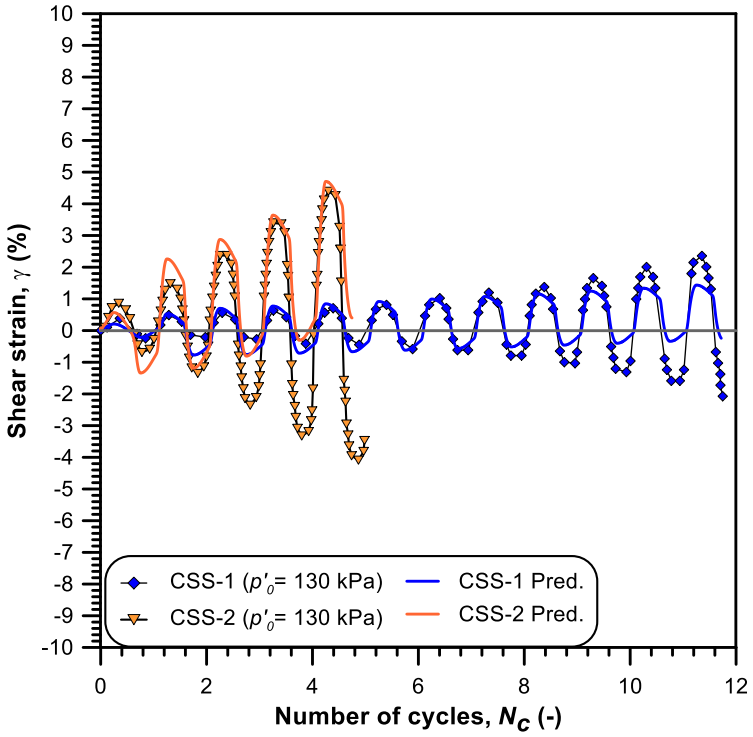

Figure 104 Experimental and predictive curves in the shear strain (γ) vs number of cycles (Nc) in undrained cyclic direct simple shear tests.

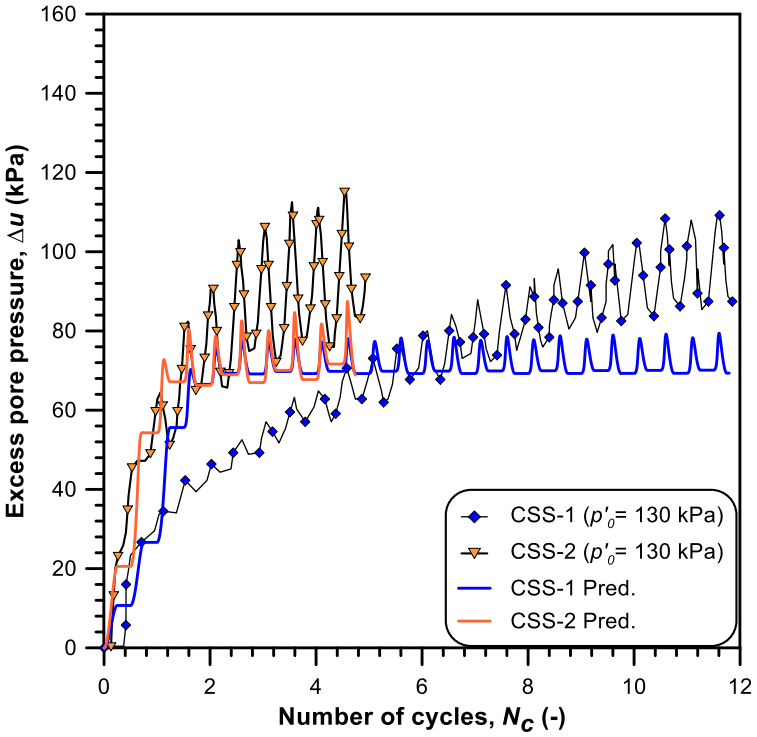

Figure 105 Experimental and predictive curves in the excess pore pressure (Δu) vs number of cycles (Nc) in undrained cyclic direct simple shear tests.

9.5. Input ground motion

Whilst a real earthquake involves multi-directional components, such study is performed using a two-dimensional model. The main shock of the Emilia 2012 earthquake sequence was characterized by a peak ground acceleration (*PGA*) equal to 0.273 g. The recording of the dominant seismic events was collected by the *MRN* station of the Italian strong-motion network (*RAN*), situated in the locality of Mirandola (Pacor et al., 2011). Such station lies on a deep soft subsoil which does not permit to use directly the data within *FE* analyses; on contrary, the other closest stations built on a rock outcrop are too far from the epicentre. A series of reference input motions at the deep seismic bedrock was obtained by de-convolving the available surface data (e.g. Evangelista et al., 2017; Chiaradonna et al., 2018), but meaningful uncertainties still affect the results. Thus, in the absence of any reliable strong motion recordings traced in the investigated area at the time of the earthquake, a number of appropriate input motions are presented in Tonni et al. (2015a). The data are selected from the *Italian Accelerometric Archive* (*ITACA*, 2011) with moment magnitude M_w from 5.50 up to 6.50 and epicentral distance in a range of 5-10 km (i.e. Tarcento, Cascia, Villetta Barrea, L'Aquila, Lauria). Since it is advisable that the recorded seismic action acts in the same direction of the plane of the examined section, the input motion of Lauria (Potenza, Italy) has been implemented in the *FE* model. The seismic input is depicted in Figure 106. The accelerogram, whose maximum value is 0.165 g, is scaled at the site peak ground acceleration (0.183 g), estimated according to Bindi et al. (2011). As shown in the graph, the seismic sequence meaningfully decreases after few seconds.

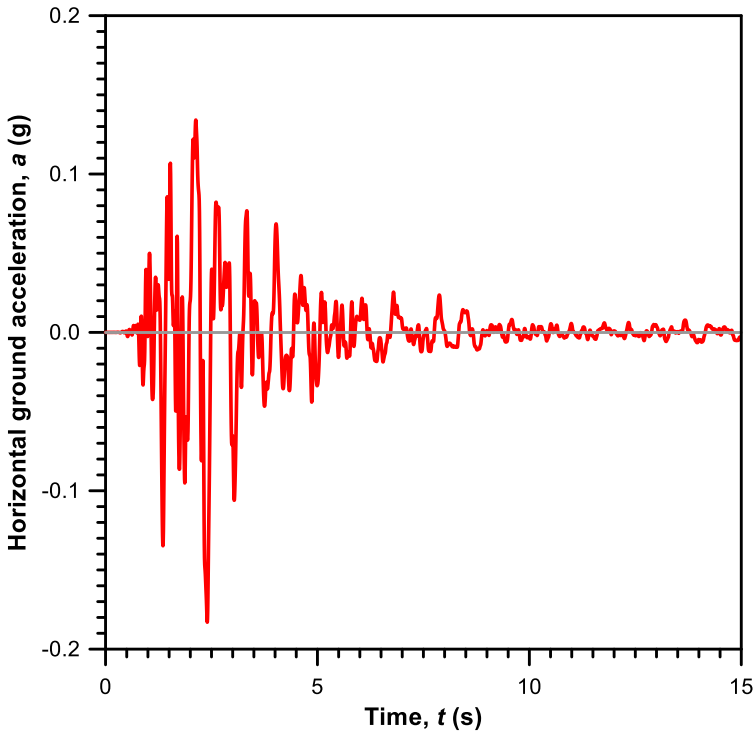

Figure 106 Seismic input (ITACA, 2011).

9.6. *1D* dynamic response of a soil column

In a preliminary phase, a representative soil column has been adopted in order to realize a first study of the dynamic response of the potentially liquefiable layers of the riverbank during the earthquake shaking. For this soil column, characterized by a depth of 120 m from the river crown, a *1D* coupled seismic analysis in effective stress has been performed. Since all the features of the numerical computation will be reported accurately in the next section, only the most significant aspects of the *FE* modelling of the column have been underlined in this paragraph. In particular, the water table is located at 4-m depth according to the in-situ investigations; thus, the Unit R is divided into a dry and a wet sub-layer. The numerical model is plotted in Figure 107, where the stratigraphy profile includes the artificial riverbank (i.e. Unit R - dry, in purple, and Unit R - wet, in brown), the sandy soils of Unit B (in light blue), the clayey Unit C (in pink) and the *Padano Aquifer* layers (i.e. Unit A - top, in blue, and Unit A - bottom, in green, with respect to *CPTU* grading characterization).

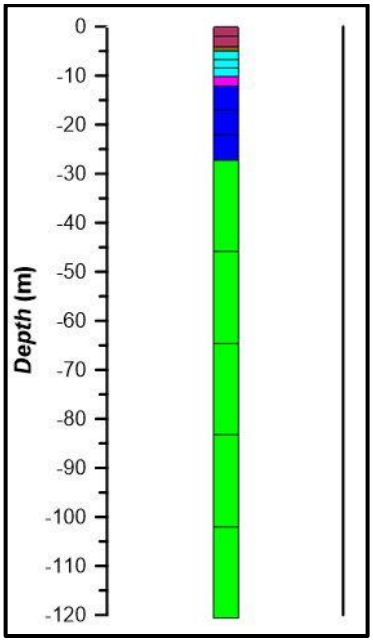

Figure 107 The representative soil column of the investigated riverbank cross-section.

Soil properties have been defined consistently with the previous laboratory testing programme and the experimental database proposed by Tonni et al. (2015a). A series of quadrilateral elements have been used to reproduce the soil column which is clamped at the bedrock. Thus, quadratic and linear shape functions have been selected for the displacement and pore pressure field, respectively. After a preliminary coupled static analysis using an elastic isotropic behaviour to apply the gravity and later introducing the *GP* formulation for granular soils to initialize the stress field, the dynamic response of the column has been calculated. The attention has been focused on the silty-sand deposit of Unit B, which has been subdivided into three elements (in light blue in Figure 107) termed 10,11,12, as shown in the scheme of Figure 108.

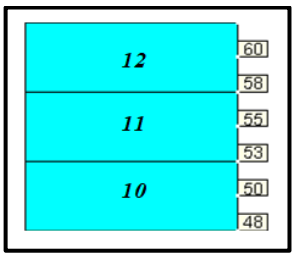

Figure 108 Elements 10,11,12 of unit B in the representative column.

Figure 109 shows the computed results in terms of pore pressure evolution (*u*) at the nodes of the three elements; in particular, after a very short time, the accumulation of excess pore pressure is evident. Taking as reference a *Gp* for each element, the time history of the mean effective pressure (*p'*) has been also observed (Figure 110) as a result of the excess pore pressure increasing.

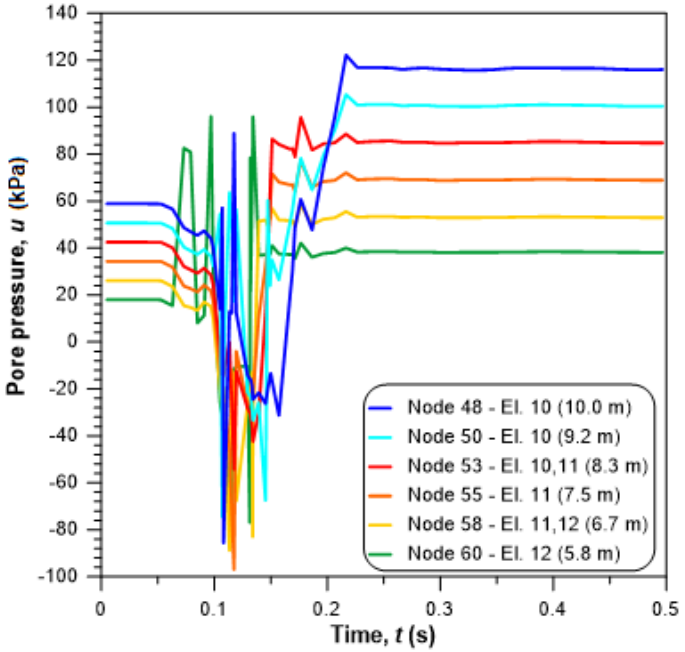

Figure 109 Pore pressure evolution at the nodes of the three elements of Unit B during the dynamic analysis of the representative column.

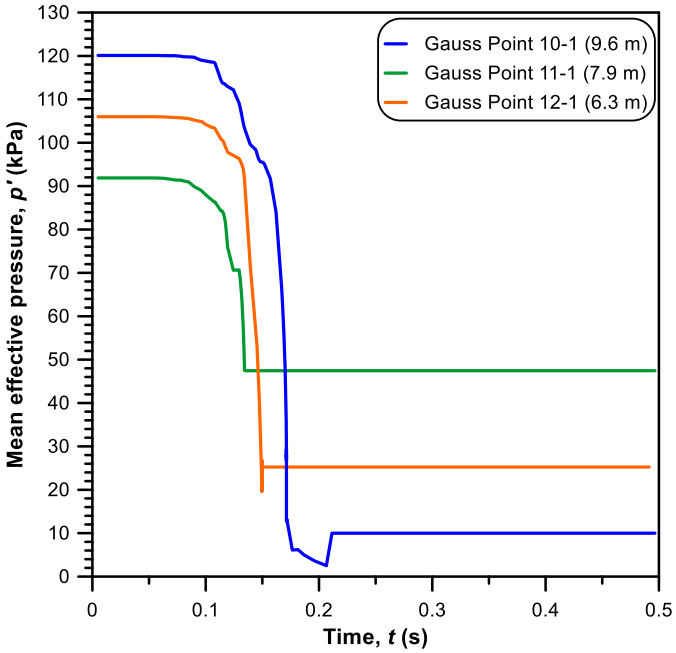

Figure 110 Mean effective pressure drop at the three elements of Unit B during the dynamic analysis of the representative column.

On the basis of the first numerical simulations at small displacement level, the outcomes demonstrate an evident reduction of the mean effective pressure in the silty-sand foundation of the riverbank under the applied seismic action.

9.7. Soil properties, conditions and numerical modelling

Since the seismic-induced evidences did not occur along the whole riverbank, this research project focuses on Section C which embodies one of the most damaged segments of the examined levee. The profile of the investigated section is depicted in Figure 112. In particular, the bedrock, composed by calcareous rocks, is assumed to be at a depth of 120 m from the river crown because of the presence of an evident discontinuity surface (Tonni et al., 2015a). The model used is a coupled formulation based on displacements and pore pressures with isoparametric mapping. Both triangles and quadrilaterals are adopted, with quadratic shape functions for the displacement field and linear shape functions for the pore pressure field. The dynamic boundary conditions in terms of acceleration and pore pressure distribution have been obtained from a couple of columns located at the extremities of the levee section far enough to reproduce free field conditions. For such purpose, each column has a width of 25 m. A unique mesh has been realized to model the whole section but the columns and the main domain have been activated at different stages.

Thus, the computational domain is composed of:

1) The left boundary column composed by a shallow layer of clay (Unit C) and the *Padano Aquifer* deposit (Unit A - top and Unit A - bottom).

2) The main domain which involves the artificial river embankment (Unit R), the natural riverbank (Unit B), the cohesive stratum (Unit C) and the *Padano Aquifer* sands (Unit A - top and Unit A - bottom).
3) The right boundary column consisting of the granular soils of Unit B, the clayey Unit C and the Padano Aquifer layer (Unit A - top and Unit A - bottom).

According to the material, element-type and association to the boundary columns or to the main domain, respectively, 14 groups are defined:

Group	*Material type*	*Element type**	*Location*
1	Unit C	*Q8P4*	Left column
2	Unit A - top	*Q8P4*	Left column
3	Unit A - bottom	*Q8P4*	Left column
4	Unit R	*Q8P4*	Main computational domain
5	Unit C	*Q8P4*	Main computational domain
6	Unit C	*T6P3*	Main computational domain
7	Unit B	*T6P3*	Main computational domain
8	Unit B	*Q8P4*	Main computational domain
9	Unit A - top	*Q8P4*	Main computational domain
10	Unit A - Bottom	*Q8P4*	Main computational domain
11	Unit B	*Q8P4*	Right column
12	Unit C	*Q8P4*	Right column
13	Unit A - top	*Q8P4*	Right column
14	Unit A - Bottom	*Q8P4*	Right column

* *Q8P4*: *Quadratic Quadrilateral element*
T6P3: Quadratic Triangular element

Table 15 Groups of the FE model.

Based on analyses carried out, most likely, Unit B is the most susceptible to liquefaction; thus, this study focuses mainly on the response of such assuming that the groundwater level corresponds to the base of the artificial river embankment. In fact, the evidences of liquefaction phenomena are most commonly observed at sites where water table is located within few meters below the ground surface. Thus, drained boundary conditions (p_w = 0) are imposed at the ground level and for the dry layer R. As regards the clayey deposit, the model parameters of unit C have

been demarked using a series of studies proposed in literature (Henkel, 1956; Balasubramanian and Chaudhry, 1978; Tonni et al., 2015a). In particular, the slope of the *CSL* (M_g), which assumes the same value of the constitutive parameter M_f because of the associative flow rule, has been determined considering an angle of shearing resistance (φ') equal to 24° according to Tonni et al. (2015a). The *Critical State Line* (*CSL*) is described by the following law in the in the *v*-log*p'* plane

$$v = 3.45 - 0.27\log(p') \quad (211)$$

and in *q*-*p'* effective stress plane

$$q = 0.70p' \quad (212)$$

The slope of the *CSL* in equations (211) and (212) has been defined by the linear regression of the results of a previous experimental database (Tonni et al., 2015a). The K_0-*Normal Compression Line* (K_0-*NCL*) has been expressed by the equation (209):

$$v = 3.70 - 0.27\log(p') \quad (213)$$

An implicit integration of the *GP* constitutive formulation within the stress framework proposed by Tonni et al. (2003) has been applied for the clayey soils of Unit C. In particular, the adopted model parameters determined by the laboratory testing programme are shown in the Table 16.

	λ_{NCL}	κ_U	Γ_{CSL}	λ
TXCID1C	0.0006	0.0002	3.45	0.27

Table 16 Model parameters and CSL features from calibration of clayey soil.

In particular, the coefficients λ_{NCL} and κ_U, which correspond to the slopes of *NCL* and of the elastic unloading path in a loading-unloading cycle, are obtained through

a linear regression of the experimental curve in the *v-p'* plane during the isotropic compression stages (Figure 111).

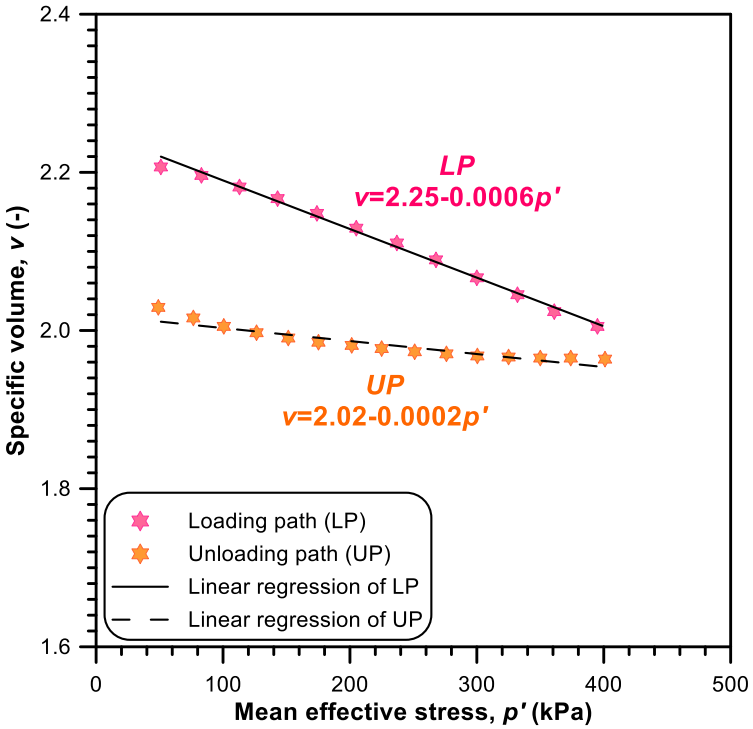

Figure 111 Loading-unloading cycle during isotropic compression stages on a representative clayey sample.

The most significant soil characteristics and material parameters are defined through the experimental testing programme including laboratory activities and site investigations (Tonni et al., 2015a), as listed in the Table 17.

Soil Unit	$K^{e}_{t,ini}$ *(kPa)*	$G_{t,ini}$ *(kPa)*	M_f *(-)*	v *(-)*	Γ_{CSL} *(-)*	M_g *(-)*	λ *(-)*
R	63000	47000	0.50	1.66	2.15	1.331	0.104
B	63000	47000	0.50	1.73	2.15	1.331	0.104
C	50000	38000	0.90	1.88	3.45	0.900	0.270
A - top	83000	63000	0.90	1.86	2.88	1.358	0.165
A - bottom	110000	84000	1.00	1.69	2.88	1.358	0.165
Additional parameters for Unit C							
β_{g0}: 0.10	H_0: 100	μ: 2	Ÿ: 0.10				

Table 17 Physical properties and model parameters for the computational domain.

In the granular soils, according to equation (103), the ratio between M_f and M_g is given by the relative density (*DR*) derived from the interpretation of a series of *CPTU*

tests (Tonni et al., 2015a). Thus, the parameter M_f is computing assuming a DR, respectively, equal to 40% for Macro-unit R & B, 65% for unit A - top and 65% for unit A - bottom.

As regards the fluid phase, the density (ρ_w = 1000 kg/m^3) and the bulk modulus (K_w =10^{10} Pa) of the water were assumed. The soil skeleton involves the definition of the density of the solid particles (ρ_s = 2600 kg/m^3), the bulk modulus of the grains (K_s = 10^{11} Pa) and the initial specific volume (v), assumed constant within the soil unit (listed in Table 17 for each layer). The permeability (k) is assumed equal to 10^{-5} m/s for the granular soils and 10^{-7} m/s for the clays, respectively. The isotropic elastic analysis includes the definition of the Young's modulus (E : from ≈ 10^7 Pa up to 10^8 Pa for the granular soils and ≈ 10^7 Pa for the clays) and the Poisson's ratio (v = 0.2). Furthermore, according to the grading characteristics, Unit A is divided into two sub-units (i.e. Unit A - top and Unit A - bottom) to distinguish the fine sands of the upper layer from the *Padano Aquifer* medium-coarse ones.

According to the study of liquefaction phenomena, the considered field variables are the displacement (u) and the pore pressure (p_w). The stress and the strain tensors are defined by four components with reference to a typical plane strain analysis. The mass matrix is diagonal, in order to improve the numerical solution in terms of stability. During the numerical computation, two checks have been performed in order to be able obtain to convergence and to have a realistic response: the first involves to avoid tensile paths, while the latter guarantees the relationship $\eta < \eta_f$. The static constraints, related to the displacement degrees of freedom (u_x,u_y), reproduce clamped conditions at the bedrock and avoid horizontal movements along the lateral boundary vertical alignments. In detail, a series of preliminary static analysis have been performed in order to obtain the initial conditions for the dynamic stages: the gravity force has been applied gradually using a ramp curve and the

self-weight of the computational domain has been evaluated. This step is necessary because the initial mean effective stress within a *GP* approach is meaningful since influences the build-up of excess pore pressure water. The integration *NR* coefficients are: $\beta_1 = 0.800$, $\beta_2 = 0.325$, $\beta_3 = 0.800$. In Figure 112, the model of the river embankment is represented.

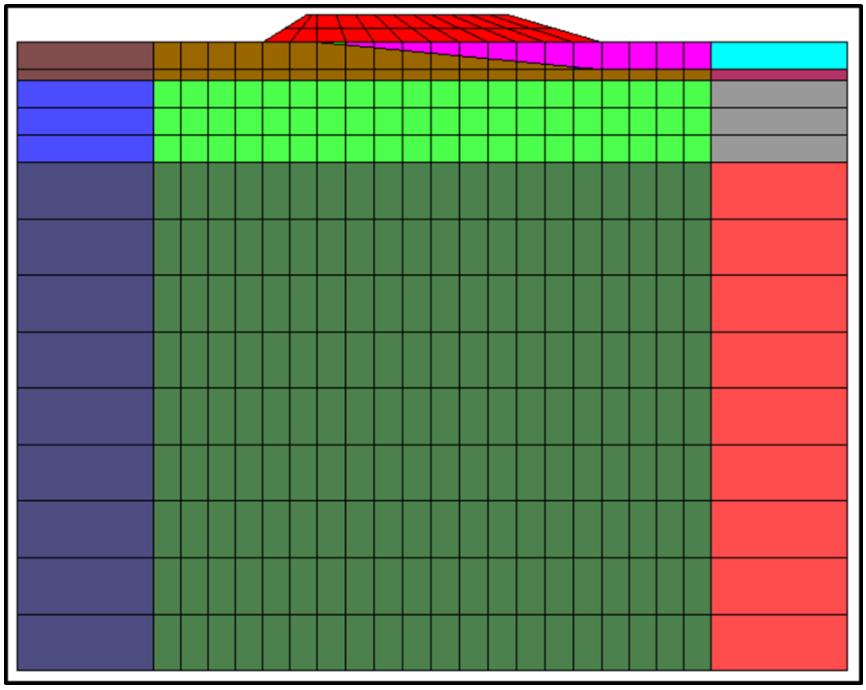

	Group 1: Q8P4; Unit C		*Group 8: Q8P4; Unit B*
	Group 2: Q8P4; Unit A - top		*Group 9: Q8P4; Unit A - top*
	Group 3: Q8P4; Unit A - bottom		*Group 10: Q8P4; Unit A - bottom*
	Group 4: Q8P4; Unit R		*Group 11: Q8P4; Unit B*
	Group 5: Q8P4; Unit C		*Group 12: Q8P4; Unit C*
	Group 6: T6P3; Unit C		*Group 13: Q8P4; Unit A - top*
	Group 7: T6P3; Unit B		*Group 14: Q8P4; Unit A - bottom*

Figure 112 FE model of Scortichino river embankment (Section C).

The first step of the numerical computation embraces the boundary columns; in particular, the sequence of numerical analyses includes:

1) A static coupled analysis in terms of displacement and pore pressure (u, p_w), in order to evaluate the initial stress distribution due to gravity. The soil behaviour is assumed isotropic elastic.
2) A static coupled analysis adopting the *GP*-based model in order to check the equilibrium of the static response. The algorithm instantly converges because the residual force vector $G(u, p_w)$ drops to zero in one iteration.
3) A coupled dynamic analysis implementing the *GP*-based model for the material characterization: the base acceleration is applied in order to obtain the dynamic boundary conditions which will be impose to the main computational domain. Both the horizontal and the vertical displacements are allowed in order to evaluate the seismic soil response; a series of links are used to maintain the condition of free-field or infinite continuum stratum.

The second step of the numerical analysis involves the study of the dynamic response of the whole levee. An appropriate computational strategy has been set: indeed, the *GP*-based model cannot be directly assigned because the non-linearities, related to the geometry and the soil material, make the convergence complicated. In particular, the slope surface as interface between Unit B and Unit C represents a meaningful critical element. According to these considerations, a series of analyses have been computed:

1) A static coupled analysis through an isotropic elastic model in order to apply gradually the gravity. At this stage, the main computational domain does not include the artificial riverbank composed of granular soils of Unit R: the excessive concentration of vertical stress in the middle of the section has been avoided. Both the Unit C and the Unit B have an initial constant specific volume equal to 1.88. These simplifications permit to obtain a preliminary vertical stress distribution of the subsoil.

2) A static coupled analysis using the Mohr-Coulomb approach as implemented by Abbo and Sloan (1993). The first step consists of the transition of the specific volume of the Unit B from 1.88 to 1.73. This strategy is adopted to limit the influence of non-symmetric conditions in the upper layers of the investigated section. The second step involves the activation of the artificial river embankment (Unit R) to reproduce the whole geometry of the main computational domain.
3) A static coupled analysis, assigning the *GP*-based constitutive equations to the layers, in order to get the initial conditions for the dynamic phase. The stress and pore pressure distributions are close enough to the numerical results obtained in the previous point in order to preserve the equilibrium: indeed, the vertical displacements (u_y) are close to zero.
4) A dynamic coupled analysis of the main computational domain within a *GP* framework. Both the base acceleration and the dynamic constraints given by the boundary columns are applied to reproduce the stress-strain response of the main computational domain under earthquake occurrence.

9.8. Results of the numerical simulations

In the present section the results of the *FE* simulations are presented. It is worth mentioning that different factors impact the numerical solutions of the model, such as the adopted mesh, the confining pressure effect and the physical properties of the deposit. Under ordinary conditions (i.e. before the seismic sequence occurrence), a soil element under the level ground is subjected to a confining stress related to the weight of the overlying strata, computed according to the experimental properties previously defined. The distribution of pore pressures derived from the static analysis within the *GP* approach has been plotted in Figure 113: it represents

the initial soil condition due to gravity. Then, the dynamic analyses have been performed for both the boundary columns and the main computational domain, focusing particular attention on the distribution of the pore pressure (u), mean effective pressure (p') and liquefaction ratio (LR). This latter term, defined by the equation (214), is equivalent to the inverse of the typical ratio of excess pore pressure to the mean effective consolidation stress (R_u), and varies in a range between 0 (i.e. complete liquefaction of the soil deposit due to the drop of the current mean effective pressure, p', up to zero) and 1 (i.e. drained condition in which $p' = p'_0$).

$$LR = \frac{p'}{p'_0} \qquad (214)$$

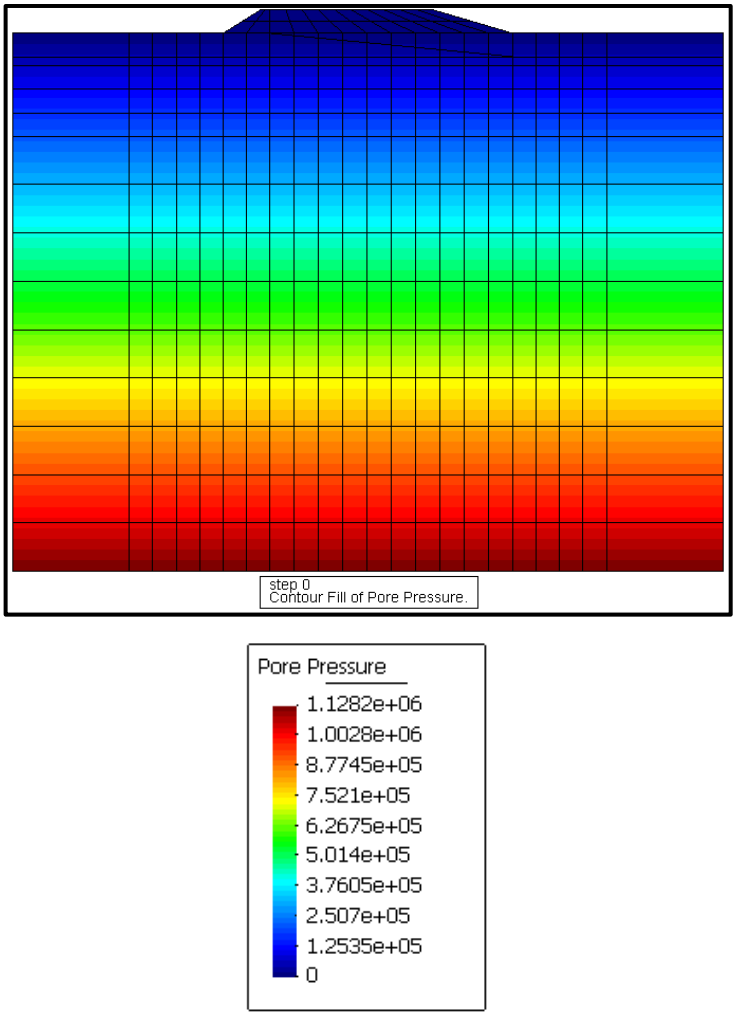

Figure 113 Hydrostatic pore pressure (in Pa) distribution of the main computational domain.

The dynamic response of the boundary columns in terms of pore pressure distribution has been depicted in Figure 114, after a shaking of few seconds.

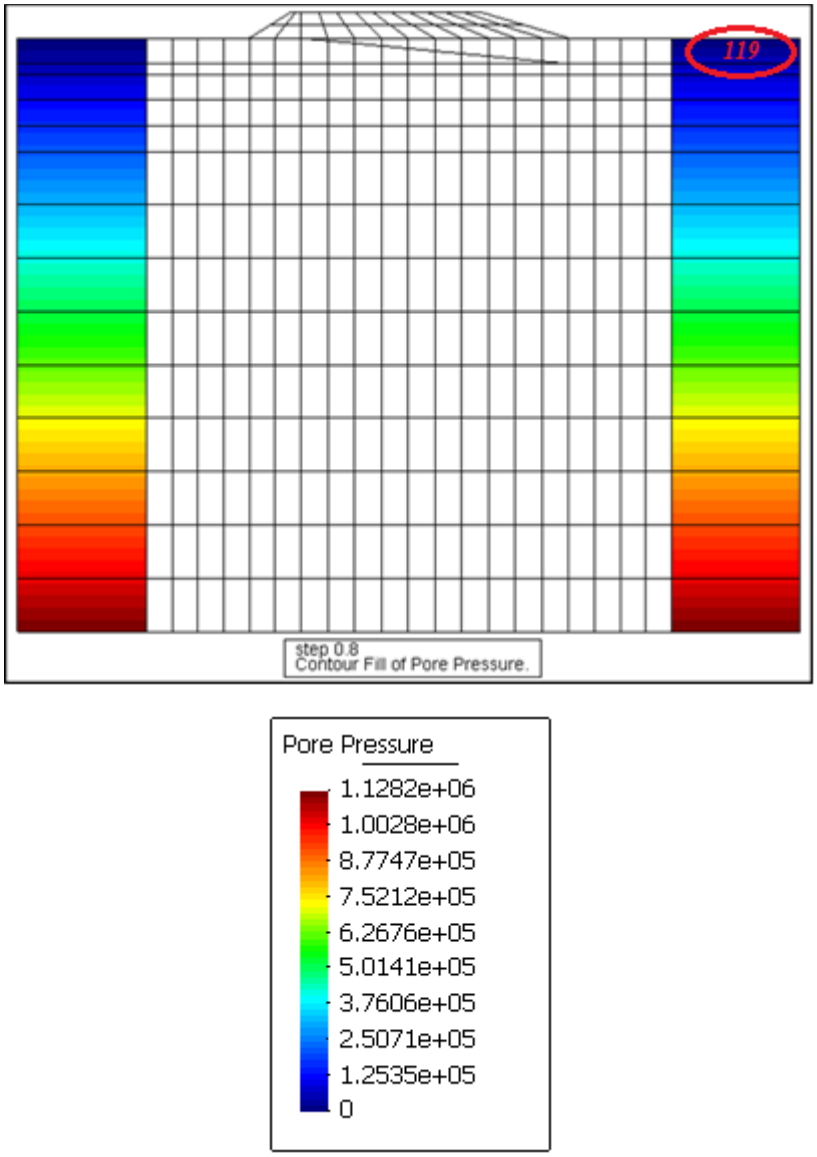

Figure 114 Distribution of pore pressure (in Pa) of the boundary columns within dynamic analysis.

It is well recognized that the basic mechanism of liquefaction within a saturated loose deposit during earthquakes is the gradual increase of excess pore pressure caused by a series of cyclic stresses induced by upward propagation of the shear waves from the underlying rock formation. Thus, the representative sample of Unit B has been analyzed during the dynamic stages of the right boundary column in

order to show the occurrence of liquefaction in the silty-sand deposit, which is especially susceptible to the phenomenon (Figure 114). In particular, the element 119 has been investigated. In the soil profile of the left column, instead, the silty-sand of Unit B does not appear because of the presence of a shallow clayey stratum. In more detail, a scheme of the element 119 is depicted in Figure 115. The nodes 621 and 662 represent the check points to assess the pore pressure evolution during the earthquake occurrence.

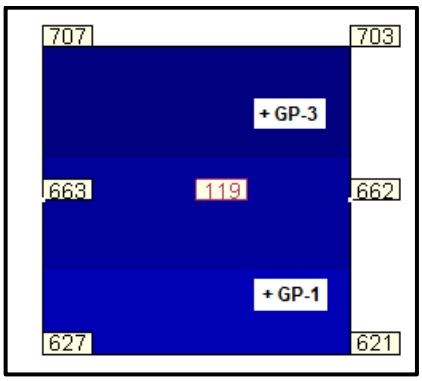

Figure 115 Element 119 of unit B in the right boundary column.

The time history of the pore pressure at small-deformation level is plotted in Figure 116.

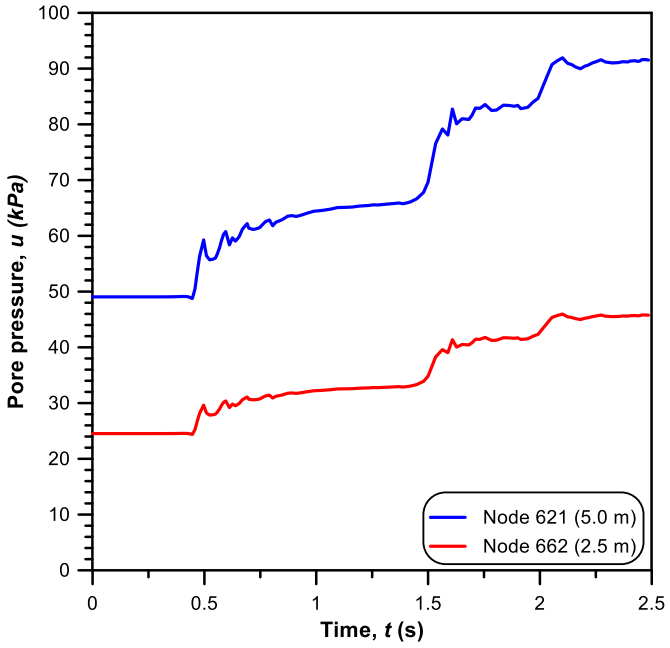

Figure 116 Pore pressure evolution at two nodes of FE model in the Unit B during the dynamic analysis of the right boundary column.

After a seismic shaking of few seconds, it is evident the accumulation of pore pressures which brings the consequent tendency of effective stresses to decrease close to zero. On the basis of the results, the dynamic analysis of the boundary column confirms the liquefaction susceptibility of the silty-sands of Unit B.

Then, the dynamic analysis of the main computational domain has been carried out.

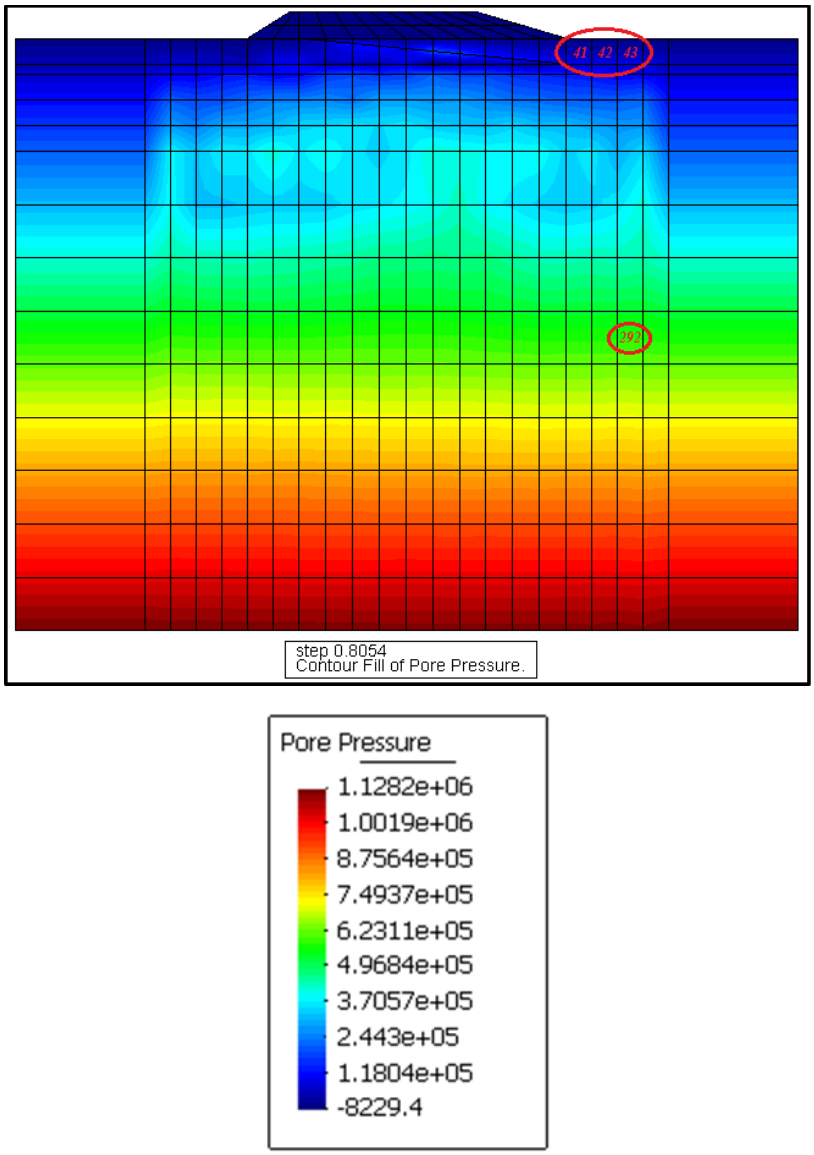

Figure 117 Representative elements and initial pore pressure distribution (in Pa) in the main computational domain.

As stated previously, some representative elements, plotted in Figure 117, have been investigated and a number of check points (i.e. nodes and *Gp*) have been considered in the analyses of the seismic loading conditions. At these nodes, the

pore pressure evolution has been assessed during the seismic shaking. Two *Gp* (i.e. the top termed *Gp-3*; the bottom called *Gp-1*) for each element are assumed as references to describe the mean effective stress drop.

Within the Unit B, which is particularly prone to liquefaction as shown by the numerical results of the boundary column, three representative elements have been evaluated: the characteristics are listed in Table 18. An element (292) of *Padano Aquifer* medium-coarse sand is also considered with the aim to compare the numerical response of granular soils characterized by different physical properties and in-situ conditions. In Table 18, the mean depth is evaluated taking as reference the base of the artificial river embankment.

Element	*Gp*	*Mean depth (m)*	*Soil Unit*
41	1 ; 3	2.50	B
42	1 ; 3	2.50	B
43	1 ; 3	2.50	B
292	1 ; 3	58.00	A - bottom

Table 18 Characteristics of the representative elements of the main computational domain.

A scheme of the three elements (41, 42, 43) is reported in Figure 118, underlying the nodes where the pore pressure is evaluated during the dynamic analysis.

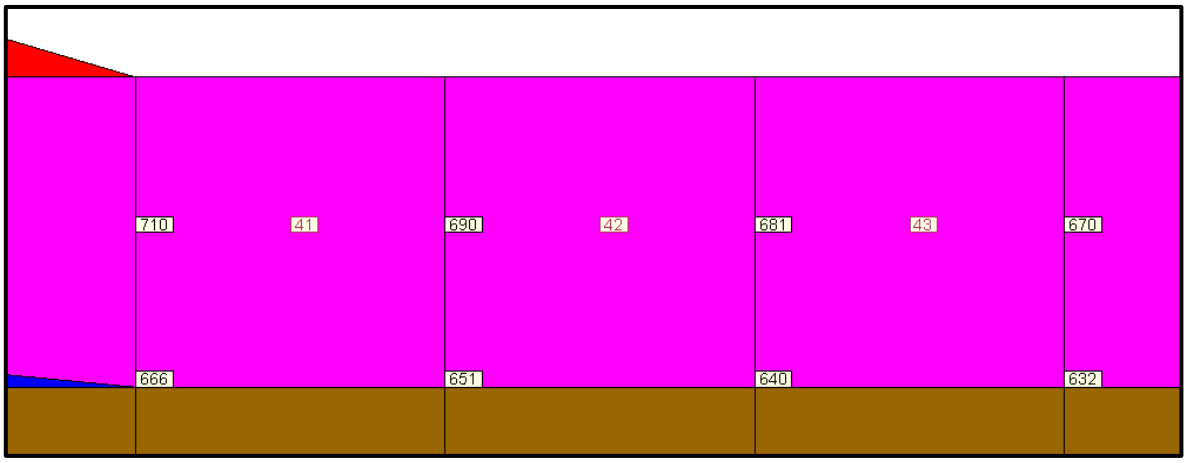

Figure 118 Elements 41, 42, 43 of unit B in the main computational domain.

The time histories of the pore pressure (*u*), mean effective pressure (*p'*) and liquefaction ratio (*LR*) for the granular soils have been analyzed considering for each element both the nodes and the *Gp*. In particular, the computed response has been reported in Figure 119, Figure 120 and Figure 121. It is well known that the non-linear site response of saturated soil deposit under dynamic conditions predominantly depends on the development of excess pore pressure. Numerical results highlight how such distribution builds up quickly and higher after few seconds of the seismic shaking: thus, the attention of the study focuses on the beginning of the dynamic stages (0.8 s) i.e. at small-deformation level. Even if the excess pore water pressure does not reach a value equal to the initial effective stress, the generation and redistribution of the stress-strain state within the soil layers can meaningfully alter the stiffness and seismic response of the granular deposit.

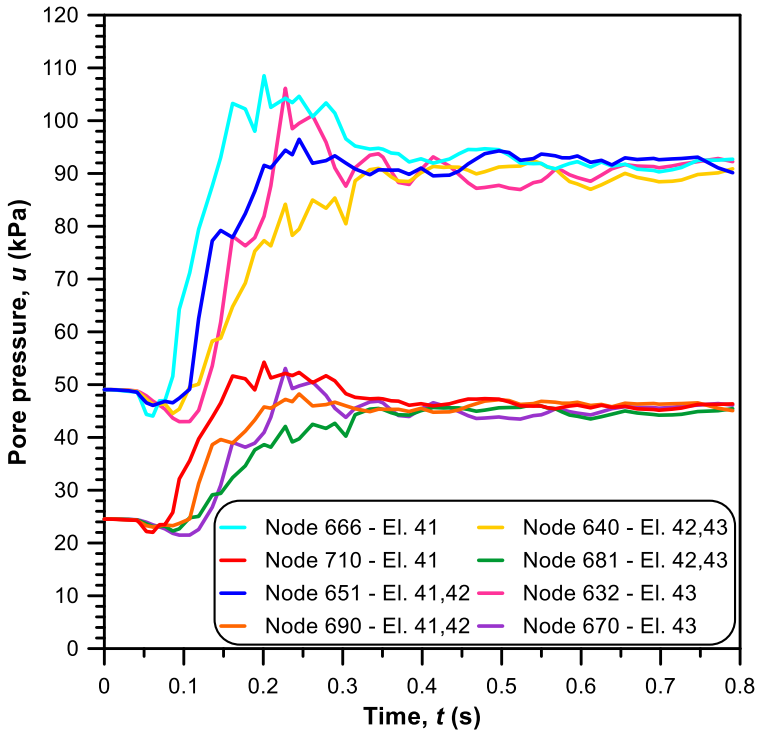

Figure 119 Time history of the pore pressure evolution for the elements 41,42 and 43 of Unit B. The deepest nodes (666, 651, 640, 632) are located at depth of 5.0 m; the depth of the shallow ones (710, 690, 681, 670) is 2.5 m.

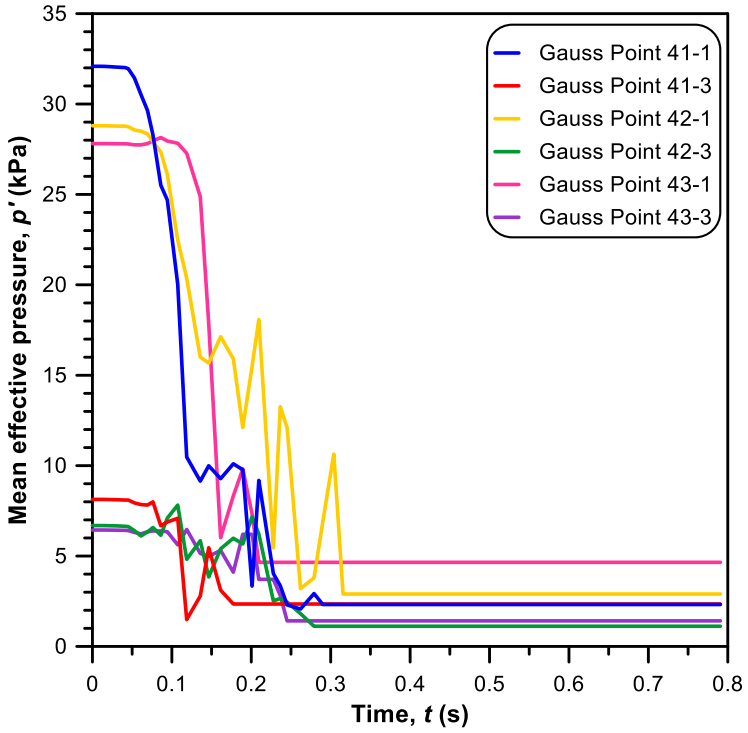

Figure 120 Time history of the mean effective stress at elements 41,42 and 43 of Unit B. The deepest Gauss Points (1) are located at depth of 3.8 m; the depth of the shallow ones (3) is 1.3 m.

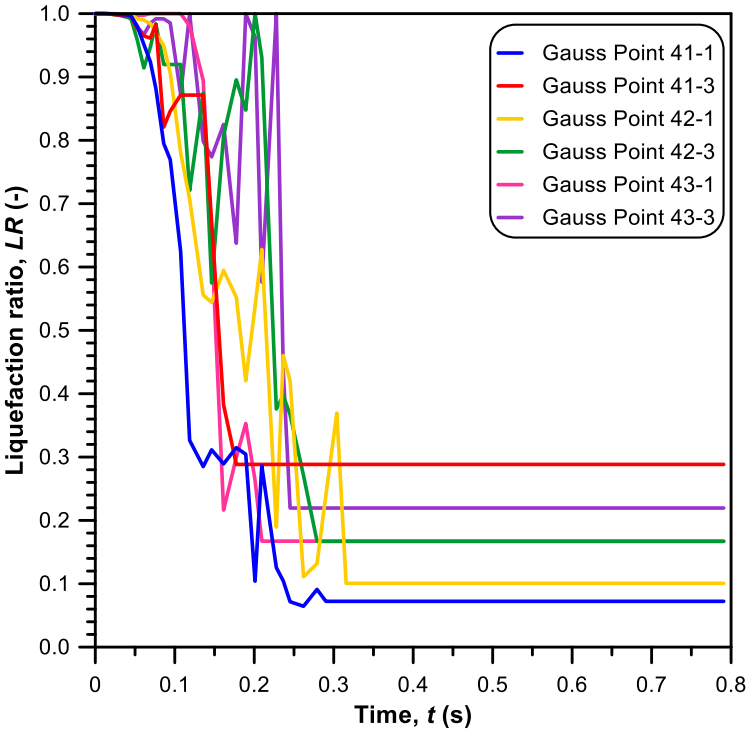

Figure 121 Time history of the LR at elements 41,42 and 43 of Unit B. The deepest Gauss Points (1) are located at depth of 3.8 m; the depth of the shallow ones (3) is 1.3 m.

The mean effective pressure decreases as a consequence of excess pore pressure development; similarly, the liquefaction ratio (*LR)* drops close to zero. In general, it is possible to note that the deepest *Gp*, *Gp-1*, reaches lower values of *LR* than the shallow one, *Gp-3*. Since this latter is closer to the ground surface a faster drainage of the excess pore pressure occurs reducing liquefaction evidences. In addition, it is worth noting that the pronounced oscillations which appear in the numerical results of the proposed *GP*-based model, most likely, are related to the introduction of an exponential formulation in the main governing laws (e.g. dilatancy and plastic modulus laws) in conjunction with the explicit integration scheme of the constitutive equations. Nevertheless, the prediction trend of the simulations is satisfactory.

The horizontal displacement time history has been depicted in Figure 122, where the moderate amount of computed displacements reproduces rather well the actual evolution.

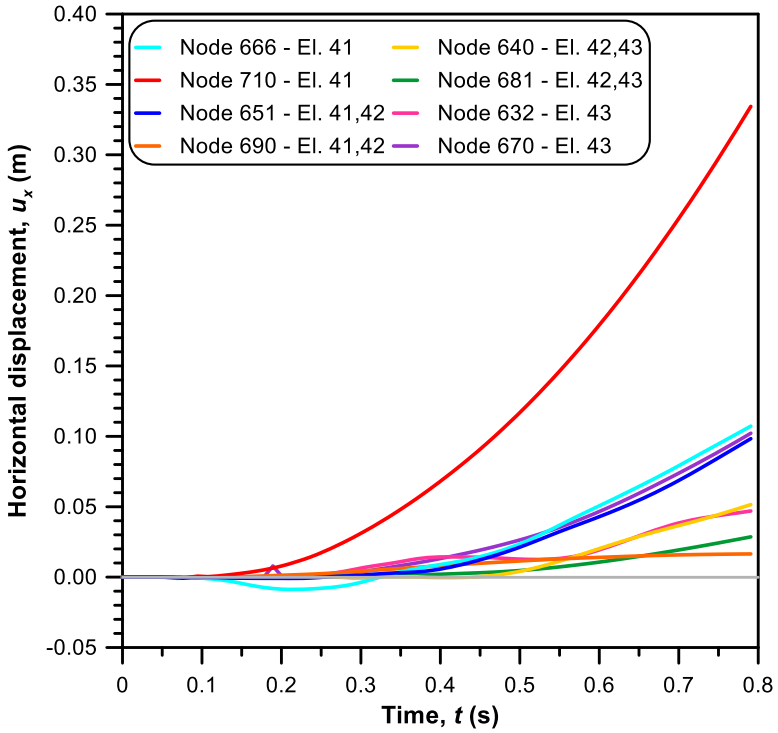

Figure 122 Time history of the horizontal displacements for the elements 41,42 and 43 of Unit B. The deepest nodes (666, 651, 640, 632) are located at depth of 5.0 m; the depth of the shallow ones (710, 690, 681, 670) is 2.5 m.

The effect of the intrinsic physical properties and in-situ conditions has been evaluated comparing in terms of *p'* and *LR* the response of two elements (43, 292) located along the same vertical but belonged to different units (i.e. Unit B and Unit A – bottom, respectively). Since Unit A is situated at greater depth and is composed mainly by medium-coarse sands i.e. the confining pressure and the relative density are greater than those of Unit B. Then, the liquefaction ratio and the mean effective pressure decrease slower than within the unit B, without meaningful seismic-induced consequences. This tendency is demonstrated in Figure 123 and Figure 124. In more detail, the plots show that in element 292 (i.e. *Padano Aquifer* sand), the mean effective pressures do not drop to zero; whereas it happens in the element 43 (i.e. Unit B). Furthermore, the effects of the ground motion have increased towards the ground surface due to the young age of the soil strata and the depositional environment. In fact, the soil amplification correlated to earthquake is a peculiarity of the 2012 Emilia seismic events.

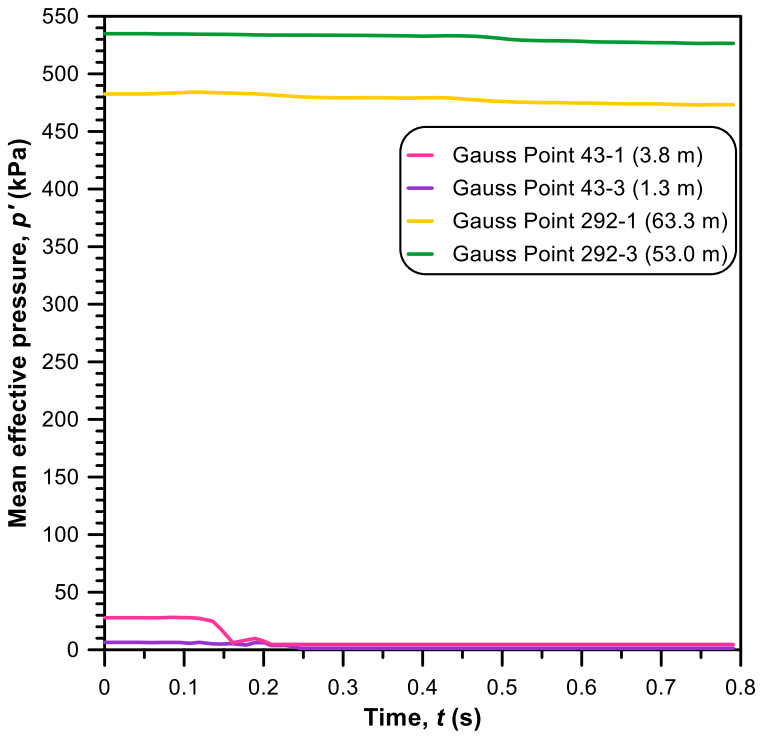

Figure 123 Time history of the mean effective pressure within elements 43 and 292.

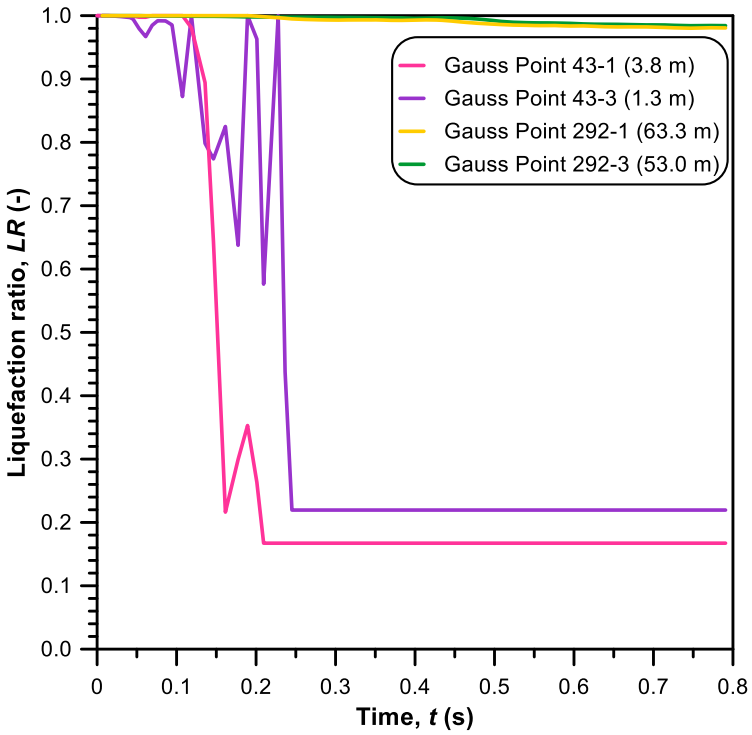

Figure 124 Time history of the LR within elements 43 and 292.

Finally, the deformed mesh with the horizontal displacement vectors is depicted in Figure 125.

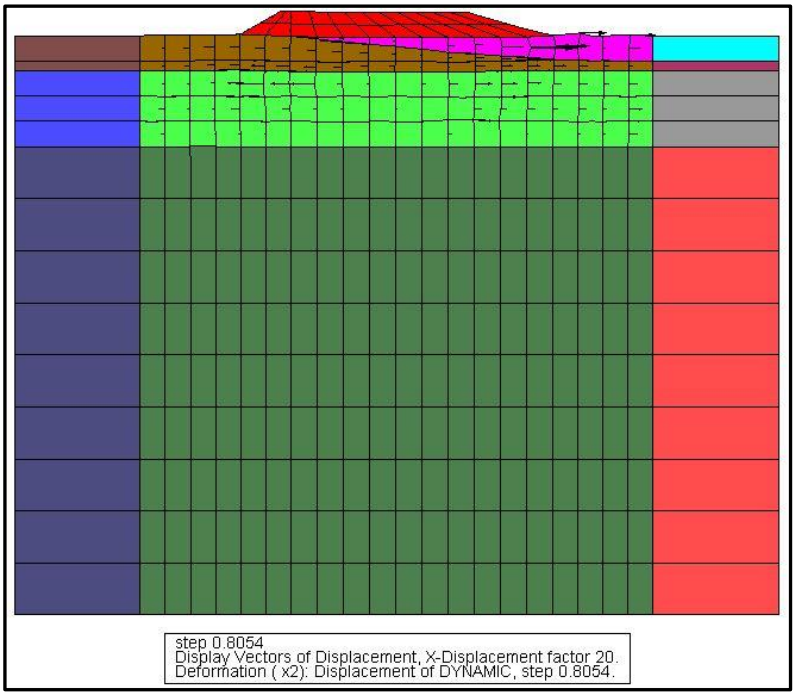

Figure 125 Deformed mesh with displacement vectors.

The shear failure consists of a diffuse mechanism: the surface of the layer of Unit B moves toward the river bed and quickly liquefies. The most significant horizontal displacement (mean value ≈ 10 cm) occurs in such granular deposit and might have triggered the observed system of cracks in the investigated area. The main cause of increasing the movements is identified through the development of plastic strains. In fact, during the first seconds of earthquake shaking, the deformations of the cross-section become enlarged continuously due to the redistribution of the pore pressure. Such high plastic strains and permanent horizontal deformations concentrated in the silty-sand unit decrease towards the bedrock defining an up-bottom trend.

In the light of the computed outcomes, it is possible to postulate that the numerical results explain reasonably well the observations which are made in the previous sections. In fact, the first liquefaction analyses seems to justify the system of cracks and ground deformations of the reference case of study. Anyway, it is important to note that a series of aspects introduces different uncertainties and it is expected that numerical adjustments would improve the results obtained within the *FE* framework in terms of convergence and stability, e.g. the introduction of more suitable input ground motion. Furthermore, the influence of the mesh and soil parameters has to be analysed in more detail.

10. Conclusion and final remarks

This research project presented in this PhD thesis deals with a modified *GP*-based model to describe the stress-strain behaviour of granular soils of loose and dense deposits under different loading and drainage conditions, thus including liquefaction phenomenon occurence. In particular, the proposed constitutive formulation was used to interpretate the response of the sediments of a riverbank and its subsoil struck by the 2012 Emilia earthquake located in Scortichino (Bondeno), known as *Canale Diversivo di Burana*. The seismic sequence, with the epicentres in the Eastern part of the Po River Plain, determined human losses, meaningfull damages to buildings and infrastructures, and seismic soil evidences at ground level i.e. lateral spreading displacements, abundant ejections of sand and water from cracks and sand boils.

A detailed study of physical properties and mechanical response together with a proper mathematical modelling of the soil behaviour was applied to understand the mechanisms which caused these destructive effects. Hence, an experimental programme, performed in the laboratories of *DICAM*, allowed an adeguate geotechnical characterization of the available soil samples obtained from the most damaged sections of the site at different depths. Such activity was devised as supplementary testing programme following the investigation campaign carried out in the same area shortly after the 2012 earthquake, which collects, most likely, a number of triaxial undrained tests. The interpretation of the experimental studies allowed to detect different soil units along the stratigraphy profile of the levee: an upper silty-sand substrate, termed Macro-unit R & B, constituting the artificial riverbank and its foundation; a thin layer of clays/silty-clays; the *Padano Aquifer* deposit, characterized by sands from fine up to medium-coarse grading with low *FC*. The mineralogical composition of both these granular units, determined through a

computer-controlled *X*-ray diffractometer, involves as main components quartz and albite in different proportions. The static characterization of the undisturbed and remoulded samples included 13 standard triaxial tests, in either drained or undrained conditions, and 9 standard floating-ring cell and K_0-cell oedometer tests. In particular, the existence of a unique *NCL* within the v-logσ'_v plane has been confirmed by the convergent compression curves of *Padano Aquifer* sands; whereas, the results of the K_0-oedometer tests on Macro-unit R & B converge at the pressure level of approximatively 1 MPa. It is important to note that this latter layer is intrinsic heterogeneous, but does not represent an example of *transitional soil*. In addition, no meaningful particle breakage was observed from the tests conducted. Particular attention was paid to the isotropic compression phase, with multiple unload-reload stages, in view of the validation of the adopted constitutive model. With respect to the drained shearing conditions, the *Padano Aquifer* sand presents generally a contractive response, except for the samples consolidated at the lowest confining pressure. The same trend could be recognized in the Macro-unit R & B, where just the undisturbed samples show moderate dilation curves. The stress-strain behaviour is typically characterized by strain-hardening responses and solely a few tests exhibit a modest peak stress ratio.

The mechanical response of the available database was interpreted combining the *GP* formulation, the *CS* theory and the state parameter concept (ψ). In fact, the numerical procedure was applied to a specific *GP* model for sandy soil proposed originally by Pastor et al. (1990), in which no yield surface nor plastic potential are explicitly defined. Some modifications were introduced in such approach in order to better simulate the stress-strain response over a wide range of stresses and densities, i.e. stress-dilatancy law and plastic modulus formulation, embedding the state parameter dependence in the constitutive equations. In greater detail, the

revised equation of stress-dilatancy is based on the study proposed by Li and Dafalias (2000); whereas, the relationship of the loading plastic modulus has the advantage of introducing within a *GP* framework a deep study on the isotropic compression behaviour of sands, including an accurate simplification of the method originally proposed by Been and Jefferies (2000). Indeed, the relationship between the plastic modulus during isotropic compression (H_0) and the tangent elastic bulk modulus (K_t^e) are expressed as a function of the sole state parameter, thus disregarding the stress factor formerly presented in the formulation. Within the rather limited interval of confining pressure analysed, far enough from grain crushing occurrence, this contribution seems to have not meaningful influence on the soil behaviour. The experimental work has been useful for the development of an adeguate calibration procedure in order to define the 12 indipendent model parameters. For this aim, a *MATLAB* numerical routine with a single node integration scheme was developed to compare experimental and model response in triaxial conditions, considering separately isotropic compression and shearing phase. Into the light of the computed results, the numerical predictions match fairly well the experimental plots: both the stress-strain curve and the volumetric behaviour of the performed drained tests are well fitted. In particular, the use of a state dependent model results in reliable predictions of the silty-sand response through a unique set of constitutive parameters over a wide range of confining pressures and relative densities. The predictive capability of the constitutive model and the effectiveness of the calibration procedure attained by the drained database were verified by reproducing a number of undrained triaxial tests with the objective of interpreting the response of the investigated materials within an overall pattern: the experimental behaviour under undrained shearing seems to be rather well represented in terms of effective stress and excess pore pressure, with a few, generally minor

improvements into the set of model parameters. Hence, the proposed formulation, although rather simple and susceptible of further developments, allows to capture correctly the global behaviour of examined granular soils.

Based on the analyses carried out, most likely, the sand boils and the large longitudinally-oriented ground cracks on the bank crown, due to the two main events of the 2012 Emilia earthquake, could be caused by liquefaction phenomena and lateral spreading, developed principally in the investigated deposits. In order to support the issues previously outlined, a geotechnical model of the riverbank has been set using the research code *GeHoMADRID*. The *FE* analyses were performed using an algorithm for the explicit integration of the constitutive equations implemented in *FORTRAN90*. As regards computational features, the discretization in space was realized by the Finite Element method known as *Galerkin residual method* and in time by the *Generalized Newmark method*. The non-linear system of equations was solved using the iterative procedure of *Newton-Raphson*. The previous experimental database was been adopted to determine the set of soil parameters of each unit. A number of preliminary tests of the solution strategy were achieved at a single-element level. In particular, quasi-static analyses were performed on a quadrilateral element, with quadratic shape functions for the displacement field and linear shape functions for the pore pressure distribution, with the aim to validate the constitutive model. Looking at the numerical results obtained from the implementation of the constitutive equations within *MATLAB* and *GeHoMADRID*, it is possible to postulate that the simulations at a single-element level achieved by the *FE* code are convergent and practically identical to the predicted *MATLAB* curves in monotonic shearing steps. As regards the whole riverbank, the sequence of numerical analyses included: first, a static coupled computation, in terms of displacement and pore pressure, in order to evaluate the

initial stress distribution due to gravity; later, a dynamic coupled analysis which designates the stress-strain response of the levee under a recorded seismic signal selected from the *Italian Accelerometric Archive* database. The dynamic boundary constraints were obtained from a couple of columns located at the estremities of the main computational domain far enough to impose free field conditions. It is clear that the dynamic analysis of a representative section of the riverbank studied by means of an advanced constitutive formulation in conjuction with a *FE* code is a complex as well as interesting task, with few previous studies in literature. Nevertheless, first simulations show as the numerical model of the riverbank coupled with a *GP* approach proves to be a powerful tool in order to reproduce the seismic-induced phenomena within the granular deposits at small-deformation level. In fact, after a seismic shaking of few seconds, the accumulation of pore pressures clarifies the consequent tendency of effective stresses to decrease close to zero in the shallow layers of Macro-unit R & B, which confirms its liquefaction susceptibility. From these considerations, the preliminary liquefaction analysis gives the idea to justify the system of cracks and ground deformations of the Italian case-study here presented. It is worth to observe that additional upgrades are undoubtly needed in order to improve the numerical response in terms of convergence and stability.

10.1. Suggestions and future developments

This research work can be considered a useful starting point for the modelling of the granular soil behaviour within an advanced constitutive framework. The performed study shows the difficulties that might be faced dealing with sands and silty-sands, susceptible to liquefaction phenomena. An additional investigation programme could be an interesting tool to complete the picture of the behaviour of the case-study under undrained conditions, including seismic piezocone and laboratory

dynamic tests. Further *FE* simulations are required to improve the analyses carried out to reproduce the site response. Indeed, other solution strategies could be applied to reach better simulations concerning soil behaviour with the aim of removing undesirable oscillations and increasing the run length in numerical results. Additional refinements could be realized regarding the reference input motion, which is affected by several uncertainties due the lack of seismic records of the 2012 Emilia-Romagna main shock. As regards cyclic behaviour, in spite of the fairly well agreement between the measured and numerical curves of the experimental testing programme, a parameter optimization technique should be carried out to find the most desired values of constitutive parameters in order to reproduce accurately the nonlinear cyclic response of liquefiable materials.

Over the last years, several geotechnical solutions have been illustrated to avoid liquefaction occurrence i.e. vertical or horizontal drains composed by granular materials able to dissipate instantaneously the excess pore pressure. Thus, numerical simulations of the investigated case study introducing a series of vertical drains such as stone columns in the subsoil model may be an interesting future goal in order to improve engineering practice, evading unnecessarily overconservative design.

References

Abbo A.J. and Sloan W., 1993, A smooth hyperbolic approximation to the Mohr-Coulomb yield criterion, Computers and Structures, 54 (3), pp. 427-441

Alarcon-Guzman A., Leonards G.A. and Chameau J.L., 1988, Undrained monotonic and cyclic strength of sands, Journal of Geotechnical Engineering, ASCE, 114 (10), pp. 1089-1108

Alessio G., Alfonsi L., Brunori C.A., Burrato P., Casula G., Cinti F.R., Civico R., Colini L., Cucci L., De Martini P.M., Falcucci E., Galadini F., Gaudiosi G., Gori S., Mariucci M.T., Montone P., Moro M., Nappi R., Nardi A., Nave R., Pantosti D., Patera A., Pesci A., Pezzo G., Pignone M., Pinzi S., Pucci S., Salvi S., Tolomei C., Vannoli P., Venuti A. and Villani F., 2013, Liquefaction phenomena associated with the Emilia earthquake sequence of May-June 2012 (Northern Italy), Natural Hazards and Earth System Sciences, 13, pp. 935-47

Altuhafi F. and Coop M.R., 2011, Changes to particle characteristics associated with the compression of sands, Géotechnique, 61 (6), pp. 459-471

Altuhafi F., O' Sullivan C. and Cavarretta I., 2013, Analysis of an Image-Based Method to Quantify the Size and Shape of Sand Particles, Journal of Geotechnical and Geoenvironmental Engineering, 139 (8), 1290-1307

Amini F. and Qi G.Z., 2000, Liquefaction Testing of Stratified Silty Sands, Journal of Geotechnical and Geoenvironmental Engineering, 126 (3), pp. 208-217

Amorosi A., Rollo F. and Boldini D., 2018, A modified bounding surface plasticity model for sand, 9th European Conference on Numerical Methods in Geotechnical Engineering At Porto, pp. 8

Andrus R.D. and Stokoe K.H.II., 2000, Liquefaction resistance of soils from shear-wave velocity, Journal of Geotechnical and Geoenvironmental Engineering,126 (11), pp. 1015-1025

Balasubramanian A.S. and Chaudhry A.R., 1978, Deformation and Strength Characteristics of Soft Bangkok Clay, Journal of Geotechnical Engineering, ASCE, 104 (9), pp. 1153-1167

Bandini V. and Coop M.R., 2011, The influence of particle breakage on the location of the critical state line of sands, Soils and Foundations, 51 (4), pp. 591-600

Bardet J.P., 2003, Advances in analysis of soil liquefaction during earthquake, International Handbook of Earthquake and Engineering Seismology

Baudet B. and Stallebrass S., 2004, A constitutive model for structured clays, Géotechnique, 54 (4), pp. 269-278

Been K. and Jefferies M., 1985, A state parameter for sand, Géotechnique, 35 (2), pp. 99-112

Been K., Jefferies M.G. and Hachey J.E., 1991, The critical state of sands, Géotechnique, 41 (3), pp. 365-381

Benahmed N., Nguyen T., Hicher P. and Nicolas M., 2015, An experimental investigation into the effects of low plastic fines content on the behaviour of sand/silt mixtures, European Journal of Environmental and Civil Engineering, 19, pp. 109-128

Bindi D., Pacor F., Luzi L., Puglia R., Massa M., Ameri G. and Paolucci R., 2011, Ground motion prediction equations derived from the Italian strong motion database, Bulletin Earthquake Engineering, 9 (6), pp. 1899-1920

Bobei D.C., Lo S.R., Wanatowski D., Gnanendran C.T. and Rahman M.M., 2009, A modified state parameter for characterizing static liquefaction of sand with fines, Canadian Geotechnical Journal, 46 (3), pp. 281-295

Boulanger R.W., Meyers M.W., Mejia L.H. and Idriss I.M., 1998, Behaviour of a fine-grained soil during the Loma Prieta earthquake, Canadian Geotechnical Journal, 35 (1), pp. 146-158

Boulanger R.W. and Idriss I.M., 2004, Evaluating the potential for liquefaction or cyclic failure of silts and clays, Rep. No. UCD/CGM- 04/01, Center for Geotechnical Modeling, Dept. of Civil and Environmental Engineering, Univ. of California, Davis, California

Boulanger R.W. and Idriss I.M., 2006, Liquefaction susceptibility criteria for silts and clays, Journal of Geotechnical and Geoenvironmental Engineering, 132 (11), pp.1413-1426

Boulanger R.W., Moug D.M., Munter S.K., Price A.B. and De Jong J.T., 2016, Evaluating liquefaction and lateral spreading in interbedded sand, silt and clay

deposits using the cone penetrometer, Australian Geomechanics Journal, 51 (4), pp. 109-128

Bray J.D., Sancio R.B., Riemer M.F. and Durgunoglu T., 2004, Liquefaction susceptibility of fine-grained soils, 11th Int. Conf. on Soil Dynamics and Earthquake Engineering, Berkely, pp. 655-662

Carraro J.A.H., Murthy T.G., Loukidis D., Salgado R. and Prezzi M., 2007, Undrained monotonic response of clean and silty sands, Géotechnique, 57 (3), pp. 273-288

Carrera A., Coop M.R. and Lancellotta R., 2011, Influence of grading on the mechanical behaviour of Stava tailings, Géotechnique, 61 (11), pp. 935-946

Casagrande A., 1976, Liquefaction and cyclic deformation of sands: a critical review, Harvard soil mechanics series 88, Harvard University, Cambridge, Massachusetts, 27 pp.

Castro G., 1969, Liquefaction of sands, Harvard soil mechanics series 87, Harvard University, Cambridge, Massachusetts

Chan C.K., 1985, Instruction Manual, CKC E/P Cyclic Loading Triaxial System Users Manual, Soil Engineering Equipment Company, San Francisco, CA

Chang W.J. and Hong M.L., 2008, Effects of clay content on liquefaction characteristics of gap graded clayey sands, Soils and Foundations, 48 (1), pp. 101-114

Chiaradonna A., Tropeano G., d'Onofrio A. and Silvestri F., 2018, Interpreting the deformation phenomena of a levee damaged during the 2012 Emilia earthquake, Soil Dynamics and Earthquake Engineering, https://doi.org/10.1016/j.soildyn.2018.04.039

Chiaro G., Indraratna B. and Tassaloti S.M.A., 2015, Predicting the behaviour of coal wash and steel slag mixtures under triaxial conditions, Canadian Geotechnical Journal, 52 (3), pp. 367-373

Cola S. and Tonni L., 2006, Adapting a Generalized Plasticity Model to Reproduce the Stress-Strain Response of Silty Soils Forming the Venice Lagoon Basin, Soil Stress-Strain Behaviour: Measurement, Modeling and Analysis Geotechnical Symposium in Roma

Cola S. and Tonni L., 2007, Adapting a Generalized Plasticity model to reproduce the stress-strain response of silty soils forming the Venice Lagoon Basin, Soil Stress-Strain Behaviour: Measurement, Modeling and Analysis, Series: Solid Mechanics and Its Applications, 146, NY: Springer, pp. 743-756

Cola S., Tonni L. and Pastor M., 2008, Mathematical modelling of Venetian sediment behaviour using Generalized Plasticity, In: Proceedings of the 12th International Conference on Computer Methods and Advances in Geomechanics (IACMAG), Goa, 2, Red Hook, NY: Curran Associates Inc., pp. 838-846

Coop M.R. and Lee I.K., 1993, The behavior of granular soils at elevated stresses, In: Proceedings of Wroth memorial symposium, Predictive soil mechanics, Thomas Telford, London, pp. 186-198

Coop M.R., Sorensen K.K., Bodas Freitas T. and Georgoutsos G., 2004, Particle breakage during shearing of a carbonate sand, Géotechnique, 54 (3), pp. 157-163

Cotecchia F. and Chandler R.J., 2000, A general framework for the mechanical behaviour of clays, Géotechnique, 50 (4), pp. 431-447

Crespellani T., Facciorusso J., Ghinelli A., Madiai C., Renzi S. and Vannucchi G., 2012, Rapporto preliminare sui diffusi fenomeni di liquefazione verificatisi durante il terremoto in pianura padana emiliana del maggio 2012. 31 maggio 2012, (Università degli Studi di Firenze, Dipartimento di Ingegneria Civile e Ambientale – sezione geotecnica), Technical report

Cubrinovski M. and Ishihara K., 2000, Flow potential of sandy soils with different grain compositions, Soils and Foundations, 40 (4), pp. 103-119

Cubrinovski M. and Rees S., 2008, Effects of Fines on Undrained Behaviour of Sands, Geotechnical Earthquake Engineering and Soil Dynamics, pp. 1-11

Cuccovillo T. and Coop M.R., 1999, On the mechanics of structured sands, Géotechnique, 49 (6), pp. 741-760

Cuomo S., Manzanal D., Moscariello M., Pastor M. and Foresta V., 2015, Application of a generalized plasticity constitutive model to a saturated pyroclastic soil of Southern Italy, In D. Manzanal and A.O. Sfriso (Eds.), IOS Press., pp. 1215-1222

Dafalias Y.F., 1986, An anisotropic critical state soil plasticity model, Mech. Res. Commun., 13 (6), pp. 341-347

Di Lernia A., Amorosi A. and Boldini D., 2014, Analisi critica di un modello costitutivo per la risposta ciclica dei terreni, Incontro Annuale Ricercatori di Geotecnica (IARG), Chieti e Pescara, pp. 6

Dyvik R., Lacasse S. and Martin R., 1985, Coefficient of lateral stress from oedometer cell, Proc. 11th International Conference on Soil Mechanics and Foundation Engineering, San Francisco, 2, pp. 1003-1006

Elgamal A., Yang Z., Parra E. and Ragheb A., 2003, A cyclic plasticity constitutive model for cohesionless soils, International Journal of Plasticity, 19, pp. 883-905

Erten D. and Maher M.H., 1995, Cyclic undrained behavior of silty sand, Soil Dynamics and Earthquake Engineering, 14 (2), pp. 115-123

Evangelista L., del Gaudio S., Smerzini C., d'Onofrio A., Festa G., Iervolino I., Landolfi L., Paolucci R., Santo A. and Silvestri F., 2017, Physics-based seismic input for engineering applications: a case study in the Aterno river valley Central Italy, Bulletin Earthquake Engineering, 15 (7), pp. 2645-2671

Facciorusso J., Madiai C. and Vannucchi G., 2016, The 2012 Emilia earthquake (Italy): Geotechnical characterization and ground response analyses of the paleo-Reno river levees, Soil Dynamics and Earthquake Engineering, 86, pp. 71-88

Fernández Merodo J.A., Pastor M., Mira P., Tonni L., Herreros M.I., Gonzalez E. and Tamagnini R., 2004, Modelling of diffuse failure mechanisms of catastrophic landslides, Computer Methods in Applied Mechanics and Engineering, 193 (27-29), pp. 2911-2939

Fioravante V., Giretti D., Abate G., Aversa S., Boldini D., Capilleri P. P., Cavallaro A., Chamlagain D., Crespellani T., Dezi F., Facciorusso J., Ghinelli A., Grasso S., Lanzo G., Madiai C., Massimino M.R., Maugeri M., Pagliaroli A., Ranieri C., Tropeano G., Santucci De Magistris F., Sica S., Silvestri F. and Vannucchi G., 2013, Earthquake geotechnical engineering aspects of the 2012 Emilia-Romagna earthquake (Italy), In: Proceedings of the Seventh International Conference on Case Histories in Geotechnical Engineering, pp. 1-34

Frost J.D. and Park J.Y., 2003, A critical assessment of the moist tamping technique, Geotechnical Testing Journal, ASTM, 26 (1), pp. 57-70

Galli P., 2000, New empirical relationships between magnitude and distance for liquefaction, Tectonophysics, 324 (3), pp. 169-187

Gajo A. and Muir Wood D, 1999, Severn-Trent sand: a kinematic-hardening constitutive model: the q-p formulation, Géotechnique, 49 (5), pp. 595-614

García Martínez M.F., Tonni L., Gottardi G. and Rocchi I., 2016, Influence of penetration rate on CPTU measurements in saturated silty soils, In: Proceedings of the 5th International Conference on Geotechnical and Geophysical Site Characterisation (ISC'5), Gold Coast (AUS), Vol 1, Sidney: Australian Geomechanics Society, pp. 473-478

Ghafghazi M., Shuttle D.A. and De Jong J.T., 2014, Particle breakage and the critical state of sand, Soils and Foundations, 54 (3), pp. 451-61

Gilbert P.A. and Marcuson W.F, 1988, Density Variation in Specimens Subjected to Cyclic and Monotonic Loads, Journal of Geotechnical Engineering, ASCE, 114 (1), pp. 1-20

Gottardi G., Amoroso S., Bardotti R., Bonzi L., Chiaradonna A., d'Onofrio A., Fioravante V., Ghinelli A., Giretti D., Lanzo G., Madiai C., Marchi M., Martelli L., Monaco P., Porcino D., Razzano R., Rosselli S., Severi P., Silvestri F., Simeoni L., Tonni L. and Vannucchi G., 2014, Analisi di stabilità di un argine danneggiato dalla sequenza sismica emiliana del 2012, Atti del XXV Convegno Nazionale di Geotecnica, Baveno

Hazirbaba K. and Rathje E., 2009, Pore pressure generation of silty sands due to induced cyclic shear strains, Journal of Geotechnical and Geoenvironmental Engineering, ASCE, 135 (12), pp. 1892-1905

Head K.H., 1986, Manual of laboratory testing, Vol. 3

Henkel D.J., 1956, The effect of overconsolidation on the behaviour of clays during shear, Géotechnique, VI, pp. 139-150

Høeg K., Dyvik R. and Sandbækken G., 2000, Strength of undisturbed versus reconstituted silt and silty sand specimens, Journal of Geotechnical and Geoenvironmental Engineering, ASCE, 126 (7), pp. 606-617

Hyodo M., Hyde A.F.L. and Aramaki N., 1998, Liquefaction of crush able soils, Géotechnique, 48 (4), pp. 527-43

Idriss I.M., Dobry R. and Singh R.D., 1978, Nonlinear behavior of soft clays during cyclic loading, Journal of Geotechnical Engineering, ASCE, 104 (12), pp. 1427-1447

Idriss I.M., Moriwaki Y., Wright S.G., Doyle E.H. and Ladd R.S., 1980, Behavior of normally consolidated clay under simulated earthquake and oceanwave loading conditions, Proc. Int. Syrup. on Soils under Cyclic and Transient Loading, 1, pp. 437-445

Idriss I. M. and Boulanger R.W., 2008, Soil liquefaction during earthquakes, Monograph, Earthquake Engineering Research Institute, Oakland, California, pp.1-181

Ishihara K., 1985, Stability of Natural Deposits During Earthquakes Proceedings of the 11th International Conference on Soil Mechanics and Foundation Engineering, San Francisco, 1, pp. 321-376

Ishihara K., 1993, Liquefaction and flow failure during earthquakes, Géotechnique, 43 (3), pp. 351-415

Ishihara K. and Koseki J., 1989, Discussion On The Cyclic Shear Strength Of Fines-Containing Sands, Earthquakes Geotechnical Engineering, Proceedings of the Eleventh International Conference on Soil Mechanics and Foundation Engineering, Rio De Janiero, Brazil, pp. 101-106

Jefferies M.G., Been K., Hachey J.E., 1990, The influence of scale on the constitutive behaviour of sand, In: Proceedings of the 43rd Canadian Geotechnical Conference, Quebec City, Canada, 1, pp. 263-273

Jefferies M., 1993, Nor-sand: A simple critical state model for sand, Géotechnique, 43 (1), pp. 91-103

Jefferies M. and Been K., 2000, Implications for critical state theory from isotropic compression of sand, Géotechnique, 50 (4), pp. 419-429

Karim M.E. and M.J. Alam, 2016, Undrained monotonic and cyclic response of sand-silt Mixtures, International Journal of Geotechnical Engineering ,10 (3), pp. 223-235

Kato S., Ishihara K. and Towhata I., 2001, Undrained shear characteristics of saturated sand under anisotropic consolidation, Soils and Foundations, 41 (1), 1-11

Katona M.G. and Zienkiewicz O.C., 1985, A unified set of single step algorithms Part 3: The Beta-m method, a generalization of the Newmark scheme, Int. J. Num. Meth. Eng., 21, pp. 1345-1359

Kishida H., 1969, Characteristics of Liquefied Sands during Mino-Owari, Tohnankai, and Fukui Earthquakes, Soils and Foundations, 9 (1), pp. 75-92

Klotz E.U. and Coop M.R., 2002, On the identification of critical state lines for sands, ASTM Geotechnical Testing Journal, 25 (3), pp. 289-302

Kokusho T., Ito F., Nagao Y. and Green A.R., 2012, Influence of non/low-plastic fines and associated aging effects on liquefaction resistance, Journal of Geotechnical and Geoenvironmental Engineering, 138 (6), pp. 747-756

Kolymbas D. and Herle I., 2005, Hypoplasticity as a Constitutive Framework for Granular soils, in Soil Constitutive Models: Evaluation, Selection and Calibration, J.A. Yamamuro and V. N. Kaliakin (eds), Geotechnical Special Publication No. 128, ASCE, pp. 257-289

Kramer S.L, 1996, Geotechnical Earthquake Engineering, Prentice-Hall International series in Civil Engineering and Engineering Mechanics, New Jersey, pp. 184-250; pp. 348-419

Kramer S.L. and Baska D.A., 2007, Estimation of permanent displacements due to lateral spreading, Journal of Geotechnical and Geoenvironmental Engineering, ASCE, 111 (6), pp. 772-792

Kramer S.L., Asl B.A., Ozener P. and Sideras S.S., 2015, Effects of liquefaction on ground surface motions, in perspectives on earthquake geotechnical engineering, Geotechnical Geological Earthquake Engineering, 37, pp. 285-309

Ladd R.S., 1978, Preparing specimens using undercompaction, ASTM Geotechnical Testing Journal 1978, 1 (1), pp. 16-23

Lade P.V. and Duncan J.M., 1975, Stress-path dependent behaviour of cohesionless soil, Journal of Geotechnical Engineering, ASCE, 101 (1), pp. 51-56

Lade P.V. and Kim M.K., 1988, Single hardening constitutive model for frictional materials II. Yield criterion and plastic work contours, Computers and Geotechnics, 6 (1), pp.13-29

Lade P.V. and Yamamuro J.A., 1997, Effects of non-plastic fines on static liquefaction of sands, Canadian Geotechnical Journal, 34 (6), pp. 918-928

Lai C.G., Bozzoni F., Mangriotis M. and Martinelli M., 2015, Soil liquefaction during the 20 may 2012 M5.9 Emilia earthquake, northern Italy: field reconnaissance and post-event assessment, Earthq Spectra, 31 (4), pp. 2351-2373

Lambe T.W. and Whitman R.V., 1969, Soil Mechanics, John Wiley and Sons, New York

Lanzo G., Vucetic M. and Doroudian M., 1997, Reduction of shear modulus at small strains in simple shear, Journal of Geotechnical and Geoenvironmental Engineering, 123 (11), pp. 1035-1042

Leroueil S. and Vaughan P.R., 1990, The general and congruent effects of structure in natural soils and weak rocks, Géotechnique, 40 (3), pp. 467-488

Li X.S. and Wang Y., 1998, Linear representation of steady-state line for sand, Journal of Geotechnical and Geoenvironmental Engineering, 124 (2), pp. 1215-1217

Li X.S., Dafalias Y.F., Wang Z.L., 1999, State-dependent dilatancy in critical-state constitutive modelling of sand, Canadian Geotechnical Journal, 36, pp. 599-611

Li X.S. and Dafalias Y. F., 2000, Dilatancy for cohesionless soils, Géotechnique, 50 (4), pp. 449-460

Ling H. and Yang S., 2006, Unified sand model based on the critical state and generalized plasticity, Journal of Engineering Mechanics, 132 (12), pp. 1380-1391

Lo S.R., Rahman M. M. and Bobei D.C., 2010, Limited flow behaviour of sand with fines under monotonic and cyclic loading, Geomechanics and Geoengineering, 5 (1), pp. 15-25

Lo Presti D. C. F., Sassu M., Luzi L., Pacor F., Castaldini D., Tosatti G., Meisina C., Zizioli D., Zucca F., Rossi G., Saccorotti G., Piccinini D., 2013, A report on the 2012 seismic sequence in Emilia (Northern Italy), Proc. 7th Int. Conf. on Case Histories in Geotechnical Engineering, Paper No. EQ-3, 30 pp.

Lopez-Querol S. and Coop M.R., 2012, Drained cyclic behaviour of loose Dogs Bay sand, Géotechnique, 62 (4), pp. 281-289

Luzzani L. and Coop M.R., 2002, On the relationship between particle breakage and the critical state of sands, Soils and Foundations, 42 (2), pp. 71-82

Maesano F.E., D'Ambrogi C., Burrato P. and Toscani G., 2015, Slip-rates of blind thrusts in slow deforming areas: examples from the Po Plain (Italy), Tectonophysics, 643, pp. 8-25

Manzanal D., Pastor M., Fernández Merodo J.A., 2011a, Generalized plasticity state parameter-based model for saturated and unsaturated soils, Part I: Saturated soil modelling, International Journal for Numerical and Analytical Methods in Geomechanics, 35 (18), pp. 1347-1362

Manzanal D., Pastor M., Fernández Merodo J.A., 2011b, Generalized plasticity state parameter-based model for saturated and unsaturated soils, Part II: Unsaturated soil modelling, International Journal for Numerical and Analytical Methods in Geomechanics, 35(18), pp. 1899-1917

Manzari M.T. and Dafalias Y.F, 1997, A two-surface critical plasticity model for sand. Géotechnique 47 (2), pp. 255-272

Marcuson W.F. III., 1978, Definition of terms related to liquefaction, Journal of Geotechnical Engineering, ASCE, 104 (9), pp. 1197-1200

Masing G., 1926, Eigenspannungen und Verfestigung beim Messing, Proc. 2nd Int. Cong. on Appl. Mech., 332-335

Matasović N. and Vucetic M., 1993, Cyclic Characterization of liquefiable sands, Journal of Geotechnical Engineering, 119 (11), pp. 1805-1822

Matasovi N. and Vucetic M., 1995, Generalized cyclic-degradation-porepressure generation model for clays, Journal of Geotechnical Engineering, 121 (1), pp. 33-42

Mayne P.W. and Kulhawy F.H., 1982, K0–OCR relationships in soil, Journal of the Geotechnical Engineering Division, 108 (6), pp. 851-872

McDowell G.R. and Bolton M.D., 1998, On the micromechanics of crushable aggregates, Géotechnique, 48 (5), pp. 667-679

McDowell G.R., 2002, A simple non-associated flow model for sand, Granular Matter, 4 (2), pp. 65-69

McDowell G.R. and Hau K.W., 2004, A generalised Modified Cam clay model for clay and sand incorporating kinematic hardening and bounding surface plasticity, Granular Matter, 6 (1), pp. 11-16

Mesri G. and Vardhanabhuti B., 2009, Compression of granular materials, Canadian Geotechnical Journal, 46 (4), pp. 369-392

Minarelli L., Amoroso S., Tarabusi G., Stefani M. and Pulelli G., 2016, Down-hole geophysical characterization of middle-upper Quaternary sequences in the Apennine Foredeep, Mirabello, Italy, Annals of Geophysics, 59 (5), 8 pp.

Mira P., 2001, Análisis por elementos finitos de problemas de rotura de geomaterials, PhD thesis, Universidad Politécnica De Madrid, pp. 257

Mira P. and Pastor M., 2002, Non-linear problems: Introduction, Numerical Modelling in Geomechanics, 6, pp. 1019-1036

Mira P., Pastor M., Li T. and Liu X., 2003, A new stabilized enhanced strain element with equal order of interpolation for soil consolidation problems, Comput. Methods Appl. Mech. Engrg., 192, pp. 4257-4277

Mira P., Tonni L., Pastor M. and Fernández Merodo J.A., 2009, A generalized midpoint algorithm for the integration of a Generalized Plasticity model for sands, International Journal for Numerical Methods in Engineering, 77 (9), pp. 1201-1223

Mogami T. and Kubo K., 1953, The behaviour of soil during vibration, Proceedings, 3rd International Conference on Soil Mechanics and Foundation Engineering, Zurich, 1, pp. 152-155

Mohammadi A. and Qadimi A., 2015, Characterizing the process of liquefaction initiation in Anzali shore sand through critical state soil mechanics, Soil Dynamics and Earthquake Engineering, 77, pp. 152-163

Monaco P., Tonni L., Gottardi G., Marchi M., Martelli L., Amoroso S. and Simeoni L., 2016, Combined use of SDMT-CPTU results for site characterization and liquefaction analysis of canal levees, Proceedings of the 5th International Conference on Geotechnical and Geophysical Site Characterisation (ISC'5), Gold Coast (AUS), 1, Sidney: Australian Geomechanics Society, pp. 615-620

Mroz Z., Norris V.A., Zienkiewicz O.C, 1978, Ananisotropic hardening model for soils and its application to cyclic loading, International Journal for Numerical and Analytical Methods in Geomechanics (2-3), pp. 203-221

Mroz Z. and Zienkiewicz O.C., 1984, Uniform formulation of constitutive equations for clays and sands, In: Mechanics of Engineering Materials, New York: Wiley, pp. 415-449

Muir Wood D., Belkheir K. and Liu D.F, 1994, Strain softening and state parameter for sand modeling, Géotechnique, 44 (2), pp. 335-339

Mulilis P.J., Seed B.H., Chan C.K., Mitchell J.K. and Arulanandan K., 1977, Effects of Sample Preparation on Sand Liquefaction, J. Geotech. D., 103 (2), pp. 91-108

Murthy T.G., Loukidis D., Carraro J.A.H., Prezzi M., Salgado R., 2007, Undrained mono-tonic response of clean and silty sands, Géotechnique, 57 (3), pp. 273-288

Nocilla A., Coop M.R. and Colleselli F., 2006, The mechanics of an Italian silt: an example of "Transitional" behavior, Géotechnique, 56 (4), pp. 261-271

Nova R. and Wood D.M., 1979, A constitutive model for sand in triaxial compression, International Journal for Numerical and Analytical Methods in Geomechanics, 3 (3), pp. 255-278

Oda M., Nemat-Nasser S. and Konishi J., 1985, Stress-induced anisotropy in granular materials, Soils and Foundations, Tokyo, 25 (3), pp. 85-97

Pacor F., Paolucci R., Luzi L., Sabetta F., Spinelli A., Gorini A., Nicoletti M., Marcucci S., Filippi L. and Dolce M., 2011, Overview of the Italian strong motion database ITACA 1.0., Bulletin Earthquake Engineering, 9 (6), pp. 1723-1739

Papadimitriou A.G., Bouckovalas G.D. and Dafalias Y.F., 2001, Plasticity model for sand under small and large cyclic strains, Journal of Geotechnical and Geoenvironmental Engineering, 127 (11), pp. 973-983

Park I.J. and Desai C.S., 2000, Cyclic behaviour and liquefaction of sand using disturbed state concept, Journal of Geotechnical and Geoenvironmental Engineering, 126 (9), pp. 834-846

Park S.S. and Kim Y.S., 2013, Liquefaction resistance of sand containing plastic fines with different plasticity, Journal of Geotechnical and Geoenvironmental Engineering, ASCE, 139 (5), pp. 825-830

Pastor M., Zienkiewicz O.C. and Leung K.H., 1985, Simple model for transient soil loading in earthquake analysis. II: non-associative models for sands, International Journal for Numerical and Analytical methods in Geomechanics, 9, pp. 477-498

Pastor M. and Zienkiewicz O.C., 1986, A generalized plasticity, hierarchical model for sand under monotonic and cyclic loading, 2nd International Symposium on Numerical Models in Geomechanic, Ghent, pp. 131-149

Pastor M., Zienkiewicz O.C. and Chan A.H.C, 1990, Generalized Plasticity and the modelling of soil behaviour, International Journal for Numerical and Analytical methods in Geomechanics, 14, pp. 151-190

Pastor M., 1991, Modelling of anisotropic sand behaviour, Computers and Geotechnics, 11 (3), pp. 173-208

Peacock W.H. and Seed H. B.,1968, Sand Liquefaction Under Cyclic Loading Simple Shear Conditions, Journal of the Soil Mechanics and Foundations Division, 94 (3), pp. 689-708

Pestana J.M. and Whittle A.J., 1995, Compression model for cohesionless soils, Géotechnique, 45 (4), pp. 611-632

Press W.H., Teukolsky S.A., Vetterling W.T. and Flannery B. P., 1992, Numerical recipes in FORTRAN, Cambridge University Press, 2nd Ed.

Prevost J.H., 1985, A simple plasticity theory for frictional cohesionless soils, Soil Dynamics And Earthquake Engineering, 4 (1), pp. 9-17

Pyke R. and Beikae M., 1993, TESS: a computer program for nonlinear ground response analysis, User's Manual, TAGA, Berkeley, Calif.

Qadimi A., 2005, The cyclic response of a carbonate sand through critical state soil mechanics, PhD thesis, London, Imperial College

Qadimi A. and Coop M.R., 2007, The undrained cyclic behaviour of a carbonate sand, Géotechnique, 57 (9), pp. 739-750

Qadimi A. and Mohammadi A., 2014, Evaluation of state indices in predicting the cyclic and monotonic strength of sands with different fines contents, Soil Dynamics And Earthquake Engineering, 66, pp. 443-458

Riemer M. and Seed R., 1997, Factors affecting apparent position of steady-state line, Journal of Geotechnical and Geoenvironmental Engineering, 123 (3), pp. 281-288

Robertson P.K., 2012, The James K. Mitchell Lecture: Interpretation of in-situ tests – some insights, Proceedings of the Proceedings of the 4th International Conference on Geotechnical and Geophysical Site Characterisation (ISC-4), Porto de Galinhas (Brazil), Taylor and Francis – Balkema, 2013, pp. 3-24

Rocchi I., 2014, An Experimental Investigation of the Influence of Weathering on Saprolitic Soils from Hong Kong, PhD thesis, City University Of Hong Kong

Romero E. and Jommi C., 2008, An insight into the role of hydraulic history on the volume changes of anisotropic clayey soils, Water Resources Research, 44, 16 pp.

Roscoe K.H. and Poorooshasb H.B., 1963, A fundamental principle of similarity in model test for earth pressure problems, Proceeding of 2nd Asian Conference on Soil Mechanics, Tokyo, Japan, pp. 134-140

Roscoe K.H. and Burland J.B., 1968, On the generalized stress–strain behaviour of 'wet' clay, In: Heyman, J., Leckie, F.A.(Eds.), Engineering Plasticity, Cambridge University Press, Cambridge, pp. 535-609

Russell A.R. and Khalili N., 2004, A bounding surface plasticity model for sands exhibiting particle crushing, Canadian Geotechnical Journal, 41 (6), pp. 1179-1192

Sandrolini F. and Franzoni E., 2010, Characterization procedure for ancient mortars' restoration: The plasters of the Cavallerizza courtyard in the Ducal Palace in Mantua (Italy), Materials Characterization, 61 (1), pp. 97-104

Sands C.M., Chandler H.W. and Guz I.A., 2011, Developing elasto-plastic models without establishing any expression for the yield function, International Journal for Numerical and Analytical methods in Geomechanics, 35, pp. 932-946

Seed H.B. and Lee K.L., 1967, Undraind strength characteristics of cohesionless soils, Journal of the Soil Mechanics and Foundations Division, 93 (6), pp. 333-360

Seed H.B., Tokimatsu K., Harder L. and Chung R.,1985, Influence Of SPT Procedures In Soil Liquefaction Resistance Evaluations, Journal of Geotechnical Engineering, ASCE, 111 (12), pp. 1425-1445

Seed R.B., Cetin K.O., Moss R.E.S., Kammerer A.M., Wu J., Pestana J.M. and Riemer M.F., 2001, Recent advances in soil liquefaction engineering and seismic site response evaluation, Proc. 4th Int. Conf. on Recent Advances in Geotechnical Earthquake Engineering and Soil Dynamics., Paper No. SPL-2, San Diego, California

Seed R.B., Cetin K.O., Moss R.E.S., Kammerer A., Wu J., Pestana J., Riemer M.F., Sancio R.B., Bray J.D., Kayen R.E. and Faris A., 2003, Recent advances in soil liquefaction engineering: A unified and consistent framework, Keynote presentation, 26th Annual ASCE Los Angeles Geotechnical Spring Seminar, Long Beach, CA

Shipton B. and Coop M.R., 2012, On the compression behaviour of reconstituted soils, Soils and Foundations, 52 (4), pp. 668-681

Sinatra L. and Foti S., 2015, The role of aftershocks in the liquefaction phenomena caused by the Emilia 2012 seismic sequence, Soil Dynamics And Earthquake Engineering, 75, pp. 234-245

Taiebat M. and Dafalias Y.F., 2010, Simple Yield Surface Expressions Appropriate for Soil Plasticity, International Journal of Geomechanics, 10 (4), pp. 161-169

Thevanayagam S., Shenthan T., Mohan S. and Liang J., 2002, Undrained fragility of clean sands, silty sands and sandy silts, Journal of Geotechnical and Geoenvironmental Engineering ASCE, 128 (10), pp. 849-859

Tohno I. and Yasuda S., 1981, Liquefaction of the Ground During the 1978 Miyagiken-Oki Earthquake, Soils and Foundations, 21 (3), pp. 18-34

Tonni L., 2002, Modellazione numerica del comportamento di terreni granulari con la Plasticità Generalizzata, Tesi di Dottorato, Dottorato di Ricerca in Ingegneria Geotecnica, Politecnico di Torino

Tonni L., Mira P., Fernández Merodo J.A. and Pastor M., 2003, FE analysis of san behaviour using a generalized plasticity model with implicit integration, VII International Conference on Computational Plasticity, COMPLAS 2003, Barcelona

Tonni L., Mira P., Pastor M. and Fernández Merodo J.A., 2005, Numerical modelling of granular soils using generalized plasticity, Proceeding of the Eleventh International Conference on Computer Methods and Advances in Geomechanics, Torino, pp. 199-206

Tonni L., Cola S. and Pastor M., 2006, A Generalized Plasticity approach for describing the behaviour of silty soils forming the Venetian lagoon basin. Numerical Methods in Geotechnical Engineering, pp. 93-99

Tonni L. and Gottardi G., 2010, Interpretation of piezocone tests in Venetian silty soils and the issue of partial drainage. Deep Foundations and Geotechnical In Situ Testing, ASCE Geotechnical Special Publication (GSP 205), pp. 367-374

Tonni L., Gottardi G., Amoroso S., Bardotti R., Bonzi L., Chiaradonna A., d'Onofrio A., Fioravante V., Ghinelli A., Giretti D., Lanzo G., Madiai C., Marchi M., Martelli L., Monaco P., Porcino D., Razzano R., Rosselli S., Severi P., Silvestri F., Simeoni L., Vannucchi G. and Aversa S., 2015a, Analisi dei fenomeni deformativi indotti dalla sequenza sismica emiliana del 2012 su un tratto di argine del Canale Diversivo di Burana (FE), Rivista Italiana di Geotecnica (2), pp. 28-58

Tonni L., Forcellini D., Osti C. and Gottardi G., 2015b, Modelling liquefaction phenomena during the May 2012 Emilia-Romagna (Italy) earthquake, In: Proceedings of the XVI European Conference on Soil Mechanics and Geotechnical Engineering (ECSMGE), Edinburgh (UK), 4, London: ICE Publishing, pp. 2225-2230

Tonni L., Gottardi G., Marchi M., Martelli L., Monaco P., Simeoni L. and Amoroso S., 2015c, SDMT-based site characterization and liquefaction analysis of canal levees damaged by the 2012 Emilia (Italy) seismic sequence, Proceedings of the 3rd International Conference on the Flat Dilatometer (DMT'15), Rome, pp. 341-348

Uriel S., 1975, Intrinsic dynamic of the quasi-static mechanics of granular soils, In Numerical Methods in Soil and Rock Mechanics, Borm G., Meissher H. (eds), Institut fu Bondenmechanik und Felsmechanik der Universitat Karlsruhe, Karlsruhe, pp. 61-70

Vaid Y.P., Sivathayalan S. and Stedman D., 1999, Influence of Specimen-Reconstituting Method on the Undrained Response of Sand, Geotechnical Testing Journal, 22 (3), pp. 187-195

Vannucchi G., Crespellani T., Facciorusso J., Ghinelli A., Madiai C., Puliti A. and Renzi S., 2012, Soil liquefaction phenomena observed in recent seismic events in Emilia- Romagna Region, Italy, Ingegneria sismica, 26 Anno XXIX – N. 2-3, pp. 20-30

Verdugo R. and Ishihara K., 1996, The steady state of sandy soils, Soil and Foundation, 36 (2), pp. 81-91

Vincens E., Yunus Y. and Cambou B., 2010, Modelling of volume change in granular materials in relation to their internal state, C. R. Mecanique, 338, pp. 615-626

Vucetic M., 1990, Normalized behavior of clay under irregular cyclic loading, Canadian Geotechnical Journal, 27, pp. 29-46

Vucetic M. and Dobry R., 1991, Effect of Soil Plasticity on Cyclic Response, Journal of Geotechnical Engineering, 117 (1), pp. 89-107

Vucetic M., 1994, Cyclic Threshold Shear Strains in Soils, Journal of Geotechnical Engineering, 120 (12), pp. 2208-2228

Wan R.G. and Guo P.J., 1998, A simple constitutive model for granular soils: modified stress-dilatancy approach, Computers and Geotechnics, 22 (2), pp. 109-133

Wang Z.L., Dafalias Y.F., Li X.S. and Makdisi F.I., 2002, State pressure index for modelling sand behaviour, Journal of Geotechnical and Geoenvironmental Engineering, 128 (6), pp. 511-519

Weng M.C. and Ling H.I., 2013, Modeling the behaviour of sandstone based on generalized plasticity concept, International Journal for Numerical and Analytical Methods in Geomechanics, 37 (14), pp. 2154-2169

Wheeler S.J., Näätänen A., Karstunen M. and Lojander M., 2003, An anisotropic model for soft clays, Canadian Geotechnical Journal, 40, pp. 403-418

Wood F.M., Yamamuro J.A. and Lade P.V., 2008, Effect of depositional method on undrained response of silty sand, Canadian Geotechnical Journal, 45 (11), pp. 1525-1537

Wu W. and Bauer E., 1993, A hypoplastic Model for barotropy and pyknotropy of granular soils, in Modern approaches to plasticity, D. Kolymbas (eds). Soil Constitutive Models. Elsevier, pp. 225-245

Yamamuro, J.A. and Lade P.V., 1998, Steady-state concepts and static liquefaction of silty sands, Journal of Geotechnical and Geoenvironmental Engineering, 124 (9), pp. 868-877

Yamamuro J. A. and Covert K. M., 2001, Monotonic and cyclic liquefaction of very loose sands with high silt content, Journal of Geotechnical and Geoenvironmental Engineering, 127 (4), pp.314-324

Yamamuro J.A. and Wood F.M., 2004, Effect of depositional method on the undrained behavior and microstructure of sand with silt, Soil Dynamics and Earthquake Engineering, 24 (9), pp. 751-760

Yang Z., Elgamal A. and Parra E., 2003, Computational Model for Cyclic Mobility and Associated Shear Deformation, Journal of Geotechnical and Geoenvironmental Engineering, ASCE, pp. 1119-1127

Yang S.L., Lacasse S. and Sandven R., 2006, Determination of the Transitional Fines Content of Mixtures of Sand and Non-plastic Fines, Geotechnical Testing Journal, 29 (2), pp. 102-107

Yoshimine M. and Ishihara K., 1998, Flow potential of sand during liquefaction, Soils and foundations, 38 (3), pp. 189-198

Yoshimine M., Nishizaki H., Amano K. and Hosono Y., 2006, Flow deformation of liquefied sand under constant shear load and its application to analysis of flow side in infinite slope, Soil Dynamics and Earthquake Engineering, 26, pp. 567-584

Youd T.L., Idriss I.M., Andrus R.D., Arango I., Castro G., Christian J.T., Dobry R., Finn W.D.L., Harder Jr. L.F., Hynes M.E., Ishihara K., Koester J.P., Liao S.S.C., Marcuson III W.F., Martin G.R., Mitchell J.K., Moriwaki Y., Power M.S., Robertson P.K., Seed R.B. and Stokoe II K.H., 2001, Liquefaction Resistance of Soils: Summary Report from the 1996 NCEER and 1998 NCEER/NSF Workshops on Evaluation of Liquefaction Resistance of Soils, Journal of Geotechnical and Geoenvironmental Engineering, ASCE, 127 (10), pp. 817-833

Youd T.L., Hansen C.M. and Bartlett S.F., 2002, Revised multilinear regression equations for prediction of lateral spread displacement, Journal of Geotechnical and Geoenvironmental Engineering, 128 (12), pp. 1007-1017

Yu F.W., 2017, Particle breakage and the critical state of sands, Géotechnique, 67 (8), pp. 713-719

Zhang H.W., Sanavia L. and Schrefler B.A., 2001, Numerical analysis of dynamic strain localization in initially water saturated dense sand with a modified generalized plasticity model, Computers and Structures, 79 (4), pp. 441-459

Zhang G., Roberson P.K. and Brachman R.W.I., 2004, Estimating liquefaction-induced lateral displacements using the Standard Penetration Test or Cone Penetration Test, Journal of Geotechnical and Geoenvironmental Engineering, pp. 861-870

Zienkiewicz O.C. and Morz Z., 1984, Generalized plasticity formulation and application to geomechanics. In Mechanics of Engineering Materials, Desai CS, Gallagher RH (eds), Wiley, pp. 655-679

Zienkiewicz O.C., Leung K.H. and Pastor M., 1985, Simple model for transient soil loading in earthquake analysis. I. basic model and its application, International Journal for Numerical and Analytical methods in Geomechanics, 9 (5), pp. 453-476

Zienkiewicz O.C., Chan A.H.C., Pastor M., Schrefler B.A. and Shiomi T., 1999, Computational Geomechanichs with Special Reference to Earthquake Engineering, John Wiley & Sons Ltd

Zlatovic S. and Ishihara K., 1997, Normalized behavior of very loose non-plastic soils: effects of fabric, Soils and Foundations, 37 (4), pp. 47-56